

Thin Shell Finite Element Formulations for Geometrically Non-Linear Analysis of Straight and Curved Pipes

By

Saher Salama Attia

A thesis submitted in partial fulfillment of the requirements for the degree of

Doctor of Philosophy

In

Structural Engineering

Department of Civil and Environmental Engineering

University of Alberta

© Saher Salama Attia, 2021

Abstract

Special finite element formulations were developed to accurately predict the structural response of straight and curved pipes. Although the ELBOW elements implemented in the ABAQUS library have been verified under in-plane and out-of-plane loading, the effect of internal pressure loading had not been well addressed. Therefore, a detailed assessment for the structural response of the ELBOW elements under internal pressure is introduced showing their limitations. One of these limitations is the inability of the ELBOW elements to model initial geometric imperfections associated with the manufacturing processes of pipes. The influence of these imperfections is tangible and cannot be ignored, particularly the initial ovality of the pipe. Thus, new finite element formulations are developed to model thin-walled straight and curved pipes with generic cross-sections to involve initial geometric imperfections.

In order to develop these new formulations, the writer adopts the cumulative learning approach through developing three families of formulations: (1) a family for initially circular straight pipes, (2) a family for initially circular curved pipes, and (3) a family for straight and curved pipes with general cross-sections.

Starting with the principle of virtual work, generalized expressions for the force vectors and the stiffness matrix are obtained in terms of a generic displacement field vector. These expressions are specialized for initially circular straight pipes in Chapter 3 by employing a cylindrical coordinate system. The accuracy of the formulations developed in Chapter 3 encouraged the writer to employ a toroidal coordinate system in conjunction with these generalized expressions to model initially circular curved pipes as introduced in Chapter 4.

An innovative idea is presented to capture initial geometric imperfections by introducing three configurations (e.g., un-deformed, deformed, reference) of the pipe under consideration. Strains and stresses induced due to the motion are formulated in the reference configuration. Although the numerical examples are focused on ovalized pipes, the mathematical approach proposed in Chapter 5 is applicable to model straight and curved pipes with generic cross-sections.

Comparisons with general shell models demonstrate the accuracy and versatility of the proposed formulations to predict the structural response of initially circular and ovalized straight and curved thin-walled pipes under various loading conditions. In addition, the effect of the follower pressure load (e.g., internal or external pressure) is properly included.

Preface

This dissertation forms a research collaboration between Mr. Saher Attia (i.e., the writer of this dissertation), Professor Samer Adeeb, Dr. Yong Li at University of Alberta, Professor Magdi Mohareb at University of Ottawa, Nader Yoosef-Ghodsi at Enbridge Inc., and Michael Martens at TC Energy.

Chapter 1 is an introductory chapter which includes previous research works relevant to the purpose of this dissertation and Chapter 6 presents a summary and conclusions. The main body of this dissertation is Chapters 2, 3, 4, and 5 which are research articles either submitted for review or published into international journals. Chapters 1 and 6 are all the original work of Mr. Attia and Chapter 2 has been published as Attia, S., Mohareb, M., Martens, M., Yoosef-Ghodsi, N., Li, Y., and Adeeb, S., 2021, “Numerical Assessment of Elbow Element Response Under Internal Pressure,” ASME. J. Pressure Vessel Technol., 143(5):051302. <https://doi.org/10.1115/1.4050091> while Chapters 3-5 have been submitted for review.

Mr. Attia was the principal investigator for all the research works carried out herein including concept formation, codes implementation, analysis, and manuscript composition. Prof. Adeeb and Prof. Mohareb provided concept improvement, technical and editorial comments, and manuscript review. All other authors reviewed the results and provided editorial comments.

Since science is cumulative and continuous effort, Mr. Attia encourages readers to feel free to use any part of this dissertation for their research. However, they must cite the research articles that formed this dissertation or the dissertation itself.

“Chess and life are action-based and irreversible games. While chess is a fair game with fixed rules, life is a biased game with contradicted rules”

Saher Attia, 2021

Acknowledgment

Life is usually a difficult journey, full of pain, stress, and struggles with flashes of happiness and satisfaction. By analogy, my PhD journey was a miniature model of the life journey. Three main parameters play a basic role to reach the end of this journey: (1) Faith, (2) Love, and (3) Support.

Faith in the Almighty Allah is a fundamental reason to move on after each pain. The trust in his greatness, plan, kindness, forgiveness was food of this journey. No words can describe my thanks to Allah. Allah does not need my thanks; however, I need his generousness.

Love of my family was oxygen and water in this journey. My mother taught me the basics of life with infinite love, great tenderness. Her support and encouragement are the light during hardships. My father is the man I always trust and value his opinions, vision, and wisdom. Seif, my brother, is my backbone.

Support of my supervisors: Prof. Samer Adeeb and Prof. Magdi Mohareb was limitless. No words can highlight their continuous help, immense knowledge, patience, and motivation. They taught me not only mechanics of solid bodies but also the mechanics of life. They were the sun which lighted the dark of my mind.

No journey nor success are without friends. Thank you all for your support. Thank you Guys 🤝.

Table of Contents

Abstract	ii
Preface	iv
Acknowledgement.....	vi
Table of Contents	vii
List of Tables.....	xii
List of Figures.....	xiv
Chapter 1 Introduction	1
1.1 Introduction.....	1
1.2 Literature review	2
1.2.1 Theoretical studies	2
1.2.2 Numerical studies.....	4
1.2.3 Finite element formulation for pipe/elbow element.....	6
1.2.4 Nonlinear treatment	9
1.2.5 Influence of initial geometric imperfections.....	11
1.2.6 Historical developments of thin shell theory	14
1.3 Problem statement.....	16
1.4 Objectives.....	17
1.5 Outline of dissertation	17
1.6 References	20
Chapter 2 Numerical Assessment of Elbow Element Response under Internal Pressure.....	23
2.1 Abstract	23
2.2 Introduction.....	23
2.3 Methodology	29
2.4 Results and Discussion.....	32
2.4.1 Results for Case I (pipe bend without straight portions)	32
2.4.2 Results for Case II (Two pipe bends connected with straight portions).....	43
2.4.3 Assessment of ASME B16.49 2017 [16] and previous stress estimates [6].	46
2.5 Conclusion.....	49
2.6 Acknowledgment	51
2.7 Funding.....	51

2.8 Nomenclature	51
2.9 Appendix 2.A – Additional Results for Case I	52
2.10 Supplemental Material - Modelling of pipe bends.....	59
2.11 References	61
Chapter 3 Shell Finite Element Formulation for Geometrically Nonlinear Analysis of Straight Thin-Walled Pipes	63
3.1 Abstract	63
3.2 Introduction	64
3.3 Assumptions	66
3.4 Formulation	67
3.4.1 Principle of virtual work	67
3.4.2 First Piola-Kirchhoff stress tensor in terms of the displacements	67
3.4.3 Virtual displacement fields in terms of virtual nodal degrees of freedom.....	68
3.5 Force Vectors and Stiffness Matrix.....	69
3.5.1 Internal and External Force Vectors	69
3.5.2 Tangent stiffness matrix.....	70
3.5.3 Approximation of the tangent stiffness matrix	71
3.5.4 Contribution of the external force vector to the stiffness matrix	71
3.6 Displacement fields in cylindrical coordinates	73
3.6.1 Geometric description.....	73
3.6.2 Normal unit vector	74
3.6.3 Displacement fields for a point offset from the middle surface.....	76
3.7 Gradient of the displacement field vector and its derivative.....	76
3.8 Interpolation Schemes	77
3.8.1 First scheme – Fourier series interpolation.....	78
3.8.2 Second scheme – Spline interpolation	79
3.8.3 Third scheme – Mixed interpolation.....	83
3.8.4 Iterative solution scheme	84
3.9 Numerical Examples	85
3.9.1 Combined axial and vertical loading	86
3.9.2 Uniform internal pressure	92
3.9.3 Combined loading.....	93
3.10 Summary	99

3.11 Appendix 3.A: Derivatives of displacement fields with respect to coordinates	100
3.12 Appendix 3.B: Derivatives of displacement fields with respect to nodal degrees of freedom.....	102
3.13 Appendix 3.C: Interpolation Schemes	106
3.14 Appendix 3.D: Strain Fields for Example 1	111
3.15 Nomenclature	112
3.16 Acknowledgments.....	115
3.17 Funding.....	115
3.18 References	115
Chapter 4 Shell Finite Element Formulation for Geometrically Nonlinear Analysis of Curved Thin-Walled Pipes	117
4.1 Abstract	117
4.2 Introduction	117
4.3 Assumptions.....	120
4.4 Overview on the formulation	121
4.5 Displacement fields in toroidal coordinates.....	122
4.5.1 Geometric description.....	122
4.5.2 Unit normal vector	123
4.5.3 Displacement fields for a point offset from the mid-surface	125
4.6 Gradient of the displacement field vector and its derivative.....	126
4.7 Interpolation Schemes	127
4.8 Rigid Body Motion	129
4.9 Examples	133
4.9.1 Example 1	134
4.9.2 Example 2	138
4.9.3 Example 3	140
4.9.4 Example 4	142
4.10 Summary and Conclusions.....	143
4.11 Appendix 4.A: Derivatives of displacement fields with respect to coordinates	145
4.12 Appendix 4.B: Derivatives of displacement fields with respect to nodal degrees of freedom.....	147
4.13 Appendix 4.C: Zero Energy Modes	153
4.14 Nomenclature	161

4.15 Acknowledgments	163
4.16 Funding.....	163
4.17 References	163
Chapter 5 Shell Finite Element Formulation of Ovalized Thin-Walled Pipes	165
5.1 Abstract	165
5.2 Introduction	165
5.2.1 Pipe finite element solutions.....	166
5.2.2 Principle of virtual work for nonlinear solutions	167
5.2.3 Influence of initial ovality on the pipe response	168
5.3 Assumptions	170
5.4 Preliminaries.....	170
5.4.1 Geometry.....	170
5.4.2 Notation.....	171
5.5 Formulation	172
5.5.1 Deformation gradient tensors.....	172
5.5.2 Strain and stress tensors expressed in the initial configuration	172
5.5.3 First Piola-Kirchhoff stress tensor in terms of deformation gradient tensors	173
5.5.4 Principle of virtual work	174
5.6 Force vectors and stiffness matrix.....	175
5.7 Displacement fields	176
5.7.1 Straight Pipes	176
5.7.2 Treatment of pipe bends.....	179
5.8 Numerical Examples	181
5.8.1 Straight Pipes	181
5.8.2 Curved Pipes	189
5.9 Summary	197
5.10 Nomenclature	198
5.11 Acknowledgments.....	200
5.12 Funding.....	200
5.13 References	201
Chapter 6 Summary & Conclusion.....	204
6.1 Summary and conclusion	204

6.2 Limitations of the developed formulations 206
6.3 Proposed future work 207
References.....208

List of Tables

Table 2. 1 Parametric runs for Case I and Case II	30
Table 2. 2 Force reaction components of the pipe bend obtained using shell and elbow formulations for Case I.....	33
Table 2. 3 Hoop stress values and stress ratios of Case I and Case II	47
Table 2. 4 Approximate equations for the elastic stress fields of a pipe bend attached to straight portions	48
Table 2. 5 Stress results of shell models, elbow models, and approximate formulas.....	49
Table 3. 1 Detailed description of the FE models.....	86
Table 3. 2 Percentage differences of the longitudinal and vertical displacements at the free end	89
Table 3. 3 Longitudinal and radial displacements at the free end	93
Table 3. 4 Longitudinal (L) and circumferential (C) stresses at the mid-span	93
Table 3. 5 Percentage differences of the longitudinal, circumferential, and radial displacements at the free end.....	97
Table 4. 1 Effect of element interpolation type on RBM - Lowest eight eigenvalues ($R = 1.5D_o$, member angle= 90° , and six Fourier modes)	131
Table 4. 2 Effect of number of Fourier modes on RBM - Lowest eight eigenvalues - (M-element with 90° angle, $R = 1.5D_o$)	132
Table 4. 3 Effect of element angle on RBM - Lowest eight eigenvalues (M- element with six Fourier modes, $R = 1.5D_o$)	132
Table 4. 4 Effect of R / D_o on RBM - Lowest eight eigenvalues (M-element with six Fourier modes, element angle= 90°).....	133
Table 4. 5 Radial and longitudinal displacements at the top section	139
Table 4. 6 von-Mises stresses (MPa) at the inner and outer surfaces ($\theta = 45^\circ$)	140
Table 4. 7 Circumferential displacement ^a at the top section.....	141
Table 4. 8 von Mises stresses (MPa) at $\theta = 45^\circ$ for the inner and outer surfaces.....	141

Table 4. C. 1 Graphical representation of eigenmodes corresponds to the lowest eight eigenvalues obtained in Table 4. 1 using Element M.....	156
Table 5. 1 Inputs of Example 1 and Example 2.....	182
Table 5. 2 Hoop stress values (MPa) at the inner and outer surfaces.....	187
Table 5. 3 Maximum hoop stress values (MPa).....	189
Table 5. 4 Initial ovality profile of the pipe bend (symmetric at $\theta = 45^\circ$).....	190
Table 5. 5 Loading cases of the curved pipe.....	191
Table 5. 6 Values of maximum longitudinal and radial displacements (mm).....	192

List of Figures

Fig. 2. 1 Geometry of the pipe bend in Case I	27
Fig. 2. 2 Geometry of the piping system in Case II	28
Fig. 2. 3 True stress-strain curve for the elasto-plastic models ($R= 1.5D_o$ - Case I)	31
Fig. 2. 4 Default-closed end condition of a pipe bend	32
Fig. 2. 5 Simulation of open-ended condition.....	32
Fig. 2. 6 Stress fields versus circumferential angle θ at section A-A ($R=5D_o$ – Fixed-Free). (a) Von Mises stress, (b) Hoop stress, and (c) Longitudinal stress	35
Fig. 2. 7 Stress fields versus circumferential angle θ at section A-A ($R=1.5D_o$ – Fixed-Free – Kinematic coupling). (a) Von Mises stress, (b) Hoop stress, and (c) Longitudinal stress.....	36
Fig. 2. 8 Stress fields versus circumferential angle θ at section A-A ($R=1.5D_o$ – Fixed-Free – Direct constraints). (a) Von Mises stress, (b) Hoop stress, and (c) Longitudinal stress	37
Fig. 2. 9 (a) Original and deformed configurations and (b) Displacements fields versus circumferential angle θ generated by the shell model (Section A-A- $R=5D_o$ – Fixed-Free)	38
Fig. 2. 10 Stress fields versus circumferential angle θ at section A-A ($R=1.5D_o$ – Fixed-Free). (a) Von Mises stress, (b) Hoop stress, and (c) Longitudinal stress	39
Fig. 2. 11 Stress fields versus circumferential angle θ at section A-A ($R=1.5D_o$ – Fixed-Fixed – Plastic analysis). (a) Von Mises stress, (b) Hoop stress, and (c) Longitudinal stress.....	41
Fig. 2. 12 Total equivalent plastic strain (PEEQ) versus circumferential angle θ at section A-A ($R=1.5D_o$ – Fixed-Fixed – Middle surface– Plastic analysis).....	42
Fig. 2. 13 (a) Maximum principal plastic strain and (b) Total longitudinal strain versus applied internal pressure at the intrados of section A-A ($R=1.5D_o$ – Fixed-Fixed – Middle surface– Plastic analysis)	42
Fig. 2. 14 Stress fields versus circumferential angle θ at section A-A (a) Von Mises stress, (b) Hoop stress, and (c) Longitudinal stress	44
Fig. 2. 15 Stress fields versus circumferential angle θ at section B-B (a) Von Mises stress, (b) Hoop stress, and (c) Longitudinal stress	46
Fig. 2. 16 Geometric properties of the cross section of the pipe bend used by Hong [6].....	48

Fig. 2. A. 1 Stress fields versus circumferential angle θ at section A-A for $R=5D_o$ (a) Von Mises stress, (b) Hoop stress, and (c) Longitudinal stress	53
Fig. 2. A. 2 Stress fields versus circumferential angle θ at section A-A for $R=1.5D_o$ (a) Von Mises stress, (b) Hoop stress, and (c) Longitudinal stress	54
Fig. 2. A. 3 Stress fields versus circumferential angle θ at section A-A for $R=5D_o$ (a) Von Mises stress, (b) Hoop stress, and (c) Longitudinal stress	55
Fig. 2. A. 4 Stress fields versus circumferential angle θ at section A-A for $R=1.5D_o$ (a) Von Mises stress, (b) Hoop stress, and (c) Longitudinal stress	56
Fig. 2. A. 5 Stress fields versus circumferential angle θ at section A-A for $R=5D_o$ (a) Von Mises stress, (b) Hoop stress, and (c) Longitudinal stress	57
Fig. 2. A. 6 Stress fields versus circumferential angle θ at section A-A for $R=1.5D_o$ (a) Von Mises stress, (b) Hoop stress, and (c) Longitudinal stress	58
Fig. 2. S. 1 Half of the pipe bend using shell element ($R=5D_o$)	59
Fig. 2. S. 2 Pipe bend using elbow element ($R=5D_o$)	60
Fig. 2. S. 3 Required changes in the input file to define the elbow section.....	61
Fig. 3. 1 (a) Pipe coordinates and vector bases and (b) Pipe displacements.....	74
Fig. 3. 2 Cross section discretization	80
Fig. 3. 3 The cantilever pipe	85
Fig. 3. 4 Displacement fields distributions along the cantilever pipe at $\varphi = 0^\circ$ (a) Longitudinal displacement, (b) Circumferential displacement, and (c) Radial displacement.....	88
Fig. 3. 5 Stress fields versus circumferential angle at the middle section $z = 5m$ (a) Longitudinal- Inner, (b) Longitudinal-Outer, (c) Circumferential-Inner, (d) Circumferential-Outer, (e) Shear- Inner, and (f) Shear-Outer.....	92
Fig. 3. 6 Displacement fields along the length of the pipe at $\varphi = 0^\circ$ (a) Longitudinal, (b) Circumferential, and (c) Radial.....	95
Fig. 3. 7 Displacement fields along the length of the pipe at $\varphi = 90^\circ$ (a) Longitudinal, (b) Circumferential, and (c) Radial.....	96

Fig. 3. 8 Stress fields versus circumferential angle at the middle section $z = 5m$ (a) Longitudinal- Inner, (b) Longitudinal-Outer, (c) Circumferential-Inner, (d) Circumferential-Outer, (e) Shear- Inner, and (f) Shear-Outer.....	99
Fig. 3. C. 1 Nodes of pipe element based on Fourier interpolation	107
Fig. 3. C. 2 Longitudinal displacements distributions corresponding to Fourier modes 1-6.....	108
Fig. 3. C. 3 Radial displacements distributions corresponding to Fourier modes 1-6.....	109
Fig. 3. C. 4 Nodes for a Spline element based on linear interpolation along the longitudinal direction and quartic spline interpolation along the circumferential direction.	110
Fig. 3. D. 1 Strain fields versus circumferential angle at the middle section $z = 5m$ (a) Longitudinal-Inner Surface, (b) Longitudinal-Outer Surface, (c) Circumferential-Inner Surface, (d) Circumferential-Outer Surface, (e) Shear-Inner Surface, and (f) Shear-Outer Surface.....	111
Fig. 4. 1 Pipe bend coordinates, vector bases, and displacement vector	123
Fig. 4. 2 Geometry of the pipe bend	134
Fig. 4. 3 Pipe bend under internal pressure.....	136
Fig. 4. 4 Stress fields versus circumferential angle at section A-A (a) Longitudinal-Inner Surface, (b) Longitudinal-Outer Surface, (c) Circumferential-Inner Surface, (d) Circumferential-Outer Surface, (e) Shear-Inner Surface, and (f) Shear-Outer Surface	138
Fig. 4. 5 Pipe bend under in-plane loading	139
Fig. 4. 6 Pipe bend under out-of-plane loading	141
Fig. 4. 7 Pipe bend under torsional moment	142
Fig. 4. 8 Shear stress distribution versus the circumferential angle for $R / D_o = 1.5$	143
Fig. 4. 9 Shear stress distribution versus the circumferential angle for $R / D_o = 5$	143
Fig. 4. C. 1 1D truss element and corresponding rigid body modes (i.e., eigenmodes) (a) Degrees of freedom of the truss element, (b) Vertical rigid body displacement mode, (c) Horizontal rigid body displacement mode, (d) Rigid body rotation mode, and (e) Combined rigid body mode.	155

Fig. 4. C. 2 Strain field distributions over the element corresponding to the first zero eigenvalue induced by magnified eigenvector $1000V_i$ (a) Longitudinal - Inner Surface, (b) Longitudinal - Middle Surface, (c) Longitudinal -Outer Surface, (d) Circumferential - Inner Surface, (e) Circumferential -Middle Surface, (f) Circumferential -Outer Surface, (g) Shear - Inner Surface, (h) Shear -Middle Surface, and (i) Shear -Outer Surface	158
Fig. 4. C. 3 Strain field distributions over the element corresponding to the second zero eigenvalue induced by magnified eigenvector $1000V_i$ (a) Longitudinal - Inner Surface, (b) Longitudinal - Middle Surface, (c) Longitudinal -Outer Surface, (d) Circumferential - Inner Surface, (e) Circumferential -Middle Surface, (f) Circumferential -Outer Surface, (g) Shear - Inner Surface, (h) Shear -Middle Surface, and (i) Shear -Outer Surface	159
Fig. 4. C. 4 Strain field distributions over the element corresponding to the third zero eigenvalue induced by magnified eigenvector $1000V_i$ (a) Longitudinal - Inner Surface, (b) Longitudinal - Middle Surface, (c) Longitudinal -Outer Surface, (d) Circumferential - Inner Surface, (e) Circumferential -Middle Surface, (f) Circumferential -Outer Surface, (g) Shear - Inner Surface, (h) Shear -Middle Surface, and (i) Shear -Outer Surface	160
Fig. 5. 1 Cross section of a pipe in three configurations.....	171
Fig. 5. 2 Pipe coordinate and vector bases in the reference configuration of a straight pipe	177
Fig. 5. 3 Pipe coordinate and vector bases in the reference configuration of a curved pipe	181
Fig. 5. 4 Geometry of straight pipe	182
Fig. 5. 5 Geometry of the imperfect pipe in Example 1	183
Fig. 5. 6 Geometry of the imperfect pipe in Example 2	183
Fig. 5. 7 Displacement field distributions along the circumferential direction at $z = 3m$. (a) Radial and (b) Circumferential.....	185
Fig. 5. 8 Hoop stress distributions under internal pressure at $z = 3m$ for the (a) Inner Surface and (b) Outer Surface.....	185
Fig. 5. 9 Hoop stress distributions under external pressure at $z = 3m$ for the (a) Inner Surface and (b) Outer Surface.....	187
Fig. 5. 10 Von Mises stress distribution along the circumferential direction at the (a) Inner Surface and (b) Outer Surface.....	189

Fig. 5. 11 Geometry of the pipe bend	190
Fig. 5. 12 Displacement field distributions along the circumferential angle at $\theta = 45^\circ$	192
Fig. 5. 13 Stress fields along the circumferential angle at $\theta = 45^\circ$ for the (a) Longitudinal - Inner Surface, (b) Longitudinal -Outer Surface, (c) Hoop - Inner Surface, and (d) Hoop -Outer Surface	194
Fig. 5. 14 Stress fields along the circumferential angle at $\theta = 45^\circ$ for the (a) Longitudinal - Inner Surface, (b) Longitudinal -Outer Surface, (c) Hoop - Inner Surface, and (d) Hoop -Outer Surface	196

Chapter 1

Introduction

1.1 Introduction

Pipeline transmission systems play a vital role in various engineering fields such as oil, gas, and petrochemical industry, in which the extracted resources and related materials are conveyed from centers of production to centers of consumption. Also, these systems form an integral part of water supply systems and bio-mechanical applications. Under general loading (e.g., mechanical loading and/or thermal loading), piping systems experience complex deformation patterns (e.g., ovalization, and warping) due to the flexibility of their hollow circular cross-sections. Efficient and accurate analysis tools are thus essential for pipe structural integrity, optimal performance, and economics.

Pipe bends (i.e., curved pipes) are commonly used in piping systems in order to allow direction changes and provide flexible loops to guard against excessive axial stresses due to thermal expansions. The geometric characteristics of pipe bends, as a doubly curved surface, provide more flexibility than straight pipes. Therefore, ovalization and warping effects are highly pronounced in the deformation patterns of pipe bends.

Beam theories based on the rigid cross-section hypothesis, are inadequate to predict the structural response of pipe bends under general loads. In contrast, shell or three-dimensional theories of

structures are well-suited for the analysis of pipe bends as these theories accurately capture the complex deformation patterns of pipe bends. However, the rather high computational cost and significant effort in building and post-processing such pipeline models make the use of these theories limited in practical design environments, particularly when modelling long lines of pipes. An efficient and computationally effective numerical tool is hence required to achieve a balance between the accuracy of the solution and the associated computational cost and modelling effort.

Over the last few decades, many researchers developed accurate and computationally effective numerical tools for the structural analysis of initially circular pipe bends. In contrast, the manufacturing process of pipe bends are associated with various types of initial geometric imperfections (e.g., initial ovality, wall thickness variability) which have a tangible influence on the structural response of pipe bends. Consequently, there is a need to develop a new numerical tool for the analysis of pipe bends that captures the effects of the initial geometric imperfections.

In the present dissertation, novel and relatively simple finite element formulations are developed that are able to accurately model initial geometric imperfections of thin-walled straight and curved pipes and properly predict the realistic structural response of imperfect pipes under general loading conditions.

1.2 Literature review

1.2.1 Theoretical studies

Due to the curvature of pipe bends, their structural response (e.g., flexibility and maximum stresses) cannot be accurately predicted based on traditional beam theories. Therefore, several

theoretical studies were conducted to properly determine the flexibility and maximum stresses of curved pipes. Different types of analysis approaches were adopted in these studies involving (1) the principle of minimum potential energy, (2) the mechanics of materials approach, and (3) thin shell theories. In the following, the writer briefly presents some studies for each analysis approach.

1.2.1.1 Minimum potential energy

Von Karman's theory [1] was the first theoretical study to investigate the structural response of pipe bends under in-plane loading. In this theory, cross-sectional deformations induced by cross-section ovalization are assumed to induce two strain components: circumferential and longitudinal in addition to the longitudinal strain based on the traditional curved beam. Von Karman characterized the radial displacement of the elbow under in-plane bending moment in terms of trigonometric series and adopted the following assumptions:

- 1- Plane sections normal to the neutral axis of an elbow were assumed to remain plane and normal to the neutral axis after deformation (i.e., warping displacements were neglected);
- 2- Longitudinal strains were assumed to be constant throughout the wall thickness;
- 3- Circumferential strains were assumed to vanish at the mid-surface (i.e., the pipe was inextensible in the radial direction);
- 4- The radius of the elbow was assumed to be much larger than the radius of the cross-section (i.e., long pipe bends); and
- 5- The effect of Poisson's ratio was ignored.

The solution (e.g., coefficients of the trigonometric series) was obtained by using the minimum potential energy principle. Based on von Karman's theory, Vigness [2] studied the structural

response of elbows subjected to out-of-plane loading while Kafka and Dunn [3] included the effect of internal pressure. Thus, von Karman's limitations were involved in Refs. [2-3].

1.2.1.2 Mechanics of Materials

Tuner and Ford [4] relaxed Assumptions 3 and 4 adopted in von Karman's study (Section 1.2.1.1) in order to capture the extensibility of pipe bends in the radial direction and extend the applicability of the theory to short pipe bends. The authors employed mechanics of materials principles to analyze a curved pipe under in-plane bending moment and compared their predictions against those obtained from von Karman's analysis. The comparison demonstrated an agreement between both predictions with a difference about 5% to 10%. In addition, Smith [5] followed this analysis approach to study the effect of out-of-plane loading.

1.2.1.3 Thin Shell theory

Clark and Reissner [6] utilized thin shell theory to investigate the response of a curved pipe subjected to in-plane bending moment. The authors derived two coupled ordinary differential equations and employed von Karman's assumptions to simply solve these governing equations. Additionally, Cheng and Thailer [7] solved the governing differential equations derived in Clark and Reissner [6] without adopting their assumptions and the solution was in the form of a series expansion.

1.2.2 Numerical studies

Various limitations (e.g., inability to capture nonlinear effects, model complex geometry of piping systems) are associated with theoretical studies; hence, numerical studies are required to

investigate the linear and nonlinear structural response of pipe bends under several boundary/loading conditions. The Finite Element (FE) method is a powerful numerical technique for solving partial differential equations, and is commonly used in solid mechanics to predict deformations and stresses of a body under external loads. Solid and shell FE formulations are well-suited elements to accurately predict the structural response of pipe bends incorporating nonlinear effects. In the following, the writer will briefly introduce some relevant studies based on solid and shell FE formulations.

Hong et al. [8] conducted three-dimensional elastic FE analyses using the C3D20R element in ABAQUS (Commercial FE Software) to generate approximate formulas for the stress fields in thin- and thick-walled bends subjected to internal pressure. These formulas can be applied for different shapes of pipe bends attached to straight portions (e.g. 90°, 45° and U bends) and various pipe bend geometries.

Using solid elements in ANSYS (Commercial FE Software), WeiB et al. [9] carried out linear and nonlinear FE analyses to study the load carrying capacity and fatigue strength of pipe bends under internal pressure, in-plane, and out-of-plane bending moments. The authors developed design curves for fatigue strength and the load carrying capacity.

Abdulhameed [10] performed shell FE analyses using the S4R element in ABAQUS to quantify the influence of the Bourdon effect on the structural response of a pipe bend under internal pressure. The effect of the in-plane bending moment direction (opening or closing) was

investigated. Additionally, new stress intensification factors were developed for pipe bends under internal pressure and in-plane bending moment.

In spite of the accuracy of solid and shell FE models in simulating the structural response of pipe bends, the modelling effort and computational cost associated with these models are prohibitive in design environments. Therefore, there is a need for special FE formulations for the analysis of pipes and elbows that are both accurate and simple to use.

1.2.3 Finite element formulation for pipe/elbow element

A special finite element formulation for the analysis of straight and/or curved pipes is required to strike a balance between the efficiency of the solution and the associated computational cost. In the following, the writer will provide various examples of linearly elastic FE formulations for pipes and elbows.

Ohtsubo and Watanabe [11] developed a ring-shaped FE formulation to analyze pipe bends under in-plane loading and/or out-of-plane loading. The authors established the strain-displacement relationships based on the Love-Kirchhoff thin shell theory. Cubic Hermitian polynomials were used to interpolate the displacement fields (e.g., longitudinal, circumferential, and radial) along the longitudinal direction while Fourier series expansions were utilized to characterize these displacement fields along the circumferential direction. At least six Fourier terms had to be used to obtain convergence. The FE formulation captured the rigid body motion only in an approximate sense.

A simple FE formulation was proposed by Bathe and Almeida [12] for the analysis of pipe bends. The authors omitted some of the von Karman's assumptions (e.g., Assumption 2, 4, and 5 in Section 1.2.1.1) in their formulation in order to express the longitudinal strains throughout the pipe wall thickness induced by bending, accurately capture the response of short pipe bends, and consider the effect of the Poisson's ratio. The displacement fields were taken as a combination of beam deformation mode (centerline displacements) characterized by cubic polynomial displacement functions and cross-sectional deformation modes expressed by Fourier series. The element was enhanced to simulate pressure stiffening [13] and interaction effects between straight and curved pipes [14]. Since the FE formulation adopted Assumption 1 (Section 1.2.1.1) of von Karman's assumptions, the element was unable to capture warping effects.

Militello and Huespe [15] improved Bathe's element [12] by omitting the plane section assumption (Assumption 1 in Section 1.2.1.1). In their formulation, the authors interpolated the longitudinal displacement field using third order Lagrangian polynomials along the longitudinal direction and Fourier series along the circumferential direction in order to simulate warping displacements.

Abo-Elkhier [16] also developed a FE formulation for the analysis of pipe bends. Although his formulation was consistent with Bathe's formulation [12] regarding the assumptions and the interpolation schemes, he adopted the kinematic constraints of the thin shell theory to obtain the strain-displacement relationships which enabled him to capture additional strain components not included in Ref [12].

Ref [12] omitted Assumptions 2, 4, and 5 of the von Karman's theory (Section 1.2.1.1) to capture bending strains throughout the elbow wall thickness, properly model short pipe bends, and include the effect of the Poisson's ratio. Additionally, Assumption 1 (Section 1.2.1.1) was relaxed in Ref [15] to simulate warping effects. However, Assumption 2 (e.g., inextensibility of the pipe in the radial direction) was employed in these Refs. Yan et al. [17] relaxed Assumption 2 to allow the pipe extensibility in the radial direction. The new formulation enabled the authors to capture the effect of internal pressure. Their formulation characterized the longitudinal, circumferential, and radial displacements in terms of Fourier series along the circumferential direction and polynomial functions along the longitudinal direction as adopted in Ref [15].

Fonseca et al [18] introduced two FE formulations to model elbows attached to straight pipes. Higher-order polynomial or trigonometric functions along the longitudinal coordinate were employed to interpolate the beam displacement fields while the circumferential variations of the displacements were interpolated using Fourier series. The formulations were limited to loading within the plane of the elbow with internal pressure.

Weicker [19-20] adopted the strain-displacement relationships derived in Ref [11] and general Fourier series expansion within the frame work of the minimum potential energy principle to formulate the equilibrium equations for thin-walled initially circular straight pipes. The analytical solution of the coupled differential equations was developed and used to develop a FE formulation based on the interpolation functions that exactly satisfy the equilibrium equations.

1.2.4 Nonlinear treatment

FE formulations introduced in Section 1.2.3 were limited to linearly elastic analysis. However, several applications require including geometric nonlinear effects. In this section, the writer will review different approaches for the treatment of geometric nonlinearity.

Most FE formulations in solid mechanics adopt the principle of virtual work to construct geometrically nonlinear FE formulations in conjunction with the Lagrangian description approach [21]. Although the internal virtual work can be formulated in terms of various energetic conjugate pairs [22-23], the most commonly used energetic conjugate pair in the Lagrangian description is the second Piola-Kirchhoff stress and conjugate virtual Green-Lagrange strain tensors.

Bathe [24] adopted the above energetic conjugate pair for constructing the nonlinear FE formulations based on an incremental approach. The author described the linearization process of the internal virtual work and showed nonlinear terms neglected in his incremental analysis in the context of total and updated Lagrangian approaches to simulate large deformation effects. His mathematical manipulations led to linear and nonlinear stiffness matrices to capture both types of analysis. The incremental approach in Ref [24] is applicable to various applications (e.g., beams, shells, solids, and pipes). Thus, Bathe and Almeida [25] employed this approach to add some nonlinear capabilities into their elbow element presented in Ref [12]. Their nonlinear element was formulated based on the total Lagrangian formulation and was able to capture large beam displacements. However, ovalization action was assumed to be small and warping displacements were omitted. The elbow element described in Ref [25] was implemented in the commercial FE

software ADINA [26]. Also, ANSYS [27] and ABAQUS [28] implemented different elbow elements for the analysis of pipe bends.

For instance, the ELBOW elements implemented in ABAQUS are fundamentally equipped to simulate ovalization and warping, continually throughout the pipe length, through polynomial interpolations while circumferential continuity is enforced by the adoption of the Fourier series expansions. Zeng et al. [29] presented a detailed description of the formulation of ELBOW elements and compared the response of a pipe bend under in-plane loading using the S4R shell, the ELBOW elements in ABAQUS and analogous elements in ADINA. Although Bryan [30] investigated the static response of the ELBOW elements under out-of-plane bending, with/without internal pressure, no comparisons were provided against shell elements. Additionally, his results did not show the variation of stresses along the circumferential direction of the cross section. Hence, there still exists a need in the pipelines industry to evaluate the response of the ELBOW elements in ABAQUS under internal pressure. Also, there is a need to assess the ability of the ABAQUS elbow elements to simulate the response of pipeline systems. Consequently, the initial objective of the present dissertation is to carry out a numerical assessment of the ELBOW elements in ABAQUS under internal pressure as shown in Chapter 2.

Within the framework of the Carrera Unified formulation (CUF) in conjunction with the total Lagrangian approach, Pagani and Carrera [31] proposed a unified formulation of geometrically nonlinear refined elastic beam theories. In their formulation, the internal virtual work was expressed in terms of the second Piola-Kirchhoff stress tensor and the virtual Green-Lagrange strain tensor. The linearization process retained the majority of nonlinear terms in contrast with

the approach presented in Ref [24] and the expressions of secant and tangent stiffness matrices were provided in a general form. This approach was later extended for shell formulation [32]. However, the effect of the follower pressure load, which is significant in pressurized piping systems, was not treated in Refs [31-32].

In contrast to the above studies, the first Piola-Kirchhoff stress tensor and the gradient of virtual displacement fields can be used as alternative energetic conjugate pair when applying the principle of virtual work. To the writer's knowledge, no FE formulations based on this particular choice of energetic conjugate pair were developed for straight or curved pipes, although it has been employed in other finite element applications involving beam [33] and shell [34-36]. The present dissertation thus adopts this energetic conjugate pair to develop geometrically nonlinear FE formulations for the analysis of straight (Chapter 3) and curved (Chapter 4) pipes by introducing a full description of linearization process and the associated mathematical manipulations¹.

1.2.5 Influence of initial geometric imperfections

There exist various manufacturing techniques (e.g., the mandrel method, the extrusion method, and the UO method) to fabricate pipe elbows. The mandrel method, for example, is a type of hot forming technique that is commonly used for elbow manufacturing. The mandrel method is summarized into three steps: (1) Cutting a straight pipe into pieces, (2) Heating these pieces using an induction heating coil, (3) Pushing these straight pieces over a die called 'mandrel'. This method leads to smaller wall thickness deviations and is suitable for shorter bending radii compared to the

¹ This energetic conjugate pair enables the writer to easily eliminate the virtual degrees of freedom vector and obtain the equilibrium equations as shown in Chapter 3.

other manufacturing methods. The manufacturing processes of elbows are associated with various initial geometric imperfections (ovality, wall thickness variation, flattening, etc.) and mechanical changes (residual stresses and strains and changes to the yield stress and corresponding plastic deformations, etc.). In the present dissertation, the writer will consider only the initial geometric imperfections, in particular the initial ovality.

The FE formulations introduced in Sections 1.2.3 and 1.2.4 assume that pipe cross-section to be initially circular. However, the manufacturing processes of pipes are associated with various initial geometric imperfections (e.g., initial ovality and wall thickness variability). Many FE solutions, based either on conventional shell or solid elements, studied the effect of initial geometric imperfections on the response of straight and curved pipes under various loading conditions. In this section, the writer reviews some of these studies.

Fallqvist [37] studied the influence of several initial geometric imperfections on the collapse pressure of straight pipelines laid in ultra-deep water and subjected to high external pressure using the solid continuum CED8R element in ABAQUS. The study showed that initial ovality was the most influential geometric imperfection characteristic as it caused a dramatic reduction in the collapse pressure. For example, the collapse pressure for a pipe with a diameter to thickness ratio $D/t=30$ and a 5% initial ovality subjected only to external pressure decreased by more than 50% when compared to a pipe with a 0% initial ovality.

Toscano [38] investigated the collapse and post-collapse behavior of straight pipes subjected to external pressure and/or bending moments. The author highlighted the significant effect of initial

ovality on collapse pressure under external pressure as reported in Ref [37]. However, the effect of initial ovality on the collapse pressure was found negligible in cases involving combinations of bending and external pressure since the ovality induced by bending action (Brazier effect) is typically higher than that induced by initial ovality.

Veerappan and Shanmugam [39] examined the effect of ovality and thinning of the pipe bend cross-section subjected to internal pressure by developing 400 axisymmetric models using PLANE82 element in ANSYS for different pipe bend radii. Imperfect pipe bends were found to experience higher stresses than initially circular pipe bends under the same internal pressure. Subsequently, the authors introduced a mathematical formula to obtain the allowable pressure for imperfect pipe bends.

Christo Michael et al. [40] carried out nonlinear FE analyses using the C3D20R element in ABAQUS to determine collapse loads of pipe bends with initial geometric imperfections under in-plane bending closing moment. Based on these analyses, the authors concluded that initial ovality must be included in the analysis of pipe bends since collapse loads tangibly decrease when initial ovality is increased. In contrast, wall thickness variability was found to have a negligible influence on collapse loads. Hence, an equation was developed to determine the collapse moment of ovalized pipe bends. In another study [41], the authors studied the response of imperfect pipe bends under a combination of in-plane bending closing moment and internal pressure and derived another expression to calculate collapse loads of pipe bends with ovality. Their study confirmed the necessity to simulate initial ovality in the modelling of pipe bends.

Buckshumiyan et al [42] followed the approach introduced in Ref [41] to investigate the influence of in-plane bending under opening moments and internal pressure on imperfect pipe bends. Nonlinear FE analyses were conducted to determine the collapse loads for various ovality and thinning percentages showing that initial ovality is the most significant aspect of geometric imperfections. Additionally, expressions based on FE analyses were developed to characterize the collapse loads of ovalized pipe bends under combined loads.

Previous studies suggest that initial geometric imperfections, particularly initial ovality, need to be considered in the analysis of straight and curved pipes. Thus, Chapter 5 of the present dissertation proposes accurate and efficient geometrically nonlinear FE formulations to analyze imperfect thin-walled straight and curved pipes under various loading conditions.

1.2.6 Historical developments of thin shell theory

The FE formulations developed in the present dissertation adopt the kinematic assumptions of the Love-Kirchhoff thin shell theory. Therefore, the writer presents a brief account on the historical developments of the elastic thin shell theory in this section.

The first successful thin shell theory was derived by Love [43] based on the theory of linear elasticity. In his theory, the author adopted kinematic assumptions to simplify the strain-displacement relationships. These assumptions can be summarized in the following:

1. Straight lines originally normal to the un-deformed mid-surface of the shell remain straight and normal to the mid-surface in the deformed configuration.
2. The thickness of the shell remains constant throughout deformation.

3. Normal stresses through the thickness of the shell are ignored.
4. The shell is assumed to be thin.
5. Displacements are assumed to be small.

Kirchhoff firstly adopted Assumptions 1-3 in his plate bending theory. Hence, these kinematic assumptions are called the Love-Kirchhoff assumptions while the shell theory that follows these assumptions is called the first-order approximation shell theory. Although the Love's thin shell theory is commonly used, it involves some inconsistencies. For example, some small terms were omitted in certain parts of the formulation while other small terms of the same order were retained in other parts of the formulation. Within the framework of the virtual work principle, Sanders [44] proposed a new thin shell theory that followed the Love-Kirchhoff assumptions. However, it eliminates the inconsistencies introduced in the Love's theory.

When a shell theory relaxes Assumption 4 (i.e., thickness/radii of curvature is considered), it is referred to as a second-order approximation shell theory. Based on the three-dimensional theory of elasticity and Assumptions 1-3 and 5, Lur'ye [45] derived the governing equations of his second-order shell theory, which retains the thickness to radii ratios in the expressions for curvature. Although the work of Novozhilov [46] was aligned with Ref [45] with respect to strain-displacement relationships, Novozhilov adopted a strain energy formulation to obtain stress resultants. Also, the author estimated the errors associated with the assumptions adopted in the theory.

Flügge [47] examined membrane and bending stresses of various types of shells (e.g., cylindrical shells, shells of revolution) under multiple loading conditions. Equilibrium equations were derived

from equilibrium conditions of an infinitesimal element of shell under consideration involving stress resultants². The author applied his theory to pressure vessel and pipe applications and provided complete solutions of special circular and elliptical cylindrical shells under pressure. The reader is referred to Ref [48] for a mathematical comparison between different thin shell theories.

1.3 Problem statement

Although the ELBOW elements implemented in ABAQUS were verified under in-plane loading and/or out-of-plane loading, the response of these elements under internal pressure is not well addressed as highlighted in Section 1.2.4. Thus, a numerical assessment of the response of the ELBOW elements under internal pressure is needed to provide a complete evaluation of these elements for the industrial community of pipelines.

Special FE formulations were developed to predict the geometrically linear and nonlinear structural response of initially circular straight and curved pipes under several loading conditions (Sections 1.2.3 and 1.2.4). Although the manufacturing process of pipes produces various types of initial geometric imperfections, these formulations are not able to model these imperfections and predict the realistic structural response of imperfect pipes under general loading. The influence of these imperfections, particularly initial ovality, on the structural response is highly pronounced and cannot be ignored (Section 1.2.5). Therefore, new FE formulations (pipe/elbow elements) are

² In the writer's opinion, while the analysis of shells in terms of stress resultants (e.g., forces and couples) is more intuitive for structural and mechanical engineers, the analysis of shells solely in terms of the displacement fields and their derivatives is more rigorous and mathematically robust for complex problems. Hence, the latter approach has been adopted in the present dissertation.

required to accurately model imperfect straight and curved pipes and properly predict their structural response under general loads.

1.4 Objectives

The objectives of the present dissertation are summarized as follows:

- 1- **Initial objective:** To numerically assess the response of the ELBOW elements implemented in ABAQUS under internal pressure to bridge this gap in the literature highlighted in Section 1.2.4. However, the inability of these elements to model initial geometric imperfection was the motivation to the main objective of the present dissertation.
- 2- **Main objective:** To develop geometrically nonlinear FE formulations for the structural analysis of straight and curved pipes with a generic cross-section involving initial geometric imperfections. This objective can be divided into three sub-objectives:
 - 1.a. To develop a FE formulation for the analysis of **initially circular straight pipes**.
 - 1.b. To develop a FE formulation for the analysis of **initially circular curved pipes**.
 - 1.c. To develop FE formulations for the analysis of **straight and curved pipes with general cross-sections**.

1.5 Outline of dissertation

The present dissertation has six chapters summarized as follows:

Chapter 1 presents an introduction of the problem, reviews the relevant literature, highlights the research gaps, and describes the problem statement, objectives, and the outline of dissertation.

Chapter 2 presents a numerical assessment of the response of the ELBOW elements implemented in ABAQUS under internal pressure. This chapter includes two case studies: (1) a standalone 90° pipe bend which is analyzed using both elastic and elasto-plastic material characterizations using shell and elbow elements; and (2) a geometrically nonlinear analysis with a materially elastic characterization of a piping system is conducting using shell, elbow, and pipe elements. Additionally, an assessment of the ASME B16.49 2017 elbow thickness equation and previously published stress estimate equations is carried out by comparisons with elbow and shell elements predictions. The content of this chapter has been published as a research paper in the Journal of Pressure Vessels and Technology [49].

Chapter 3 focuses on developing generalized expressions of the internal and external force vectors and the stiffness matrix based on the principle of virtual work formulated in terms of the first Piola-Kirchhoff stress tensor and the gradient of virtual displacement fields. These generalized expressions are specialized to initially circular thin-walled straight pipes (by employing the cylindrical coordinate system). The displacement fields are characterized using cubic Hermitian function along the longitudinal direction. Three different interpolation schemes are investigated along the circumferential direction (i.e., Fourier series, Spline interpolation, and Mixed Fourier/Spline interpolation). Numerical examples and comparisons against shell analysis in ABAQUS are presented to assess the accuracy of the formulations developed. This chapter is aligned with Sub-objective 2.a and its content has been submitted to an international journal (under review).

In Chapter 4, the generalized expressions derived in Chapter 3 are specialized to initially circular curved pipes by adopting a toroidal coordinate system. Fourier series expansions are adopted to characterize the displacement fields along the circumferential direction while three different interpolation schemes are proposed to characterize the displacement fields along the longitudinal direction. Eigenvalues analyses are carried out to assess the ability of each interpolation scheme for representing rigid body motion. Various examples are introduced to compare the predictions of the formulations developed with those obtained from the conventional general shell models. The content of this chapter has been submitted to an international Journal (under review) and achieves Sub-objective 2.b.

Chapter 5 introduces an innovative methodology to capture initial geometric imperfections when modelling straight and curved pipes. The idea is to utilize an initially circular cross-sectional pipe configuration as a mediator configuration (e.g., reference configuration with no imperfections) between the un-deformed (e.g., imperfect pipes) and deformed configurations. This chapter presents the required mathematical manipulations to characterize the strains/stresses induced by the motion of the pipe from the un-deformed to the deformed configurations while referencing these strains to the mediator configuration. The first Piola-Kirchhoff stress tensor formulated in the reference configuration is obtained in terms of these strains. Since the initial ovality is the most significant geometric imperfection, the numerical examples in this chapter are focused on the response of initially ovalized straight and curved pipes under various loading conditions. The predictions of the proposed formulations are compared to those obtained from the conventional general shell models. The content of this chapter has been submitted to an International Journal (under review).

Chapter 6 presents a summary and conclusion of this research work and provides recommendations for further research work.

This present dissertation is written in a paper-based format. Each main chapter (i.e., Chapters 2-5) takes the form of a stand-alone research paper. Thus, the introductory sections in each of these chapters may have included unavoidable repetitions.

1.6 References

- [1] Von Karman, T., 1911, "Ueber Die Formänderung Dünnwandiger Rohre, Insbesondere Federnder Ausgleichrohre," *Z. Ver. Deut. Ing.*, 55(Part2), pp.1889–1895.
- [2] Vigness, I., 1943, "Elastic Properties of Curved Tubes," *J. Appl. Mech.*, 55, pp.102–120.
- [3] Kafka, P. G., and Dunn, M. B., 1953, "Stiffness of Curved Circular Tubes with Internal Pressure," Boeing Airplane, Chicago, IL.
- [4] Turner, C. E., and Ford, H., 1957, "Examination of the Theories for Calculating the Stresses in Pipe Bends Subjected to In-Plane Bending," *Proc. Inst. Mech. Engrs.*, 171: 513-515.
- [5] Smith, R. T., 1967, "Theoretical Analysis of the Stresses in Pipe Bends Subjected to Out-of-Plane Bending," *J. Mech. Eng. Sci.*, 9(2).
- [6] Clark, R.A., and Reissner, E., 1951, "Bending of Curved Tubes," *Advances in Applied Mechanics*, Academic Press, New York, Vol. 2, pp.93-122.
- [7] Cheng, D. H., and Thailer, H. J., 1968, "In-Plane Bending of Curved Circular Tubes," *J. Eng. Ind. Trans.*, ASME Paper No. 68-PVP-12.
- [8] Hong, S.-P., An, J.-H., Kim, Y.-J., Nikbin, K., and Budden, P. J., 2011, "Approximate Elastic Stress Estimates for Elbow Under Internal Pressure," *Int. J. Mech. Sci.*, 53(7), pp. 526–535.
- [9] WeiB, E., Lietzmann, A., and Rudolph, J., 1996 "Linear and Nonlinear Finite-Element Analysis of Pipe Bends," *Int. J. Pres. Ves. & Piping.*, 67, pp. 211-217.
- [10] Abdulhamed, D., 2017 "The Behavior of Pipe Bends under Internal Pressure and In-Plane Bending Loading," Doctoral dissertation, University of Alberta, Edmonton, Canada.
- [11] Ohtsubo, H., and Watanabe, O., 1978, "Stress Analysis of Pipe Bends by Ring Elements," *ASME J. Pressure Vessel Technol.*, 100(1), pp. 112–122.
- [12] Bathe, K. J., and Almeida, C. A., 1980, "A Simple and Effective Pipe Elbow Element, Linear Analysis," *J. Appl. Mech.*, 47(1), pp. 100–193.
- [13] Bathe, K. J., and Almeida, C. A., 1982, "A Simple and Effective Pipe Elbow Element, Pressure Stiffening Effects," *J. Appl. Mech.*, 49(4), pp. 914–915.
- [14] Bathe, K. J., and Almeida, C. A., 1982, "A Simple and Effective Pipe Elbow Element, Interaction Effects," *J. Appl. Mech.*, 49, pp. 165–171.

- [15] Militello, C., and Huespe, A. E., 1988, "A Displacement- Based Pipe Elbow Element," *Comput. Struct.*, 29(2), pp. 339–343.
- [16] Abo-Elkhier, M., 1990, "Analysis of Pipe Bends Using Pipe Elbow Element," *Comput. Struct.*, 37(1), pp. 9–15.
- [17] Yan, A. M., Jospin, R. J., and Nguyen, D. H., 1999, "An Enhanced Pipe Elbow Element- Application in Plastic Limit Analysis of Pipe Structures," *Int. J. Numer. Methods. Eng.*, 46(3), pp.409-431.
- [18] Fonseca, E. M. M., de Melo, F. J. M. Q., and Oliveira, C. A. M., 2006, "Numerical Analysis of Piping Elbows for In-Plane Bending and Internal Pressure," *Thin-Walled Struct.*, 44, pp.393-398.
- [19] Weicker, K., Salahifar, R., and Mohareb., M., 2010, "Shell Analysis of Thin-Walled Pipes. Part I-Field equations and solution," *Int. J. Pres. Ves. & Piping.*, 87, pp.402-413.
- [20] Weicker, K., Salahifar, R., and Mohareb., M., 2010, "Shell Analysis of Thin-Walled Pipes. Part II-Finite Element Formulation," *Int. J. Pres. Ves. & Piping.*, 87, pp.414-423.
- [21] Basaran, S., 2008, "Lagrangian and Eulerian Descriptions in Solid Mechanics and Their Numerical Solutions in hpk Framework," Doctoral dissertation, The University of Kansas, Kansas, United states.
- [22] Holzapfel, G. A., 2000, "Nonlinear Solid Mechanics: A Continuum Approach for Engineering," Chichester: Wiley.
- [23] Bonet, J., and Wood, R., 2008, "Nonlinear Continuum Mechanics for Finite Element Analysis," Cambridge: Cambridge University Press. doi:10.1017/CBO9780511755446
- [24] Bathe, K. J., 1996, "Finite Element Procedures in Engineering analysis," Prentice Hall, New Jersey.
- [25] Bathe, K. J., and Almeida, C. A., 1982, "A Simple and Effective Pipe Elbow Element, Some Nonlinear Capabilities," *J. Appl. Mech.*, 49(1), pp.165–173.
- [26] ADINA R& D, Inc.2012. Theory and Modeling Guide Volume I
- [27] ANSYS, Inc. ELBOW290, Retrieved from https://www.mm.bme.hu/~gyebro/files/ans_help_v182/ans_elem/Hlp_E_ELBOW290.html
- [28] Simulia ABAQUS. 2017.User’s Manual version 6.6 documentation
- [29] Zeng, L., Jansson, L. G., and Venev, Y., 2014, "On Pipe Elbow Elements in ABAQUS and Benchmark Test," ASME Paper No. PVP2014-28920.
- [30] Bryan, B. J., 1994, Static Analysis of a Piping System with Elbows (WSRCMS-94-075), Minneapolis, MN.
- [31] Pagani, A., and Carrera, E., 2018, "Unified formulation of geometrically nonlinear refined beam theories," *Mech. Adv. Mater. Struc.*, 25(1), pp. 15-31
- [32] Wu, B., Pagani, A., Chen, W. Q., and Carrera, E., 2019, "Geometrically nonlinear refined shell theories by Carrera Unified Formulation," *Mech. Adv. Mater. Struc.*, DOI: 10.1080/15376494.2019.1702237
- [33] Duan, L., Zhao, J., 2019, "A geometrically exact cross-section deformable thin-walled beam finite element based on generalized beam theory," *Comput. Struct.*, 218, pp.32-59.
- [34] Meroueh, K. A., 1986, "On a Formulation of a Nonlinear Theory of Plates and Shells with Applications," *Comput. Struct.*, 24(5), pp. 691-705.
- [35] Campello, E. M. B., Pimenta, P. M., Wriggers, P., 2003, "A triangular finite shell element based on a fully nonlinear shell formulation," *Computational Mechanics*, 31, pp. 505-518.
- [36] Ivannikov, V., Tiago, C., Pimenta, P. M., 2014, "On the boundary conditions of the geometrically nonlinear Kirchhoff-Love shell theory," *Int. J. Solids Struct*, 51, pp. 3101-3112.

- [37] Fallqvist, B., "Collapse of thick deepwater pipelines due to hydrostatic pressure," Master dissertation, Royal Institute of Technology, Stockholm, Sweden.
- [38] Toscano, R. G., 2009, "Collapse and post-collapse behavior of steel pipes under external pressure and bending. Application to deep-water pipelines," Doctoral dissertation, Universidad de Buenos Aires, Argentina.
- [39] Veerappan, A. R., Shanmugam, S., 2006, "Stress analysis of pipe bends subjected to internal pressure fluid pressure using the finite element technique," *J. Strain Analysis*, 41(8), pp. 561-573.
- [40] Christo Michael, T., Veerappan, A. R., Shanmugam, S., 2012, "Effect of ovality and variable wall thickness on collapse loads in pipe bends subjected to in-plane bending closing moment," *Eng. Fract. Mech.*, 79, pp.138-148.
- [41] Christo Michael, T., Veerappan, A. R., Shanmugam, S., 2012, "Comparison of plastic limit and collapse loads in pipe bends with shape imperfections under in-plane bending and an internal pressure," *Int. J. Pres. Ves. & Piping.*, 99-100, pp.23-33
- [42] Buckshumiyan, A., Veerappan, A. R., Shanmugam, S., 2014, "Determination of collapse loads in pipe bends with ovality and variable wall thickness under internal pressure and in-plane opening moment," *Int. J. Pres. Ves. & Piping.*, 123-124, pp.1-9.
- [43] Love, A.E.H., 1892, "A treatise on the Mathematical Theory of Elasticity," 1st Edition, Cambridge University Press.
- [44] Sanders, J.L., 1959, "An Improved First Approximation Theory for Thin Shells," NASA TR-R24
- [45] Lur'ye, A.I., 1940, "General theory of elastic shells," *Prikl Mat Mekh*, vol.4, No.4, pp. 7-34
- [46] Novozhilov, V.V., 1964, "Theory of Thin Elastic Shells," 2nd Edition, P. Noordhoff, Groningen
- [47] Flugge, W., 1973. "Stresses in Shells," Springer-Verlag, New York Heidelberg Berlin
- [48] Salahifar, R., 2011 "Analysis of Pipelines Systems under Harmonic Forces," Doctoral dissertation, University of Ottawa, Ontario, Canada.
- [49] Attia, S., Mohareb, M., Martens, M., Yoosef-Ghodsi, N., Li, Y., and Adeeb, S., 2021, "Numerical Assessment of Elbow Element Response Under Internal Pressure," *ASME. J. Pressure Vessel Technol.*, 143(5): 051302. <https://doi.org/10.1115/1.4050091>

Chapter 2

Numerical Assessment of Elbow Element Response under Internal Pressure

2.1 Abstract

This chapter presents a detailed assessment for the response of the ELBOW elements in ABAQUS under internal pressure. Two main cases are considered: (1) a standalone 90° pipe bend which was analyzed using both elastic and elasto-plastic material characterizations using shell and elbow elements; and (2) a geometrically nonlinear analysis with a materially elastic characterization of a piping system was conducting using shell, elbow, and pipe elements. Although the results show the capabilities of elbow elements to simulate the response of pipe bends in the elastic regime, the elements do not provide reliable predictions beyond the elastic range. Additionally, an assessment of the ASME B16.49 2017 elbow thickness equation and previously published stress estimate equations was carried out by comparisons with elbow and shell elements predictions.

2.2 Introduction

Pipeline transmission systems play a vital role for various industries. Two main interests in the analysis and design of pipelines subjected to different loading conditions are structural integrity and computational cost. Pipe bends are typically required for introducing flexibility in the installation and routing of piping systems. In addition to the traditional deformation modes of a beam, the mechanical behavior of a pipe bend involves phenomena such as ovalization, warping,

and the Bourdon effect [1-10]. These phenomena need to be captured to properly analyze and design a pipeline system.

Many theoretical and experimental studies paid great attention to simulating the complex physical behavior of pipe bends. Von Karman's analysis [1] considered the ovalization of pipe bends under in-plane loading by adding two additional strain components to the traditional strain field in the curved beam theory. These additional components were circumferential and longitudinal strains due to the ovalization. Extending the work of Von Karman [1], out-of-plane loading effects were included by Vigness [2] and internal pressure effects by Kafka [3]. A simple linear analysis approach was presented by Dodge and Moore [4] in which the stresses of curved beam theory, used to simulate a pipe bend, were scaled using factors to account for ovalization and internal pressure effects. Further research works focused on the influence of internal pressure on the hoop and longitudinal stresses on the behavior of thin- and thick-walled bends [4-6]. Despite the benefits of theoretical studies, limitations still exist in predicting the actual behavior of pipe bends, especially for nonlinear effects; hence making it imperative for numerical modeling methods to be employed.

The Finite Element (FE) method is well suited for capturing the complex structural response of pipe bends. Hong et al. [6] performed three-dimensional elastic FE analyses to generate approximate formulas for the stress fields in thin- and thick-walled bends subjected to internal pressure. These formulas can be applied for different shapes of pipe bends attached to straight portions (e.g. 90°, 45° and U bends) and various pipe bend geometries. The pressure inside a pipe bend generates an in-plane outward force causing straightening out of the pipe bend, a

phenomenon known as the Bourdon effect. Due to the Bourdon effect, pipe bends are subjected to additional stresses and strains. Hence, shell FE analyses were performed by Abdulhameed et al. [7] to investigate these additional stresses and deformations. However, these FE formulations are computationally cost-prohibitive in a design environment. Thus, FE formulations that capture ovalization, warping, and internal pressure effects in addition to beam-type deformations are needed. Based on von Karman's analysis [1], Bathe and Almeida [8-10] introduced FE formulations for linear and nonlinear analyses including the internal pressure effect. However, their FE formulations neglected warping displacements in pipe bends. Therefore, Militello and Huespe [11] improved Bathe's formulation to capture warping. The study achieved the required continuity by using the Hermitian interpolation instead of the penalty procedure followed in Bathe's formulation. In recent decades, other formulations have also been proposed in a bid to improve the accuracy of the simulations of pipe bend behavior [12, 13].

A series of elbow elements have been implemented in ABAQUS to provide efficient modelling for both linear and nonlinear analyses of piping systems [17]. The "ELBOW31" and "ELBOW32" elements in ABAQUS are fundamentally equipped to simulate ovalization and warping, continually, throughout the pipe length through polynomial interpolations while circumferential continuity is enforced by the adoption of the Fourier series approximation. While "ELBOW31" element is formulated using linear interpolation along the length of the elbow element, "ELBOW32" element uses quadratic interpolation. Zeng et al. [14] presented a detailed description of the formulation of these elbow elements and compared the behavior of a pipe bend under in-plane loading using S4R shell, ELBOW31, and ELBOW32 elements in ABAQUS and analogous elements in ADINA. Although Bryan [15] demonstrated the behavior of ELBOW31 in static

analysis of a piping system under out-of-plane bending, with/without internal pressure, he did not compare this behavior with shell elements. Additionally, his results did not show the variation of stresses along the circumferential direction of the cross section. Hence, there still exists an essential need in the pipelines industry to evaluate the behavior of elbow elements under internal pressure only. Also, there is a need to assess the ability of the ABAQUS elbow elements to simulate the behavior of pipeline systems.

Hoop stresses induced by internal pressure at the intrados of a pipe bend are typically greater than those at the extrados of the pipe bend. Hence, ASME B16.49-2017[16] proposed an equation for the minimum wall thickness required at the intrados of a pipe bend. As shown in Eq. (2.1), the wall thickness (T_I) at the intrados of a pipe bend is to be increased by a factor (code factor) that depends on the bend radius (R) and the outer diameter (D_o) of the pipe bend, compared to nominal wall thickness of a straight pipe (t).

$$T_I \geq \left[\frac{4 \left(\frac{R}{D_o} \right) - 1}{4 \left(\frac{R}{D_o} \right) - 2} \right] \times t \quad (2.1)$$

Within the above context, the present study has four major objectives:

- 1- To evaluate the behavior of ELBOW31 & ELBOW32 elements under internal pressure against shell element behavior (S4R). Towards this goal, a standalone 90° pipe bend, shown in Fig. 2. 1, is tested for two different pipe bend radii ($R= 5 D_o$ and $R= 1.5 D_o$) under various boundary conditions (Case I). The von Mises, hoop, and longitudinal stresses as well as the deformed shape along the circumferential direction of the central cross section are investigated.

- 2- To assess the ability of ABAQUS elbow elements to model the whole piping systems and assess their compatibility with pipe elements whose formulation excludes ovalization and warping. Hence, the piping system shown in Fig. 2. 2 is considered. This system comprises two 90° pipe bends ($R=1.5 D_o$) connected together by a small straight horizontal segment ($L_h=1.5 D_o$), while the other ends are attached to straight vertical segments with length $L_v=5 D_o$. The ends of the vertical segments are completely constrained. The stresses at the center of the pipe bend and at the interface between the elbow and horizontal segment are investigated (Case II).
- 3- To check the conservativeness of the pipe bend thickness equation proposed in ASME B16.49-2017[16] against the analyses performed in the present study.
- 4- To compare the stress fields predicted by the present study at the center and ends of a pipe bend attached to straight portions against the predictions of the equations proposed by Hong [6].

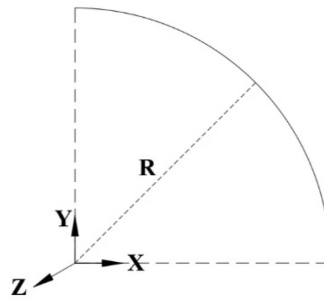


Fig. 2. 1 Geometry of the pipe bend in Case I

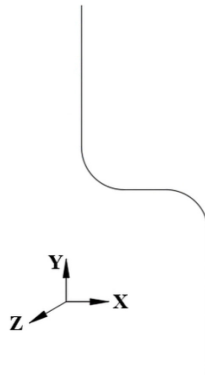


Fig. 2. 2 Geometry of the piping system in Case II

The outer diameter (D_o) and the wall thickness (t) of the pipe bends and straights portions are 1066.8 mm and 9.525 mm respectively (high diameter to thickness ratio) while Young modulus (E) and poisson ratio (ν) are 210 GPa and 0.3 respectively. The chosen internal pressure level $P = 4 \text{ MPa}$ would induce a hoop stress about $0.77 F_y$ in a straight pipe for a X42 pipe grade.

Based on the manufacturing process, pipe bends can be classified to field bend, induction bend, and elbow fitting. Each one of these bends has specific requirements for the geometric characteristics and operating conditions. However, pipe bends used in the present study do not consider the manufacturing process. Additionally, the initial imperfections and combined effect of bending and internal pressure are not included. This study considered a relatively flexible pipe with the ratio of outer diameter (D_o) to wall thickness (t) of 112.

2.3 Methodology

The performed FE models in the present study are shown in Table 2. 1. For the long pipe bend radius ($R= 5D_o$) in Case I, elastic geometrically nonlinear analyses were carried out using three FE formulations (e.g. S4R, ELBOW31, and ELBOW32) within ABAQUS. Each model employed three different boundary conditions. The models were replicated for short pipe bend radius ($R= 1.5D_o$) in Case I. Additionally, four models were considered to verify the effect of the geometric nonlinearity (Model #S10) and assess the behavior of elbow elements under elasto-plastic material characterization shown in Fig. 2. 3 (Models # S11, S12, and S13). Additionally, elastic geometrically nonlinear analysis of the piping system in Case II was implemented three times. The first two models were using S4R shell and ELBOW31 elements, respectively, while the third model was using ELBOW31 for pipe bends and PIPE31 for straight portions. While the approximate mesh size was 30 mm for all the models, the number of Fourier modes was six for all elbow element models. While the bend ends were free to ovalize and warp, ovality and warping displacements were deactivated at the restrained ends in the elbow element models in order to emulate fixed end support conditions.

Modelling the piping systems using shell elements can be performed using the ABAQUS graphical user interface (GUI), whereas using elbow elements requires editing the input file. Firstly, the cross section of a pipe bend is defined as a beam section with pipe profile through ABAQUS GUI. Secondly, the input file should be modified to assign the pipe bend radius, orientation point, number of integration points through the wall thickness and around the circumference, and number of Fourier modes (See Supplemental Material - Modelling of pipe bends).

Table 2. 1 Parametric runs for Case I and Case II

Case #	Geometry	Model #	Analysis Type		Element	Boundary conditions ³
			Material	Geometry		
Case I	90° bend (R/D _o = 5)	L1	Elastic	Non-linear	S4R	FR
		L2				FF
		L3				HH
		L4	Elastic	Non-linear	ELBOW31	FR
		L5				FF
		L6				HH
		L7	Elastic	Non-linear	ELBOW32	FR
		L8				FF
		L9				HH
	90° bend (R/D _o = 1.5)	S1	Elastic	Non-linear	S4R	FR
		S2				FF
		S3				HH
		S4	Elastic	Non-linear	ELBOW31	FR
		S5				FF
		S6				HH
		S7	Elastic	Non-linear	ELBOW32	FR
		S8				FF
		S9				HH
		S10	Elastic	Linear	Elbow 31	FR
S11		Elasto - Plastic	Non-linear	S4R	FF	
S12		Elasto - Plastic	Non-linear	Elbow 31	FF	
S13 ⁴	Elasto - Plastic	Non-linear	Elbow 31	FF		
Case II	Piping system	P1	Elastic	Non-linear	S4R	FF
		P2	Elastic	Non-linear	Elbow 31	FF
		P3	Elastic	Non-linear	Combined ⁵	FF

³ FR: Fixed – Free

FF: Fixed – Fixed

HH: Hinged – Hinged (All nodal displacements were restrained at both ends)

⁴ Integration points were 18 and 3 along the circumferential direction and through the thickness respectively for all elbow models except model # S13. They are 50 and 11 respectively.

⁵ Combined: ELBOW31 elements were used for pipe bends while PIPE31 elements were employed for straight portions

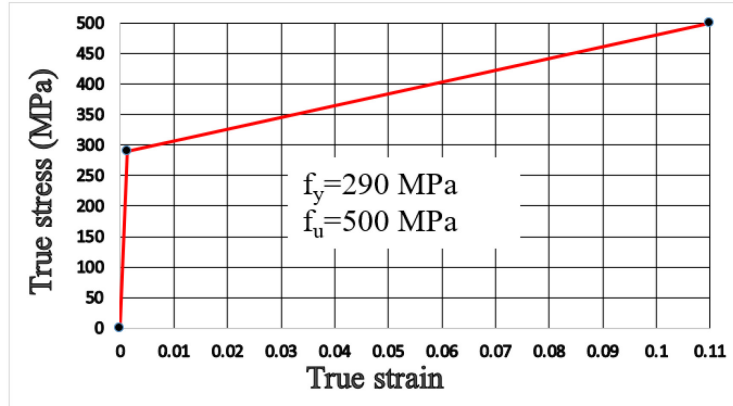


Fig. 2. 3 True stress-strain curve for the elasto-plastic models ($R= 1.5D_0$ - Case I)

By default, both ends of the ABAQUS pipe and elbow elements are “closed”. Therefore, the internal pressure causes two outward forces (F1 and F2 in Fig. 2. 4) equal to the integration of the applied pressure over the deformed end cross section. The forces F1 and F2 are in equilibrium with the outward force generated by the Bourdon effect; hence the force reaction results are zero in closed-ended elbows. In order to capture and quantify the Bourdon effect’s force in ABAQUS, the ends of elbow elements should be modeled as open-ended elbow similar to shell element model. There is no option in ABAQUS to simulate the open-ended elbow. Consequently, additional end forces R1 and R2 should be applied externally along in the tangential direction of the elbow centerline as shown in Fig. 2. 5 to counter-balance the actions of F1 and F2. In this study, R1 and R2 were simply calculated by multiplying the applied pressure by the area of the un-deformed end cross section and underwent to the deformations of the end nodes to maintain their orthogonality on the end cross sections. While predicting the reactions requires including these forces in the modelling of any piping system (e.g. Case I & Case II) in order to quantify force due to the Bourdon effect, the stresses can be correctly determined without applying these forces at the restrained ends along the tangential direction of the element (e.g., fixed end & hinged end).

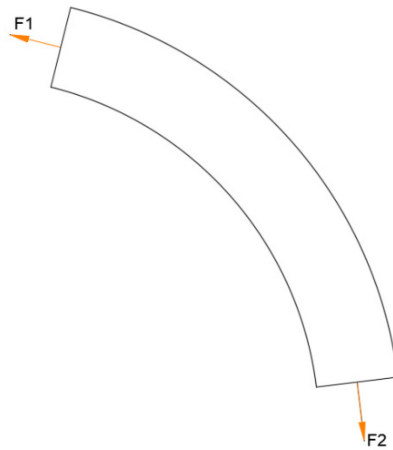


Fig. 2. 4 Default-closed end condition of a pipe bend

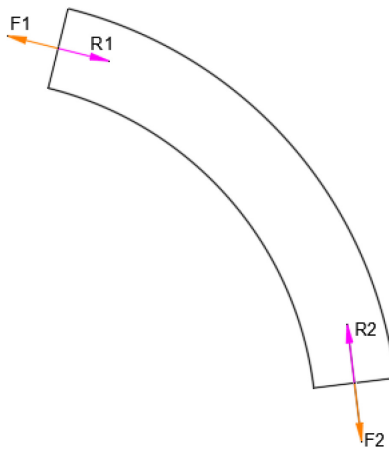


Fig. 2. 5 Simulation of open-ended condition

2.4 Results and Discussion

2.4.1 Results for Case I (pipe bend without straight portions)

The elbow element models effectively capture the in-plane outward force generated due to the Bourdon effect as shown in Table 2. 2. The percentage difference is calculated based on Eq. (2.2) and is less than 1 % in all cases except for the y-direction force in the fixed-free case ($R=1.5D_o$),

which is 1.14 %. Also, the obtained reactions indicate close correspondence to the values calculated using Abdulhameed's equations⁶ [7] which are shown in Eq. (2.3).

$$\text{Percentage difference (\%)} = \frac{\text{Shell output variable} - \text{Elbow output variable}}{\text{Shell output variable}} \times 100 \quad (2.2)$$

$$F_x = Pr^2\pi \sin \alpha \quad (2.3a)$$

$$F_y = Pr^2\pi (1 - \cos \alpha) \quad (2.3b)$$

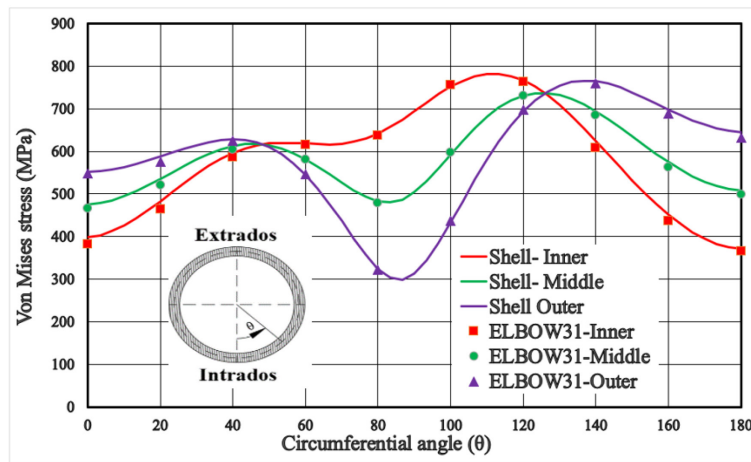
Table 2. 2 Force reaction components of the pipe bend obtained using shell and elbow formulations for Case I

		S4R		ELBOW 31		Percentage difference	
BCs	R/D _o	F _x (KN)	F _y (KN)	F _x (KN)	F _y (KN)	F _x (%)	F _y (%)
Fixed-Free	1.5	-3455	-3390	-3447	-3352	0.22	1.14
Fixed-Fixed		-3453	-3453	-3449	-3449	0.14	0.14
Hinged-Hinged		-3453	-3453	-3449	-3449	0.11	0.11
Fixed-Free	5	-3438	-3092	-3432	-3109	0.16	0.57
Fixed-Fixed		-3453	-3453	-3449	-3449	0.13	0.13
Hinged-Hinged		-3457	-3457	-3450	-3451	0.18	0.18
Analytical Eq		-3512	-3512				

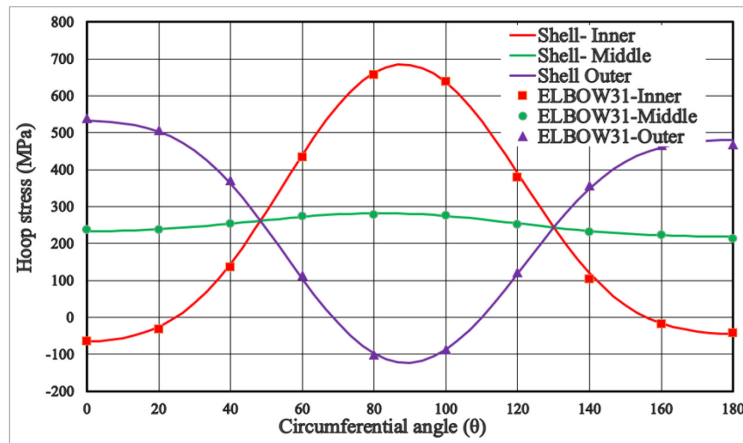
The results of von Mises σ_{vM} , hoop, and longitudinal stresses for the two pipe bend radii ($R= 5 D_o$ & $R= 1.5 D_o$) at cross-section A-A of the fixed-free case are presented in Fig. 2. 6 and Fig. 2. 7 respectively, while the other cases (e.g. Fixed-Fixed & Hinged-Hinged cases) are included in Appendix 2.A – Additional Results for Case I. For the long pipe bend radius ($R=5 D_o$), the FEA results show that the hoop stress distribution of the pipe bend subjected to internal pressure is

⁶ The equation provided in Ref [7] to calculate F_y contains an error which is corrected in Eq.2.3b. In case of a straight pipe $\alpha = 0$, the outward force generated due to the Bourdon effect is zero ($F_x = F_y = 0$).

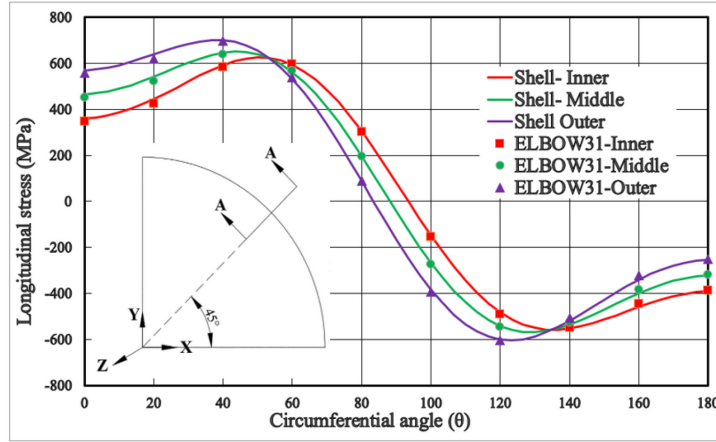
approximately sinusoidal due to the ovalization of the cross section as shown in Fig. 2. 6b. Also, the patterns of radial and circumferential displacements confirmed these results. While the outer surface was subjected to tensile circumferential stresses at the intrados and extrados, the inner surface had compressive circumferential stresses at the same positions. Additionally, the pipe bend experienced tensile longitudinal stresses below the neutral axis and compressive longitudinal stresses above the neutral axis because the internal pressure acted as in-plane distributed opening bending moment as shown in Fig. 2. 6c. Excellent agreement is obtained between shell element results and elbow element results in case of $R=5D_o$ where the percentage difference, based on Eq. (2.2), was less than 4 % as shown in Fig. 2. 6.



(a)



(b)



(c)

Fig. 2. 6 Stress fields versus circumferential angle θ at section A-A ($R=5D_o$ – Fixed-Free). (a) Von Mises stress, (b) Hoop stress, and (c) Longitudinal stress

For the short pipe bend radius ($R=1.5 D_o$), the pattern of von Mises, hoop, and longitudinal stresses distributions are nearly similar to those in case of $R=5 D_o$. However, there was a tangible difference for the stress magnitudes between shell element and elbow element results as shown in Fig. 2. 7. The percentage differences between shell and elbow results at the middle surface of the intrados, based on Eq. (2.2), are 26.26%, 17.26%, and 51 % for von Mises, hoop, and longitudinal stresses respectively. The difference between shell and elbow element results is attributed to the modelling of the restraints as we chose to employ the kinematic coupling constraints in the shell models at the ends to allow radial deformation (For more details, see Supplemental Material - Modelling of pipe bends). Applying the boundary conditions directly to the end surface of the shell elements is observed to lead to a closer agreement between the stresses obtained from shell and elbow models as shown in Fig. 2. 8. Although ABAQUS documentation indicates that elbow element is allowed to deform radially by default, our latter observation shows that the radial deformation is set to zero at the supports in the elbow element formulation. The deformation results, shown in Fig. 2. 9,

further illustrate the capability of the elbow element to capture the similar deformation distribution of the shell model.

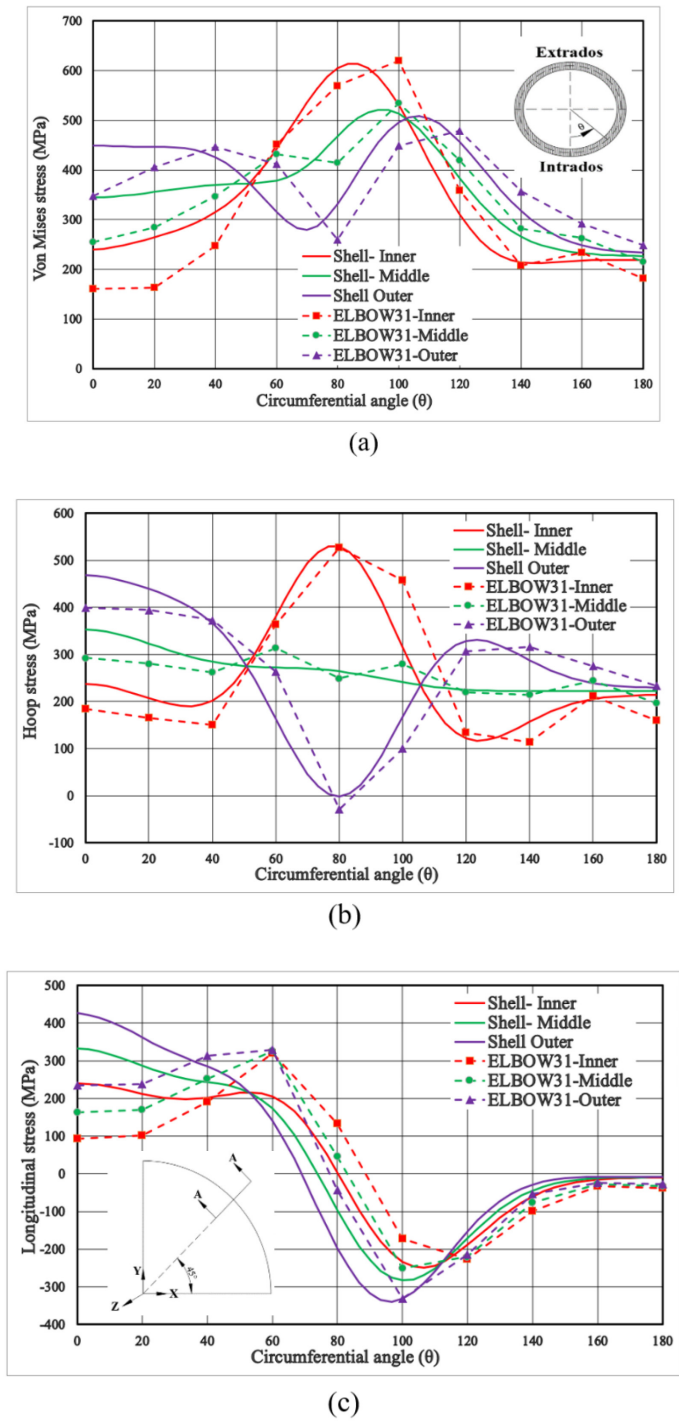
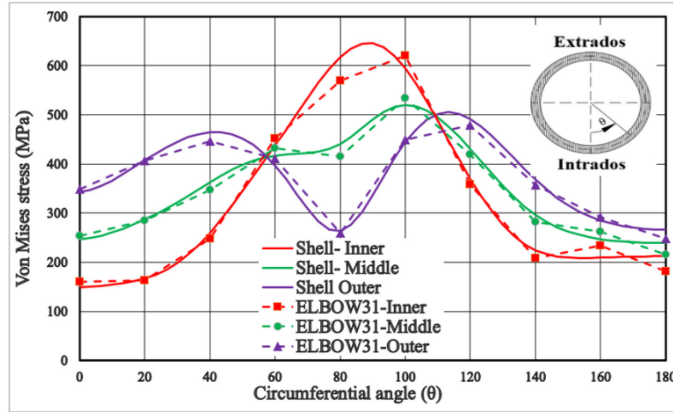
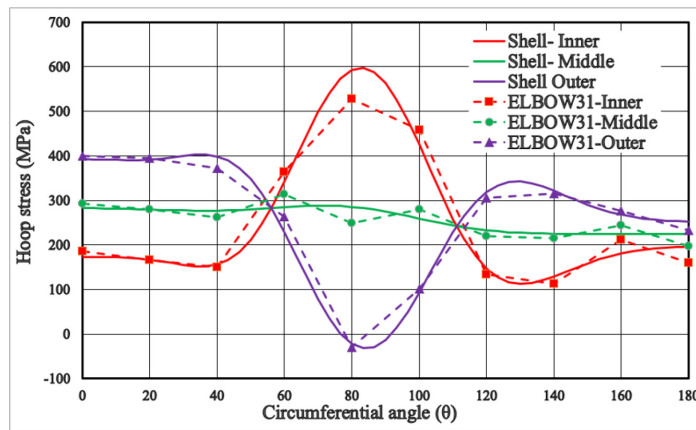


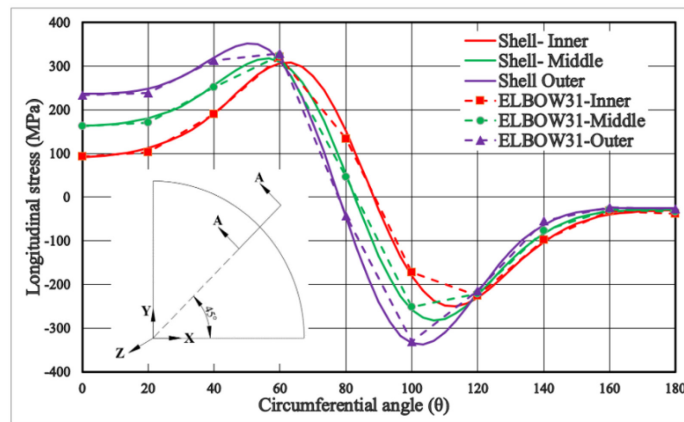
Fig. 2. 7 Stress fields versus circumferential angle θ at section A-A ($R=1.5D_o$ – Fixed-Free – Kinematic coupling). (a) Von Mises stress, (b) Hoop stress, and (c) Longitudinal stress



(a)



(b)



(c)

Fig. 2. 8 Stress fields versus circumferential angle θ at section A-A ($R=1.5D_0$ – Fixed-Free – Direct constraints). (a) Von Mises stress, (b) Hoop stress, and (c) Longitudinal stress

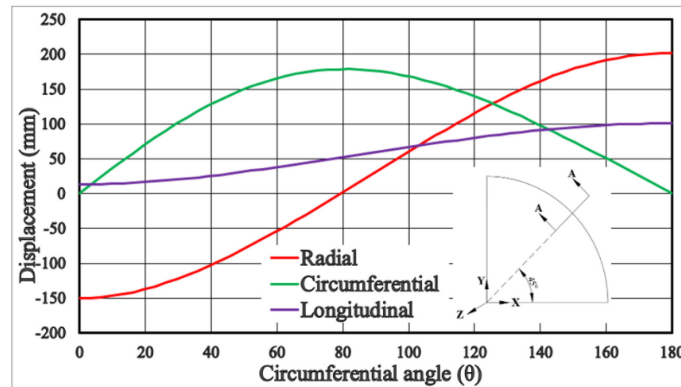
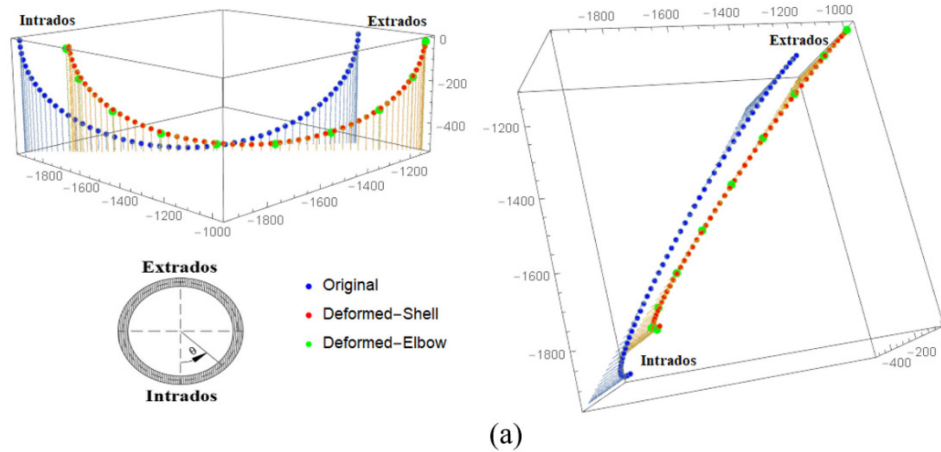
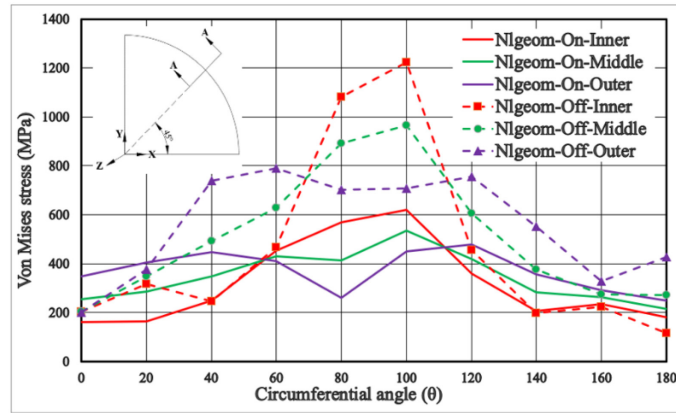


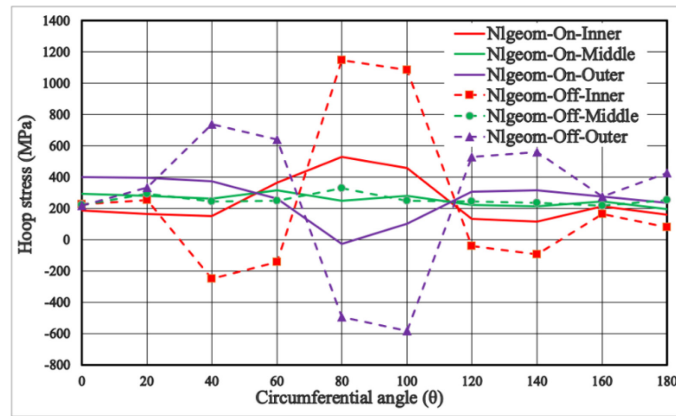
Fig. 2. 9 (a) Original and deformed configurations and (b) Displacements fields versus circumferential angle θ generated by the shell model (Section A-A-R=5D_o – Fixed-Free)

Activating the geometric nonlinearity option in the modelling of elbow model results into good agreement with the results of geometrically nonlinear shell model as shown in Fig. 2. 6 and Fig. 2. 8. Deactivation the geometric nonlinearity option led to a significant difference compared to geometrically nonlinear analysis as shown in Fig. 2. 10. At the intrados, although the geometrically nonlinear analysis predicted stresses that differed from the inner to outer surfaces, the deactivation of geometric nonlinearity generated identical stresses for the inner and outer surfaces. Although the hoop stresses of the middle surface in both analyses are almost similar, there was a large difference in the stresses predicted at the inner and outer surfaces, which exceeded 50 % (Fig. 2.

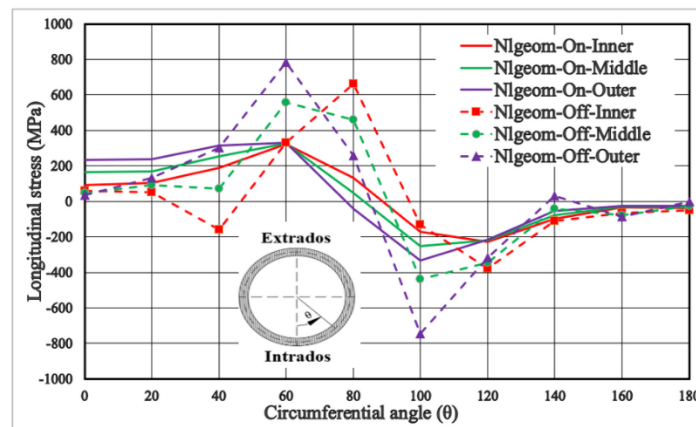
10b). While deactivating geometric nonlinearity leads to conservative solutions, a correct simulation of pipe bend response necessitates the activation of geometric nonlinearity.



(a)



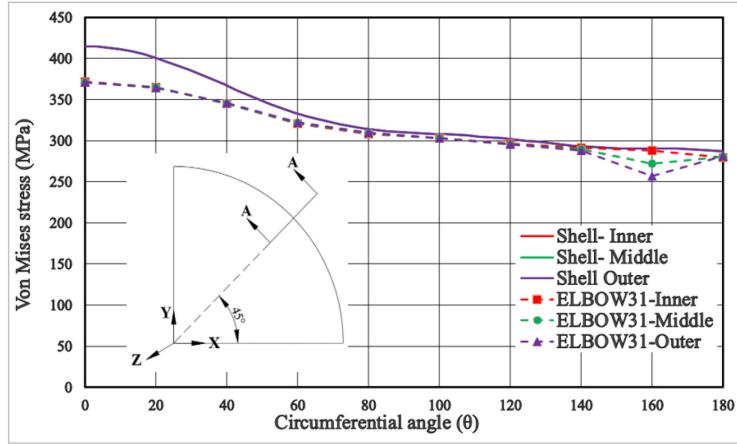
(b)



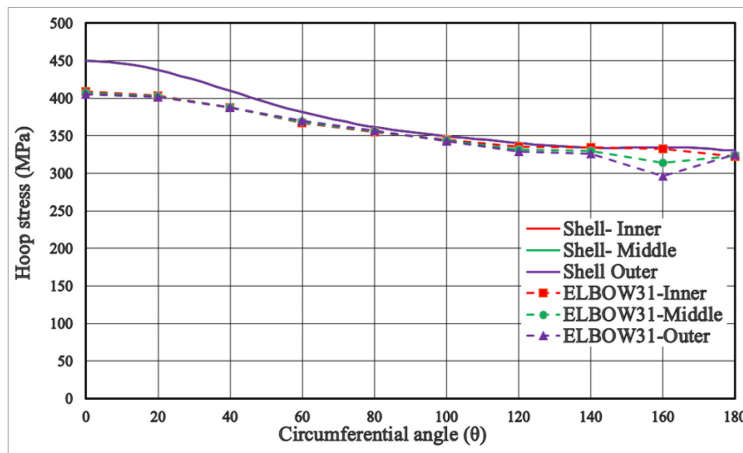
(c)

Fig. 2. 10 Stress fields versus circumferential angle θ at section A-A ($R=1.5D_o$ – Fixed-Free).
 (a) Von Mises stress, (b) Hoop stress, and (c) Longitudinal stress

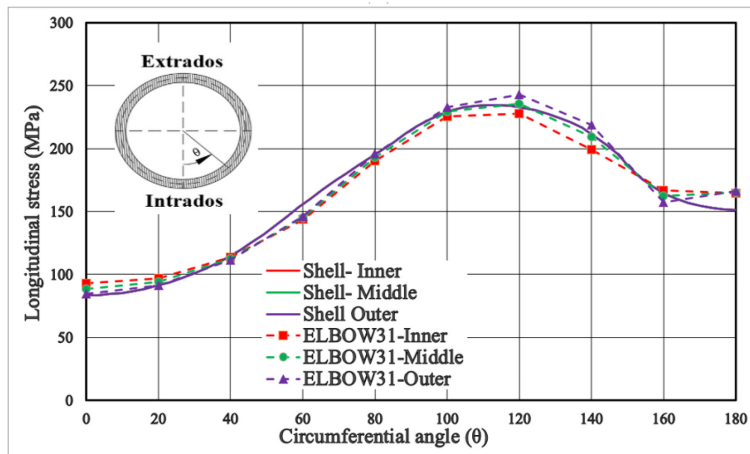
The results of elastic FE analysis for the fixed-fixed case ($R=1.5D_o$) shown in (Appendix 2.A – Additional Results for Case I) illustrated that the maximum von Mises stress was around 225Mpa. In order to evaluate the elasto-plastic response (Fig. 2. 3) of the same problem, the internal pressure was increased to 6.5 MPa. The von Mises, hoop, and longitudinal stress distributions at the central section of the pipe bend (Sec A-A) as predicted by the elasto-plastic shell and elbow models are illustrated in Fig. 2. 11. In the plastic zone ($\theta =0^\circ$ to $\theta =140^\circ$), both models predict no difference between the von Mises stress results for the three surfaces. However, the shell model was found to be more flexible in simulating large plastic strains at the intrados (Fig. 2. 12). Consequently, the von Mises and hoop stresses at the intrados were higher for the shell model and the percentage difference for the middle surface based on Eq. (2.2) were 10.5 % and 9.5 % respectively. On the other hand, the longitudinal stresses were nearly equal in both models as shown in Fig. 2. 11c. Although the elbow model exhibited plastification at the intrados, the maximum principal plastic strains predicted by the elbow model differed drastically from those predicted by the shell model after attaining an internal pressure of 5.2 MPa as shown in Fig. 2. 13a. Below a maximum principal plastic strain of 0.2 %, the difference between the shell and elbow models was negligible. Additionally, the total longitudinal strains depicted in Fig. 2. 13b showed an agreement between the shell and elbow model predictions when the longitudinal strains are below 0.05%. Although the previous elbow results were based on small number of integration points (Model# S12), an increase in the number of integration points in model# S13 did not tangibly change the stress results. It is concluded that the Elbow element is based on a small strain formulation. Further research studies are recommended to investigate the accuracy of ELBOW31 for predicting the longitudinal strains for geohazard applications.



(a)



(b)



(c)

Fig. 2. 11 Stress fields versus circumferential angle θ at section A-A ($R=1.5D_o$ – Fixed-Fixed – Plastic analysis). (a) Von Mises stress, (b) Hoop stress, and (c) Longitudinal stress

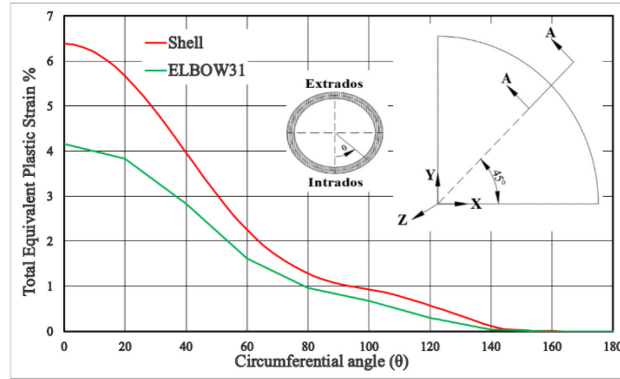
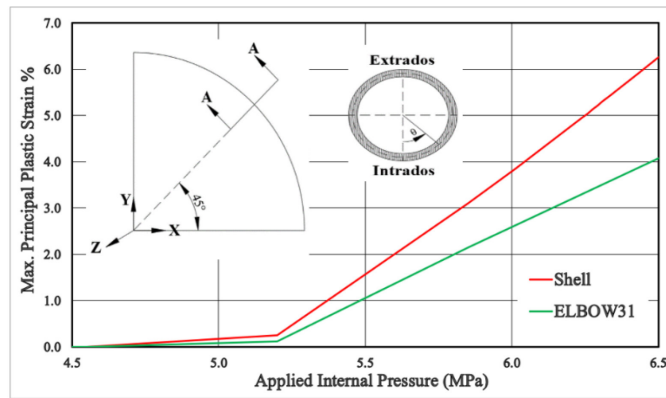
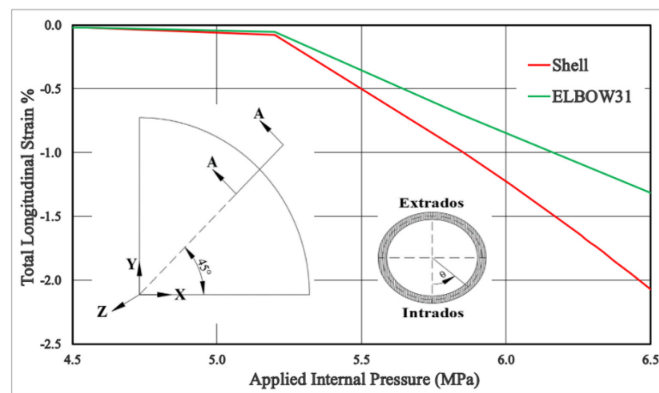


Fig. 2. 12 Total equivalent plastic strain (PEEQ) versus circumferential angle θ at section A-A ($R=1.5D_o$ – Fixed-Fixed – Middle surface– Plastic analysis)



(a)



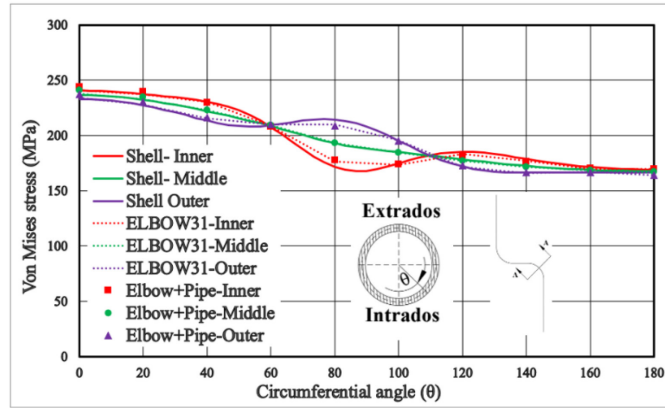
(b)

Fig. 2. 13 (a) Maximum principal plastic strain and (b) Total longitudinal strain versus applied internal pressure at the intrados of section A-A ($R=1.5D_o$ – Fixed-Fixed – Middle surface– Plastic analysis)

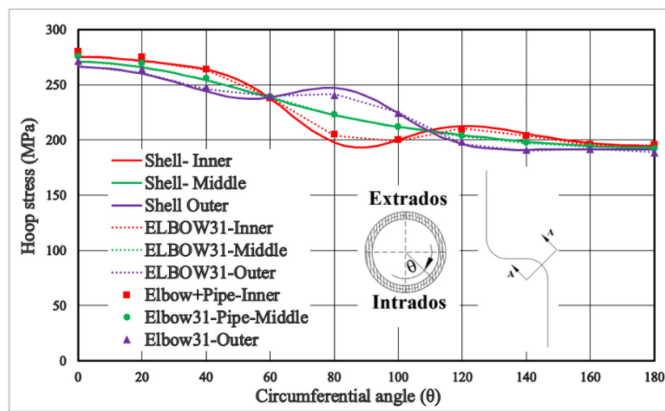
2.4.2 Results for Case II (Two pipe bends connected with straight portions)

Pipe bends are typically subjected to stresses higher than a straight pipe under the same loading. These high stresses would be redistributed when pipe bends are connected to straight segments in reality. Hence the adjacent straight segments would be subjected to stresses higher than the expected stresses in a straight pipe under the same loading. Two cross sections were investigated: the first cross section at the center of the pipe bend and the second cross section at the beginning of the straight portion.

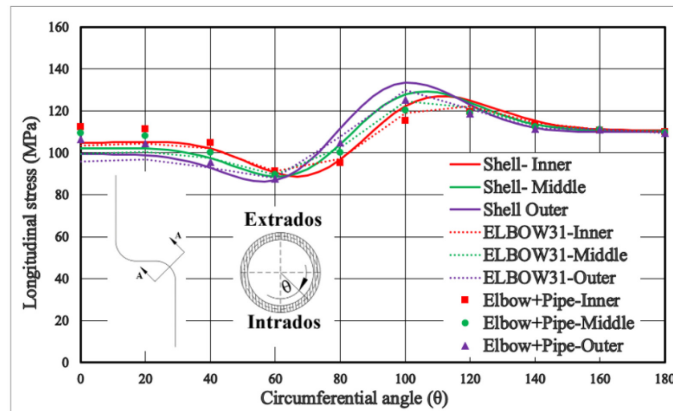
The von Mises and hoop stresses at the centre of the pipe bend (Sec A-A) have similar stress distribution patterns; with the highest value at the intrados ($\theta=0^\circ$) and the lowest value at the extrados ($\theta=180^\circ$). Stresses at the inner surface are higher at the intrados, while those at the outer surface are higher at the crown position ($\theta=90^\circ$) as shown in Fig. 2. 14a and Fig. 2. 14b. The results obtained for shell elements, elbow elements, or combined (elbow&pipe) elements are almost identical. Elbow elements and combined elements can capture the von Mises and hoop stresses at the different surfaces of a pipe bend effectively. On the other hand, longitudinal stresses at the centre of the pipe bend (Sec A-A) have a different stress distribution. The difference between the stresses at the inner and outer surfaces is more pronounced at the intrados and crown, but relatively negligible at the extrados. Whereas the elbow model predicts longitudinal stresses similar to the shell model, a higher error is obtained for the combined model especially at the intrados and crown, as shown in Fig. 2. 14.c.



(a)



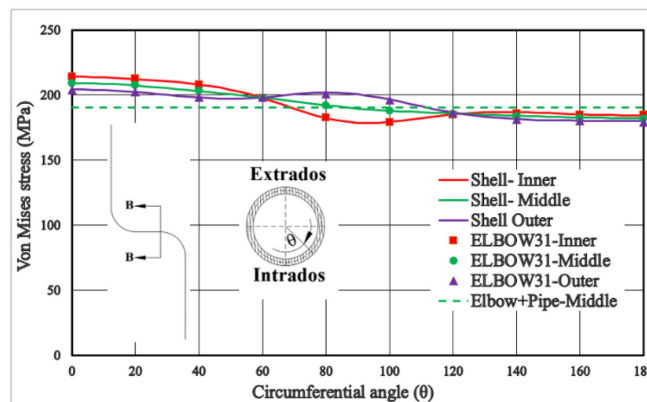
(b)



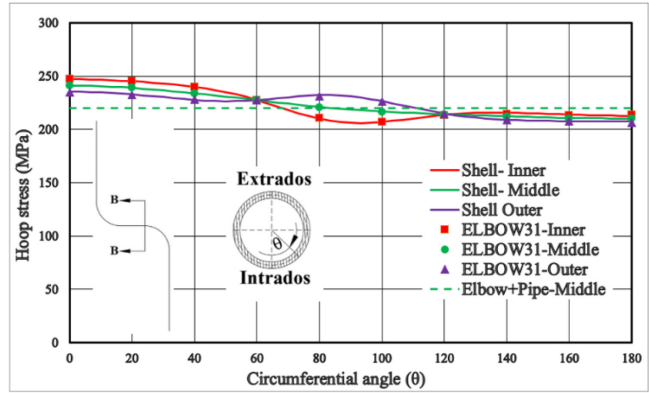
(c)

Fig. 2. 14 Stress fields versus circumferential angle θ at section A-A (a) Von Mises stress, (b) Hoop stress, and (c) Longitudinal stress

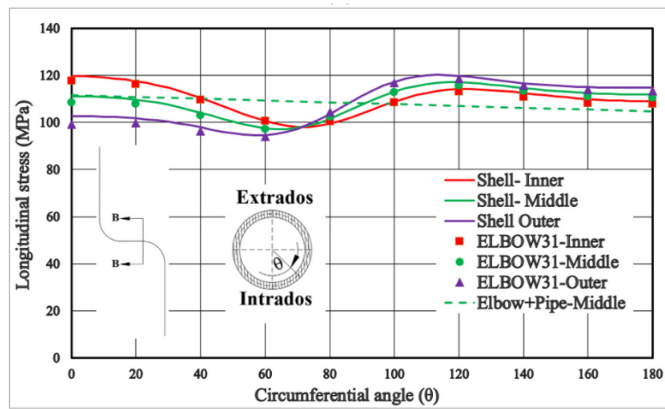
The stress distribution patterns of the von Mises, hoop, and longitudinal stresses evaluated at the starting node of the straight portions (Sec B-B) are similar to those at the centre of the pipe bend (Sec A-A). In addition, the results for the elbow model completely agree with those of the shell model at the different surfaces. The combined model shows only the stress values at the middle surface because the pipe element (PIPE31) was used to model the straight portions. Hence, the results are almost constant along the circumference of the pipe as shown in Fig. 2. 15. The percentage difference between the elbow and combined models at the intrados are 8.85% and 8.66% for the Von Mises and hoop stresses respectively. While the combined model presents a good approximation of the longitudinal stresses at the intrados and crown, there is a difference of 5.27% at the extrados. Consequently, it is recommended to use ELBOW elements in the modelling of the straight portions adjacent to pipe bends, while PIPE elements can be utilized for the remaining straight segments in long pipeline transmission systems.



(a)



(b)



(c)

Fig. 2. 15 Stress fields versus circumferential angle θ at section B-B (a) Von Mises stress, (b) Hoop stress, and (c) Longitudinal stress

2.4.3 Assessment of ASME B16.49 2017 [16] and previous stress estimates [6].

2.4.3.1 ASME B16.49 2017 [16]

Clause 2.2 of ASME B16.49 2017 provides the recommended ratio of the minimum wall thickness at the intrados of a pipe bend to that of a straight pipe as given in Eq. (2.1). In order to check the appropriateness of ASME equation, this factor was compared to the ratio between the value of the hoop stress at the intrados extracted from the analyses of Cases I and II using elbow elements to the hoop stress of a straight pipe as shown in Table 2. 3. In most cases, the code factor is greater than the defined stress ratio below in all elastic analyses in this study. An exception is observed in

the short pipe bend radius ($R=1.5D_o$) analysis with a fixed-free boundary conditions in which stress ratio is 1.3. A parametric study is recommended in order to verify the ASME equation in the case of plastic analysis to investigate the effect of geometric parameters of the pipe bends (pipe bend radius, outer diameter, wall thickness, and pipe bend angle), different boundary conditions, and characteristics of stress-strain relationship.

$$\text{Stress Ratio} = \frac{\text{Hoop stress at intrados at middle surface}}{\frac{P \times D_o}{2 \times t}}$$

Table 2. 3 Hoop stress values and stress ratios of Case I and Case II

	Case I							Case II
	R=5D _o			R=1.5D _o				
Analysis type	Elastic			Elastic			Plastic	Elastic
Boundary Conditions	FR	FF	HH	FR	FF	HH	FF	FF
Code Factor	1.06			1.25				
Hoop stresses (MPa)	237	230	231	292	239	239	450	271
Stress ratio	1.06	1.03	1.03	1.30	1.07	1.07	1.23	1.21

2.4.3.2 Approximate stress equations [6]

Based on three-dimensional elastic FE analysis, Hong [6] proposed a series of approximate equations to calculate the elastic longitudinal, hoop and radial stresses at the center and the end of a thin or thick pipe bend attached to straight portions (Table 2. 4). These equations are applicable for 90°, 45°, and U elbows. The results of these equations were compared to results of this study. The comparison showed that the percentage difference of elbow models is generally lower compared to the approximate equations. Although these equations provide a good estimate of the stresses, the difference between the stresses obtained by elbow models and Hong's equations is

sometimes between 5 % and 10 % at some locations. Table 2. 5 shows the comparison and percentage difference compared to shell results. The percentage difference is also calculated using Eq. (2.2).

Table 2. 4 Approximate equations for the elastic stress fields of a pipe bend attached to straight portions

Position	Pipe bend type	Approximate stress equations
Centre of a pipe bend	Thick-walled	$\sigma_h = P \left[\frac{(r_o/r)^2+1}{(r_o/r_i)^2-1} \right] \left(\frac{2R+r_m \cos \alpha}{2R+2r_m \cos \alpha} \right)$
		$\sigma_l = P \left[\frac{1}{(r_o/r_i)^2-1} \right] \left\{ \left(\frac{R+r_m \cos \alpha}{R+r \cos \alpha} \right)^3 - \cos 2\alpha \left(1 + \frac{\alpha}{\pi} \right) \left(\frac{r_o-r_i}{2R} \right) \right\}$
End of a pipe bend	Thin-walled	$\sigma_h = \frac{P r_i}{t} \left(\frac{4R+3r_m \cos \alpha}{4R+4r_m \cos \alpha} \right)$
		$\sigma_l = \frac{P r_i}{2t}$

Where

σ_h & σ_l are hoop and longitudinal stress respectively

r_o, r_m, r_i are outer, mean, inner radius of a pipe as shown in Fig. 2. 16

r, α are polar coordinate for a pipe bend as shown in Fig. 2. 16

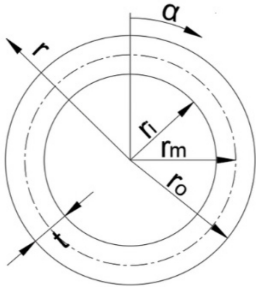


Fig. 2. 16 Geometric properties of the cross section of the pipe bend used by Hong [6]

Table 2. 5 Stress results of shell models, elbow models, and approximate formulas

Section	Position	Stress Type	Surface	Stresses (MPa)			Percentage difference (%)	
				Shell	Elbow	Equations	Elbow	Equations
Center of a pipe bend	Intrados	Hoop	Inner	275	276	277	0.10	0.51
			Outer	266	267	272	0.28	2.11
			Middle	271	271	274	0.19	1.29
		Longitudinal	Inner	105	103	106	1.44	1.51
			Outer	99	96	109	3.50	10.05
			Middle	102	100	108	2.44	5.70
	Extrados	Hoop	Inner	195	195	194	0.18	0.16
			Outer	192	189	191	1.40	0.30
			Middle	193	192	193	0.60	0.24
		Longitudinal	Inner	111	110	109	0.65	1.65
			Outer	110	109	108	0.69	2.45
			Middle	111	110	108	0.67	2.05
End of a pipe bend	Intrados	Hoop	Middle	241	241	247	0.15	2.44
		Longitudinal	Middle	111	108	110	2.47	1.06
	Extrados	Hoop	Middle	210	210	206	0.19	1.86
		Longitudinal	Middle	112	111	110	1.12	1.64

2.5 Conclusion

Pipe bends are primary components in piping systems which have a complex structural behavior to loading. Although solid or shell FE formulations are best-suited for simulating this complex behavior, they are computationally expensive. Elbow elements are special FE that provide a more computationally cost-effective option for simulating the mechanical behavior of pipe bends. Modelling of the elbow element and evaluation of its results under internal pressure, are vital requirements for appropriate design of piping systems. This chapter gives a detailed description of

the modelling and a complete evaluation of the elbow element for pipe bends under internal pressure. The results of this study can be summarized as follows:

- ✓ Elbow elements can efficiently capture the sophisticated behavior of a pipe bend under internal pressure.
- ✓ While end loads for adjoining elements are self-equilibrating, the end force acting on an element located at the end of a pipe requires the application of an externally applied concentrated longitudinal force to simulate the open-ended pipe condition.
- ✓ There is no notable difference between the results of reactions and stresses in the circumferential direction between the responses of ELBOW31 and ELBOW32.
- ✓ The modelling techniques for boundary conditions have a tangible effect on the stress results, especially in pipe elbows with a short bend radius ($R=1.5D_o$).
- ✓ The two proposed modelling techniques for piping systems (elbow model and combined model) have no significant effect on the predicted stresses at the middle of a pipe bend, except for the longitudinal stresses at the intrados and crown positions.
- ✓ The adjacent straight portions attached to pipe bends are typically subjected to higher hoop stresses compared to the stresses expected in a straight pipe segment; hence, the thickness intended for a straight pipe would be insufficient in an elbow.
- ✓ Activating geometric nonlinearity is necessary to capture the realistic response of pipe bends.
- ✓ Based on the stress-strain curve adopted in the present paper, the predictions of the shell and elbow models for the maximum principal plastic strain and total longitudinal strain deviate starting from 0.2 % and 0.05 % respectively.

- ✓ The proposed ASME B16.49 2017 equation of the wall thickness of pipe bends is a conservative estimate for an elastic material characterization.
- ✓ The equations developed by Hong [6] provide an excellent estimate of the elastic stress fields.

2.6 Acknowledgment

Authors express their gratitude to TransCanada Pipelines Ltd, and Enbridge Pipelines Inc. for technical assistance and discussions.

2.7 Funding

This work was supported by Mitacs Accelerate, and Enbridge Pipelines Inc.

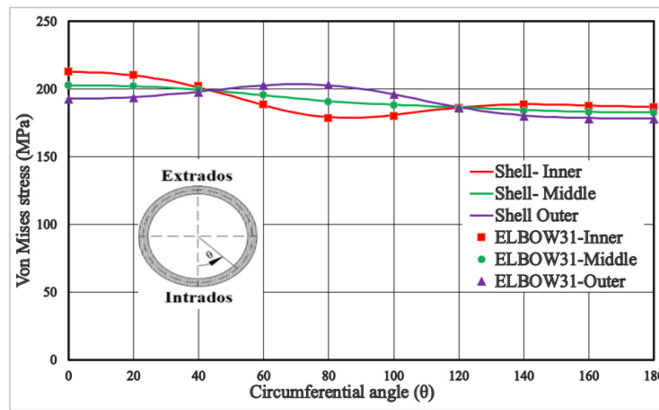
2.8 Nomenclature

E	Young's modulus
ν	Poisson's ratio
D_o	Outer diameter of pipe bends and straight portions
r	Outer radius of pipe bends
R	Pipe bend radius
t	Wall Thickness of pipe bend and the straight portions
L_h	Length of horizontal straight portion
L_v	Length of vertical straight portions
P	Internal pressure
F_x & F_y	Components of the in-plane outward force generated by the Bourdon effect in x and y directions respectively
α	Total bend angle

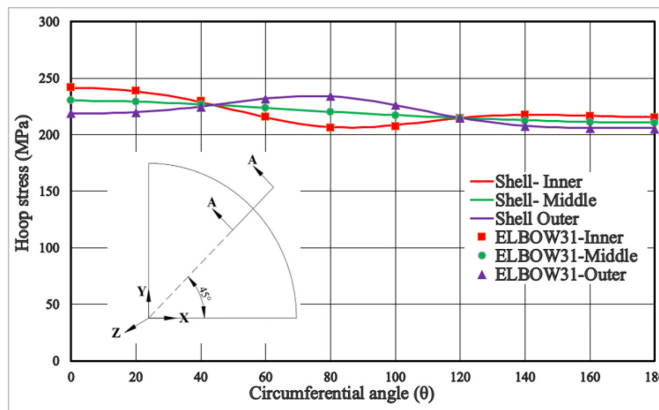
σ_{vM} Von Mises stress that is a stress measure related to the second invariant of the deviatoric stress tensor J_2 , defined as $\sigma_{vM} = \sqrt{3J_2}$

2.9 Appendix 2.A – Additional Results for Case I

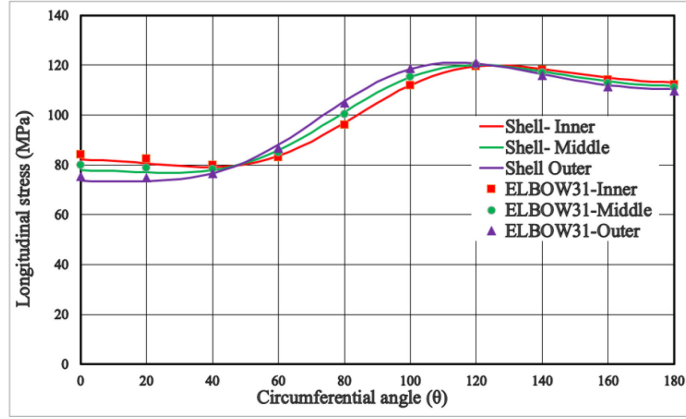
For fixed-fixed case, Fig. 2. A. 1 and Fig. 2. A. 2 present von Mises, hoop, and longitudinal stress distributions along the circumferential direction at section A-A for $R=5D_o$ and $R=1.5D_o$, respectively.



(a)

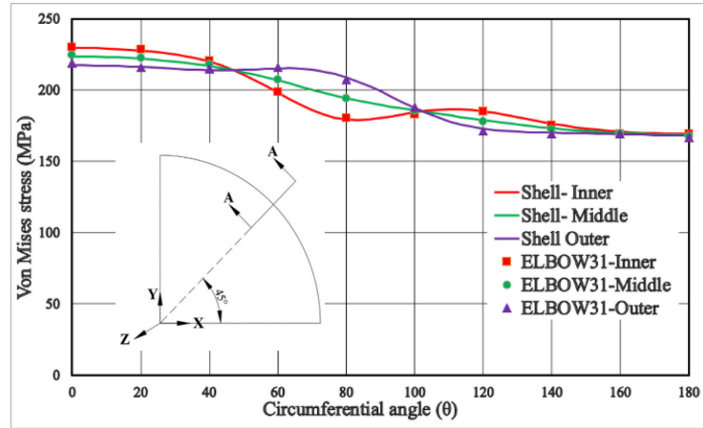


(b)

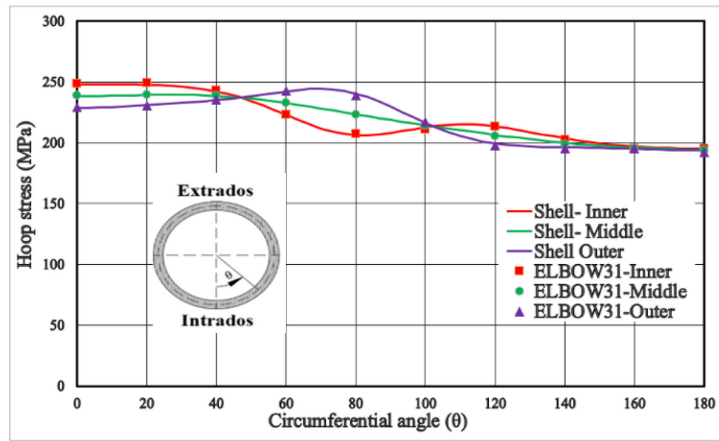


(c)

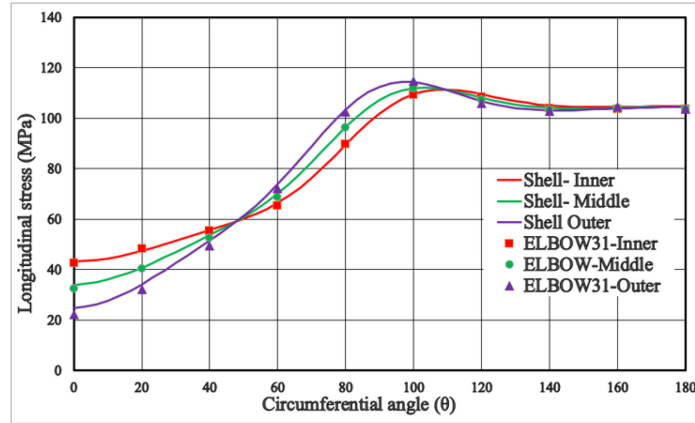
Fig. 2. A. 1 Stress fields versus circumferential angle θ at section A-A for $R=5D_o$. (a) Von Mises stress, (b) Hoop stress, and (c) Longitudinal stress



(a)



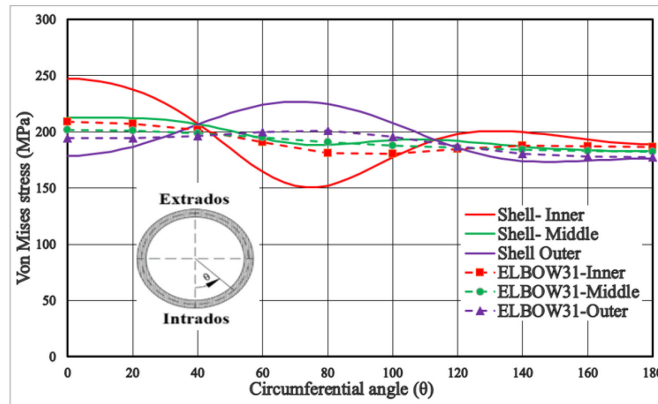
(b)



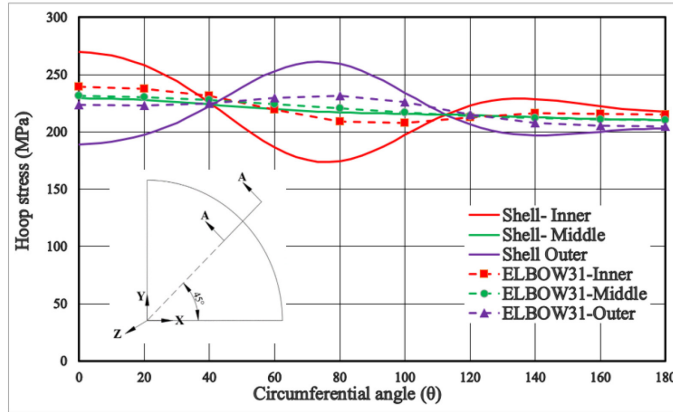
(c)

Fig. 2. A. 2 Stress fields versus circumferential angle θ at section A-A for $R=1.5D_0$ (a) Von Mises stress, (b) Hoop stress, and (c) Longitudinal stress

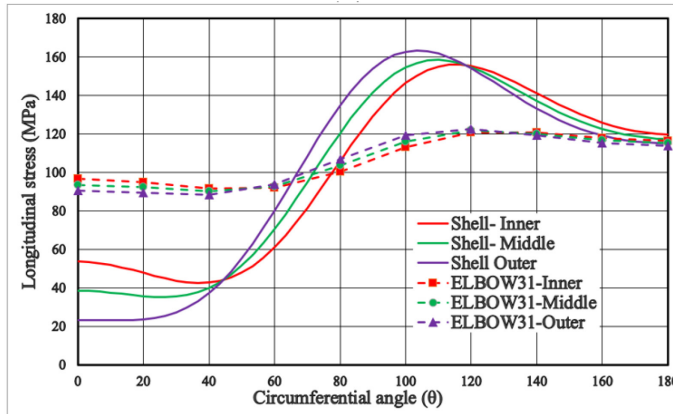
For hinged-hinged case using kinematic coupling constraint, Fig. 2. A. 3 and Fig. 2. A. 4 present von Mises, hoop, and longitudinal stress distributions along the circumferential direction at section A-A for $R=5D_0$ and $R=1.5D_0$, respectively.



(a)

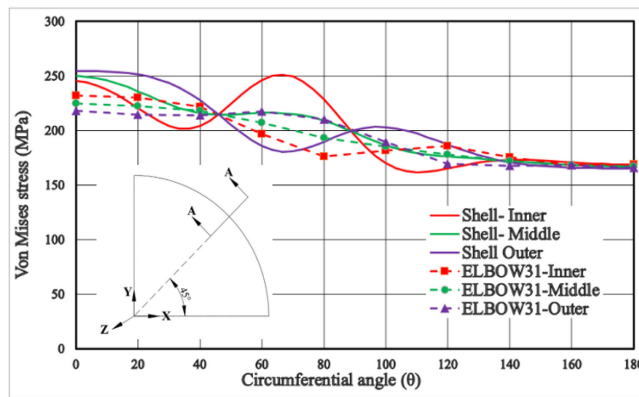


(b)

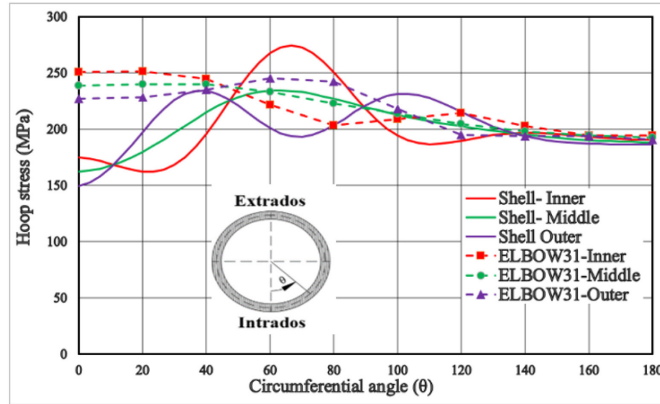


(c)

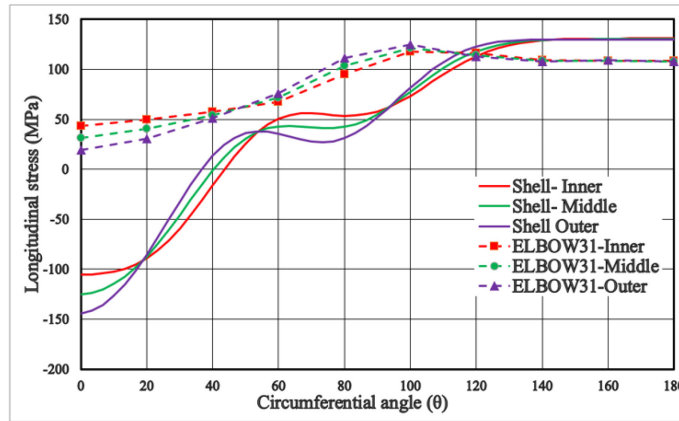
Fig. 2. A. 3 Stress fields versus circumferential angle θ at section A-A for $R=5D_o$ (a) Von Mises stress, (b) Hoop stress, and (c) Longitudinal stress



(a)



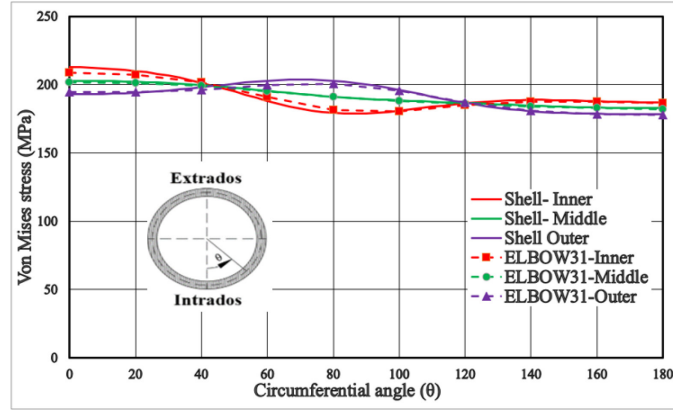
(b)



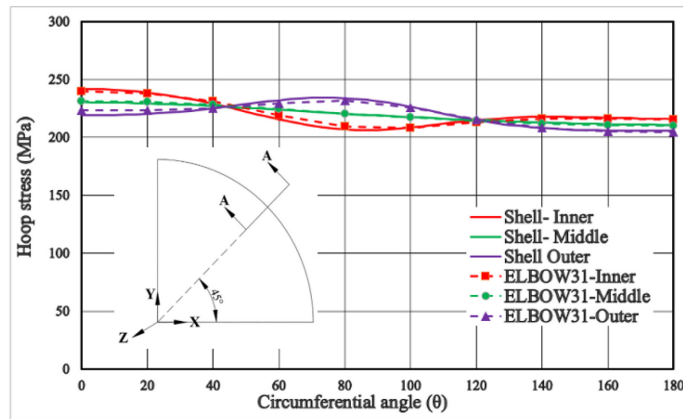
(c)

Fig. 2. A. 4 Stress fields versus circumferential angle θ at section A-A for $R=1.5D_0$ (a) Von Mises stress, (b) Hoop stress, and (c) Longitudinal stress

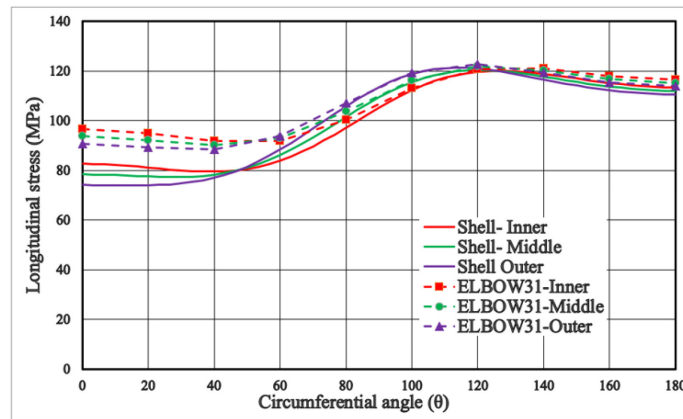
For hinged-hinged case using direct constraint, Fig. 2. A. 5 and Fig. 2. A. 6 present von Mises, hoop, and longitudinal stress distributions along the circumferential direction at section A-A for $R=5D_0$ and $R=1.5D_0$, respectively.



(a)

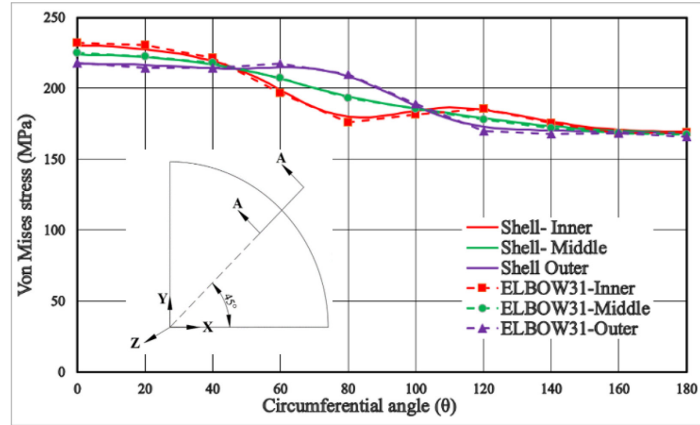


(b)

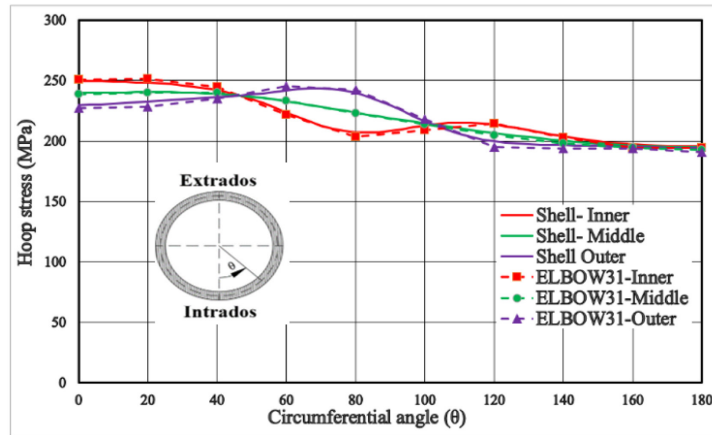


(c)

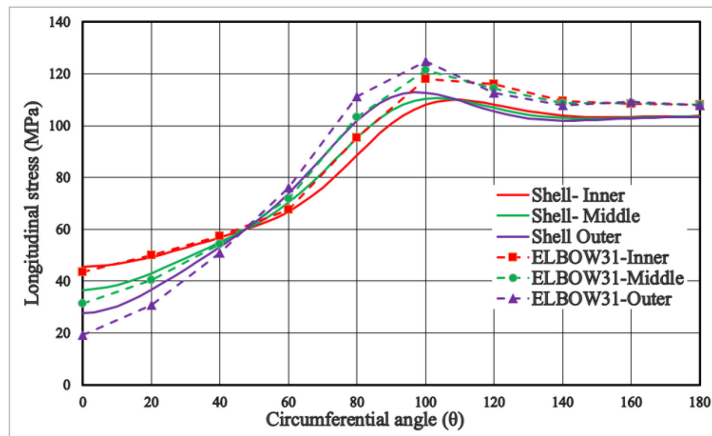
Fig. 2. A. 5 Stress fields versus circumferential angle θ at section A-A for $R=5D_o$. (a) Von Mises stress, (b) Hoop stress, and (c) Longitudinal stress



(a)



(b)



(c)

Fig. 2. A. 6 Stress fields versus circumferential angle θ at section A-A for $R=1.5D_o$, (a) Von Mises stress, (b) Hoop stress, and (c) Longitudinal stress

2.10 Supplemental Material - Modelling of pipe bends

Shell element (S4R)

Due to the symmetry, only half of the pipe bend was considered as shown in Fig. 2. S. 1 ($R=5D_o$). Three-dimensional deformable shell using the sweep option was employed to model the problem. Moreover, the inner surface of the pipe bend was drawn to apply internal pressure in the next steps. Shell elements were four noded doubly curved elements employing reduced integration (S4R). In addition, the approximate size of the element was 30mm. A homogenous shell section was defined with constant thickness knowing that shell offset was the bottom surface. In order to implement kinematic coupling, firstly, two reference points were selected at the ends of the pipe bend. Secondly, a cylindrical coordinate system was created at each end. Finally, a kinematic coupling constraint was defined and the first displacement (U1) at the created coordinate system was released to allow the radial deformation.

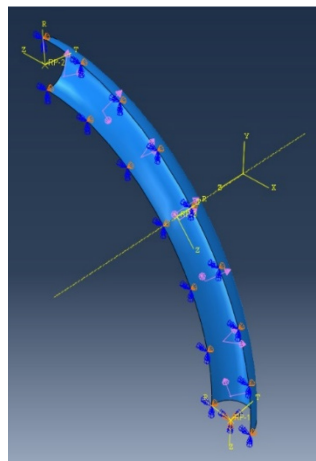


Fig. 2. S. 1 Half of the pipe bend using shell element ($R=5D_o$)

Elbow element (ELBOW31 & ELBOW32)

Centerline of the pipe bend is drawn using three-dimensional deformable wire in plane X-Y as shown in Fig. 2. S. 2 ($R=5D_o$). ELBOW 31 or ELBOW32 was chosen from the element library in ABAQUS with mesh size approximately equal to 30 mm as well. The definition of the elbow cross section firstly required choosing pipe section. Secondly, assigning the pipe section to the problem. Finally, the section was modified by changing the input file as shown in Fig. 2. S. 3. The required changes in the input file were:

- 1- Name of the section.
- 2- Adding the bend radius in the same line of the radius and thickness of a pipe.
- 3- Adding the orientation point [17].
- 4- Adding the integration points around the circumferential and through the thickness and Fourier modes respectively.
- 5- Ovality and warping were prevented at the restrained ends (supports).

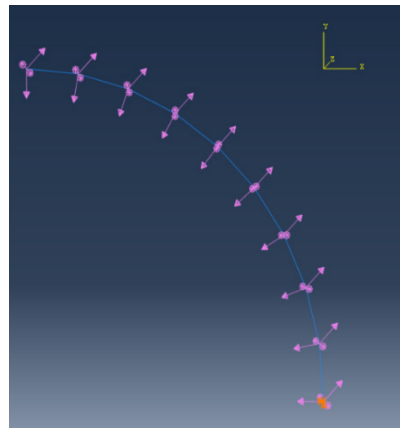


Fig. 2. S. 2 Pipe bend using elbow element ($R=5D_o$)

```

*Nset, nset=Set-3, generate
*Elset, elset=Set-3, generate

*Beam Section, elset=Set-2, material=Material-1, temperature=GRADIENTS, section=PIPE
533.4, 9.525
0, 0, -1.
End Part

** Section: Section-1, Profile: Profile-1
*Beam Section, elset=Set-2, material=Material-1, temperature=GRADIENTS, section=ELBOW
533.4, 9.525, 5334
200, 200, 0
3, 18, 6
End Part

** Name: BC-1 Type: Displacement/Rotation
*Boundary
_PickedSet4, 1, 1
_PickedSet4, 2, 2
_PickedSet4, 3, 3
_PickedSet4, 4, 4
_PickedSet4, 5, 5
_PickedSet4, 6, 6
_PickedSet4, nowarp
_PickedSet4, nooval

```

Fig. 2. S. 3 Required changes in the input file to define the elbow section

2.11 References

- [1] Von Karman, T., 1911, "Ueber Die Formänderung Dummwandiger Rohre, Insbesondere Federnder Ausgleichrohre," Z. Ver. Deut. Ing., 55(Part2), pp.1889–1895.
- [2] Vigness, I., 1943, "Elastic Properties of Curved Tubes," J. Appl. Mech., 55, pp.102–120.
- [3] Kafka, P. G., and Dunn, M. B., 1953, Stiffness of Curved Circular Tubes with Internal Pressure, Boeing Airplane, Chicago, IL.
- [4] Flugge, W., 1973, Stress in Shells, Springer-Verlag, Berlin and New York.
- [5] Goodall, I. W., 1978, "Lower Bound Limit Analysis of Curved Tubes Loaded by Combined Internal Pressure and In-Plane Bending Moment," Central Electricity Generating Board, London, UK, Research Division Report RD/B N4360.
- [6] Hong, S.-P., An, J.-H., Kim, Y.-J., Nikbin, K., and Budden, P. J., 2011, "Approximate Elastic Stress Estimates for Elbow Under Internal Pressure," Int.J. Mech. Sci., 53(7), pp. 526–535.
- [7] Abdulhamed, D., Adeeb, S., Cheng, R., and Martens, M., 2016, "The Influence of the Bourdon Effect on Pipe Elbow," ASME Paper No. IPC2016-64659.
- [8] Bathe, K. J., and Almeida, C. A., 1980, "A Simple and Effective Pipe Elbow Element, Linear Analysis," J. Appl. Mech., 47(1), pp. 100–193.
- [9] Bathe, K. J., and Almeida, C. A., 1982, "A Simple and Effective Pipe Elbow Element, Some Nonlinear Capabilities," J. Appl. Mech., 49(1), pp.165–173.
- [10] Bathe, K. J., and Almeida, C. A., 1982, "A Simple and Effective Pipe Elbow Element, Pressure Stiffening Effects," J. Appl. Mech., 49(4), pp. 914–915.
- [11] Militello, C., and Huespe, A. E., 1988, "A Displacement- Based Pipe Elbow Element," Comput. Struct., 29(2), pp. 339–343.
- [12] Ohtsubo, H., and Watanabe, O., 1978, "Stress Analysis of Pipe Bends by Ring Elements," ASME J. Pressure Vessel Technol., 100(1), pp. 112–122.
- [13] Abo-Elkhier, M., 1990, "Analysis of Pipe Bends Using Pipe Elbow Element," Comput. Struct., 37(1), pp. 9–15.

- [14] Zeng, L., Jansson, L. G., and Venev, Y., 2014, “On Pipe Elbow Elements in ABAQUS and Benchmark Test,” ASME Paper No. PVP2014-28920.
- [15] Bryan, B. J., 1994, Static Analysis of a Piping System with Elbows (WSRCMS-94-075), Minneapolis, MN.
- [16] ASME, 2017, “Factory-Made, Wrought Steel, Butt Welding Introduction Bends for Transportation and Distribution Systems,” ASME Standard No. ASMEB16.49-2017.
- [17] Simulia, 2017, “ABAQUS, User’s Manual Version 6.13 Documentation,” Simulia, Johnston, RI.

Chapter 3

Shell Finite Element Formulation for Geometrically Nonlinear Analysis of Straight Thin-Walled Pipes

3.1 Abstract

A family of new geometrically nonlinear finite elements is formulated for the simulation of the structural response in the elastic regime of straight pipes with circular cross-sections under various loading conditions. The first Piola-Kirchhoff stress tensor is employed within the principle of virtual work framework in conjunction with a total Lagrangian approach. The Green-Lagrange strain tensor is adopted to capture the finite deformation-small strain effects. The formulations are based on the kinematic assumptions of the thin shell theory and capture the follower effects due to pressure load. Three schemes are proposed to interpolate the displacement fields in the circumferential direction: (1) a Fourier series expansion, (2) a quartic spline interpolation, and (3) a mixed interpolation combining Fourier series and splines. The performance and prediction accuracy of the elements are assessed through comparisons with finite element models based on shell and elbow elements in ABAQUS under various loading conditions. The results demonstrate the ability of the elements to predict the displacement and stress fields. In particular, the element based on Fourier series interpolation is shown to provide accurate predictions.

Keywords

Shell Finite Element Formulation, Nonlinear Analysis, Circular Cylindrical Pipe, First Piola-Kirchhoff Stress Tensor, Virtual Work Principle, Spline Interpolation.

3.2 Introduction

Pipeline systems provide effective means of transporting oil and chemicals from centers of production to centers of consumption. Efficient and accurate analysis for pipeline systems is an essential requirement for their structural integrity. The flexibility of hollow circular cross-sections of pipes leads to phenomena such as ovalization and warping in addition to the traditional deformation modes of beams with rigid cross-sections. In order to properly analyze and design pipeline systems, pipe models have to capture ovalization and warping phenomena [1-9]. Although various theoretical and experimental studies [1-5] were carried out for pipeline systems, limitations still exist in predicting the realistic behavior especially in the nonlinear regime of deformation. Solid and shell finite elements (FE) [6-9] are suitable to simulate the structural response of pipeline systems. However, the high computational cost associated with these elements prohibits their use in a design environment. Consequently, special formulations are required to predict the mechanical behavior with a reasonable computational cost. While these special formulations were developed for analysis of pipe bends, they can be used for straight pipes by setting the reciprocal of the pipe bend radius to be zero.

Several FE formulations for the linear analysis of straight and curved pipes were introduced by previous researchers [10-16]. A ring-shaped finite element was developed based on the kinematic constraints of the thin Love-Kirchhoff shell theory [10]. Fourier series interpolation was employed to characterize the variation of the displacement fields in the circumferential direction while Hermitian functions were employed to interpolate the displacement fields along longitudinal direction. The formulation as presented did not satisfy the rigid body motion criterion for curved pipe segments. A simple FE formulation was proposed based on the von Karman theory [1], in

which the displacement fields were taken as a combination of beam deformation mode (centerline displacements) characterized by cubic polynomial displacement functions and cross-sectional deformation modes expressed by Fourier series [11]. The element was further improved to simulate pressure stiffening [12] and interaction effects between the curved and straight pipes [13]. The proposed element ignored warping deformations, which may contribute tangibly to pipe bend deformations [14]. A treatment for warping deformation was proposed in Ref [14] by expressing the longitudinal displacement field as a Fourier series. For straight pipes, an accurate and computationally efficient FE formulation was developed based on thin shell theory [15-16]. While the exact shape functions were obtained for each Fourier mode by solving the equilibrium equations, the formulation is limited to linearly elastic analysis.

Most formulations adopt the principle of virtual work to develop the geometrically nonlinear FE formulations in conjunction with the Lagrangian description approach [17]. There are two common forms of the internal virtual work expression within the Lagrangian description [18-19]: The first employs the second Piola-Kirchhoff stress tensor and the Green-Lagrange strain tensor, and the second adopts the first Piola-Kirchhoff stress tensor and the gradient of the virtual displacement. A detailed description for constructing classical nonlinear FE formulations using the first form was presented in Ref [20] while fully nonlinear FE formulations based on Carrera Unified Formulation (CUF) are provided in Ref [21] for beams and Ref [22] for shells without kinematic constraints. The Elbow elements within FE software packages (e.g. ABAQUS [23], ADINA [24], and ANSYS [25]) are all based on the first form of the internal virtual work. Also based on the first form, recent three-dimensional nonlinear FE formulations for straight and curved pipes with variable cross section were introduced in Refs. [26-28]. To the authors' knowledge, no FE formulations based

on the second form have been reported, although it has been employed in other finite element applications involving beam [29] and shell [30-32].

The current study develops a family of geometrically nonlinear FE formulations for circular straight pipes based on the second form of the internal virtual work. The formulation differs in three aspects from the ones in Refs. [26-27]: (1) the form adopted for the internal virtual work, (2) the present formulation is based on a thin shell theory kinematics while that in Refs. [26-27] is a three-dimensional formulation, and (3) the present study formulates the pressure effect as a follower pressure using the first Piola-Kirchhoff stress tensor. Although the conceptual approach provided in Refs. [21-22] and the present study for linearization of nonlinear equilibrium equations is quite similar, the mathematical application is completely different due to using two different forms of the internal virtual work. In addition, the contribution of follower pressure loads (e.g., significant loading condition in piping systems) in the stiffness matrix was not reported in Refs. [21-22] while that contribution is highlighted in the present study.

3.3 Assumptions

The FE formulation presented in this study is based on the following assumptions:

1. Pipe material is linearly elastic isotropic and follows the Saint-Venant-Kirchhoff material constitutive model.
2. Initially, the pipe has a perfectly circular thin-walled cross section.
3. The formulation is based on the kinematics of the Love-Kirchhoff thin shell theory.
4. The normal stress component in the radial direction is negligible.
5. Pressure load acts as a follower force.

3.4 Formulation

3.4.1 Principle of virtual work

The principle of virtual work for static equilibrium expressed in the reference configuration is given by ⁷

$$\int_{V_o} \mathbf{P} : (\bar{\mathbf{u}} \otimes \nabla^T) dV_o = \int_{S_o} (\tilde{\mathbf{T}}_{\mathbf{N}} \cdot \bar{\mathbf{u}}) dS_o + \int_{V_o} (\tilde{\mathbf{B}} \cdot \bar{\mathbf{u}}) dV_o \quad (3.1)$$

in which all integrations are performed over the reference volume V_o and reference surface S_o that encloses volume V_o . The left hand side denotes the internal virtual work \bar{U} as the inner product (denoted by $:$) of the first Piola-Kirchhoff stress tensor \mathbf{P} and the gradient of the virtual displacement fields $(\bar{\mathbf{u}} \otimes \nabla^T)$, in which $\bar{\mathbf{u}}$ is the virtual displacement fields, ∇ is the gradient operator with respect to the reference configuration, and \otimes denotes the dyadic product. The right hand side of Eq. (3.1) refers to the external virtual work \bar{V} , formulated in the reference configuration, due to the applied traction $\tilde{\mathbf{T}}_{\mathbf{N}}$ on the reference area dS_o defined by the normal vector \mathbf{N} and the body force $\tilde{\mathbf{B}}$ per unit reference volume.

3.4.2 First Piola-Kirchhoff stress tensor in terms of the displacements

The first Piola-Kirchhoff stress tensor \mathbf{P} is related to the second Piola-Kirchhoff stress tensor \mathbf{S} through $\mathbf{P} = \mathbf{F}\mathbf{S}$ in which $\mathbf{F} = (\mathbf{u} \otimes \nabla^T) + \mathbf{I}$ is the deformation gradient tensor of the displacement vector \mathbf{u} and \mathbf{I} is the identity tensor. The second Piola-Kirchhoff stress tensor \mathbf{S} is related to the

⁷ The principle of virtual work can be mathematically derived based on the equilibrium equations (equations of motion) from the principle of conservation of linear momentum in the deformed (spatial) and the reference (material) configurations. The principle of conservation of angular momentum leads to an additional three constraint equations on the Cauchy stress tensor leading to its symmetry property. The equivalent three constraint equations in terms of the first Piola-Kirchhoff stress tensor are provided in Ref [35].

Green-Lagrange strain tensor \mathbf{E} through $\mathbf{S} = \mathbf{C} : \mathbf{E}$ in which \mathbf{C} is the Saint-Venant-Kirchhoff material constitutive tensor (Assumption 1, Section 3.3), and the Green-Lagrange strain tensor is related to the displacement fields through $\mathbf{E} = \frac{1}{2} \left[(\mathbf{u} \otimes \nabla^T) + (\nabla \otimes \mathbf{u}^T) + (\nabla \otimes \mathbf{u}^T)(\mathbf{u} \otimes \nabla^T) \right]$. The

first Piola-Kirchhoff stress tensor is thus expressed in terms of the displacement fields though

$$\mathbf{P} = \mathbf{F}(\mathbf{C} : \mathbf{E}) = \frac{1}{2} \left[(\mathbf{u} \otimes \nabla^T) + \mathbf{I} \right] \left[\mathbf{C} : \left[(\mathbf{u} \otimes \nabla^T) + (\nabla \otimes \mathbf{u}^T) + (\nabla \otimes \mathbf{u}^T)(\mathbf{u} \otimes \nabla^T) \right] \right] \quad (3.2)$$

3.4.3 Virtual displacement fields in terms of virtual nodal degrees of freedom

The displacement fields \mathbf{u} are assumed to be nonlinear functions of the nodal degrees of freedom \mathbf{d} , i.e.,

$$\mathbf{u} = \mathbf{u}(\mathbf{d}) \quad (3.3)$$

Without loss of generality, the arbitrarily virtual displacement field vector $\bar{\mathbf{u}}$ is taken to be related to the virtual degrees of freedom vector $\bar{\mathbf{d}}$ through

$$\bar{\mathbf{u}} = \frac{\partial \mathbf{u}}{\partial \mathbf{d}} \bar{\mathbf{d}} \quad (3.4)$$

From Eq.(3.4), one can express the gradient of the virtual displacement fields as $\bar{\mathbf{u}} \otimes \nabla^T = \left[(\partial \mathbf{u} / \partial \mathbf{d}) \bar{\mathbf{d}} \right] \otimes \nabla^T$, and recover the following relationship between the gradients of the displacements and virtual displacements

$$\frac{\partial (\bar{\mathbf{u}} \otimes \nabla^T)}{\partial \bar{\mathbf{d}}} = \left(\frac{\partial \mathbf{u}}{\partial \mathbf{d}} \right) \otimes \nabla^T = \frac{\partial (\mathbf{u} \otimes \nabla^T)}{\partial \mathbf{d}} \quad (3.5)$$

From Eq.(3.2) and(3.4), by substituting into Eq.(3.1), a generalized expression of the principle of virtual work can be obtained in terms of the displacement fields $\mathbf{u} = \mathbf{u}(\mathbf{d})$ as

$$\begin{aligned}
& \int_{V_o} \left[\frac{1}{2} [(\mathbf{u} \otimes \nabla^T) + \mathbf{I}] [\mathbf{C} : [(\mathbf{u} \otimes \nabla^T) + (\nabla \otimes \mathbf{u}^T) + (\nabla \otimes \mathbf{u}^T)(\mathbf{u} \otimes \nabla^T)] \right] : \left[\left(\frac{\partial \mathbf{u}}{\partial \mathbf{d}} \bar{\mathbf{d}} \right) \otimes \nabla^T \right] dV_o \\
& = \int_{S_o} \left[\tilde{\mathbf{T}}_N \cdot \left(\frac{\partial \mathbf{u}}{\partial \mathbf{d}} \bar{\mathbf{d}} \right) \right] dS_o + \int_{V_o} \left[\tilde{\mathbf{B}} \cdot \left(\frac{\partial \mathbf{u}}{\partial \mathbf{d}} \bar{\mathbf{d}} \right) \right] dV_o
\end{aligned} \tag{3.6}$$

3.5 Force Vectors and Stiffness Matrix

By taking the partial derivatives of Eq.(3.6) with respect to the virtual degrees of freedom vector $\bar{\mathbf{d}}$, the equilibrium equations can be expressed in terms of the displacement fields $\mathbf{u} = \mathbf{u}(\mathbf{d})$ as

$$\mathbf{F}^{(I)}(\mathbf{d}) - \mathbf{F}^{(E)}(\mathbf{d}) = \mathbf{0} \tag{3.7}$$

$$\mathbf{F}^{(I)} = \int_{V_o} \left[\frac{1}{2} [(\mathbf{u} \otimes \nabla^T) + \mathbf{I}] [\mathbf{C} : [(\mathbf{u} \otimes \nabla^T) + (\nabla \otimes \mathbf{u}^T) + (\nabla \otimes \mathbf{u}^T)(\mathbf{u} \otimes \nabla^T)] \right] : \left[\frac{\partial (\mathbf{u} \otimes \nabla^T)}{\partial \mathbf{d}} \right] dV_o \tag{3.8}$$

$$\mathbf{F}^{(E)} = \int_{S_o} \left[\left(\frac{\partial \mathbf{u}}{\partial \mathbf{d}} \right)^T \tilde{\mathbf{T}}_N \right] dS_o + \int_{V_o} \left[\left(\frac{\partial \mathbf{u}}{\partial \mathbf{d}} \right)^T \tilde{\mathbf{B}} \right] dV_o \tag{3.9}$$

in which $\mathbf{F}^{(I)}(\mathbf{d})$ is the internal force vector and $\mathbf{F}^{(E)}(\mathbf{d})$ is the external force vector.

3.5.1 Internal and External Force Vectors

Eqs. (3.7)-(3.9) represent a nonlinear system of equations in the unknown nodal displacement vector \mathbf{d} . The internal and external force vectors are approximated using Taylor series as

$$\mathbf{F}^{(I)}(\mathbf{d}) \approx \mathbf{F}^{(I)}(\mathbf{d}_g) + \mathbf{K}^T \Big|_{\mathbf{d}=\mathbf{d}_g} (\mathbf{d} - \mathbf{d}_g) \tag{3.10}$$

$$\mathbf{F}^{(E)}(\mathbf{d}) \approx \mathbf{F}^{(E)}(\mathbf{d}_g) + \mathbf{K}^F \Big|_{\mathbf{d}=\mathbf{d}_g} (\mathbf{d} - \mathbf{d}_g) \tag{3.11}$$

where $\mathbf{F}^{(I)}(\mathbf{d}_g)$ and $\mathbf{F}^{(E)}(\mathbf{d}_g)$ are the internal and external force vectors at a given nodal

displacement vector \mathbf{d}_g , $\mathbf{K}^T = (\partial \mathbf{F}^{(I)}(\mathbf{d}) / \partial \mathbf{d})$ is the tangent stiffness matrix, and $\mathbf{K}^F = (\partial \mathbf{F}^{(E)}(\mathbf{d}) / \partial \mathbf{d})$ is the contribution of the external force vector to the stiffness matrix. From Eqs.(3.10) and (3.11), by substituting into Eq.(3.7), one recovers the following linearized system of equations in the nodal displacement vector \mathbf{d}

$$\mathbf{R}(\mathbf{d}_g) + \mathbf{K}|_{\mathbf{d}=\mathbf{d}_g} (\mathbf{d} - \mathbf{d}_g) = \mathbf{0} \quad (3.12)$$

where $\mathbf{R}(\mathbf{d}_g) = \mathbf{F}^{(I)}(\mathbf{d}_g) - \mathbf{F}^{(E)}(\mathbf{d}_g)$ is the residual force vector and $\mathbf{K}|_{\mathbf{d}=\mathbf{d}_g} = \mathbf{K}^T|_{\mathbf{d}=\mathbf{d}_g} - \mathbf{K}^F|_{\mathbf{d}=\mathbf{d}_g}$ is the stiffness matrix at a given nodal displacement vector \mathbf{d}_g . The nodal displacement vector \mathbf{d} corresponding to a zero residual force vector is obtained by iteratively solving Eq.(3.12).

3.5.2 Tangent stiffness matrix

In subsections 3.5.2 to 3.5.4, indicial notation with respect to the nodal degrees of freedom d_i (or d_j) where $i, j = 1, 2, \dots, n$, n being the total number of the nodal degrees of freedom, will be utilized to explicitly express the components of the tangent stiffness matrix $K^T|_{ij}$ and the contribution of the external force vector to the stiffness matrix $K^F|_{ij}$. In subsection 3.5.1, we recall that the tangent stiffness matrix has been defined as the derivative of the internal force vector with respect to the degrees of freedom vector. From Eq.(3.2) and by taking the partial derivative of Eq.(3.8) with respect to d_j , the components of the exact tangential stiffness matrix $K^T|_{ij}$ are expressed as

$$K^T|_{ij} = \frac{\partial}{\partial d_j} \left(\int_{V_o} \mathbf{P} : \frac{\partial(\mathbf{u} \otimes \nabla^T)}{\partial d_i} dV_o \right) = \int_{V_o} \left[\frac{\partial \mathbf{P}}{\partial d_j} : \frac{\partial(\mathbf{u} \otimes \nabla^T)}{\partial d_i} + \mathbf{P} : \frac{\partial}{\partial d_j} \left(\frac{\partial(\mathbf{u} \otimes \nabla^T)}{\partial d_i} \right) \right] dV_o \quad (3.13)$$

in which $\partial \mathbf{P} / \partial d_j$ is obtained by differentiation of Eq.(3.2) as

$$\begin{aligned} \frac{\partial \mathbf{P}}{\partial d_j} = \frac{1}{2} & \left[\left(\frac{\partial(\mathbf{u} \otimes \nabla^T)}{\partial d_j} \right) \left[\mathbf{C} : \left((\mathbf{u} \otimes \nabla^T) + (\nabla \otimes \mathbf{u}^T) + (\nabla \otimes \mathbf{u}^T)(\mathbf{u} \otimes \nabla^T) \right) \right] \right. \\ & \left. + \left[(\mathbf{u} \otimes \nabla^T) + \mathbf{I} \right] \left[\mathbf{C} : \left(\frac{\partial(\mathbf{u} \otimes \nabla^T)}{\partial d_j} + \frac{\partial(\nabla \otimes \mathbf{u}^T)}{\partial d_j} + \frac{\partial(\nabla \otimes \mathbf{u}^T)}{\partial d_j} (\mathbf{u} \otimes \nabla^T) + (\nabla \otimes \mathbf{u}^T) \frac{\partial(\mathbf{u} \otimes \nabla^T)}{\partial d_j} \right) \right] \right] \quad (3.14) \end{aligned}$$

3.5.3 Approximation of the tangent stiffness matrix

The present formulation employs an approximation of the tangential stiffness matrix that neglects the second order derivative terms (e.g., $\partial \left[\frac{\partial(\mathbf{u} \otimes \nabla^T)}{\partial d_i} \right] / \partial d_j$) leading to Eq.(3.15)

$$K_A^T|_{ij} \approx \int_{V_o} \left(\frac{\partial \mathbf{P}}{\partial d_j} : \frac{\partial(\mathbf{u} \otimes \nabla^T)}{\partial d_i} \right) dV_o \quad (3.15)$$

3.5.4 Contribution of the external force vector to the stiffness matrix

The derivative of the external force vector with respect to d_j is obtained by differentiating Eq.(3.9), yielding

$$K^F|_{ij} = \int_{S_o} \left(\frac{\partial \tilde{\mathbf{T}}_{\mathbf{N}}}{\partial d_j} \cdot \frac{\partial \mathbf{u}}{\partial d_i} + \tilde{\mathbf{T}}_{\mathbf{N}} \cdot \frac{\partial^2 \mathbf{u}}{\partial d_i \partial d_j} \right) dS_o + \int_{V_o} \left(\frac{\partial \tilde{\mathbf{B}}}{\partial d_j} \cdot \frac{\partial \mathbf{u}}{\partial d_i} + \tilde{\mathbf{B}} \cdot \frac{\partial^2 \mathbf{u}}{\partial d_i \partial d_j} \right) dV_o \quad (3.16)$$

Again, the second order derivatives (e.g. $\partial^2 \mathbf{u} / \partial d_i \partial d_j$) are neglected so that the approximate contribution $K_A^F|_{ij}$ of the external force vector to the stiffness matrix is given by

$$K_A^F|_{ij} \approx \int_{S_o} \left(\frac{\partial \tilde{\mathbf{T}}_N}{\partial d_j} \cdot \frac{\partial \mathbf{u}}{\partial d_i} \right) dS_o + \int_{V_o} \left(\frac{\partial \tilde{\mathbf{B}}}{\partial d_j} \cdot \frac{\partial \mathbf{u}}{\partial d_i} \right) dV_o \quad (3.17)$$

In cases where the applied traction $\tilde{\mathbf{T}}_N$ is independent of the deformation, its derivative $\partial \tilde{\mathbf{T}}_N / \partial d_j$ vanishes and the applied traction does not contribute to the stiffness matrix (e.g., $K_A^F|_{ij} = 0$).

Conversely, when the applied traction $\tilde{\mathbf{T}}_N$ depends on the orientation of the deformed surface \mathbf{d} (as may be the case in the case of follower pressure), $\partial \tilde{\mathbf{T}}_N / \partial d_j$ does not vanish and contributes to the stiffness matrix (e.g. $K_A^F|_{ij} \neq 0$). In the case of a follower pressure load P , the state of stress in the

deformed configuration is given by the Cauchy stress tensor $\boldsymbol{\sigma} = P\mathbf{I}$, where \mathbf{I} is the identity tensor, and the equivalent first Piola-Kirchhoff stress tensor \mathbf{P}_E in the un-deformed configuration is $\mathbf{P}_E = \det(\mathbf{F}) \boldsymbol{\sigma}^T \mathbf{F}^{-T}$ [33], where $\det(\mathbf{F})$ is the determinant of the deformation gradient tensor. The corresponding traction $\tilde{\mathbf{T}}_N$ is thus expressed by

$$\tilde{\mathbf{T}}_N = \mathbf{P}_E \hat{\mathbf{N}} = \det(\mathbf{F}) \boldsymbol{\sigma}^T \mathbf{F}^{-T} \hat{\mathbf{N}} \quad (3.18)$$

and $\hat{\mathbf{N}}$ is the unit vector normal to the area where tractions are applied in the un-deformed configuration. The partial derivative of Eq.(3.18), with respect nodal degrees of freedom d_j is given by

$$\frac{\partial \tilde{\mathbf{T}}_N}{\partial d_j} = \frac{\partial}{\partial d_j} \left(\det(\mathbf{F}) \boldsymbol{\sigma}^T \mathbf{F}^{-T} \hat{\mathbf{N}} \right) = \left(\frac{\partial \det(\mathbf{F})}{\partial d_j} \boldsymbol{\sigma}^T \mathbf{F}^{-T} + \det(\mathbf{F}) \boldsymbol{\sigma}^T \frac{\partial \mathbf{F}^{-T}}{\partial d_j} \right) \hat{\mathbf{N}} \quad (3.19)$$

Using the following mathematical identities in [34]

$$\begin{aligned}\frac{\partial \det(\mathbf{F})}{\partial d_j} &= \det(\mathbf{F}) \operatorname{tr} \left[\mathbf{F}^{-1} \frac{\partial \mathbf{F}}{\partial d_j} \right] = \det \left[(\mathbf{u} \otimes \nabla^T) + \mathbf{I} \right] \operatorname{tr} \left[\left[(\mathbf{u} \otimes \nabla^T) + \mathbf{I} \right]^{-1} \frac{\partial (\mathbf{u} \otimes \nabla^T)}{\partial d_j} \right] \\ \frac{\partial \mathbf{F}^{-T}}{\partial d_j} &= -\mathbf{F}^{-T} \frac{\partial \mathbf{F}^T}{\partial d_j} \mathbf{F}^{-T} = - \left[(\mathbf{u} \otimes \nabla^T) + \mathbf{I} \right]^{-T} \frac{\partial (\mathbf{u} \otimes \nabla^T)^T}{\partial d_j} \left[(\mathbf{u} \otimes \nabla^T) + \mathbf{I} \right]^{-T}\end{aligned}\quad (3.20)$$

Eq.(3.19) can be written as

$$\begin{aligned}\frac{\partial \tilde{\mathbf{T}}_{\mathbf{N}}}{\partial d_j} &= \left[\det \left[(\mathbf{u} \otimes \nabla^T) + \mathbf{I} \right] \operatorname{tr} \left[\left[(\mathbf{u} \otimes \nabla^T) + \mathbf{I} \right]^{-1} \frac{\partial (\mathbf{u} \otimes \nabla^T)}{\partial d_j} \right] \boldsymbol{\sigma}^T \mathbf{F}^{-T} \right. \\ &\quad \left. - \det(\mathbf{F}) \boldsymbol{\sigma}^T \left[(\mathbf{u} \otimes \nabla^T) + \mathbf{I} \right]^{-T} \frac{\partial (\mathbf{u} \otimes \nabla^T)^T}{\partial d_j} \left[(\mathbf{u} \otimes \nabla^T) + \mathbf{I} \right]^{-T} \right] \hat{\mathbf{N}}\end{aligned}\quad (3.21)$$

The contribution $K_A^F|_{ij}$ of the external force vector to the stiffness matrix is then obtained from

Eq.(3.21), by substituting into Eq.(3.17).

3.6 Displacement fields in cylindrical coordinates

The previous section focused on expressing the internal and external force vectors and the stiffness matrix expressions in terms of generic displacement fields \mathbf{u} . The present section specializes the previous equations for the case of thin circular cylindrical shells.

3.6.1 Geometric description

Fig. 3. 1a depicts the un-deformed configuration of the middle surface of an initially circular thin-walled straight pipe, with mid-surface radius r_m and wall thickness h . The coordinates of a material point within the pipe (Fig. 3. 1a) are defined by three coordinates expressed in the cylindrical coordinate system as (z, φ, ζ) along the longitudinal, circumferential, and radial

directions $\{\mathbf{e}_z, \mathbf{e}_\varphi, \mathbf{e}_r\}$ respectively, with $r(\zeta) = r_m + \zeta$. Under loading, Point A on the un-deformed configuration of the middle surface moves to Point A* in the deformed configuration by undergoing a displacement vector \mathbf{u}_0 (Fig. 3. 1b) given by

$$\mathbf{u}_0(z, \varphi) = u_{oz} \mathbf{e}_z + u_{o\varphi} \mathbf{e}_\varphi + u_{or} \mathbf{e}_r(\varphi) \quad (3.22)$$

in which $u_{ok} = u_{ok}(z, \varphi)$ and $k = z, \varphi, r$. Based on Assumption 3 (Section 3.3), the displacement field vector $\mathbf{u} = \mathbf{u}(z, \varphi, \zeta)$ of a generic point that is offset by a radial distance ζ from the middle surface, is expressed as

$$\mathbf{u}(z, \varphi, \zeta) = \mathbf{u}_0(z, \varphi) + \zeta(\hat{\mathbf{n}}(z, \varphi) - \hat{\mathbf{N}}(z, \varphi)) \quad (3.23)$$

in which $\hat{\mathbf{n}}$ is the unit vector normal to the deformed middle surface and $\hat{\mathbf{N}}$ is the unit vector normal to the un-deformed middle surface.

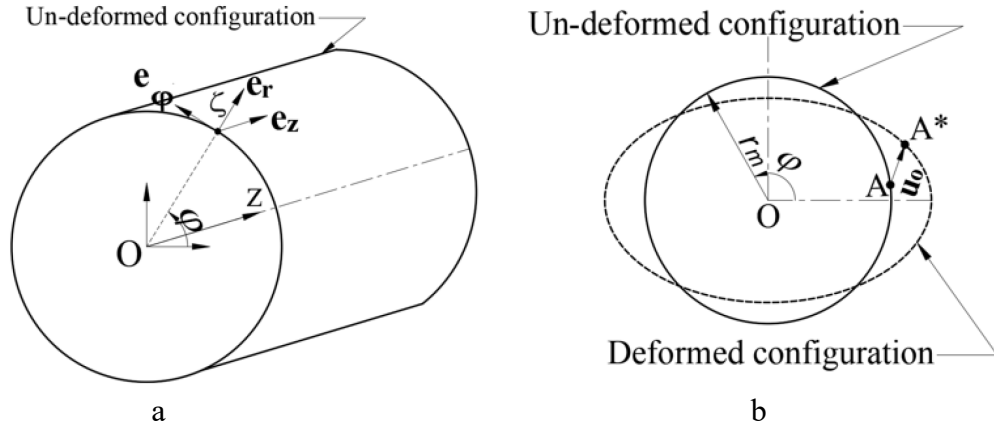


Fig. 3. 1 (a) Pipe coordinates and vector bases and (b) Pipe displacements

3.6.2 Normal unit vector

While the normal unit vector to the un-deformed middle surface is given by $\hat{\mathbf{N}} = \mathbf{e}_r$, the unit vector normal to the deformed middle surface is given by kinematic considerations. The position vector

$\mathbf{r}_0 = \mathbf{r}_0(z, \varphi)$ for a point on the middle surface in the deformed configuration is related to the position vector \mathbf{R}_0 in the un-deformed configuration as given by

$$\mathbf{R}_0(z, \varphi) = z\mathbf{e}_z + r_m\mathbf{e}_r(\varphi) \quad (3.24)$$

through the relation

$$\mathbf{r}_0(z, \varphi) = \mathbf{R}_0(z, \varphi) + \mathbf{u}_0(z, \varphi) \quad (3.25)$$

The normal vector \mathbf{n} in the deformed configuration is given by

$$\mathbf{n} = (\partial\mathbf{r}_0/\partial z) \times (\partial\mathbf{r}_0/\partial\varphi) = n_1(z, \varphi)\mathbf{e}_z + n_2(z, \varphi)\mathbf{e}_\varphi(\varphi) + n_3(z, \varphi)\mathbf{e}_r(\varphi) \quad (3.26)$$

where n_1, n_2 and n_3 are the components of the normal vector in the deformed configuration.

From Eq.(3.22) and(3.24), by substituting into Eq.(3.25), the position vector of the middle surface in the deformed configuration and its derivatives are given by

$$\begin{aligned} \mathbf{r}_0(z, \varphi) &= [z + u_{oz}(z, \varphi)]\mathbf{e}_z + u_{o\varphi}(z, \varphi)\mathbf{e}_\varphi(\varphi) + [r_m + u_{or}(z, \varphi)]\mathbf{e}_r(\varphi) \\ \partial\mathbf{r}_0/\partial z &= [1 + u_{oz,z}(z, \varphi)]\mathbf{e}_z + u_{o\varphi,z}(z, \varphi)\mathbf{e}_\varphi(\varphi) + u_{or,z}(z, \varphi)\mathbf{e}_r(\varphi) \\ \partial\mathbf{r}_0/\partial\varphi &= u_{oz,\varphi}(z, \varphi)\mathbf{e}_z + [r_m + u_{o\varphi,\varphi}(z, \varphi) + u_{or}(z, \varphi)]\mathbf{e}_\varphi(\varphi) + [u_{or,\varphi}(z, \varphi) - u_{o\varphi}(z, \varphi)]\mathbf{e}_r(\varphi) \end{aligned} \quad (3.27)$$

where subscripts with $(,)$ refer to the partial derivative of the argument function with respect to the quantity following the comma. From Eqs. (3.27), by substituting into Eq.(3.26), one recovers the normal vector \mathbf{n} . The components of vector \mathbf{n} are given by

$$\begin{aligned} n_1 &= u_{o\varphi,z}(z, \varphi)[u_{or,\varphi}(z, \varphi) - u_{o\varphi}(z, \varphi)] - u_{or,z}(z, \varphi)[r_m + u_{o\varphi,\varphi}(z, \varphi) + u_{or}(z, \varphi)] \\ n_2 &= u_{or,z}(z, \varphi)u_{oz,\varphi}(z, \varphi) - [1 + u_{oz,z}(z, \varphi)][u_{or,\varphi}(z, \varphi) - u_{o\varphi}(z, \varphi)] \\ n_3 &= [1 + u_{oz,z}(z, \varphi)][r_m + u_{o\varphi,\varphi}(z, \varphi) + u_{or}(z, \varphi)] - u_{o\varphi,z}(z, \varphi)u_{oz,\varphi}(z, \varphi) \end{aligned} \quad (3.28)$$

and the components of the normal unit vector $\hat{\mathbf{n}}$ are given by

$$\hat{n}_i = n_i / \sqrt{n_1^2 + n_2^2 + n_3^2} \quad i = 1, 2, 3 \quad (3.29)$$

3.6.3 Displacement fields for a point offset from the middle surface

The displacement field vector $\mathbf{u}(z, \varphi, \zeta) = (u_z, u_\varphi, u_r)$ for a generic point offset from the middle surface is related to the displacement fields $\mathbf{u}_0 = (u_{oz}, u_{o\varphi}, u_{or})$ at the pipe mid-surface from Eqs.(3.22),(3.28) and(3.29), by substituting into Eq.(3.23), yielding

$$\mathbf{u}(z, \varphi, \zeta) = u_z \mathbf{e}_z + u_\varphi \mathbf{e}_\varphi(\varphi) + u_r \mathbf{e}_r(\varphi) \quad (3.30)$$

in which

$$\begin{aligned} u_z(z, \varphi, \zeta) &= u_{oz}(z, \varphi) + \zeta \hat{n}_1(z, \varphi) \\ u_\varphi(z, \varphi, \zeta) &= u_{o\varphi}(z, \varphi) + \zeta \hat{n}_2(z, \varphi) \\ u_r(z, \varphi, \zeta) &= u_{or}(z, \varphi) + \zeta \hat{n}_3(z, \varphi) - \zeta \end{aligned} \quad (3.31)$$

3.7 Gradient of the displacement field vector and its derivative

The gradient operator in cylindrical coordinates is given by $\nabla = \langle \partial/\partial z \mid (1/r)\partial/\partial\varphi \mid \partial/\partial r \rangle^T$ in which coordinate r is related to coordinate ζ through $r(\zeta) = r_m + \zeta$, and the gradient of the displacement field vector \mathbf{u} is given by

$$\mathbf{u} \otimes \nabla^T = \begin{bmatrix} u_{z,z} & [1/(r_m + \zeta)]u_{z,\varphi} & u_{z,\zeta} \\ u_{\varphi,z} & [1/(r_m + \zeta)](u_{\varphi,\varphi} + u_r) & u_{\varphi,\zeta} \\ u_{r,z} & [1/(r_m + \zeta)](u_{r,\varphi} - u_\varphi) & u_{r,\zeta} \end{bmatrix} \quad (3.32)$$

The derivatives of the displacement fields (u_z, u_φ, u_r) with respected to z , φ and ζ are given in Appendix 3.A: Derivatives of displacement fields with respect to coordinates . From Eqs.(3.28), (3.29), (3.31), and (3.A.1) to (3.A.16) (See Section 3.11), by substituting into Eq.(3.32), one can express the components of Eq.(3.32) in terms of the components $(u_{oz}, u_{o\varphi}, u_{or})$ of the displacement

field vector \mathbf{u}_0 and their derivatives with respect to z and φ . Eqs.(3.8) and (3.15) involve the derivatives of the gradient $\mathbf{u} \otimes \nabla^T$ of the displacement field vector with respect to the nodal degrees of freedom d_j that is given by

$$\left(\mathbf{u} \otimes \nabla^T\right)_{,d_j} = \begin{bmatrix} \left(u_{z,z}\right)_{,d_j} & [1/(r_m + \zeta)]\left(u_{z,\varphi}\right)_{,d_j} & \left(u_{z,\zeta}\right)_{,d_j} \\ \left(u_{\varphi,z}\right)_{,d_j} & [1/(r_m + \zeta)]\left(u_{\varphi,\varphi} + u_r\right)_{,d_j} & \left(u_{\varphi,\zeta}\right)_{,d_j} \\ \left(u_{r,z}\right)_{,d_j} & [1/(r_m + \zeta)]\left(u_{r,\varphi} - u_\varphi\right)_{,d_j} & \left(u_{r,\zeta}\right)_{,d_j} \end{bmatrix} \quad (3.33)$$

The components of $\left(\mathbf{u} \otimes \nabla^T\right)_{,d_j}$ involve the derivatives with respect to d_j of the components of the displacement field vector (u_z, u_φ, u_r) provided in Appendix 3.B: Derivatives of displacement fields with respect to nodal degrees of freedom (See Eqs.(3.B.5) to (3.B.16)). Knowing the components of the second order tensor appearing in Eq.(3.33), the internal force vector (Eq.(3.8)) and the tangent stiffness matrix (Eq.(3.15)) can be obtained. In addition, Eqs.(3.B.1) to (3.B.4) obtained in Section 3.12 provide the derivatives of the displacement field vector (u_z, u_φ, u_r) with respect to d_j involved in the mathematical expressions of the external force vector (Eq.(3.9)) and its contribution to the stiffness matrix (Eq.(3.17)). Consequently, the internal and external force vectors and the stiffness matrix can be determined in terms of the components $(u_{oz}, u_{o\varphi}, u_{or})$ of the mid-surface displacement vector \mathbf{u}_0 and their derivatives with respect to z , φ , and d_j .

3.8 Interpolation Schemes

The displacement fields $\mathbf{u}_0 = (u_{oz}, u_{o\varphi}, u_{or})$ at the pipe mid-surface are interpolated along the longitudinal and circumferential directions. Regarding the circumferential direction, three

interpolation schemes are attempted: (1) A Fourier series expansion (2) a spline interpolation, and (3) a mixed interpolation adopting the first term of the Fourier expansion along with a spline interpolation. These are detailed in the following:

3.8.1 First scheme – Fourier series interpolation

Fourier series are employed to characterize the variation of the displacement fields along the circumferential direction while cubic Hermitian functions are used to characterize the variation of the displacement fields along the longitudinal direction. The longitudinal, circumferential, and radial displacement fields at the pipe mid-surface are expressed as

$$u_{ok}(z, \varphi) = g_{0k}(z) + \sum_{i=1}^{i=m} [f_{ik}(z) \cos(i\varphi) + g_{ik}(z) \sin(i\varphi)] \quad k = z, \varphi, r \quad (3.34)$$

where $f_{ik}(z)$ ($i = 1, 2, \dots, m$) and $g_{ik}(z)$ ($i = 0, 1, 2, \dots, m$) are related to the degrees of freedom $d_{fk,ij}$ and $d_{gk,ij}$ ($j = 1, 2, 3, 4$) through

$$\begin{aligned} g_{0k}(z) &= \sum_{j=1}^4 H_j(z) d_{gk,0j} \\ f_{ik}(z) &= \sum_{j=1}^4 H_j(z) d_{fk,ij} \\ g_{ik}(z) &= \sum_{j=1}^4 H_j(z) d_{gk,ij} \end{aligned} \quad (3.35)$$

From Eq.(3.35), by substituting into Eq.(3.34), one obtains

$$u_{ok}(z, \varphi) = \sum_{j=1}^4 H_j(z) d_{gk,0j} + \sum_{i=1}^{i=m} \sum_{j=1}^{j=4} [H_j(z) \cos(i\varphi) d_{fk,ij} + H_j(z) \sin(i\varphi) d_{gk,ij}] \quad (3.36)$$

Eq.(3.36) can be expressed in a vector form as

$$u_{ok}(z, \varphi) = \langle \mathbf{L}(z, \varphi) \rangle_{1 \times 4(2m+1)}^T \{ \mathbf{d} \}_{k \ 4(2m+1) \times 1} \quad (3.37)$$

in which $\langle \mathbf{L}(z, \varphi) \rangle_{1 \times 4(2m+1)}^T$ is the vector of shape functions defined as

$$\langle \mathbf{L}(z, \varphi) \rangle^T = \langle \mathbf{H}(z)^T \mid \cos \varphi \mathbf{H}(z)^T \mid \sin \varphi \mathbf{H}(z)^T \mid \cos 2\varphi \mathbf{H}(z)^T \mid \sin 2\varphi \mathbf{H}(z)^T \mid \dots \mid \cos m\varphi \mathbf{H}(z)^T \mid \sin m\varphi \mathbf{H}(z)^T \rangle^T \quad (3.38)$$

where

$$\mathbf{H}(z) = \begin{Bmatrix} 2(z/L)^3 - 3(z/L)^2 + 1 \\ z[(z/L) - 1]^2 \\ -2(z/L)^3 + 3(z/L)^2 \\ (z^2/L)[(z/L) - 1] \end{Bmatrix} \quad (3.39)$$

and $\langle \mathbf{d} \rangle_k^T$ is the vector of degrees of freedom along direction k and is defined as

$$\langle \mathbf{d} \rangle_k^T = \langle \mathbf{d}_{g0}^T \mid \mathbf{d}_{f,1}^T \mid \mathbf{d}_{g,1}^T \mid \mathbf{d}_{f,2}^T \mid \mathbf{d}_{g,2}^T \mid \dots \mid \mathbf{d}_{f,m}^T \mid \mathbf{d}_{g,m}^T \rangle_k \quad (3.40)$$

where

$$\mathbf{d}_{f,i} = \begin{Bmatrix} d_{f,i1} \\ d_{f,i2} \\ d_{f,i3} \\ d_{f,i4} \end{Bmatrix}, \quad \mathbf{d}_{g,i} = \begin{Bmatrix} d_{g,i1} \\ d_{g,i2} \\ d_{g,i3} \\ d_{g,i4} \end{Bmatrix}$$

and $d_{f,i1}, d_{f,i3}, d_{g,i1}$, and $d_{g,i3}$ are the nodal displacements while $d_{f,i2}, d_{f,i4}, d_{g,i2}$, and $d_{g,i4}$ are the nodal rotations. The reader is referred to Appendix 3.C: Interpolation Schemes for more details.

3.8.2 Second scheme – Spline interpolation⁸

The cross section under consideration is divided into four segments S_p , where $p = 1, 2, 3, 4$, as shown in Fig. 3. 2.

⁸ The number of degrees of freedom for a single element using spline interpolation is lower than that using Fourier series interpolation. To the writer's knowledge, the spline interpolation scheme was not attempted within pipe FE formulations in the literature. Therefore, it was of interest to assess the ability of spline interpolation to accurately characterize displacement fields along the circumferential direction.

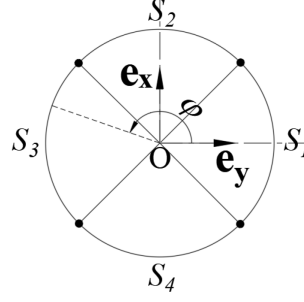


Fig. 3. 2 Cross section discretization

Quartic spline functions are introduced for each segment S_p ($p = 1, 2, 3, 4$) (Fig. 3. 2) which satisfy inter-segment continuity up to the third derivatives at intersection points $(\varphi_{o1}, \varphi_{o2}, \varphi_{o3}, \varphi_{o4}) = \left(-\frac{\pi}{4}, \frac{\pi}{4}, \frac{3\pi}{4}, \frac{5\pi}{4}\right)$ in order to characterize the variation of the displacement fields along the circumferential direction, while the variation of the displacement fields along the longitudinal direction is characterized using two interpolation scenarios; linear Lagrangian interpolation, and Cubic Hermitian interpolation:

a) Linear Lagrangian interpolation

$$u_{ok}(z, \varphi) = \begin{cases} \sum_{j=1}^{j=4} Q_j(\varphi, \varphi_{o1}) [H_1^*(z)u_{jk1} + H_2^*(z)u_{jk2}] & \varphi_{o1} \leq \varphi \leq \varphi_{o2} \\ \sum_{j=1}^{j=4} Q_j(\varphi, \varphi_{o2}) [H_1^*(z)u_{jk1} + H_2^*(z)u_{jk2}] & \varphi_{o2} \leq \varphi \leq \varphi_{o3} \\ \sum_{j=1}^{j=4} Q_j(\varphi, \varphi_{o3}) [H_1^*(z)u_{jk1} + H_2^*(z)u_{jk2}] & \varphi_{o3} \leq \varphi \leq \varphi_{o4} \\ \sum_{j=1}^{j=4} Q_j(\varphi, \varphi_{o4}) [H_1^*(z)u_{jk1} + H_2^*(z)u_{jk2}] & \varphi_{o4} \leq \varphi \leq \varphi_{o1} \end{cases} \quad k = z, x, y \quad (3.41)$$

Eq.(3.41) can be expressed in a vector form as

$$u_{ok}(z, \varphi) = \begin{cases} \left\langle \mathbf{L}_1^*(z, \varphi) \right\rangle_{1 \times 8}^T \{\mathbf{d}\}_{k8 \times 1} & \varphi_{o1} \leq \varphi \leq \varphi_{o2} \\ \left\langle \mathbf{L}_2^*(z, \varphi) \right\rangle_{1 \times 8}^T \{\mathbf{d}\}_{k8 \times 1} & \varphi_{o2} \leq \varphi \leq \varphi_{o3} \\ \left\langle \mathbf{L}_3^*(z, \varphi) \right\rangle_{1 \times 8}^T \{\mathbf{d}\}_{k8 \times 1} & \varphi_{o3} \leq \varphi \leq \varphi_{o4} \\ \left\langle \mathbf{L}_4^*(z, \varphi) \right\rangle_{1 \times 8}^T \{\mathbf{d}\}_{k8 \times 1} & \varphi_{o4} \leq \varphi \leq \varphi_{o1} \end{cases} \quad (3.42)$$

where $\left\langle \mathbf{L}_i^*(z, \varphi) \right\rangle_{1 \times 8}^T$ is the vector of shape functions defined as

$$\left\langle \mathbf{L}_i^*(z, \varphi) \right\rangle^T = \left\langle Q_1(\varphi, \varphi_{oi}) H_1^*(z) \mid Q_1(\varphi, \varphi_{oi}) H_2^*(z) \mid \dots \mid Q_4(\varphi, \varphi_{oi}) H_1^*(z) \mid Q_4(\varphi, \varphi_{oi}) H_2^*(z) \right\rangle \quad (3.43)$$

and $\langle \mathbf{d} \rangle_{k8 \times 1}^T$ is the vector of degrees of freedom along direction k and is defined as

$$\langle \mathbf{d} \rangle_k^T = \langle u_{1k1} \quad u_{1k2} \quad u_{2k1} \quad u_{2k2} \quad u_{3k1} \quad u_{3k2} \quad u_{4k1} \quad u_{4k2} \rangle \quad (3.44)$$

In Eq.(3.41), the spline interpolations in the circumferential direction are

$$\begin{aligned} Q(\varphi, \varphi_{o1}) &= \langle Q_{11}(\varphi - \varphi_{o1}) \quad Q_{12}(\varphi - \varphi_{o1}) \quad Q_{13}(\varphi - \varphi_{o1}) \quad Q_{14}(\varphi - \varphi_{o1}) \rangle \\ Q(\varphi, \varphi_{o2}) &= \langle Q_{14}(\varphi - \varphi_{o2}) \quad Q_{11}(\varphi - \varphi_{o2}) \quad Q_{12}(\varphi - \varphi_{o2}) \quad Q_{13}(\varphi - \varphi_{o2}) \rangle \\ Q(\varphi, \varphi_{o3}) &= \langle Q_{13}(\varphi - \varphi_{o3}) \quad Q_{14}(\varphi - \varphi_{o3}) \quad Q_{11}(\varphi - \varphi_{o3}) \quad Q_{12}(\varphi - \varphi_{o3}) \rangle \\ Q(\varphi, \varphi_{o4}) &= \langle Q_{12}(\varphi - \varphi_{o4}) \quad Q_{13}(\varphi - \varphi_{o4}) \quad Q_{14}(\varphi - \varphi_{o4}) \quad Q_{11}(\varphi - \varphi_{o4}) \rangle \end{aligned} \quad (3.45)$$

in which

$$\begin{aligned} Q_{11}(\varphi - \varphi_{oi}) &= \frac{137}{228} + \frac{388t_i}{285} - \frac{8t_i^2}{19} + \frac{536t_i^3}{285} + \frac{268t_i^4}{285} \\ Q_{12}(\varphi - \varphi_{oi}) &= \frac{-23}{228} - \frac{68t_i}{285} + \frac{8t_i^2}{19} + \frac{376t_i^3}{285} - \frac{4t_i^4}{5} \\ Q_{13}(\varphi - \varphi_{oi}) &= \frac{-23}{228} + \frac{68t_i}{285} + \frac{8t_i^2}{19} - \frac{376t_i^3}{285} + \frac{188t_i^4}{285} \\ Q_{14}(\varphi - \varphi_{oi}) &= \frac{137}{228} - \frac{388t_i}{285} - \frac{8t_i^2}{19} + \frac{536t_i^3}{285} - \frac{4t_i^4}{5} \end{aligned} \quad t_i = \frac{2}{\pi}(\varphi - \varphi_{oi}) \quad i = 1, 2, 3, 4 \quad (3.46)$$

Here, the displacement along the circumferential and radial directions are related to the displacements along the Cartesian coordinates (u_{ox}, u_{oy}) (Fig. 3. 2) through

$$\begin{aligned} u_{o\varphi} &= u_{ox} \cos \varphi - u_{oy} \sin \varphi \\ u_{or} &= u_{ox} \sin \varphi + u_{oy} \cos \varphi \end{aligned} \quad (3.47)$$

b) Cubic Hermitian interpolation

$$u_{ok}(z, \varphi) = \begin{cases} \sum_{j=1}^{j=4} Q_j(\varphi, \varphi_{o1}) [H_1(z)u_{jk1} + H_2(z)\theta_{jk1} + H_3(z)u_{jk2} + H_4(z)\theta_{jk2}] & \varphi_{o1} \leq \varphi \leq \varphi_{o2} \\ \sum_{j=1}^{j=4} Q_j(\varphi, \varphi_{o2}) [H_1(z)u_{jk1} + H_2(z)\theta_{jk1} + H_3(z)u_{jk2} + H_4(z)\theta_{jk2}] & \varphi_{o2} \leq \varphi \leq \varphi_{o3} \\ \sum_{j=1}^{j=4} Q_j(\varphi, \varphi_{o3}) [H_1(z)u_{jk1} + H_2(z)\theta_{jk1} + H_3(z)u_{jk2} + H_4(z)\theta_{jk2}] & \varphi_{o3} \leq \varphi \leq \varphi_{o4} \\ \sum_{j=1}^{j=4} Q_j(\varphi, \varphi_{o4}) [H_1(z)u_{jk1} + H_2(z)\theta_{jk1} + H_3(z)u_{jk2} + H_4(z)\theta_{jk2}] & \varphi_{o4} \leq \varphi \leq \varphi_{o1} \end{cases} \quad (3.48)$$

in which $k = z, x, y$. Eq.(3.48) can be expressed in a vector form as

$$u_{ok}(z, \varphi) = \begin{cases} \langle \mathbf{L}_1^{**}(z, \varphi) \rangle_{1 \times 16}^T \{ \mathbf{d} \}_{k16 \times 1} & \varphi_{o1} \leq \varphi \leq \varphi_{o2} \\ \langle \mathbf{L}_2^{**}(z, \varphi) \rangle_{1 \times 16}^T \{ \mathbf{d} \}_{k16 \times 1} & \varphi_{o2} \leq \varphi \leq \varphi_{o3} \\ \langle \mathbf{L}_3^{**}(z, \varphi) \rangle_{1 \times 16}^T \{ \mathbf{d} \}_{k16 \times 1} & \varphi_{o3} \leq \varphi \leq \varphi_{o4} \\ \langle \mathbf{L}_4^{**}(z, \varphi) \rangle_{1 \times 16}^T \{ \mathbf{d} \}_{k16 \times 1} & \varphi_{o4} \leq \varphi \leq \varphi_{o1} \end{cases} \quad (3.49)$$

where $\langle \mathbf{L}_i^{**}(z, \varphi) \rangle_{1 \times 16}^T$ is the vector of Hermitian shape functions and is defined as

$$\langle \mathbf{L}_i^{**}(z, \varphi) \rangle^T = \langle Q_1(\varphi, \varphi_{oi})H_1(z) \mid Q_1(\varphi, \varphi_{oi})H_2(z) \mid \dots \mid Q_4(\varphi, \varphi_{oi})H_3(z) \mid Q_4(\varphi, \varphi_{oi})H_4(z) \rangle \quad (3.50)$$

and $\langle \mathbf{d} \rangle_{k16 \times 1}^T$ is the vector of degrees of freedom along direction k and is defined as

$$\langle \mathbf{d} \rangle_k^T = \langle u_{1k1} \mid \theta_{1k1} \mid u_{2k1} \mid \dots \mid u_{4k2} \mid \theta_{4k2} \rangle \quad (3.51)$$

in which the linear Lagrangian interpolation along the longitudinal direction is

$$\langle H_1^*(z) \mid H_2^*(z) \rangle = \langle 1-z/L \mid z/L \rangle \text{ while the cubic Hermitian interpolation is given in Eq.(3.39)}$$

$\mathbf{H}(z) = \langle H_1(z) \ H_2(z) \ H_3(z) \ H_4(z) \rangle$. The reader is referred to Appendix 3.C: Interpolation Schemes for more details.

3.8.3 Third scheme – Mixed interpolation

This scheme adopts spline interpolation (described under section 3.8.2) in addition to the first Fourier term $(\cos \varphi, \sin \varphi)$ along the circumferential direction with linear Lagrangian interpolation along the longitudinal direction. The longitudinal displacement at the pipe mid-surface is expressed as

$$u_{oz}(z, \varphi) = \begin{cases} \left[H_1^*(z)u_{z1}^* + H_2^*(z)u_{z2}^* \right] \cos \varphi + \left[H_1^*(z)u_{z1}^{**} + H_2^*(z)u_{z2}^{**} \right] \sin \varphi + \sum_{j=1}^{j=4} Q_j(\varphi, \varphi_{o1}) \left[H_1^*(z)u_{jz1} + H_2^*(z)u_{jz2} \right] & \varphi_{o1} \leq \varphi \leq \varphi_{o2} \\ \left[H_1^*(z)u_{z1}^* + H_2^*(z)u_{z2}^* \right] \cos \varphi + \left[H_1^*(z)u_{z1}^{**} + H_2^*(z)u_{z2}^{**} \right] \sin \varphi + \sum_{j=1}^{j=4} Q_j(\varphi, \varphi_{o2}) \left[H_1^*(z)u_{jz1} + H_2^*(z)u_{jz2} \right] & \varphi_{o2} \leq \varphi \leq \varphi_{o3} \\ \left[H_1^*(z)u_{z1}^* + H_2^*(z)u_{z2}^* \right] \cos \varphi + \left[H_1^*(z)u_{z1}^{**} + H_2^*(z)u_{z2}^{**} \right] \sin \varphi + \sum_{j=1}^{j=4} Q_j(\varphi, \varphi_{o3}) \left[H_1^*(z)u_{jz1} + H_2^*(z)u_{jz2} \right] & \varphi_{o3} \leq \varphi \leq \varphi_{o4} \\ \left[H_1^*(z)u_{z1}^* + H_2^*(z)u_{z2}^* \right] \cos \varphi + \left[H_1^*(z)u_{z1}^{**} + H_2^*(z)u_{z2}^{**} \right] \sin \varphi + \sum_{j=1}^{j=4} Q_j(\varphi, \varphi_{o4}) \left[H_1^*(z)u_{jz1} + H_2^*(z)u_{jz2} \right] & \varphi_{o4} \leq \varphi \leq \varphi_{o1} \end{cases} \quad (3.52)$$

while the circumferential and radial displacements are respectively expressed as

$$u_{o\varphi}(z, \varphi) = u_{ox} \cos \varphi - u_{oy} \sin \varphi + \begin{cases} \left[H_1^*(z)u_{\varphi 1}^* + H_2^*(z)u_{\varphi 2}^* \right] \cos \varphi + \left[H_1^*(z)u_{\varphi 1}^{**} + H_2^*(z)u_{\varphi 2}^{**} \right] \sin \varphi & \varphi_{o1} \leq \varphi \leq \varphi_{o2} \\ \left[H_1^*(z)u_{\varphi 1}^* + H_2^*(z)u_{\varphi 2}^* \right] \cos \varphi + \left[H_1^*(z)u_{\varphi 1}^{**} + H_2^*(z)u_{\varphi 2}^{**} \right] \sin \varphi & \varphi_{o2} \leq \varphi \leq \varphi_{o3} \\ \left[H_1^*(z)u_{\varphi 1}^* + H_2^*(z)u_{\varphi 2}^* \right] \cos \varphi + \left[H_1^*(z)u_{\varphi 1}^{**} + H_2^*(z)u_{\varphi 2}^{**} \right] \sin \varphi & \varphi_{o3} \leq \varphi \leq \varphi_{o4} \\ \left[H_1^*(z)u_{\varphi 1}^* + H_2^*(z)u_{\varphi 2}^* \right] \cos \varphi + \left[H_1^*(z)u_{\varphi 1}^{**} + H_2^*(z)u_{\varphi 2}^{**} \right] \sin \varphi & \varphi_{o4} \leq \varphi \leq \varphi_{o1} \end{cases} \quad (3.53)$$

$$u_{or}(z, \varphi) = u_{ox} \sin \varphi + u_{oy} \cos \varphi + \begin{cases} \left[H_1^*(z)u_{r1}^* + H_2^*(z)u_{r2}^* \right] \cos \varphi + \left[H_1^*(z)u_{r1}^{**} + H_2^*(z)u_{r2}^{**} \right] \sin \varphi & \varphi_{o1} \leq \varphi \leq \varphi_{o2} \\ \left[H_1^*(z)u_{r1}^* + H_2^*(z)u_{r2}^* \right] \cos \varphi + \left[H_1^*(z)u_{r1}^{**} + H_2^*(z)u_{r2}^{**} \right] \sin \varphi & \varphi_{o2} \leq \varphi \leq \varphi_{o3} \\ \left[H_1^*(z)u_{r1}^* + H_2^*(z)u_{r2}^* \right] \cos \varphi + \left[H_1^*(z)u_{r1}^{**} + H_2^*(z)u_{r2}^{**} \right] \sin \varphi & \varphi_{o3} \leq \varphi \leq \varphi_{o4} \\ \left[H_1^*(z)u_{r1}^* + H_2^*(z)u_{r2}^* \right] \cos \varphi + \left[H_1^*(z)u_{r1}^{**} + H_2^*(z)u_{r2}^{**} \right] \sin \varphi & \varphi_{o4} \leq \varphi \leq \varphi_{o1} \end{cases} \quad (3.54)$$

in which displacements u_{ox} and u_{oy} have been defined in spline interpolation (second scheme) ,

$u_{z1}^*, u_{z2}^*, u_{z1}^{**}, u_{z2}^{**}, u_{\varphi 1}^*, u_{\varphi 2}^*, u_{\varphi 1}^{**}, u_{\varphi 2}^{**}, u_{r1}^*, u_{r2}^*, u_{r1}^{**}$, and u_{r2}^{**} are additional degrees of freedom above

those defined in in spline interpolation (second scheme).

3.8.4 Iterative solution scheme

The steps of the iterative solution scheme are

1- Assume initial values of the degrees of freedom vector \mathbf{d}_1

Loop on the iteration number

- 2- Based on the interpolation scheme, calculate the components of the displacement field vector \mathbf{u}_0 and their derivatives with respect to z , φ , and d_j
- 3- From Eqs. (3.28), (3.A.11) to (3.A.16), and (3.B.17) to (3.B.25), calculate the components of the unit vector \mathbf{n} and their derivatives with respect to z , φ , and d_j
- 4- From Eqs.(3.32) and (3.A.1) to (3.A.9), calculate the gradient of the displacement fields
- 5- From Eq.(3.33) and (3.B.5) to (3.B.13), calculate the derivative of the gradient of the displacement fields with respect to d_j

6- From Eqs.(3.8), (3.9), (3.15), and(3.17), calculate the internal $\mathbf{F}^{(I)}$ and external $\mathbf{F}^{(E)}$ force vectors, the approximated stiffness matrix $K_A^T|_{ij}$, and the approximated contribution of the external force vector $K_A^F|_{ij}$, respectively.

7- Calculate an improved value of the degrees of freedom vector by setting $\mathbf{d} = \mathbf{d}_{g+1}$

8- Check the convergence of the force and displacement. If satisfied exit the iteration loop.

End loop on iterations

3.9 Numerical Examples

A 10m long cantilever pipe with wall thickness $h = 10mm$ and mid-surface radius $r_m = 505mm$ is used as shown in Fig. 3. 3. The pipe is analyzed under three loading cases: (1) Combined axial and vertical loading, (2) Uniform internal pressure, and (3) Combined axial, vertical, normal loading and internal pressure to demonstrate the capability of the newly developed elements. The pipe material is steel with Young’s modulus $E = 200GPa$ and Poisson’s ratio $\nu = 0.3$. Both ends of the pipe are open. The pipe is modelled using the three elements developed in the present study, as well as the existing shell element S4R, and pipe element ELBOW31 within the ABAQUS library. All degrees of freedom at the cantilever root are restrained while all degrees of freedom at the cantilever tip are kept free. The detailed description of all FE models is given in Table 3. 1.

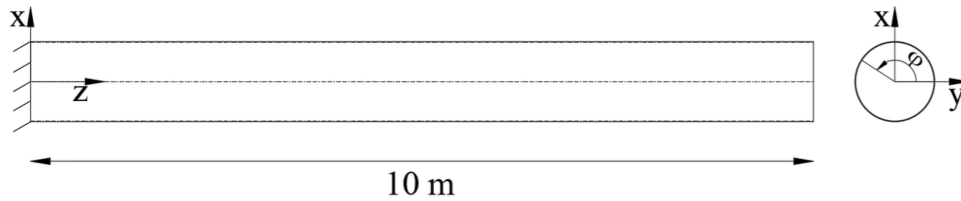


Fig. 3. 3 The cantilever pipe

Table 3. 1 Detailed description of the FE models

	Interpolation	Element	Description	# Elements	# Degrees of freedom	Gauss Integration points		
						z	φ	r
Present formulation	Fourier	PIPE-F-3	Fourier terms $m = 3$	30	1302	5	18	3
		PIPE-F-6	Fourier terms $m = 6$	30	2418	5	30	3
	Spline	PIPE-S-L	Lagrangian interpolation	50	612	2	5	3
		PIPE-S-H	Hermitian interpolation	25	624	3	5	3
	Mixed	PIPE-M-L	Lagrangian interpolation	50	918	2	10	3
ABAQUS	S4R	General shell element	12800	77184	1		5	
	ELBOW31	Fourier terms $m = 6$	50	2652	1	20	3	

3.9.1 Combined axial and vertical loading

The pipe (Fig. 3. 3) is subjected at the free end to an axial compressive traction of 300 MPa (corresponding to 48% of the Euler buckling load) and a vertical downward traction of 15 MPa, i.e., the applied traction vector $\tilde{\mathbf{T}}_N$ in cylindrical coordinates is $\tilde{\mathbf{T}}_N = \{-300, -15 \cos \varphi, -15 \sin \varphi\}^T$. In the S4R model, the traction is lumped as nodal forces at the free end and as two concentrated forces at the centroid of the free end in the ELBOW31 model.

Displacement predictions

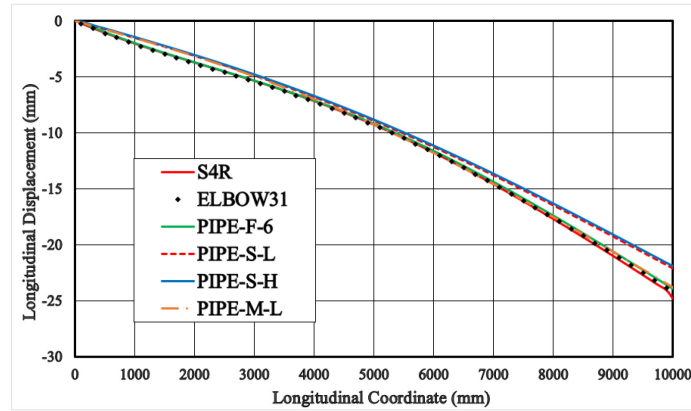
The longitudinal, circumferential, and radial displacement distributions along the span of the pipe are shown in Fig. 3. 4. The comparison between the nonlinear responses as predicted by Abaqus using S4R and ELBOW31 models and those based on the present elements exhibits the ability of the present elements to capture the geometric nonlinear response. Overlaid for the comparison in Fig. 3. 4.b is the vertical displacement as predicted by a linear solution of the conventional Euler-

Bernoulli beam theory and the second order beam-column⁹ analysis that accounts for stiffness softening due to axial compression. All solutions significantly depart from the linearly elastic solution, suggesting that geometrically nonlinear effects are successfully captured by the models¹⁰. In particular, the predictions of the PIPE-F-6 element are in an excellent agreement with those of the ABAQUS models. In contrast, the PIPE-S-L and PIPE-S-H elements predict a slightly stiffer response relative to the longitudinal and circumferential displacements. The superior performance of PIPE-F-6 relative to the PIPE-S-L and PIPE-S-H elements is attributed to the fact that the former exactly captures the rigid body motion in the plane of the cross-section through the Fourier expansion, while in later elements, the spline interpolation simulates rigid body motion only in an approximate sense. By adding the first Fourier mode (which corresponds to the rigid body motion in the plane of the cross-section) to the Spline interpolation, the resulting mixed interpolation in PIPE-M-L is observed to tangibly improve the performance of the element as evidenced by the flexible response more than the analytical solution of the governing differential derived based on the rigid cross section assumption. However, these elements (PIPE-S-L, PIPE-S-H, and PIPE-M-L) are unable to accurately capture the radial displacement distribution associated with cross sectional ovalization due to the coarse discretization of the displacement fields in the circumferential direction. Table 3. 2 provides the percentage differences between the free end displacement predictions of the present elements, and those based on ELBOW 31 model, relative to those of S4R model at various circumferential angles. The percentage differences of the ELBOW31 and PIPE-F-6 elements are less than 4 % for all cases except the longitudinal

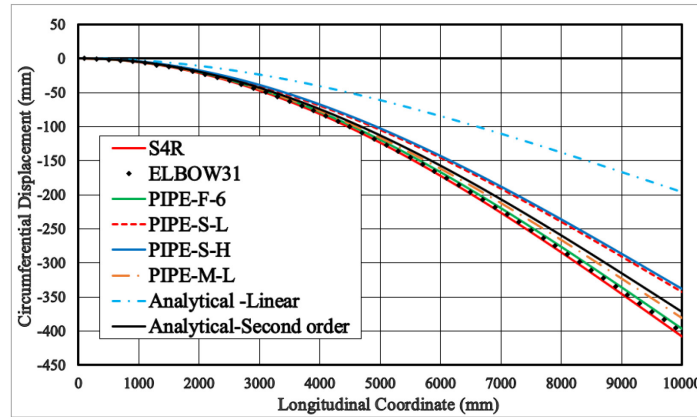
⁹ Second order analysis of a beam with flexural rigidity EI subjected to an axial load F_a and a vertical load at the free end is $EIv'''' + F_a v'' = 0$. The linear solution is obtained by setting $F_a = 0$.

¹⁰ The vertical displacement at the free end obtained from the nonlinear solution is about twice that obtained from the linear solution showcasing the importance of incorporating the geometric nonlinearity in the problem.

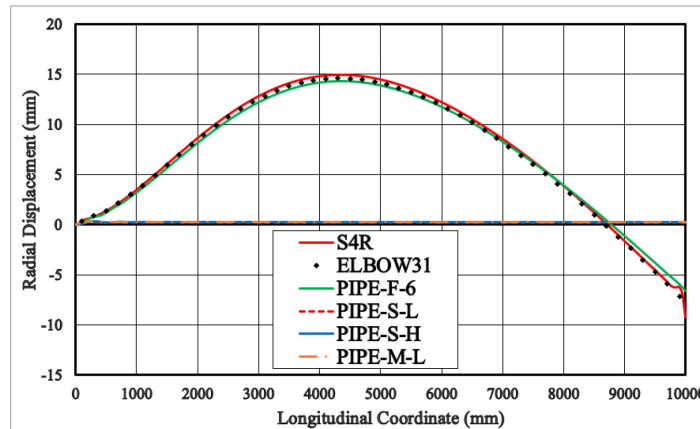
displacement at $\varphi = 90^\circ$ where the percentage differences are 19.9 % for the ELBOW31 element and 11.3 % for the PIPE-F-6 element.



a



b



c

Fig. 3. 4 Displacement fields distributions along the cantilever pipe at $\varphi = 0^\circ$ (a) Longitudinal displacement, (b) Circumferential displacement, and (c) Radial displacement

Table 3. 2 Percentage differences of the longitudinal and vertical displacements at the free end¹¹

		Percentage difference %					
	φ	ELBOW31	PIPE-F-6	PIPE-S-L	PIPE-S-H	PIPE-M-L	Second order analysis
Longitudinal	0°/180°	3.8	3.1	10.7	11.6	3.9	-
	90°	19.9	11.3	18.7	18.8	5.6	-
	270°	1.1	1.8	15.6	16.3	7.6	-
Vertical	0°/180°	3.0	2.9	16.2	17.2	6.8	8.8
	90°	2.8	2.7	14.4	15.5	4.7	7.1
	270°	2.6	2.6	17.3	18.3	7.9	9.9

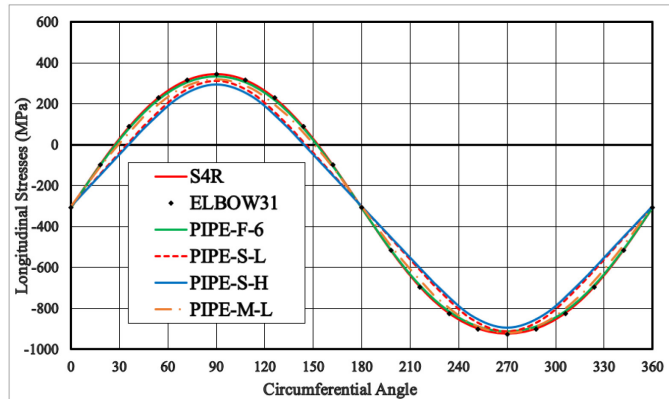
Stress predictions

Fig. 3. 5 depicts the distributions of the longitudinal, circumferential, and shear stresses along the circumferential direction at pipe mid-span (Fig. 3. 3) for the inner and outer surfaces. All models exhibit (Fig. 3. 5a, b) a similar oscillatory response with a peak tensile stress at $\varphi = 90^\circ$ and a peak compressive stress at $\varphi = 270^\circ$, with compressive stresses at 0° , and 180° that fall in between these peak values. Also, the circumferential stress distributions at the inner and outer surfaces exhibit oscillatory distributions with a higher frequency. At the inner surface, the pipe experiences tensile stresses at $\varphi = 90^\circ$ and 270° and compressive stresses at $\varphi = 0^\circ$ and 180° , while the behavior is reversed at the outer surface (Fig. 3. 5c, d). Shear stress distributions (Fig. 3. 5e, f) follow a distribution similar to that based on the mechanics of material solution where they peak at the neutral axis $\varphi = 0^\circ, 180^\circ$, and vanish at the top and bottom generators $\varphi = 90^\circ, 270^\circ$. PIPE-F-6 element predicts stress distributions at the inner and outer surfaces that are in close agreement to those based on the ABAQUS S4R and ELBOW31 models. Although the PIPE-S-L, PIPE-S-H, PIPE-M-L elements reasonably simulate the longitudinal stress distributions, they are unable to

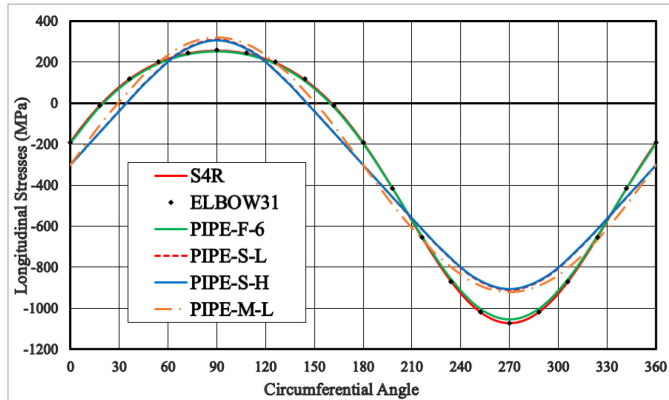
¹¹ The percentage difference of a model is calculated using the following equation

$$\text{Percentage difference \%} = \frac{\text{S4R solution} - \text{model's solution}}{\text{S4R solution}} \times 100$$

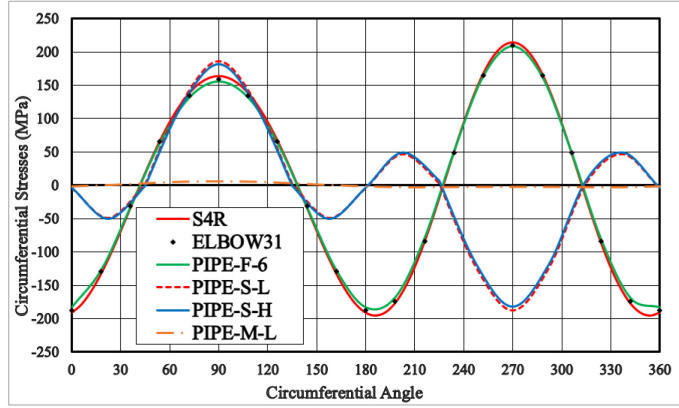
accurately predict the circumferential and shear stress distributions. This is attributed to the approximate representation of rigid body motion when adopting circumferential spline interpolation in the case of PIPE-S-L and PIPE-S-H elements and due to the coarse circumferential discretization of the displacement fields in PIPE-S-L, PIPE-S-H, PIPE-M-L elements. In addition, the strain field distributions for Example 1 are provided in Appendix 3.D: Strain Fields for Example 1.



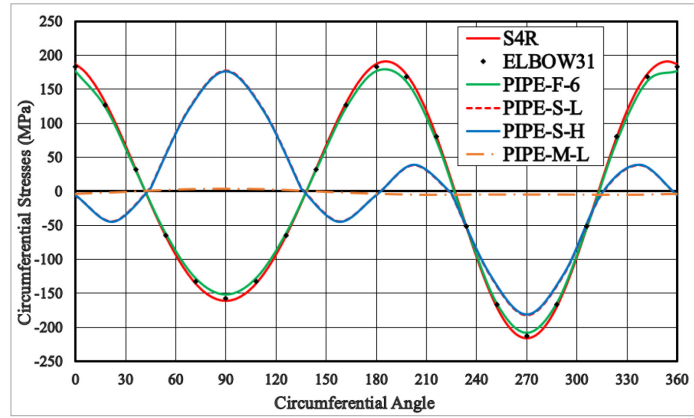
a



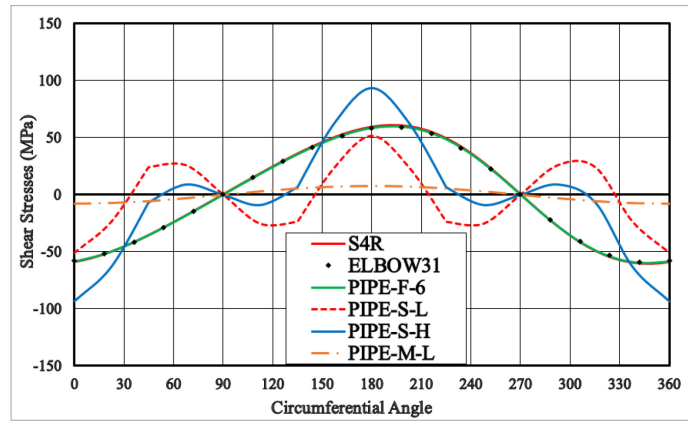
b



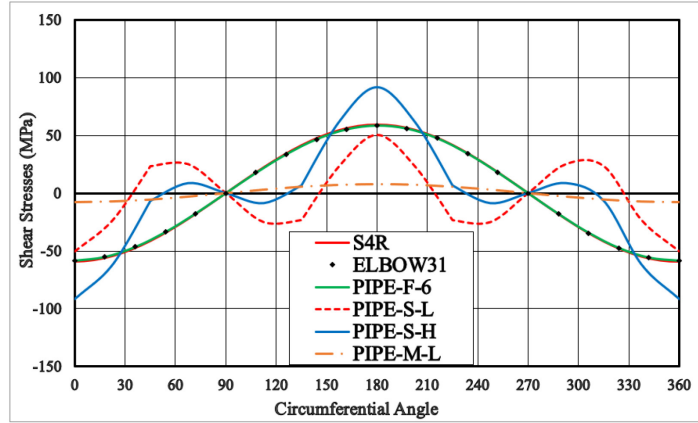
c



d



e



f

Fig. 3. 5 Stress fields versus circumferential angle at the middle section $z = 5m$ (a) Longitudinal- Inner, (b) Longitudinal-Outer, (c) Circumferential-Inner, (d) Circumferential-Outer, (e) Shear- Inner, and (f) Shear-Outer

3.9.2 Uniform internal pressure

An internal pressure $P = 30MPa$ is applied uniformly normal to the internal surface of the pipe (Fig. 3. 3). The corresponding applied traction \tilde{T}_N is obtained from Eq.(3.18).

Displacement predictions

With the exception of the region near the end support, the pipe expands uniformly in the radial direction and contracts longitudinally. Table 3. 3 provides the longitudinal and radial displacements at the free end and the percentage differences as predicted by the ELBOW31, PIPE-F-3, PIPE-S-L, PIPE-S-H, and PIPE-M-L models, in comparison to those predicted by the S4R model. The predictions of the developed elements are in an excellent agreement with the predictions of S4R model and the analytical solution based on the ring analysis. As expected, given the axisymmetric nature of the problem, the element developed based on Fourier series using a single mode (PIPE-F-1) predicts identical displacements to that based on three modes (PIPE-F-3) element for this loading case. Comparatively, the predictions of ELBOW31 show a larger difference from that predicted by the S4R element, especially for the radial displacement.

Table 3. 3 Longitudinal and radial displacements at the free end

	Displacement (mm) and percentage difference %						
	S4R	ELBOW31	PIPE-F-3	PIPE-S-L	PIPE-S-H	PIPE-M-L	Analytical
Longitudinal	-22.7	-22.0	-22.3	-22.4	-22.4	-22.4	-22.5
%	-	3.0	1.7	1.3	1.3	1.3	0.9
Radial	3.8	8.7	3.8	3.8	3.8	3.8	3.8
%	-	-128.9	1.1	1.1	1.1	1.1	-0.8

Stress predictions

The longitudinal and circumferential stresses at the mid-span are provided in Table 3. 4. The circumferential stresses at the inner surface predicted by the present elements are in excellent agreement with the ABAQUS model prediction and the analytical solution. Given that developed elements are able to capture the variation of the circumferential stresses through the wall thickness, the stresses at the inner surface differ slightly from those at the outer surface. In contrast, the ABAQUS model and the analytical solution are unable to capture the through-thickness variation of the circumferential stresses.

Table 3. 4 Longitudinal (L) and circumferential (C) stresses at the mid-span

		Stresses (MPa)						
		S4R	ELBOW31	PIPE-F-3	PIPE-S-L	PIPE-S-H	PIPE-M-L	Analytical
Inner surface	L	0	11.2	4.97	-1.98	-1.98	-1.98	0
	C	1518	1500	1513	1489	1489	1489	1500
Outer surface	L	0	11.2	-4.84	-11.3	-11.3	-11.3	0
	C	1518	1500	1481	1459	1459	1459	1500

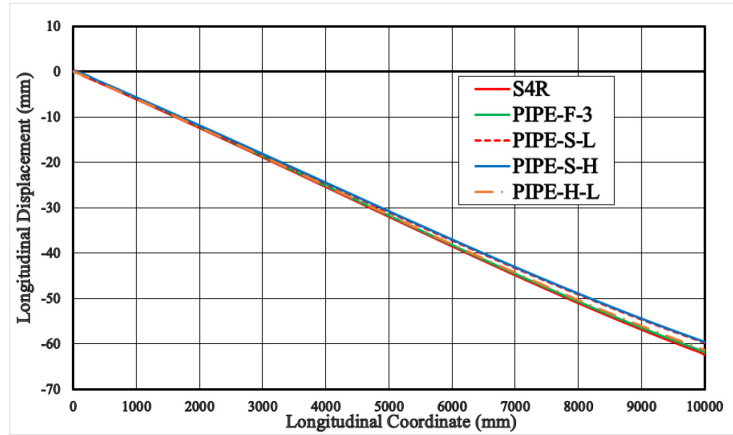
3.9.3 Combined loading

The pipe (Fig. 3. 3) is subjected at the free end to an axial compressive traction of $300MPa$ (corresponding to 48% of the Euler buckling load), a vertical downward traction of $15MPa$ (i.e., along the negative direction of the X-axis), and an additional traction of $15MPa$ acting along the

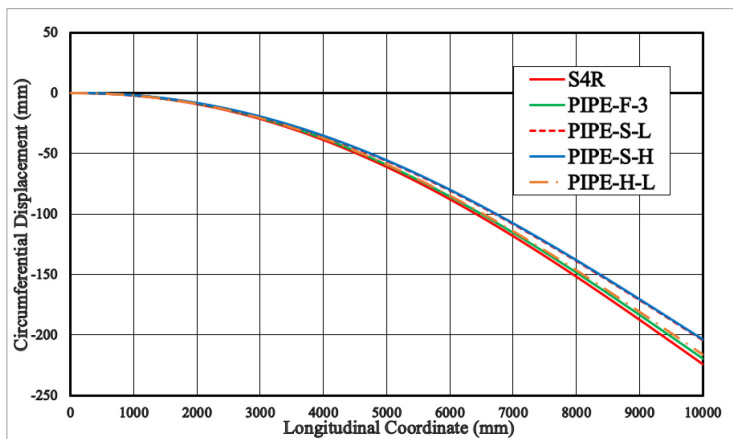
positive direction of the Y-axis. Additionally, uniform internal pressure $P = 30MPa$ is applied normal to the internal surface of the pipe. The corresponding applied traction $\tilde{\mathbf{T}}_N$ is $\tilde{\mathbf{T}}_N = \tilde{\mathbf{T}}_N|_1 + \tilde{\mathbf{T}}_N|_2$ where $\tilde{\mathbf{T}}_N|_1 = \{(-300), (-15 \cos \varphi - 15 \sin \varphi), (-15 \sin \varphi + 15 \cos \varphi)\}$ and $\tilde{\mathbf{T}}_N|_2$ is obtained from Eq. (3.18).

Displacement predictions

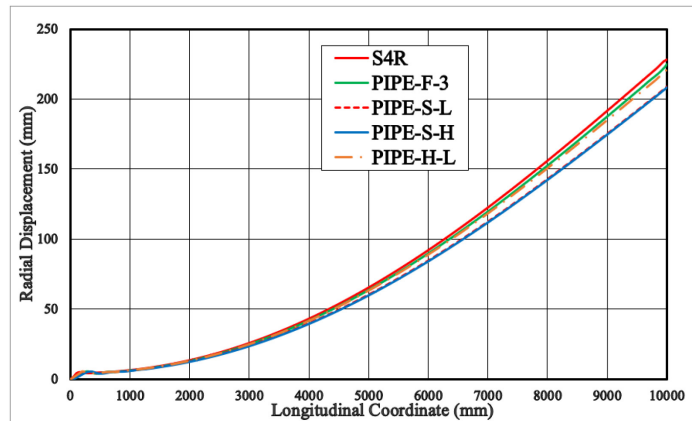
Given the symmetry of the problem, displacement predictions at $\varphi = 0^\circ$ and $\varphi = 270^\circ$ are identical while displacements predictions at $\varphi = 90^\circ$ and $\varphi = 180^\circ$ have the same trend. The longitudinal, circumferential, and radial displacement distributions along the span of the pipe at $\varphi = 0^\circ$ and $\varphi = 90^\circ$ are given in Fig. 3. 6 and Fig. 3. 7. Under the defined loads, the ELBOW31 model was unable to achieve the convergence. The predictions of S4R are thus used for the comparison with the predictions of the elements developed in the present study. The elements developed are able to effectively predict the nonlinear response. The predictions of PIPE-F-3 and PIPE-M-L elements were found to be very close to those generated by S4R element while those of elements PIPE-S-L and PIPE-S-H exhibited a slightly stiffer response. Table 3. 5 provides the percentage differences between the displacements at the free end as determined by PIPE-F-3, PIPE-S-L, PIPE-S-H, and PIPE-M-L compared to those of the S4R model. The percentage differences of PIPE-F-3 and PIPE-M-L elements are less than 3 % and 5 % respectively at various circumferential angles.



a

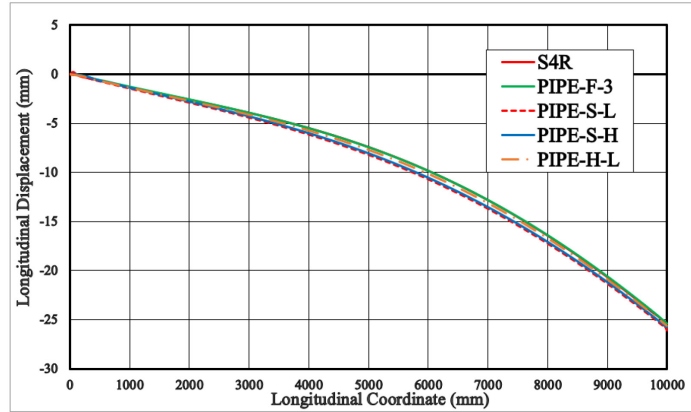


b

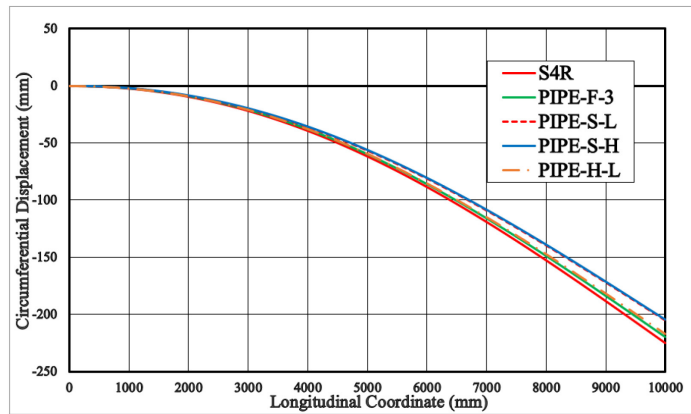


c

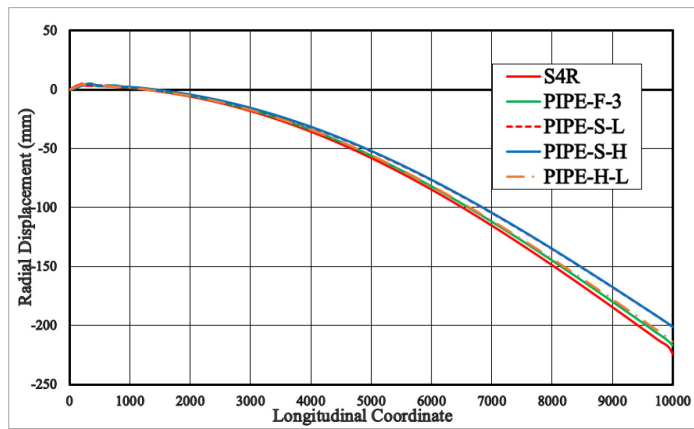
Fig. 3. 6 Displacement fields along the length of the pipe at $\varphi = 0^\circ$ (a) Longitudinal, (b) Circumferential, and (c) Radial



a



b



c

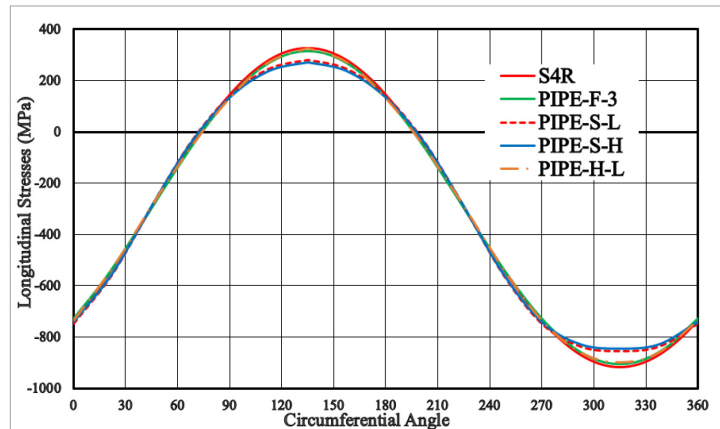
Fig. 3. 7 Displacement fields along the length of the pipe at $\varphi = 90^\circ$ (a) Longitudinal, (b) Circumferential, and (c) Radial

Table 3. 5 Percentage differences of the longitudinal, circumferential, and radial displacements at the free end

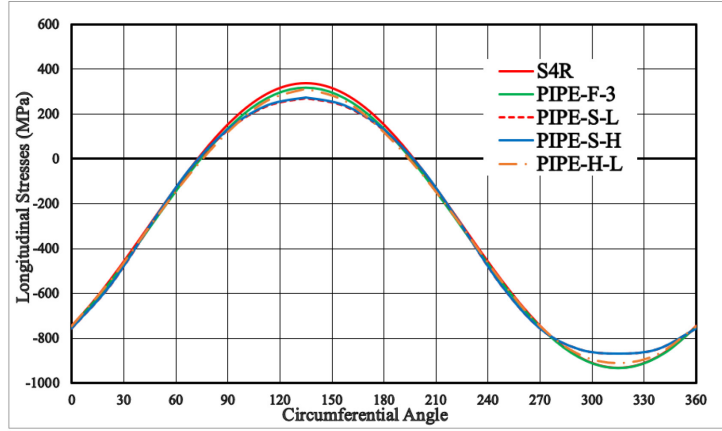
φ		Percentage difference %			
		PIPE-F-3	PIPE-S-L	PIPE-S-H	PIPE-M-L
0° or 270°	longitudinal	0.8	4.2	4.5	1.5
	circumferential	2.2	8.8	9.1	3.5
	radial	1.6	8.5	8.7	3.2
90° or 180°	longitudinal	2.8	0.5	1.2	1.8
	circumferential	2.2	8.9	9.1	3.6
	radial	3	10.1	10.3	4.7

Stress predictions

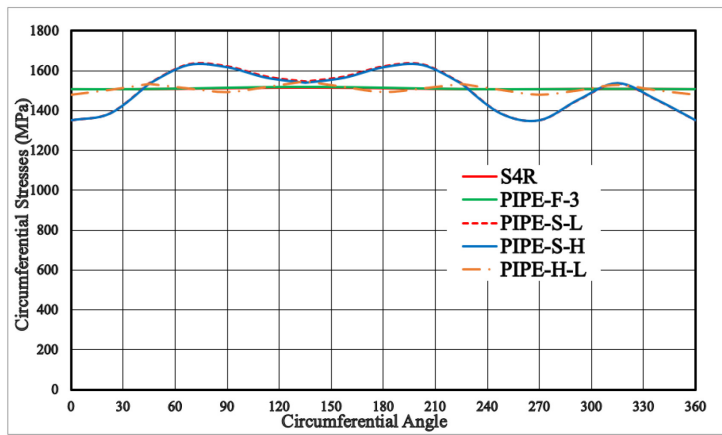
The longitudinal, circumferential, radial stress distributions along the circumferential direction at the mid-span for the inner and outer surfaces are given in Fig. 3. 8. The elements developed accurately capture the longitudinal stress distribution especially the PIPE-F-3 element (Fig. 3. 8a, b). Regarding the circumferential and shear stress distributions, PIPE-F-3 is the only element, within the elements developed, that closely predicts the stresses to S4R element's predictions. The difference between the circumferential stresses at the outer surface between S4R element and PIPE-F-3 element is attributed to the ability of PIPE-F-3 to predict the variation of the circumferential stresses through the wall thickness while the S4R element does not capture this variation.



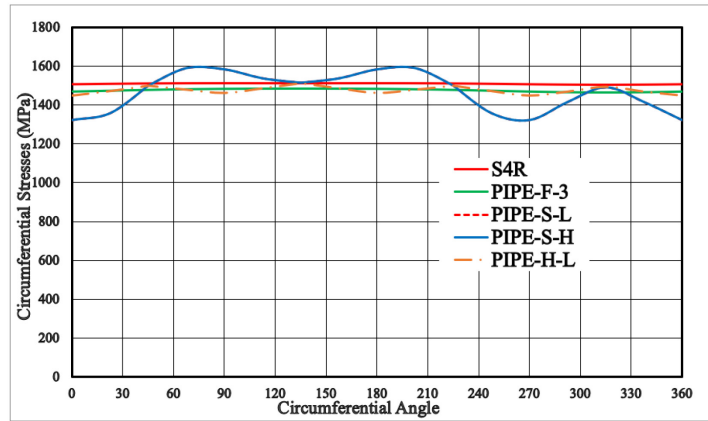
a



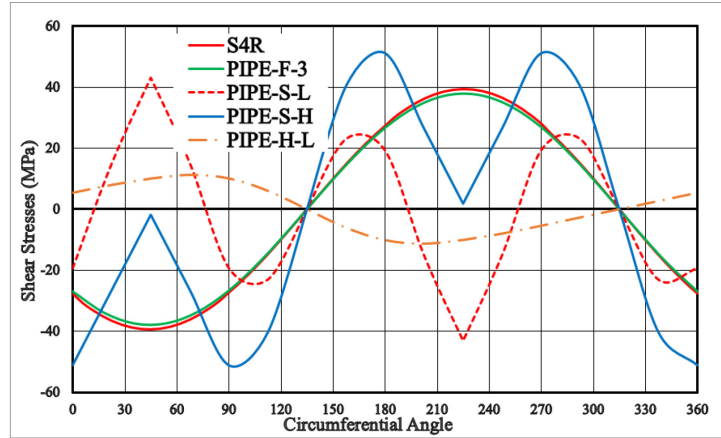
b



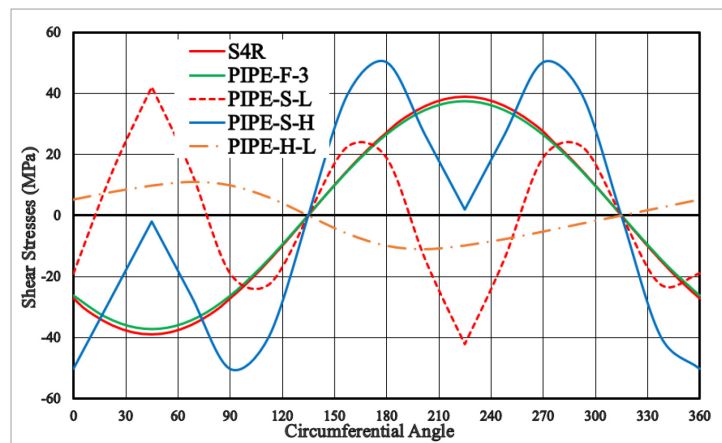
c



d



e



f

Fig. 3. 8 Stress fields versus circumferential angle at the middle section $z = 5m$ (a) Longitudinal-
Inner, (b) Longitudinal-Outer, (c) Circumferential-Inner, (d) Circumferential-Outer, (e) Shear-
Inner, and (f) Shear-Outer

3.10 Summary

A family of FE formulations for the analysis of straight pipes was formulated and implemented to simulate the elastic structural response. The underlying formulations are based on the Love-Kirchhoff thin shell theory assumptions and capture finite deformation-small strain effects in conjunction with the Saint-Venant-Kirchhoff constitutive model. Within the principle of the virtual work framework, the formulations adopt the first Piola-Kirchhoff stress tensor and the gradient of the virtual displacement fields in order to capture the geometric nonlinearity. Additionally, the formulations accurately tackle the nonlinearity caused by follower pressure load. The element

developed based on Fourier expansion series is superior for simulating the realistic mechanical behavior of straight pipes under various loading conditions. Although the elements developed based on spline interpolation and mixed interpolation cannot accurately predict the circumferential and shear stress distributions, PIPE-M-L element is able to accurately capture the longitudinal stresses and displacement fields while PIPE-S-L and PIPE-S-H elements can reasonably simulate them.

3.11 Appendix 3.A: Derivatives of displacement fields with respect to coordinates

This appendix presents the derivatives of the components (u_z, u_φ, u_r) of the displacement field vector \mathbf{u} with respect to coordinates z, φ , and ζ . By differentiation on Eq.(3.31) with respect to z, φ and ζ , one obtains

$$u_{z,z} = u_{oz,z} + \zeta \widehat{n}_{1,z} \quad (3.A.1)$$

$$u_{\varphi,z} = u_{o\varphi,z} + \zeta \widehat{n}_{2,z} \quad (3.A.2)$$

$$u_{r,z} = u_{or,z} + \zeta \widehat{n}_{3,z} \quad (3.A.3)$$

$$u_{z,\varphi} = u_{oz,\varphi} + \zeta \widehat{n}_{1,\varphi} \quad (3.A.4)$$

$$u_{\varphi,\varphi} = u_{o\varphi,\varphi} + \zeta \widehat{n}_{2,\varphi} \quad (3.A.5)$$

$$u_{r,\varphi} = u_{or,\varphi} + \zeta \widehat{n}_{3,\varphi} \quad (3.A.6)$$

$$u_{z,\zeta} = \widehat{n}_1 = n_1 / \sqrt{n_1^2 + n_2^2 + n_3^2} \quad (3.A.7)$$

$$u_{\varphi,\zeta} = \widehat{n}_2 = n_2 / \sqrt{n_1^2 + n_2^2 + n_3^2} \quad (3.A.8)$$

$$u_{r,\zeta} = \widehat{n}_3 - 1 = n_3 / \sqrt{n_1^2 + n_2^2 + n_3^2} - 1 \quad (3.A.9)$$

The partial derivative of a component \hat{n}_i (Eq.(3.29)) with respect to the coordinates $\alpha = z, \varphi$ is given by

$$\hat{n}_{i,\alpha} = \frac{n_{i,\alpha}}{\sqrt{n_1^2 + n_2^2 + n_3^2}} - n_i \frac{n_1 n_{1,\alpha} + n_2 n_{2,\alpha} + n_3 n_{3,\alpha}}{(n_1^2 + n_2^2 + n_3^2)^{1.5}} \quad \text{where } i = 1, 2, 3 \text{ and } \alpha = z, \varphi \quad (3.A.10)$$

Eqs.(3.A.7)-(3.A.9) are mathematical expressions in terms of the components (n_1, n_2, n_3) of the vector \mathbf{n} normal to the shell mid-surface in the deformed configuration which can be obtained by Eq.(3.28). While Eqs.(3.A.1)-(3.A.6) depend upon the derivatives of these components (n_1, n_2, n_3) with respect to coordinates z and φ . These derivatives are recovered by differentiation on Eq.(3.28), yielding

$$n_{1,z} = \left[u_{o\varphi,zz} (u_{or,\varphi} - u_{o\varphi}) + u_{o\varphi,z} (u_{or,\varphi z} - u_{o\varphi,z}) - u_{or,zz} (r_m + u_{o\varphi,\varphi} + u_{or}) - u_{or,z} (u_{o\varphi,\varphi z} + u_{or,z}) \right] \quad (3.A.11)$$

$$n_{1,\varphi} = \left[u_{o\varphi,z\varphi} (u_{or,\varphi} - u_{o\varphi}) + u_{o\varphi,z} (u_{or,\varphi\varphi} - u_{o\varphi,\varphi}) - u_{or,z\varphi} (r_m + u_{o\varphi,\varphi} + u_{or}) - u_{or,z} (u_{o\varphi,\varphi\varphi} + u_{or,\varphi}) \right] \quad (3.A.12)$$

$$n_{2,z} = u_{or,zz} u_{oz,\varphi} + u_{or,z} u_{oz,\varphi z} - u_{oz,zz} (u_{or,\varphi} - u_{o\varphi}) - (1 + u_{oz,z}) (u_{or,\varphi z} - u_{o\varphi,z}) \quad (3.A.13)$$

$$n_{2,\varphi} = u_{or,z\varphi} u_{oz,\varphi} + u_{or,z} u_{oz,\varphi\varphi} - u_{oz,z\varphi} (u_{or,\varphi} - u_{o\varphi}) - (1 + u_{oz,z}) (u_{or,\varphi\varphi} - u_{o\varphi,\varphi}) \quad (3.A.14)$$

$$n_{3,z} = u_{oz,zz} (r_m + u_{o\varphi,\varphi} + u_{or}) + (1 + u_{oz,z}) (u_{o\varphi,\varphi z} + u_{or,z}) - u_{o\varphi,zz} u_{oz,\varphi} - u_{o\varphi,z} u_{oz,\varphi z} \quad (3.A.15)$$

$$n_{3,\varphi} = u_{oz,z\varphi} (r_m + u_{o\varphi,\varphi} + u_{or}) + (1 + u_{oz,z}) (u_{o\varphi,\varphi\varphi} + u_{or,\varphi}) - u_{o\varphi,z\varphi} u_{oz,\varphi} - u_{o\varphi,z} u_{oz,\varphi\varphi} \quad (3.A.16)$$

Eqs. (3.A.1) to (3.A.16), (3.28), (3.29), and (3.31) provide the components of the gradient of the displacement fields appearing in Eq.(3.32) in terms of the components $(u_{oz}, u_{o\varphi}, u_{or})$ of the displacement field vector \mathbf{u}_o at the middle surface and their derivatives with respect to coordinates z and φ .

3.12 Appendix 3.B: Derivatives of displacement fields with respect to nodal degrees of freedom

The derivatives of the components (u_z, u_φ, u_r) of the displacement field vector \mathbf{u} with respect to the nodal degrees of freedom d_j are obtained by differentiation of Eq.(3.31) with respect to d_j , yielding

$$(u_z)_{,d_j} = (u_{oz})_{,d_j} + \zeta \widehat{n}_{1,d_j} \quad (3.B.1)$$

$$(u_\varphi)_{,d_j} = (u_{o\varphi})_{,d_j} + \zeta \widehat{n}_{2,d_j} \quad (3.B.2)$$

$$(u_r)_{,d_j} = (u_{or})_{,d_j} + \zeta \widehat{n}_{3,d_j} \quad (3.B.3)$$

in which

$$\widehat{n}_{i,d_j} = \frac{n_{i,d_j}}{\sqrt{n_1^2 + n_2^2 + n_3^2}} - n_i \frac{n_1 n_{1,d_j} + n_2 n_{2,d_j} + n_3 n_{3,d_j}}{(n_1^2 + n_2^2 + n_3^2)^{1.5}} \quad \text{where } i = 1, 2, 3 \quad (3.B.4)$$

Eqs. (3.B.1) to (3.B.4) are used to determine the components of the external force vector (Eq.(3.9)) and its contribution to the stiffness matrix (Eq.(3.17)). In order to obtain the components of $(\mathbf{u} \otimes \nabla^T)_{,d_j}$ appearing in Eq.(3.33), the differentiation of Eqs. (3.A.1) to (3.A.9) with respect to d_j is taken as

$$(u_{z,z})_{,d_j} = (u_{oz,z})_{,d_j} + \zeta (\widehat{n}_{1,z})_{,d_j} \quad (3.B.5)$$

$$(u_{\varphi,z})_{,d_j} = (u_{o\varphi,z})_{,d_j} + \zeta (\widehat{n}_{2,z})_{,d_j} \quad (3.B.6)$$

$$(u_{r,z})_{,d_j} = (u_{or,z})_{,d_j} + \zeta (\widehat{n}_{3,z})_{,d_j} \quad (3.B.7)$$

$$(u_{z,\varphi})_{,d_j} = (u_{oz,\varphi})_{,d_j} + \zeta (\widehat{n}_{1,\varphi})_{,d_j} \quad (3.B.8)$$

$$\left(u_{\varphi,\varphi}\right)_{,dj} = \left(u_{o\varphi,\varphi}\right)_{,dj} + \zeta \left(\widehat{n}_{2,\varphi}\right)_{,dj} \quad (3.B.9)$$

$$\left(u_{r,\varphi}\right)_{,dj} = \left(u_{or,\varphi}\right)_{,dj} + \zeta \left(\widehat{n}_{3,\varphi}\right)_{,dj} \quad (3.B.10)$$

$$\left(u_{z,\zeta}\right)_{,dj} = \widehat{n}_{1,dj} \quad (3.B.11)$$

$$\left(u_{\varphi,\zeta}\right)_{,dj} = \widehat{n}_{2,dj} \quad (3.B.12)$$

$$\left(u_{r,\zeta}\right)_{,dj} = \widehat{n}_{3,dj} \quad (3.B.13)$$

in which $\widehat{n}_{i,dj}$ is given in Eq.(3.B.4) and $\left(\widehat{n}_{i,\alpha}\right)_{,dj}$ can be obtained by differentiation of Eq.(3.A.10)

with respect to d_j as , where $i = 1, 2, 3$ and $\alpha = z, \varphi$,

$$\left(\widehat{n}_{i,\alpha}\right)_{,dj} = \left[\frac{n_{i,\alpha}}{\sqrt{n_1^2 + n_2^2 + n_3^2}} - n_i \frac{n_1 n_{1,\alpha} + n_2 n_{2,\alpha} + n_3 n_{3,\alpha}}{\left(n_1^2 + n_2^2 + n_3^2\right)^{1.5}} \right]_{,dj} = T_1 - T_2 \quad (3.B.14)$$

$$T_1 = \frac{n_{i,\alpha}}{\sqrt{n_1^2 + n_2^2 + n_3^2}} \Big|_{,dj} = \frac{\left(n_{i,\alpha}\right)_{,dj}}{\sqrt{n_1^2 + n_2^2 + n_3^2}} - n_{i,\alpha} \frac{n_1 n_{1,dj} + n_2 n_{2,dj} + n_3 n_{3,dj}}{\left(n_1^2 + n_2^2 + n_3^2\right)^{1.5}} \quad (3.B.15)$$

$$T_2 = n_i \frac{n_1 n_{1,\alpha} + n_2 n_{2,\alpha} + n_3 n_{3,\alpha}}{\left(n_1^2 + n_2^2 + n_3^2\right)^{1.5}} \Big|_{,dj} = n_{i,dj} \frac{n_1 n_{1,\alpha} + n_2 n_{2,\alpha} + n_3 n_{3,\alpha}}{\left(n_1^2 + n_2^2 + n_3^2\right)^{1.5}} + n_i T_3 \quad (3.B.16)$$

$$T_3 = \frac{n_1 n_{1,\alpha} + n_2 n_{2,\alpha} + n_3 n_{3,\alpha}}{\left(n_1^2 + n_2^2 + n_3^2\right)^{1.5}} \Big|_{,dj} = \left[n_{1,dj} n_{1,\alpha} + n_1 \left(n_{1,\alpha}\right)_{,dj} + n_{2,dj} n_{2,\alpha} + n_2 \left(n_{2,\alpha}\right)_{,dj} + n_{3,dj} n_{3,\alpha} + n_3 \left(n_{3,\alpha}\right)_{,dj} \right] / \left(n_1^2 + n_2^2 + n_3^2\right)^{1.5} - 3 \left(n_1 n_{1,\alpha} + n_2 n_{2,\alpha} + n_3 n_{3,\alpha}\right) \left(n_1 n_{1,dj} + n_2 n_{2,dj} + n_3 n_{3,dj}\right) / \left(n_1^2 + n_2^2 + n_3^2\right)^{2.5}$$

Eqs. (3.B.5) to (3.B.16) are used to determine the components of $(\mathbf{u} \otimes \nabla^T)_{,d_j}$ appearing in Eq.(3.33). Knowing these components, the internal force vector (Eq.(3.8)) and the tangent stiffness matrix (Eq.(3.15)) can be obtained. The mathematical identities in this appendix (Eqs. (3.B.1) to (3.B.16)) involve the derivatives of the components (n_1, n_2, n_3) of the vector \mathbf{n} normal to the shell mid-surface in the deformed configuration with respect to d_j . These derivatives are recovered by differentiation of Eq.(3.28) as

$$n_{1,d_j} = (u_{o\phi,z})_{,d_j} (u_{or,\phi} - u_{o\phi}) + u_{o\phi,z} \left[(u_{or,\phi})_{,d_j} - (u_{o\phi})_{,d_j} \right] - (u_{or,z})_{,d_j} (r_m + u_{o\phi,\phi} + u_{or}) - u_{or,z} \left[(u_{o\phi,\phi})_{,d_j} + (u_{or})_{,d_j} \right] \quad (3.B.17)$$

$$n_{2,d_j} = (u_{or,z})_{,d_j} u_{oz,\phi} + u_{or,z} (u_{oz,\phi})_{,d_j} - (u_{oz,z})_{,d_j} [u_{or,\phi} - u_{o\phi}] - (1 + u_{oz,z}) \left[(u_{or,\phi})_{,d_j} - (u_{o\phi})_{,d_j} \right] \quad (3.B.18)$$

$$n_{3,d_j} = (u_{oz,z})_{,d_j} (r_m + u_{o\phi,\phi} + u_{or}) + (1 + u_{oz,z}) \left[(u_{o\phi,\phi})_{,d_j} + (u_{or})_{,d_j} \right] - (u_{o\phi,z})_{,d_j} u_{oz,\phi} - u_{o\phi,z} (u_{oz,\phi})_{,d_j} \quad (3.B.19)$$

By differentiation on Eqs. (3.A.11) to (3.A.16) with respect to d_j , one obtains

$$\begin{aligned} (n_{1,z})_{,d_j} = & \left[(u_{o\phi,zz})_{,d_j} (u_{or,\phi} - u_{o\phi}) + u_{o\phi,zz} \left[(u_{or,\phi})_{,d_j} - (u_{o\phi})_{,d_j} \right] + (u_{o\phi,z})_{,d_j} (u_{or,\phi z} - u_{o\phi,z}) \right. \\ & + u_{o\phi,z} \left[(u_{or,\phi z})_{,d_j} - (u_{o\phi,z})_{,d_j} \right] - (u_{or,zz})_{,d_j} (r_m + u_{o\phi,\phi} + u_{or}) - u_{or,zz} \left[(u_{o\phi,\phi})_{,d_j} + (u_{or})_{,d_j} \right] \\ & \left. - (u_{or,z})_{,d_j} (u_{o\phi,\phi z} + u_{or,z}) - u_{or,z} \left[(u_{o\phi,\phi z})_{,d_j} + (u_{or,z})_{,d_j} \right] \right] \end{aligned} \quad (3.B.20)$$

$$\begin{aligned}
(n_{1,\varphi})_{,d_j} &= \left[(u_{o\varphi,z\varphi})_{,d_j} (u_{or,\varphi} - u_{o\varphi}) + u_{o\varphi,z\varphi} \left[(u_{or,\varphi})_{,d_j} - (u_{o\varphi})_{,d_j} \right] + (u_{o\varphi,z})_{,d_j} (u_{or,\varphi\varphi} - u_{o\varphi,\varphi}) \right. \\
&\quad \left. + u_{o\varphi,z} \left[(u_{or,\varphi\varphi})_{,d_j} - (u_{o\varphi,\varphi})_{,d_j} \right] - (u_{or,z\varphi})_{,d_j} (r_m + u_{o\varphi,\varphi} + u_{or}) \right. \\
&\quad \left. - u_{or,z\varphi} \left[(u_{o\varphi,\varphi})_{,d_j} + (u_{or})_{,d_j} \right] - (u_{or,z})_{,d_j} (u_{o\varphi,\varphi\varphi} + u_{or,\varphi}) - u_{or,z} \left[(u_{o\varphi,\varphi\varphi})_{,d_j} + (u_{or,\varphi})_{,d_j} \right] \right] \quad (3.B.21)
\end{aligned}$$

$$\begin{aligned}
(n_{2,z})_{,d_j} &= \left[(u_{or,zz})_{,d_j} u_{oz,\varphi} + u_{or,zz} (u_{oz,\varphi})_{,d_j} + (u_{or,z})_{,d_j} u_{oz,\varphi z} + u_{or,z} (u_{oz,\varphi z})_{,d_j} \right. \\
&\quad \left. - (u_{oz,zz})_{,d_j} (u_{or,\varphi} - u_{o\varphi}) - u_{oz,zz} \left[(u_{or,\varphi})_{,d_j} - (u_{o\varphi})_{,d_j} \right] - (u_{oz,z})_{,d_j} (u_{or,\varphi z} - u_{o\varphi,z}) \right. \\
&\quad \left. - (1 + u_{oz,z}) \left[(u_{or,\varphi z})_{,d_j} - (u_{o\varphi,z})_{,d_j} \right] \right] \quad (3.B.22)
\end{aligned}$$

$$\begin{aligned}
(n_{2,\varphi})_{,d_j} &= \left[(u_{or,z\varphi})_{,d_j} u_{oz,\varphi} + u_{or,z\varphi} (u_{oz,\varphi})_{,d_j} + (u_{or,z})_{,d_j} u_{oz,\varphi\varphi} + u_{or,z} (u_{oz,\varphi\varphi})_{,d_j} \right. \\
&\quad \left. - (u_{oz,z\varphi})_{,d_j} (u_{or,\varphi} - u_{o\varphi}) - u_{oz,z\varphi} \left[(u_{or,\varphi})_{,d_j} - (u_{o\varphi})_{,d_j} \right] - (u_{oz,z})_{,d_j} (u_{or,\varphi\varphi} - u_{o\varphi,\varphi}) \right. \\
&\quad \left. - (1 + u_{oz,z}) \left[(u_{or,\varphi\varphi})_{,d_j} - (u_{o\varphi,\varphi})_{,d_j} \right] \right] \quad (3.B.23)
\end{aligned}$$

$$\begin{aligned}
(n_{3,z})_{,d_j} &= \left[(u_{oz,zz})_{,d_j} (r_m + u_{o\varphi,\varphi} + u_{or}) + u_{oz,zz} \left[(u_{o\varphi,\varphi})_{,d_j} + (u_{or})_{,d_j} \right] + (u_{oz,z})_{,d_j} (u_{o\varphi,\varphi z} + u_{or,z}) \right. \\
&\quad \left. + (1 + u_{oz,z}) \left[(u_{o\varphi,\varphi z})_{,d_j} + (u_{or,z})_{,d_j} \right] - (u_{o\varphi,zz})_{,d_j} u_{oz,\varphi} - u_{o\varphi,zz} (u_{oz,\varphi})_{,d_j} \right. \\
&\quad \left. - (u_{o\varphi,z})_{,d_j} u_{oz,\varphi z} - u_{o\varphi,z} (u_{oz,\varphi z})_{,d_j} \right] \quad (3.B.24)
\end{aligned}$$

$$\begin{aligned}
(n_{3,\varphi})_{,d_j} &= \left[(u_{oz,z\varphi})_{,d_j} (r_m + u_{o\varphi,\varphi} + u_{or}) + u_{oz,z\varphi} \left[(u_{o\varphi,\varphi})_{,d_j} + (u_{or})_{,d_j} \right] \right. \\
&\quad \left. + (u_{oz,z})_{,d_j} (u_{o\varphi,\varphi\varphi} + u_{or,\varphi}) + (1 + u_{oz,z}) \left[(u_{o\varphi,\varphi\varphi})_{,d_j} + (u_{or,\varphi})_{,d_j} \right] \right. \\
&\quad \left. - (u_{o\varphi,z\varphi})_{,d_j} u_{oz,\varphi} - u_{o\varphi,z\varphi} (u_{oz,\varphi})_{,d_j} - (u_{o\varphi,z})_{,d_j} u_{oz,\varphi\varphi} - u_{o\varphi,z} (u_{oz,\varphi\varphi})_{,d_j} \right] \quad (3.B.25)
\end{aligned}$$

Eqs. (3.B.17) to (3.B.25) are mathematical expressions required to determine the Eqs. (3.B.1) to (3.B.16) in terms of the components $(u_{oz}, u_{o\phi}, u_{or})$ of the displacement field vector \mathbf{u}_o at the middle surface and their derivatives with respect to z , ϕ , and d_j . Eqs. (3.B.1) to (3.B.16) are involved in the mathematical expressions of the internal (Eq.(3.8)) and external (Eq.(3.9)) force vectors and the stiffness matrix (Eqs.(3.15) and (3.17)).

3.13 Appendix 3.C: Interpolation Schemes

This appendix presents illustrations of the degrees of freedom associated with each interpolation scheme proposed in Chapter 3.

Fourier series interpolation

The proposed cylindrical element has two nodes as shown in Fig. 3. C. 1. The total number of degrees of freedom (DOFs) in the proposed element is $12 + 24m$ (i.e., $6 + 12m$ DOFs at each node, where m is the number of Fourier modes). These degrees of freedom are related to the longitudinal, circumferential, and radial displacements. For example, there are $2 + 4m$ DOFs at each node that are related to the longitudinal displacement. These DOFs consist of two physical DOFs representing longitudinal translation DOF and its derivative that are related to the axisymmetric response of the element (i.e., related to the zero Fourier mode) and four DOFs related to each Fourier mode that are related to the non-axisymmetric distribution of the displacements. The circumferential distributions corresponding to each Fourier mode up to the sixth mode are shown in Fig. 3. C. 2 in which the blue lines depict the un-deformed surface as a datum from which the longitudinal displacements based on Fourier mode distributions are depicted. The displacement pattern of the first Fourier mode corresponds to the longitudinal displacements associated with

planar bending (akin to conventional beam theories) while higher modes 2-6 provides means to capture the warping behavior of the cross section.

Similarly, the DOFs related to the Fourier modes of the radial displacements are depicted in Fig. 3. C. 3 up to the sixth mode. The first Fourier mode for the radial displacement characterizes the displacement of the pipe cross-section in its own plane, while the second mode characterizes its ovalization and higher modes characterize other cross-sectional distortional modes.

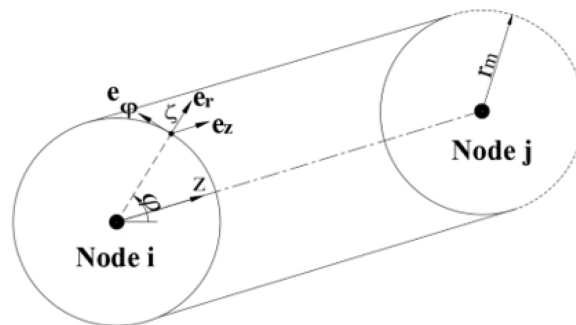


Fig. 3. C. 1 Nodes of pipe element based on Fourier interpolation

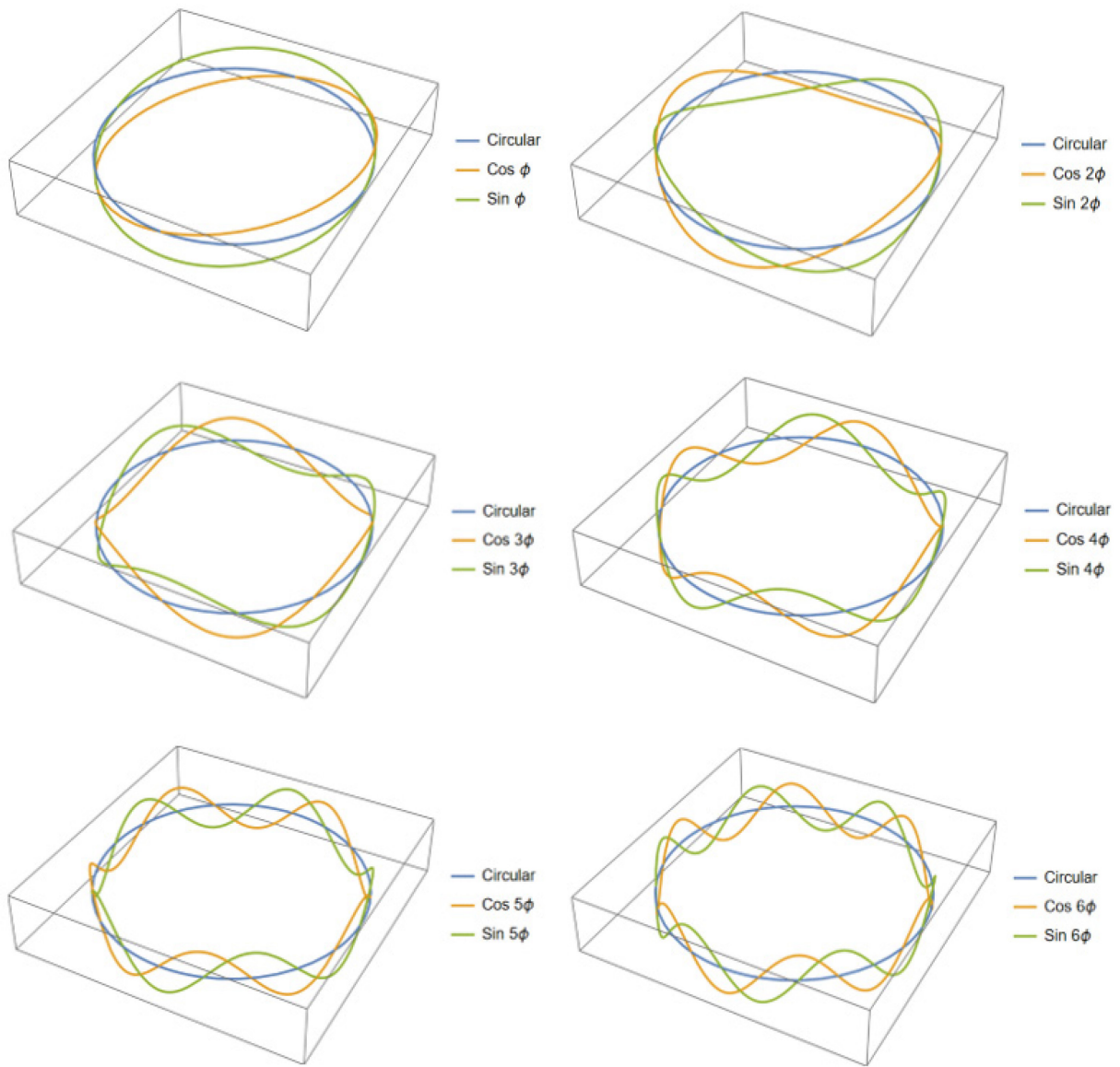


Fig. 3. C. 2 Longitudinal displacements distributions corresponding to Fourier modes 1-6

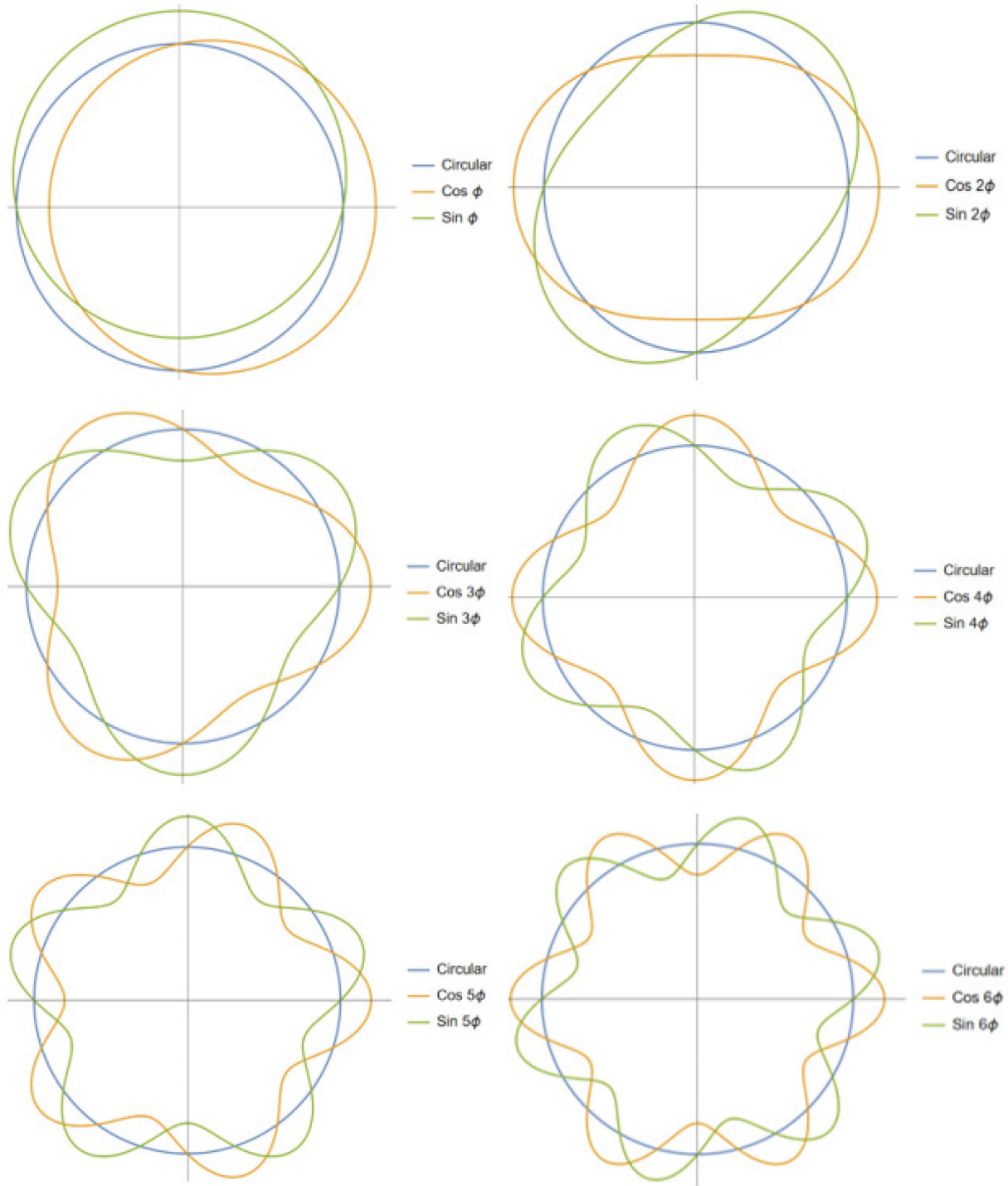


Fig. 3. C. 3 Radial displacements distributions corresponding to Fourier modes 1-6

Spline interpolation

The proposed pipe element also consists of two end cross-sections as shown in Fig. 3. C. 1. Each cross-section has four nodes as shown in Fig. 3. C. 4 with three nodal displacements per node. Each of the three displacement fields is interpolated along the circumferential direction by quartic splines as illustrated in Section 3.8.2. In the longitudinal direction, two options have been considered. Option 1: Using linear interpolation along the longitudinal direction, each end cross-section would have 12 DOFs. Therefore, the total number of DOFs of the proposed element is 24. Option 2: Using Hermitian interpolation along the longitudinal direction, each of the two end cross-sections, would have four nodes, with six degrees of freedom per node (i.e., three nodal displacements and three nodal rotations). In this case, the element would have 2 cross-sections x 4 nodes per cross-section x 6 DOFs per node totaling of the proposed element are 48 DOFs.

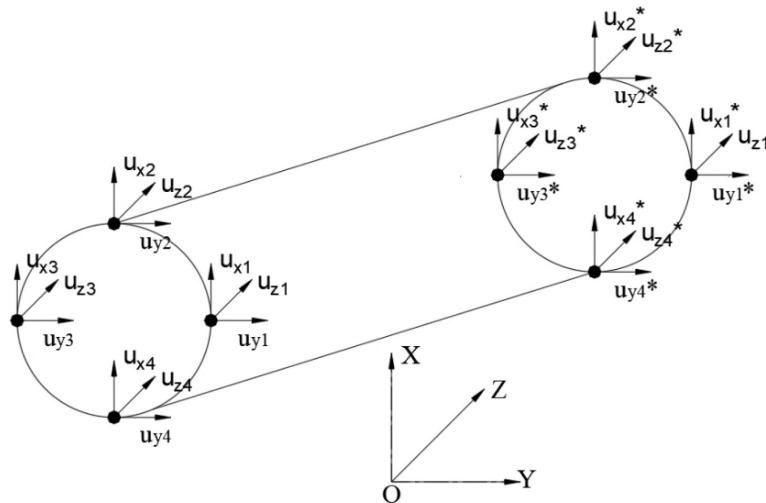


Fig. 3. C. 4 Nodes for a Spline element based on linear interpolation along the longitudinal direction and quartic spline interpolation along the circumferential direction.

3.14 Appendix 3.D: Strain Fields for Example 1

The longitudinal, circumferential, and shear strain distributions along the circumferential direction at the pipe mid-span for example 1 are shown in Fig. 3. D. 1. The discussion provided in Section 3.9.1 about the agreement between the predictions of the developed elements in this chapter and the S4R element in ABQUS is applicable here for these strain field distributions.

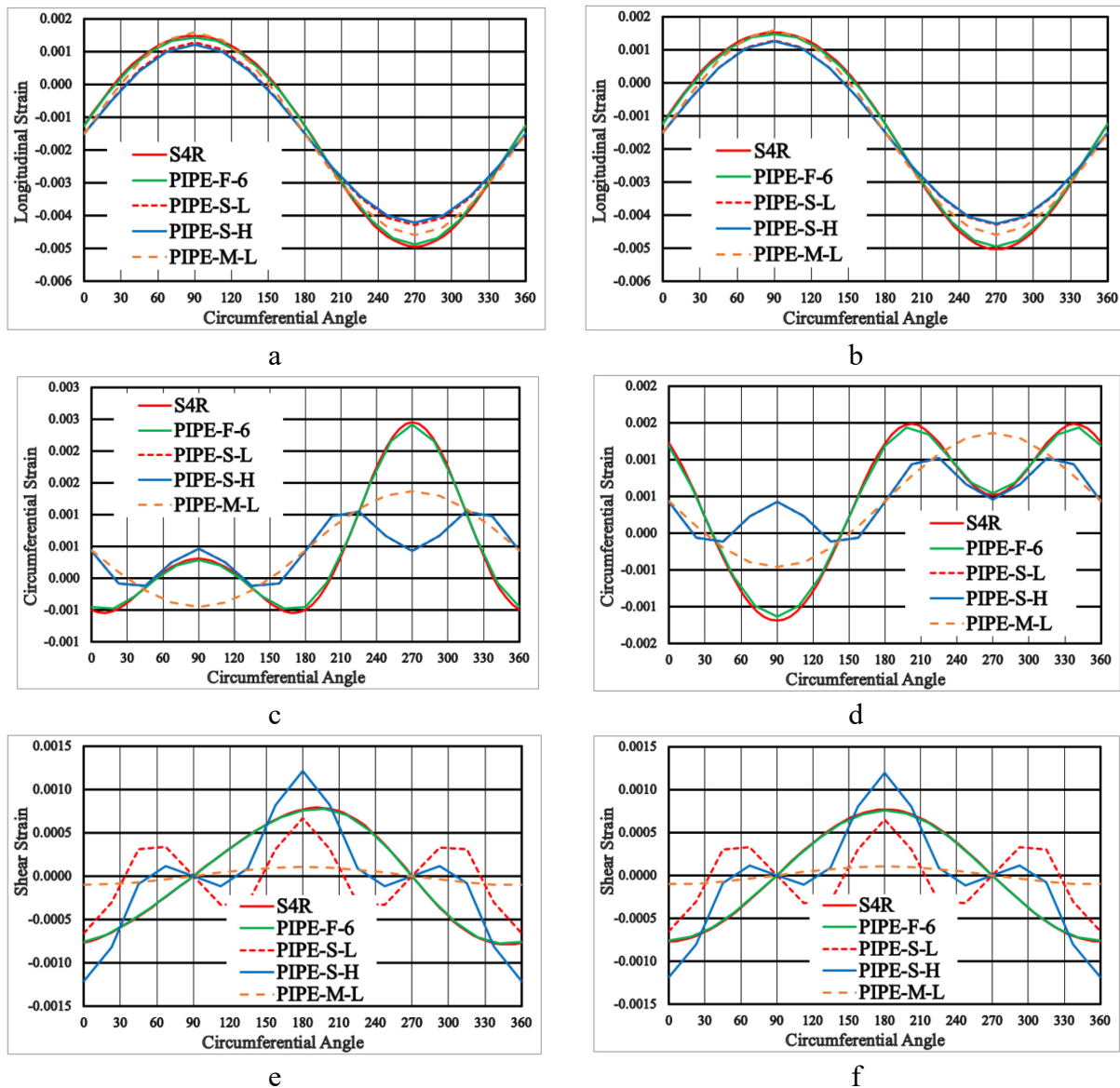


Fig. 3. D. 1 Strain fields versus circumferential angle at the middle section $z = 5m$ (a) Longitudinal-Inner Surface, (b) Longitudinal-Outer Surface, (c) Circumferential-Inner Surface, (d) Circumferential-Outer Surface, (e) Shear-Inner Surface, and (f) Shear-Outer Surface.

3.15 Nomenclature

A	A point on the middle surface of the un-deformed configuration
A^*	The point on the middle surface of the deformed configuration
$\tilde{\mathbf{B}}$	Body force vector per unit reference volume
\mathbf{C}	Saint-Venant-Kirchhoff constitutive tensor
\mathbf{d}	Vector of degrees of freedom
d_i, d_j	Components of degrees of freedom vector
$\bar{\mathbf{d}}$	Vector of virtual degrees of freedom
\mathbf{E}	Green-Lagrange stress tensor
E	Young's Modulus
\mathbf{e}_r	Unit vector in the radial direction
\mathbf{e}_z	Unit vector in the longitudinal direction
\mathbf{e}_φ	Unit vector in the circumferential direction
\mathbf{F}	Deformation gradient tensor
$\mathbf{F}^{(I)}$	Internal force vector
$\mathbf{F}^{(E)}$	External force vector
H_1, H_2, H_3, H_4	Cubic Hermitian functions
H_1^*, H_2^*	Linear Lagrangian functions
h	Pipe wall thickness
\mathbf{I}	Identity tensor
\mathbf{K}	Stiffness matrix
\mathbf{K}^F	Exact contribution of the external force vector in the stiffness matrix
\mathbf{K}^T	Exact tangent stiffness matrix
\mathbf{K}_A^F	Approximated contribution of the external force vector in the stiffness matrix
\mathbf{K}_A^T	Approximated tangent stiffness matrix
$K^F _{ij}$	Components of the exact contribution of the external force vector in the stiffness matrix

$K^T _{ij}$	Components of the exact tangential stiffness matrix
$K_A^T _{ij}$	Components of the approximate contribution of the external force vector in the stiffness matrix
$K_A^F _{ij}$	Components of the approximate tangential stiffness matrix
\mathbf{L}	Vector of shape functions for Fourier series interpolation
\mathbf{L}^*	Vector of Lagrangian shape functions for spline interpolation
\mathbf{L}^{**}	Vector of Hermitian shape functions for spline interpolation
L	Length of the element
m	Total Fourier terms /modes
\mathbf{N}	Vector normal to the middle surface in the un-deformed configuration
$\hat{\mathbf{N}}$	Unit vector normal to the middle surface in the un-deformed configuration
\mathbf{n}	Vector normal to the middle surface in the deformed configuration
$\hat{\mathbf{n}}$	Unit vector normal to the middle surface in the deformed configuration
n	Total number of the nodal degrees of freedom
n_1, n_2, n_3	Components of the normal vector \mathbf{n}
$\hat{n}_1, \hat{n}_2, \hat{n}_3$	Components of the normal unit vector $\hat{\mathbf{n}}$
\mathbf{P}	The first Piola-Kirchhoff stress tensor
P	The follower pressure load
\mathbf{P}_E	The equivalent first Piola-Kirchhoff stress tensor to the Cauchy stress tensor induced due to the follower pressure load P
Q	Spline interpolation functions in the circumferential direction
\mathbf{R}	Residual force vector
\mathbf{R}_0	The position vector of a point on the middle surface in the un-deformed configuration
\mathbf{r}_0	The position vector of a point on the middle surface in the deformed configuration
r	Radial coordinate as measured from the origin point
r_m	Mid-surface radius

\mathbf{S}	Second Piola-Kirchhoff stress tensor
S_o	The original surface that encloses volume V_o
$\tilde{\mathbf{T}}_N$	Applied traction vector per unit reference surface dS_0 normal to the unit vector $\hat{\mathbf{N}}$
\bar{U}	The internal virtual work
\mathbf{u}	Displacement vector for a generic point
$\bar{\mathbf{u}}$	Virtual displacement vector for a generic point
\mathbf{u}_o	Displacement vector for a point on the middle surface
u_{or}	Radial displacement of a point on the middle surface
u_{ox}	Displacement in x-direction a point on the middle surface
u_{oy}	Displacement in y-direction a point on the middle surface
u_{oz}	Longitudinal displacement of a point on the middle surface
$u_{o\varphi}$	Circumferential displacement of a point on the middle surface
u_r	Radial displacement
u_z	Longitudinal displacement
u_φ	Circumferential displacement
V_o	The original volume
\bar{V}	The external virtual work
z	Longitudinal coordinate
∇	The gradient operator with respect to the un-deformed configuration
ζ	Radial coordinate as measured from the middle surface
ν	Poisson's ratio
$\boldsymbol{\sigma}$	The Cauchy stress tensor
φ	Circumferential coordinate

3.16 Acknowledgments

The authors express their gratitude to TC Energy, and Enbridge Pipelines Inc. for their technical assistance and discussions.

3.17 Funding

Partial funding was provided by: NSERC, MITACS, Enbridge Pipelines Inc., and TC Energy.

3.18 References

- [1] Von Karman, T., 1911, "Ueber Die Formänderung Dünnwandiger Rohre, Insbesondere Federnder Ausgleichrohre," *Z. Ver. Deut. Ing.*, 55(Part2), pp.1889–1895.
- [2] Vigness, I., 1943, "Elastic Properties of Curved Tubes," *J. Appl. Mech.*, 55, pp.102–120.
- [3] Kafka, P. G., and Dunn, M. B., 1953, "Stiffness of Curved Circular Tubes with Internal Pressure," Boeing Airplane, Chicago, IL.
- [4] Wood, J. D., 1958, "The flexure of a uniformly pressurized circular, cylindrical shell" *J. Appl. Mech.*, 25, pp. 453-458.
- [5] Dodge, W. G., and Moore, S. E., 1972, "Stress Indices and Flexibility Factors for Moment Loadings on Elbows and Curved Pipes," *Welding Research Council Bulletin* 179.
- [6] Hong, S.-P., An, J.-H., Kim, Y.-J., Nikbin, K., and Budden, P. J., 2011, "Approximate Elastic Stress Estimates for Elbow Under Internal Pressure," *Int. J. Mech. Sci.*, 53(7), pp. 526–535.
- [7] WeiB, E., Lietzmann, A., and Rudolph, J., 1996 "Linear and Nonlinear Finite-Element Analysis of Pipe Bends," *Int. J. Pres. Ves. & Piping.*, 67, pp. 211-217.
- [8] Abdulhamed, D., Adeeb, S., Cheng, R., and Martens, M., 2016, "The Influence of the Bourdon Effect on Pipe Elbow," *ASME Paper No. IPC2016-64659*.
- [9] Abdulhamed, D., 2017 "The Behavior of Pipe Bends under Internal Pressure and In-Plane Bending Loading," *Doctoral dissertation, University of Alberta, Edmonton, Canada*.
- [10] Ohtsubo, H., and Watanabe, O., 1978, "Stress Analysis of Pipe Bends by Ring Elements," *ASME J. Pressure Vessel Technol.*, 100(1), pp. 112–122.
- [11] Bathe, K. J., and Almeida, C. A., 1980, "A Simple and Effective Pipe Elbow Element, Linear Analysis," *J. Appl. Mech.*, 47(1), pp. 100–193.
- [12] Bathe, K. J., and Almeida, C. A., 1982, "A Simple and Effective Pipe Elbow Element, Pressure Stiffening Effects," *J. Appl. Mech.*, 49(4), pp. 914–915.
- [13] Bathe, K. J., and Almeida, C. A., 1982, "A Simple and Effective Pipe Elbow Element, Interaction Effects," *J. Appl. Mech.*, 49, pp. 165–171.
- [14] Militello, C., and Huespe, A. E., 1988, "A Displacement- Based Pipe Elbow Element," *Comput. Struct.*, 29(2), pp. 339–343.
- [15] Weicker, K., Salahifar, R., and Mohareb., M., 2010, "Shell Analysis of Thin-Walled Pipes. Part I-Field equations and solution," *Int. J. Pres. Ves. & Piping.*, 87, pp.402-413.

- [16] Weicker, K., Salahifar, R., and Mohareb., M., 2010, "Shell Analysis of Thin-Walled Pipes. Part II-Finite Element Formulation," *Int. J. Pres. Ves. & Piping.*, 87, pp.414-423.
- [17] Basaran, S., 2008, "Lagrangian and Eulerian Descriptions in Solid Mechanics and Their Numerical Solutions in hpk Framework," Doctoral dissertation, The University of Kansas, Kansas, United states.
- [18] Holzapfel, G. A., 2000, "Nonlinear Solid Mechanics: A Continuum Approach for Engineering," Chichester: Wiley.
- [19] Bonet, J., and Wood, R., 2008, "Nonlinear Continuum Mechanics for Finite Element Analysis," Cambridge: Cambridge University Press. doi:10.1017/CBO9780511755446
- [20] Bathe, K. J., 1996, "Finite Element Procedures in Engineering analysis," Prentice Hall, New Jersey.
- [21] Pagani, A., and Carrera, E., 2018, "Unified formulation of geometrically nonlinear refined beam theories," *Mech. Adv. Mater. Struc.*, 25(1), pp. 15-31
- [22] Wu, B., Pagani, A., Chen, W. Q., and Carrera, E., 2019, "Geometrically nonlinear refined shell theories by Carrera Unified Formulation," *Mech. Adv. Mater. Struc.*, DOI: 10.1080/15376494.2019.1702237
- [23] Simulia ABAQUS. 2017. User's Manual version 6.6 documentation
- [24] ADINA R& D, Inc. 2012. Theory and Modeling Guide Volume I
- [25] ANSYS, Inc. ELBOW290, Retrieved from https://www.mm.bme.hu/~gyebro/files/ans_help_v182/ans_elem/Hlp_E_ELBO290.htm
- [26] Li, T., 2016, "On the formulation of a pipe element for a pipe structure with variable wall thickness," *Ocean Eng.* 117, 398–410.
- [27] Li, T., 2017, "On the formulation of a pipe element II: An orthogonal polynomial pipe element," *Ocean Eng.* 129, 279–290.
- [28] Li, T., 2017, "On the formulation of a 3D smooth curved pipe finite element with arbitrary variable cross-section," *Thin-Walled Structures.* 117, 314–331.
- [29] Duan, L., Zhao, J., 2019, "A geometrically exact cross-section deformable thin-walled beam finite element based on generalized beam theory," *Comput. Struct.*, 218, pp.32-59.
- [30] Meroueh, K. A., 1986, "On a Formulation of a Nonlinear Theory of Plates and Shells with Applications," *Comput. Struct.*, 24(5), pp. 691-705.
- [31] Campello, E. M. B., Pimenta, P. M., Wriggers, P., 2003, "A triangular finite shell element based on a fully nonlinear shell formulation," *Computational Mechanics*, 31, pp. 505-518.
- [32] Ivannikov, V., Tiago, C., Pimenta, P. M., 2014, "On the boundary conditions of the geometrically nonlinear Kirchhoff-Love shell theory," *Int. J. Solids Struct.*, 51, pp. 3101-3112.
- [33] Adeeb, S. First and Second Piola Kirchhoff Stress Tensors. Retrieved from <https://sameradeeb-new.srv.ualberta.ca/stress/first-and-second-piola-kirchhoff-stress-tensors/>
- [34] Petersen, K., Pedetsen, M. The Matrix Cookbook. Retrieved from <https://www.ics.uci.edu/~welling/teaching/KernelsICS273B/MatrixCookBook.pdf>
- [35] http://homepages.engineering.auckland.ac.nz/~pkel015/SolidMechanicsBooks/Part_III/Chapter_3_Stress_Mass_Momentum/Stress_Balance_Principles_Complete.pdf

Chapter 4

Shell Finite Element Formulation for Geometrically Nonlinear Analysis of Curved Thin-Walled Pipes

4.1 Abstract

A family of shell finite elements is developed for the geometrically nonlinear analysis of pipe bends. The constitutive description follows the Saint-Venant-Kirchhoff model. The first Piola-Kirchhoff stress and the conjugate gradient of the virtual displacement fields are adopted within the framework of the virtual work principle. Three C^1 continuous schemes are used to interpolate the displacement fields in the longitudinal direction while Fourier series are used for circumferential interpolation. Eigenvalue analyses are conducted to assess the ability of the elements to represent rigid body motion. Comparisons with other shell and elbow models demonstrate the accuracy and versatility of the formulation.

Keywords

Toroidal shells, Geometrically nonlinear finite element, First Piola-Kirchhoff stress tensor, Virtual work principle, Eigenvalue analyses, Elbows.

4.2 Introduction

The energy industry commonly utilizes pipeline transmission systems to convey the extracted oil and gas resources and related materials to centres of consumption. The structural integrity of these transmission systems is essential for their economics, safety, and optimal performance. The

complex deformation shape of pipes with the concomitant ovalization can lead to a markedly high computational cost associated with the analysis and design of these systems. Therefore, it is imperative to investigate and propose efficient solutions that balance the high computational cost with the accuracy of the structural/mechanical analysis techniques for the components of the piping system.

Pipe bends are commonly used in piping systems in order to allow direction changes and provide flexible loops to guard against excessive axial stresses due to thermal expansions. Traditional beam deformation analysis is inadequate in accurately predicting the structural response of pipe bends associated with ovalization and warping of the pipe cross section. Theoretical studies [1-5] were the cornerstone for understating the mechanical behavior of pipe bends. However, various limitations (e.g., loading type and geometric properties) are associated with these studies particularly when incorporating nonlinear effects.

Efficient numerical analysis tools are required to properly analyze structural systems with pipe bends. Although solid and shell finite elements (FE) formulations [6-9] can accurately predict the structural response of pipe bends, these elements are prohibitively expensive to use in a practical design environment due to their high computational and modelling cost, particularly when modelling long pipelines. Therefore, there is a need to develop computationally-effective FE formulations that are able to simulate the structural response of pipe bends accurately and efficiently.

Many researchers developed linear FE formulations to model pipe bends. Ohtsubo and Watanabe [10] proposed a ring-shaped FE formulation based on the kinematic constraints of the thin shell theory. Their proposed formulation utilized Fourier series and cubic Hermitian functions to interpolate the displacement fields along the circumferential and longitudinal directions, respectively. The FE formulation, however, does not capture all the rigid body modes. Bathe and Almeida [11] employed the von Karman theory [1] to develop a simple FE formulation where the beam displacement mode expressed by cubic polynomial function was integrated with cross-sectional deformation modes characterized by Fourier series in the circumferential direction. Although additional enhancements were added to involve pressure stiffening [12] and interaction effects between the straight and curved pipes [13], the element did not capture warping displacements [14]. Militello and Huespe tackled warping deformation by adding Fourier series for the displacement field of the longitudinal direction. Fonseca et al [15] introduced two FE formulations to model elbows attached to straight pipes. Higher-order polynomial or trigonometric functions along the longitudinal coordinate were employed to interpolate the beam displacement fields while the circumferential variations of the displacements were interpolated using Fourier series. The formulations were limited to loading within the plane of the elbow with internal pressure.

Nonlinear FE formulations in solid mechanics are commonly based on the principle of virtual work expressed in the Lagrangian description [16]. The internal virtual work can be expressed using various stress tensors and their energy conjugate strains [17-18]. Bathe [19] provided the specifics of developing nonlinear FE formulations by adopting the second Piola-Kirchhoff stress tensor and the Green-Lagrange strain tensor. Based on this approach, most commercial FE software (e.g.

ABAQUS [20], ADINA [21], and ANSYS [22]) developed elbow elements to simulate the nonlinear response of pipe bends. Li [23-25] recently developed three-dimensional nonlinear FE formulations to predict the mechanical behavior of initially non-circular straight and curved pipes. On the other hand, nonlinear FE formulations for beams [26] and shells [27-29] adopted the first Piola-Kirchhoff stress tensor and the gradient of the virtual displacement fields within the internal virtual work expression as an alternative methodology. To the authors' knowledge, such an approach has not been used to formulate/develop nonlinear FE formulations for curved pipes.

Within this context, the present study formulates and implements toroidal thin shell FE formulations aimed at predicting the geometric nonlinear structural response of pipe bends in the elastic regime. Additionally, these formulations adopt the first Piola-Kirchhoff stress and the gradient of the virtual displacement fields within the internal virtual work framework. The formulations capture the follower effect due to hydrostatic pressure.

4.3 Assumptions

The following assumptions are adopted in the present formulation:

1. The Saint-Venant-Kirchhoff constitutive model is employed in order to characterize the linearly elastic isotropic response of pipe material.
2. The elbow cross-section is assumed to be initially circular.
3. The kinematic constraints of the Love-Kirchhoff thin shell theory are adopted, i.e.,
 - I. Straight lines normal to the un-deformed mid-surface of the shell remain straight and normal to the mid-surface of the deformed configuration.
 - II. The thickness of the shell remains constant throughout deformation.

4. The normal stress component along the radial direction is considered negligible.
5. The pressure load is treated as a follower load.

4.4 Overview on the formulation

The writer introduced a detailed description of the formulation adopted in the present study in Chapter 3. In this section, an overview on the formulation is presented. For static equilibrium, the principle of virtual work referred to the reference configuration is expressed as

$$\int_{V_o} \mathbf{P} : (\bar{\mathbf{u}} \otimes \nabla^T) dV_o = \int_{S_o} (\tilde{\mathbf{T}}_N \cdot \bar{\mathbf{u}}) dS_o + \int_{V_o} (\tilde{\mathbf{B}} \cdot \bar{\mathbf{u}}) dV_o \quad (4.1)$$

where the reference volume V_o and its enclosing reference surface S_o are utilized to implement all integrations. The inner product of the first Piola-Kirchhoff stress tensor \mathbf{P} and the gradient of the virtual displacement fields $(\bar{\mathbf{u}} \otimes \nabla^T)$, the left-hand-side of Eq.(4.1), represents the internal virtual work while the external virtual work is expressed in terms of the applied traction vector $\tilde{\mathbf{T}}_N$ and the body force vector $\tilde{\mathbf{B}}$ on the right-hand-side of Eq.(4.1). The virtual displacement field vector $\bar{\mathbf{u}}$ is assumed to be a nonlinear function of the nodal degrees of freedom vector \mathbf{d} and is related to the virtual nodal degrees of freedom vector $\bar{\mathbf{d}}$ through $\bar{\mathbf{u}} = (\partial \mathbf{u} / \partial \mathbf{d}) \bar{\mathbf{d}}$, where \mathbf{u} is the displacement field vector. The partial derivative of Eq.(4.1) with respect to the virtual nodal degrees of freedom vector $\bar{\mathbf{d}}$ yields the general equilibrium equations in terms of the nodal degrees of freedom vector \mathbf{d} as given in Eq.(4.2)

$$\mathbf{F}^{(I)}(\mathbf{d}) - \mathbf{F}^{(E)}(\mathbf{d}) = \mathbf{0} \quad (4.2)$$

in which the internal force vector is $\mathbf{F}^{(I)} = \int_{V_o} \mathbf{P} : \left[\partial (\mathbf{u} \otimes \nabla^T) / \partial \mathbf{d} \right] dV_o$ and the external force

vector is $\mathbf{F}^{(E)} = \int_{S_o} [(\partial \mathbf{u} / \partial \mathbf{d})^T \tilde{\mathbf{T}}_N] dS_o + \int_{V_o} [(\partial \mathbf{u} / \partial \mathbf{d})^T \tilde{\mathbf{B}}] dV_o$. The system of nonlinear equations provided in Eq.(4.2) can be approximated using Taylor series and solved iteratively as expressed in Eq.(4.3)

$$\mathbf{R}(\mathbf{d}_g) + \mathbf{K}|_{\mathbf{d}=\mathbf{d}_g} (\mathbf{d} - \mathbf{d}_g) = \mathbf{0} \quad (4.3)$$

where $\mathbf{R}(\mathbf{d}_g) = \mathbf{F}^{(I)}(\mathbf{d}_g) - \mathbf{F}^{(E)}(\mathbf{d}_g)$ and $\mathbf{K}|_{\mathbf{d}=\mathbf{d}_g} = \mathbf{K}^T|_{\mathbf{d}=\mathbf{d}_g} - \mathbf{K}^F|_{\mathbf{d}=\mathbf{d}_g}$ are the residual force

vector and the stiffness matrix at given nodal degrees of freedom vector \mathbf{d}_g . The tangent stiffness

matrix \mathbf{K}^T is approximated by the expression $\mathbf{K}_A^T = \int_{V_o} ([\partial \mathbf{P} / \partial \mathbf{d}] : [\partial (\mathbf{u} \otimes \nabla^T) / \partial \mathbf{d}]) dV_o$ and the

approximate contribution of the external force vector in the stiffness matrix is

$$\mathbf{K}_A^F = \int_{S_o} [(\partial \mathbf{u} / \partial \mathbf{d})^T (\partial \tilde{\mathbf{T}}_N / \partial \mathbf{d})] dS_o + \int_{V_o} [(\partial \mathbf{u} / \partial \mathbf{d})^T (\partial \tilde{\mathbf{B}} / \partial \mathbf{d})] dV_o. \text{ The mathematical expressions}$$

of the internal and external force vectors and the stiffness matrix are in terms of a generic displacement field vector \mathbf{u} . In the following section, the displacement field vector will be specialized for thin-walled toroidal shells.

4.5 Displacement fields in toroidal coordinates

4.5.1 Geometric description

An initially circular thin-walled pipe bend (Fig. 4. 1) is considered with a mid-surface pipe bend radius R , a mid-surface cross section radius r_m , and a wall thickness h . Two orthogonal curvilinear coordinates θ and φ are utilized to define material points located on the mid-surface of the pipe bend. A normal coordinate ζ is adopted to express the offset distance of a point from the mid-surface (Fig. 4. 1). A material point located on the mid-surface of the pipe bend, under

loading (Fig. 4. 1), undergoes a displacement field vector $\mathbf{u}_0 = \{u_{o\theta}, u_{o\varphi}, u_{or}\}$ along the longitudinal, circumferential, and radial directions $\{\mathbf{e}_\theta, \mathbf{e}_\varphi, \mathbf{e}_r\}$ respectively where $r(\zeta) = r_m + \zeta$, i.e.,

$$\mathbf{u}_0(\theta, \varphi) = u_{o\theta}\mathbf{e}_\theta(\theta) + u_{o\varphi}\mathbf{e}_\varphi(\theta, \varphi) + u_{or}\mathbf{e}_r(\theta, \varphi) \quad (4.4)$$

The displacement field vector $\mathbf{u} = \mathbf{u}(\theta, \varphi, \zeta)$ of a generic material point offset from the mid-surface is obtained, from Assumption 3 (Section 4.3), as

$$\mathbf{u}(\theta, \varphi, \zeta) = \mathbf{u}_0(\theta, \varphi) + \zeta(\hat{\mathbf{n}}(\theta, \varphi) - \hat{\mathbf{N}}(\theta, \varphi)) \quad (4.5)$$

where $\hat{\mathbf{n}}$ and $\hat{\mathbf{N}}$ are the unit vectors normal to the deformed and un-deformed mid-surfaces respectively.

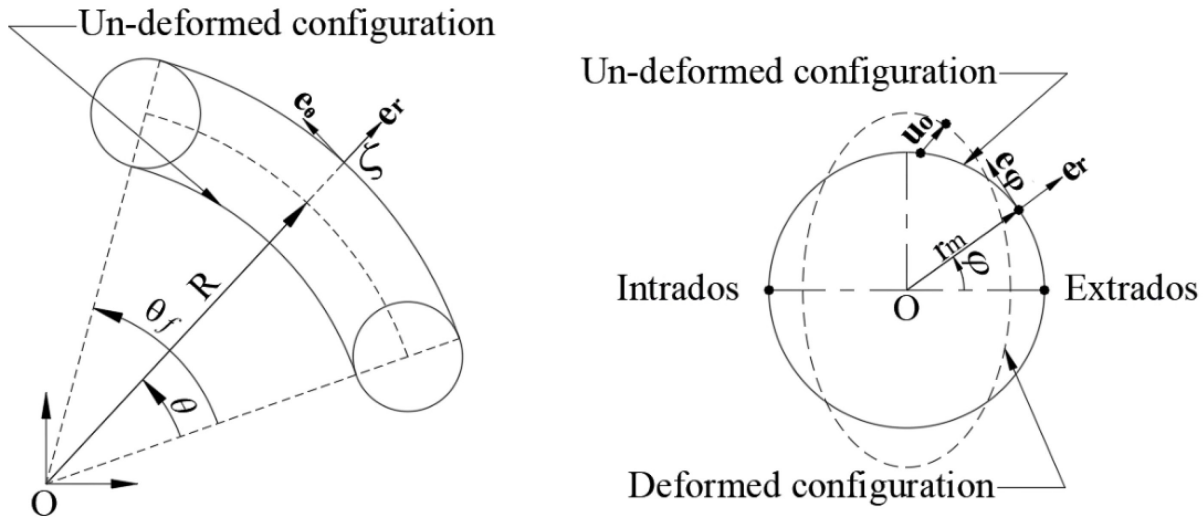


Fig. 4. 1 Pipe bend coordinates, vector bases, and displacement vector

4.5.2 Unit normal vector

In the un-deformed configuration, the unit vector normal to the mid-surface is $\hat{\mathbf{N}} = \mathbf{e}_r$. In contrast, kinematic considerations must be employed to obtain the unit vector $\hat{\mathbf{n}}$ normal to the deformed

mid-surface. The position vector $\mathbf{r}_o(\theta, \varphi)$ in the deformed configuration for a point on the mid-surface is obtained by adding the position vector $\mathbf{R}_o(\theta, \varphi) = [R \cos \varphi + r_m] \mathbf{e}_r(\theta, \varphi) - [R \sin \varphi] \mathbf{e}_\varphi(\theta, \varphi)$ of the point on the un-deformed mid-surface to the displacement vector $\mathbf{u}_o(\theta, \varphi)$ of the point (Eq.(4.4)) yielding

$$\mathbf{r}_o(\theta, \varphi) = u_{o\theta} \mathbf{e}_\theta(\theta) + [-R \sin \varphi + u_{o\varphi}] \mathbf{e}_\varphi(\theta, \varphi) + [R \cos \varphi + r_m + u_{or}] \mathbf{e}_r(\theta, \varphi) \quad (4.6)$$

The vector \mathbf{n} normal to mid-surface in the deformed configuration is obtained from the cross product

$$\mathbf{n} = (\partial \mathbf{r}_o / \partial \theta) \times (\partial \mathbf{r}_o / \partial \varphi) = n_1(\theta, \varphi) \mathbf{e}_\theta(\theta) + n_2(\theta, \varphi) \mathbf{e}_\varphi(\theta, \varphi) + n_3(\theta, \varphi) \mathbf{e}_r(\theta, \varphi) \quad (4.7)$$

where n_1, n_2 and n_3 are the components of the normal vector in the deformed configuration.

By differentiating Eq.(4.6) with respect to coordinates θ and φ , one obtains

$$\begin{aligned} \partial \mathbf{r}_o / \partial \theta &= [R + r_m \cos \varphi + u_{o\theta, \theta}(\theta, \varphi) - u_{o\varphi}(\theta, \varphi) \sin \varphi + u_{or}(\theta, \varphi) \cos \varphi] \mathbf{e}_\theta(\theta) \\ &\quad + [u_{o\varphi, \theta}(\theta, \varphi) + u_{o\theta}(\theta, \varphi) \sin \varphi] \mathbf{e}_\varphi(\theta, \varphi) + [u_{or, \theta}(\theta, \varphi) - u_{o\theta}(\theta, \varphi) \cos \varphi] \mathbf{e}_r(\theta, \varphi) \\ \partial \mathbf{r}_o / \partial \varphi &= [u_{o\theta, \varphi}(\theta, \varphi)] \mathbf{e}_\theta(\theta) + [r_m + u_{o\varphi, \varphi}(\theta, \varphi) + u_{or}(\theta, \varphi)] \mathbf{e}_\varphi(\theta, \varphi) \\ &\quad + [u_{or, \varphi}(\theta, \varphi) - u_{o\varphi}(\theta, \varphi)] \mathbf{e}_r(\theta, \varphi) \end{aligned} \quad (4.8)$$

in which $(,)$ indicates to the partial derivative of the preceding argument with respect to the coordinate following the comma. Components n_1, n_2 , and n_3 of vector \mathbf{n} are recovered by equating the coordinates of Eq.(4.7) and Eq.(4.8) yielding

$$\begin{aligned}
n_1 &= \left[u_{o\varphi,\theta}(\theta, \varphi) + u_{o\theta}(\theta, \varphi) \sin \varphi \right] \left[u_{or,\varphi}(\theta, \varphi) - u_{o\varphi}(\theta, \varphi) \right] \\
&\quad - \left[u_{or,\theta}(\theta, \varphi) - u_{o\theta}(\theta, \varphi) \cos \varphi \right] \left[r_m + u_{o\varphi,\varphi}(\theta, \varphi) + u_{or}(\theta, \varphi) \right] \\
n_2 &= \left[u_{or,\theta}(\theta, \varphi) - u_{o\theta}(\theta, \varphi) \cos \varphi \right] \left[u_{o\theta,\varphi}(\theta, \varphi) \right] \\
&\quad - \left[R + r_m \cos \varphi + u_{o\theta,\theta}(\theta, \varphi) - u_{o\varphi}(\theta, \varphi) \sin \varphi + u_{or}(\theta, \varphi) \cos \varphi \right] \left[u_{or,\varphi}(\theta, \varphi) - u_{o\varphi}(\theta, \varphi) \right] \\
n_3 &= \left[R + r_m \cos \varphi + u_{o\theta,\theta}(\theta, \varphi) - u_{o\varphi}(\theta, \varphi) \sin \varphi + u_{or}(\theta, \varphi) \cos \varphi \right] \left[r_m + u_{o\varphi,\varphi}(\theta, \varphi) + u_{or}(\theta, \varphi) \right] \\
&\quad - \left[u_{o\varphi,\theta}(\theta, \varphi) + u_{o\theta}(\theta, \varphi) \sin \varphi \right] \left[u_{o\theta,\varphi}(\theta, \varphi) \right]
\end{aligned} \tag{4.9}$$

The components of the unit vector $\hat{\mathbf{n}}$ normal to the deformed mid-surface are expressed as Eq.(4.10)

$$\hat{n}_i = n_i / \sqrt{n_1^2 + n_2^2 + n_3^2} \quad i = 1, 2, 3 \tag{4.10}$$

4.5.3 Displacement fields for a point offset from the mid-surface

Eq.(4.5) relates the displacement field vector $\mathbf{u}(\theta, \varphi, \zeta) = (u_\theta, u_\varphi, u_r)$ of a generic point located at a distance ζ from the mid-surface to the displacement field vector $\mathbf{u}_o(\theta, \varphi) = (u_{o\theta}, u_{o\varphi}, u_{or})$ of a point on the mid-surface. From Eqs.(4.4) and(4.10), by substituting into Eq.(4.5), one can recover $\mathbf{u}(\theta, \varphi, \zeta)$ as

$$\mathbf{u}(\theta, \varphi, \zeta) = u_\theta \mathbf{e}_\theta(\theta) + u_\varphi \mathbf{e}_\varphi(\theta, \varphi) + u_r \mathbf{e}_r(\theta, \varphi) \tag{4.11}$$

where

$$\begin{aligned}
u_\theta(\theta, \varphi, \zeta) &= u_{o\theta}(\theta, \varphi) + \zeta \hat{n}_1(\theta, \varphi) \\
u_\varphi(\theta, \varphi, \zeta) &= u_{o\varphi}(\theta, \varphi) + \zeta \hat{n}_2(\theta, \varphi) \\
u_r(\theta, \varphi, \zeta) &= u_{or}(\theta, \varphi) + \zeta \hat{n}_3(\theta, \varphi) - \zeta
\end{aligned} \tag{4.12}$$

4.6 Gradient of the displacement field vector and its derivative

In a toroidal coordinate system, the gradient operator is expressed by $\nabla = \langle (1/s)\partial/\partial\theta \mid (1/r)\partial/\partial\varphi \mid \partial/\partial r \rangle^T$ where parameter $s = R + (r_m + \zeta)\cos\varphi$ and coordinate $r = r_m + \zeta$ have been defined. The gradient of the displacement field vector \mathbf{u} thus can be expressed as

$$\mathbf{u} \otimes \nabla^T = \begin{bmatrix} (1/s)[u_{\theta,\theta} - u_\varphi \sin\varphi + u_r \cos\varphi] & (1/r)u_{\theta,\varphi} & u_{\theta,\zeta} \\ (1/s)[u_{\varphi,\theta} + u_\theta \sin\varphi] & (1/r)(u_{\varphi,\varphi} + u_r) & u_{\varphi,\zeta} \\ (1/s)[u_{r,\theta} - u_\theta \cos\varphi] & (1/r)(u_{r,\varphi} - u_\varphi) & u_{r,\zeta} \end{bmatrix} \quad (4.13)$$

The components of the second order tensor $\mathbf{u} \otimes \nabla^T$ involve the components of the displacement field vector $(u_\theta, u_\varphi, u_r)$ given in Eq.(4.12) and their derivatives with respect to coordinates θ, φ , and ζ provided in Eqs.(4.A.1) to (4.A.9) in Appendix 4.A: Derivatives of displacement fields with respect to coordinates . From all mathematical identities expressed in Section 4.11 (Eqs.(4.A.1) to (4.A.16)) and Eqs.(4.9), (4.10), and (4.12) , by substituting into Eq.(4.13), the gradient of the displacement field vector shown in Eq.(4.13) can be obtained in terms of the components of the displacement field vector $(u_{o\theta}, u_{o\varphi}, u_{or})$ of the mid-surface and their derivatives with respect to coordinates θ and φ . The mathematical expressions for the internal force vector \mathbf{F}^I and the tangent stiffness matrix \mathbf{K}_A^T provided under Section 4.4 require the derivatives of the gradient of the displacement field vector $\mathbf{u} \otimes \nabla^T$ with respect to the nodal degrees of freedom d_j which is given by

$$\left(\mathbf{u} \otimes \nabla^T \right)_{,d_j} = \begin{bmatrix} (1/s) \left[\left(u_{\theta,\theta} \right)_{,d_j} - u_{\varphi,d_j} \sin \varphi + u_{r,d_j} \cos \varphi \right] & (1/r) \left(u_{\theta,\varphi} \right)_{,d_j} & \left(u_{\theta,\zeta} \right)_{,d_j} \\ (1/s) \left[\left(u_{\varphi,\theta} \right)_{,d_j} + u_{\theta,d_j} \sin \varphi \right] & (1/r) \left[\left(u_{\varphi,\varphi} \right)_{,d_j} + u_{r,d_j} \right] & \left(u_{\varphi,\zeta} \right)_{,d_j} \\ (1/s) \left[\left(u_{r,\theta} \right)_{,d_j} - u_{\theta,d_j} \cos \varphi \right] & (1/r) \left[\left(u_{r,\varphi} \right)_{,d_j} - u_{\varphi,d_j} \right] & \left(u_{r,\zeta} \right)_{,d_j} \end{bmatrix} \quad (4.14)$$

By using Eqs.(4.B.1) and (4.B.6) to (4.B.14) (Section 4.12), the second order tensor in Eq.(4.14) can be expressed in terms of components $(u_{o\theta}, u_{o\varphi}, u_{or})$ of the displacement field vector of a point on the mid-surface and their derivatives with respect to θ , φ , and d_j . Also, the external force vector \mathbf{F}^E and its contribution to the stiffness matrix \mathbf{K}_A^F involve the derivatives of components of the displacement field vector $(u_\theta, u_\varphi, u_r)$ with respect to d_j which are introduced in Eq. (4.B.1).

. The force vectors and the stiffness matrix are obtained in terms of components $(u_{o\theta}, u_{o\varphi}, u_{or})$ of the displacement field vector of the mid-surface and their derivatives with respect to θ , φ , and d_j .

. These components are presented in the following section.

4.7 Interpolation Schemes

The present study introduces three C^l continuity interpolation schemes along the longitudinal direction and Fourier series expansion¹² along the circumferential direction in order to describe the displacement fields $\mathbf{u}_o = (u_{o\theta}, u_{o\varphi}, u_{or})$ at the pipe bend mid-surface. The displacement fields are assumed to take the form

¹² The physical significance of the Fourier interpolation scheme is similar to that described in Appendix 3.C: Interpolation Schemes

$$u_{ok}(\theta, \varphi) = \langle \mathbf{L}(\theta, \varphi) \rangle_{1 \times 4(2m+1)}^T \{ \mathbf{d} \}_k \{ \mathbf{d} \}_{k \times 4(2m+1) \times 1} \quad k = \theta, \varphi, r \quad (4.15)$$

where $\{ \mathbf{d} \}_k \{ \mathbf{d} \}_{k \times 4(2m+1) \times 1}$ is the vector of degrees of freedom and $\langle \mathbf{L}(\theta, \varphi) \rangle_{1 \times 4(2m+1)}^T$ is the vector of interpolation functions

$$\langle \mathbf{L}(\theta, \varphi) \rangle^T = \langle \mathbf{H}(\theta)^T \mid \cos \varphi \mathbf{H}(\theta)^T \mid \sin \varphi \mathbf{H}(\theta)^T \mid \cos 2\varphi \mathbf{H}(\theta)^T \mid \sin 2\varphi \mathbf{H}(\theta)^T \mid \dots \mid \cos m\varphi \mathbf{H}(\theta)^T \mid \sin m\varphi \mathbf{H}(\theta)^T \rangle \quad (4.16)$$

in which $\mathbf{H}(\theta)$ is the vector of shape functions along the longitudinal direction and m is the number of Fourier modes. Ohtsubo and Watanabe [10] employed the well-known Hermitian functions to interpolate the displacement fields along the longitudinal direction. Such Hermitian interpolation scheme will be referred to as H. In addition, the present study proposes two shape functions for interpolation along the longitudinal direction:

a- Fully Trigonometric function (F)

The displacement function is assumed to take the form $f(\theta) = a_1 \sin \theta + a_2 \cos \theta + a_3 \sin 2\theta + a_4 \cos 2\theta$. By enforcing C^1 continuity, corresponding shape functions are found to take the form:

$$\mathbf{H}(\theta) = \left\{ \begin{array}{l} \frac{\csc^3(0.5\theta_f) \sin^2[(\theta - \theta_f)/2] [\sin(\theta - 1.5\theta_f) + \sin(\theta - 0.5\theta_f) + 4\sin(\theta + 0.5\theta_f) + 2\sin(1.5\theta_f)]}{2(2 + \cos \theta_f)} \\ \frac{2[2\cos(0.5\theta) + \cos(0.5\theta - \theta_f)] \csc^2(0.5\theta_f) \sin(0.5\theta) \sin^2[(\theta - \theta_f)/2]}{2 + \cos \theta_f} \\ - \frac{\csc^3(0.5\theta_f) \sin^2(0.5\theta) [\cos(0.5\theta_f)(-1 + 4\cos \theta_f) \sin \theta - (1 + 2\cos \theta) \sin(1.5\theta_f)]}{2 + \cos \theta_f} \\ \frac{\csc^2(0.5\theta_f) \sin^2(0.5\theta) [\sin \theta + 2\sin(\theta - \theta_f) - \sin \theta_f]}{2 + \cos \theta_f} \end{array} \right\} \quad (4.17)$$

The element based on the interpolation scheme in Eq.(4.17) will be referred to as the F element.

b- Mixed Polynomial Trigonometric function (M)

The displacement function is assumed to take the form $f(\theta) = a_0 + a_1\theta + a_2 \sin \theta + a_3 \cos \theta$. By enforcing C^1 continuity, corresponding shape functions are found to take the form:

$$\mathbf{H}(\theta) = \left\{ \begin{array}{l} \frac{(-\theta + \theta_f) \cos(0.5\theta_f) + \sin(\theta - 0.5\theta_f) - \sin(0.5\theta_f)}{\theta_f \cos(0.5\theta_f) - 2 \sin(0.5\theta_f)} \\ \frac{\csc^2(0.5\theta_f) [-\theta + \theta_f \cos(\theta - \theta_f) + (\theta - \theta_f) \cos \theta_f - \sin \theta + \sin(\theta - \theta_f) + \sin \theta_f]}{-4 + 2\theta_f \cot(0.5\theta_f)} \\ -\frac{-\theta \cos(0.5\theta_f) + \sin(\theta - 0.5\theta_f) + \sin(0.5\theta_f)}{\theta_f \cos(0.5\theta_f) - 2 \sin(0.5\theta_f)} \\ \frac{\csc^2(0.5\theta_f) (\theta - \theta_f + \theta_f \cos \theta - \theta \cos \theta_f - \sin \theta + \sin(\theta - \theta_f) + \sin \theta_f)}{4 - 2\theta_f \cot(0.5\theta_f)} \end{array} \right\} \quad (4.18)$$

The element based on the interpolation scheme in Eq.(4.18) will be referred to as the M element. In all cases, Gauss Quadrature is adopted to carry out the required integrations.

4.8 Rigid Body Motion¹³

In order to develop an accurate FE formulation, the proposed displacement fields must guarantee an adequate representation of rigid body motions (RBM). Although an exact representation of RBM is preferred, the majority of assumed displacement fields in curved thin shell FE accommodate RBM only in an approximate manner. The approximate representation of RBM is improved by reducing the element size (e.g., [30]). The Hermitian interpolation shape functions adopted in Ref [10] to characterize the distribution of displacement fields in the longitudinal direction were able to approximately capture RBM and reasonably predict the response of pipe

¹³ Monotonic convergence can be satisfied if the developed finite element is complete (i.e., it represents rigid body motion and constant strain state) and conforming (i.e., compatibility conditions are satisfied). Patch test, which assess the ability of an assemblage of elements to induce constant strain state, is recommended to ensure the convergence for the non-conforming elements. The reader is referred to Ref [19] for more details.

bends in the context of linear analysis. Ref [11] highlighted the approximate nature of the RBM representation in Ref [10] as a drawback and proposed an improved element that combines beam deformation modes capturing RBM with cross-sectional deformation modes. Several FE formulations for modeling of pipe bends [12-15] followed the approach presented in Ref [11].

The present study follows an approach akin to that in Ref [10] while significantly improves the approximate representation of RBM. Each RBM mode corresponds to a zero eigenvalue of the element stiffness matrix. Hence, in the context of a small deformation analysis, an element stiffness matrix with six zero eigenvalues implies its ability to exactly represent the six independent degrees of freedom characterizing RBM without inducing strains/stresses¹⁴. In large deformation analysis, the presence of six zero eigenvalues would be a necessary, though not sufficient, to represent RBM modes. A series of linear eigenvalue analyses are thus conducted on the unconstrained stiffness matrix of the elements developed in the present study to extract their lowest eight eigenvalues in order to investigate the effect of (a) the interpolation scheme adopted (H, F, and M), (b) the number of Fourier modes (# Modes=2, 4, 6, 8, and 10), (c) the bend radius to outer diameter ratio ($R / D_o = 1.5, 3.0, \text{ and } 5.0$), and (d) the element angle ($10^\circ, 30^\circ, 60^\circ, \text{ and } 90^\circ$). The pipe element considered has an outer diameter $D_o = 1066.8\text{mm}$ and a wall thickness $h = 9.525\text{mm}$. Pipe material is steel with a Young's modulus $E = 210\text{GPa}$ and Poisson's ratio $\nu = 0.3$.

¹⁴ In general, all zero eigenvalues do not necessarily correspond to RBM modes since an element stiffness matrix may have spurious zero eigenvalues. In general, such spurious zero eigenvalues are attributed to an insufficient order of numerical integration. Eigenvalue analyses provided in this section are carried out using 5, 30, and 3 integration points along the longitudinal, circumferential, and radial directions, respectively. When increasing the number of integration points to 10, 50, and 5, the eigenvalues provided in Tables 4.1-4.4 do not change which may imply true (non-spurious) zero energy modes. More details are provided in Appendix 4.C: Zero Energy Modes

Table 4. 1 provides a comparison of the lowest eight eigenvalues for element types H, F, and M using six Fourier modes for the case where the elements have a 90° angle and $R/D_o = 1.5$. The M element is able to exactly capture three out of the six RBM modes and approximately captures the remaining three RBM modes as evidenced by fact that eigenvalues 4-6 are negligible compared to eigenvalue 7 (the first eigenmode associated with non-RBM, and hence inducing stresses/strains). Comparatively, Element F exactly captures two out of the six RBM modes, approximately captures two RBM modes, while the remaining two RBM modes are associated with a relatively high eigenvalue when compared to the seventh eigenmode, suggesting that the element may not be suitable to represent the 90-degree element investigated herein. Element H exactly captures one out of the six RBM modes and captures the remaining RBM modes approximately as shown by the fact that the eigenvalues 2-6 are significantly lower than eigenvalue 7. Among the three elements investigated, Element M thus provides the most accurate RBM representation for the present problem.

Table 4. 1 Effect of element interpolation type on RBM - Lowest eight eigenvalues ($R = 1.5D_o$, member angle= 90° , and six Fourier modes)

Element Type	H	F	M
Eigenvalue 1	0	0	0
Eigenvalue 2	3	0	0
Eigenvalue 3	7	1	0
Eigenvalue 4	20	5	1
Eigenvalue 5	52	1390	3
Eigenvalue 6	81	1438	8
Eigenvalue 7	633	1693	703
Eigenvalue 8	938	2289	949

Table 4. 2 provides a comparison of the lowest eight eigenvalues for various number of Fourier modes using Element M with a 90° angle and $R/D_o = 1.5$. The lowest six eigenvalues remain unchanged as the number of Fourier modes is increased from 2 to 8. Conversely, eigenvalues 7

and 8 tangibly decrease with increasing the number of Fourier modes. Nearly, no change in the eigenvalues is observed when the number of Fourier modes is increased from 8 to 10. The ratio of the RBM eigenvalues (ranging 0 at mode 1 to 8 at mode 6) to the converged 7th eigenvalue of 693 may be indicative of the error induced by the RBM approximation within the element for the present problem.

Table 4. 2 Effect of number of Fourier modes on RBM - Lowest eight eigenvalues - (M-element with 90° angle, $R = 1.5D_o$)

Fourier Modes	2	4	6	8	10
Eigenvalue 1	0	0	0	0	0
Eigenvalue 2	0	0	0	0	0
Eigenvalue 3	0	0	0	0	0
Eigenvalue 4	1	1	1	1	1
Eigenvalue 5	3	3	3	3	3
Eigenvalue 6	8	8	8	8	8
Eigenvalue 7	6613	826	703	693	693
Eigenvalue 8	7075	1065	949	938	937

Table 4. 3 provides the lowest eight eigenvalues for various elbow angles for Element M with six Fourier modes when $R / D_o = 1.5$. As the elbow angle decreases from 90° to 10°, the eigenvalues of the six RBM modes reduce in value, suggesting the importance of reducing the element angle for an accurate RBM representation.

Table 4. 3 Effect of element angle on RBM - Lowest eight eigenvalues (M- element with six Fourier modes, $R = 1.5D_o$)

Elbow angle	10°	30°	60°	90°
Eigenvalue 1	0	0	0	0
Eigenvalue 2	0	0	0	0
Eigenvalue 3	0	0	0	0
Eigenvalue 4	0	0	0	1
Eigenvalue 5	0	1	2	3
Eigenvalue 6	6	12	11	8
Eigenvalue 7	12	53	221	703
Eigenvalue 8	12	54	255	949

Table 4. 4 provides the eigenvalues for Element M with six Fourier modes for an element angle of 90° as the ratio R/D_o is varied. As R/D_o increases, the element become more capable of capturing RBM as reflected by the decrease in the eigenvalues of RBM modes. For the larger R/D_o value, the element has essentially negligibly small RBM eigenvalues in comparison to the seventh non-RBM eigenvalue of 398.

Table 4. 4 Effect of R/D_o on RBM - Lowest eight eigenvalues (M-element with six Fourier modes, element angle= 90°)

R/D_o	1.5	3	5
Eigenvalue 1	0	0	0
Eigenvalue 2	0	0	0
Eigenvalue 3	0	0	0
Eigenvalue 4	1	0	0
Eigenvalue 5	3	0	0
Eigenvalue 6	8	1	0
Eigenvalue 7	703	680	398
Eigenvalue 8	949	865	562

In conclusion, the linear eigenvalue analyses show that, in the context of small deformation analysis, Element M with six Fourier modes accurately represents RBM when the element angle is of the order 10° . In the following section, the performance of Element M, the number of Fourier modes specified, and elbow angle chosen will be investigated under finite deformations analysis for various loading cases.

4.9 Examples

A 90° pipe bend (Fig. 4. 2) with open ends has an outer diameter $D_o = 1066.8mm$ and a wall thickness $h = 9.525$. Material is steel with a Young's modulus $E = 210GPa$ and Poisson's ratio $\nu = 0.3$. The pipe bend is analyzed under several loading conditions. The bottom end of the pipe

bend is completely fixed whereas the top end is taken as free in Example 1 and rigid¹⁵ in the following examples. The pipe bend is modelled using Element M, with six Fourier modes, as well as the S4R shell element, and the ELBOW31 element within the ABAQUS library for comparison. Solutions based on Element M with six Fourier modes will be referred as “Present” subsequently. The number of Gauss integration points taken is five along the longitudinal direction, thirty along the circumferential direction, and three along the radial direction.

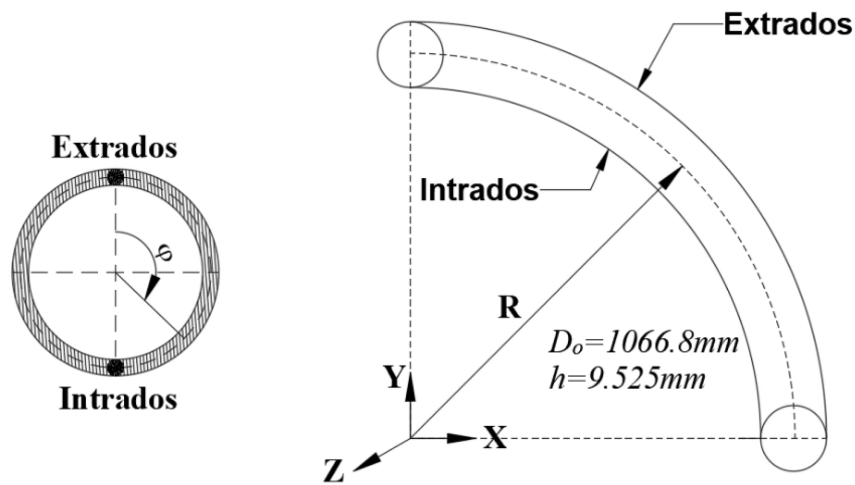


Fig. 4. 2 Geometry of the pipe bend

4.9.1 Example 1

A follower uniform internal pressure $P = 3.5MPa$ is applied normal to the inner surface of the pipe bend (Fig. 4. 2). The ratio R / D_o is taken as 1.5. The pressure would induce a hoop stress

¹⁵ Rigid means that a cross section cannot ovalize and warp (i.e., no change is allowed in the cross section). In order to enforce the top cross section to rigidly deform,

- (a) a rigid constraint which constrains the motion of the top section to the motion of the centroid of the top section, is employed in S4R shell models.
- (b) a special boundary condition is utilized in ELBOW31 models by using the NODEFORM keyword in Abaqus.
- (c) Degrees of freedom of Fourier modes higher than the first mode were set to zero in Element M proposed in the present study.

of about $0.67F_y$ in a straight pipe with a X42 (yield strength $F_y = 290MPa$). Geometrically linear¹⁶ (L) and nonlinear (N) analyses are carried out within the present formulation, the S4R shell model and the ELBOW31 model in ABAQUS for comparison¹⁷. The longitudinal, hoop, and shear stress distributions along the circumferential direction of the mid-section (sec A-A in Fig. 4. 3) at the inner and outer surfaces are presented in Fig. 4. 4. The stresses predicted by the present formulation are in an excellent agreement with those of the S4R shell and the ELBOW31 models in ABAQUS both for linear and nonlinear solutions (Fig. 4. 4). The peak longitudinal stress predicted by linear analyses is nearly twice as much as those based on the nonlinear analyses at the inner and outer surfaces (Fig. 4. 4a-b). Additionally, Fig. 4. 4c and Fig. 4. 4d show a noticeable difference between the peak hoop stress values predicted by the linear and nonlinear analyses where the peak hoop stresses based on the linear analyses are more than twice those based on the nonlinear analyses. While the difference between the shear stress predicted by the linear and nonlinear analyses is highly pronounced at the inner surface (Fig. 4. 4e), both types of analyses predict closer values at the outer surface (Fig. 4. 4f). All stress fields exhibit an oscillatory response along the circumferential direction of sec A-A. In terms of magnitude, the hoop stresses are the dominated stresses. The example shows the ability of the present formulation to accurately predict the geometrically linear and nonlinear structural response of pipe bends under internal pressure.

¹⁶ The linear solution is extracted from the present nonlinear FE formulation by applying an internal pressure of 0.035 MPa (1 % of the peak internal pressure to be applied) and subsequently magnifying the results by scaling them by a factor 100

¹⁷ While the present model and the ELBOW31 model adopt six Fourier modes, the number of elements is 10 and 84 elements, respectively. Typical dimension of the elements in the shell model is 30 mm.

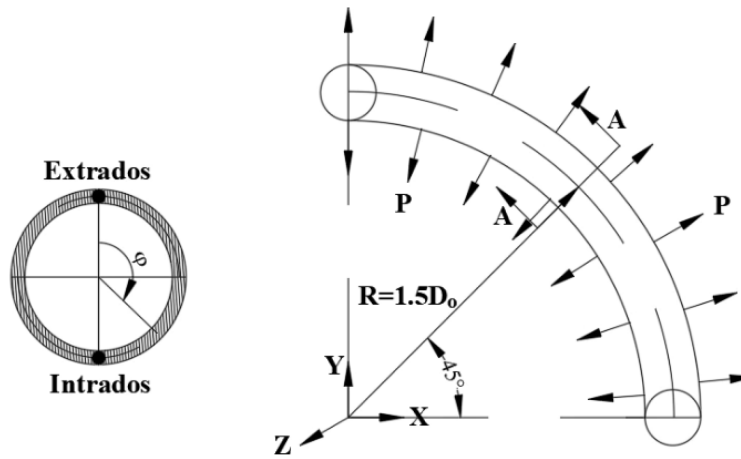
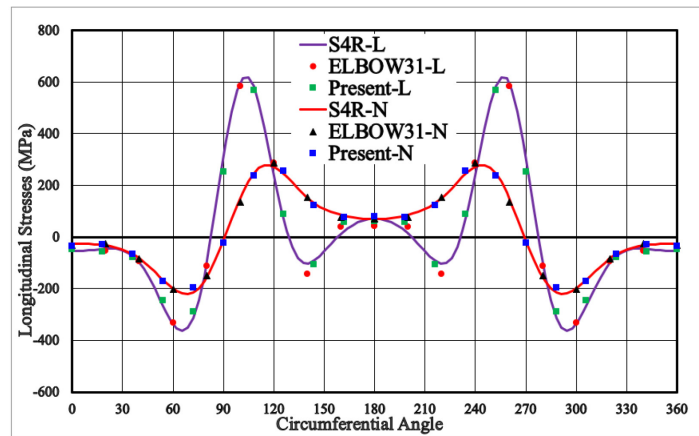
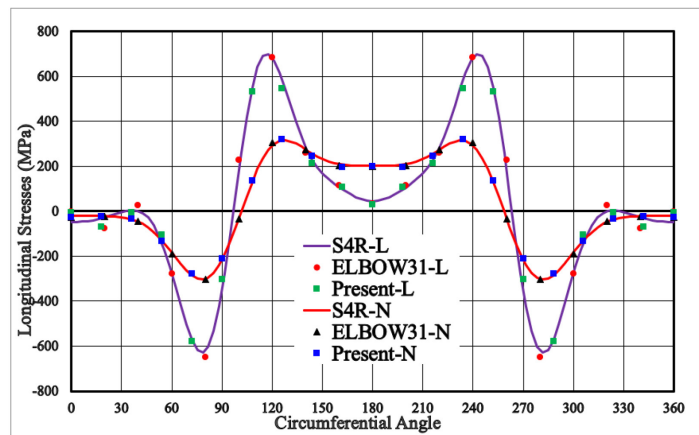


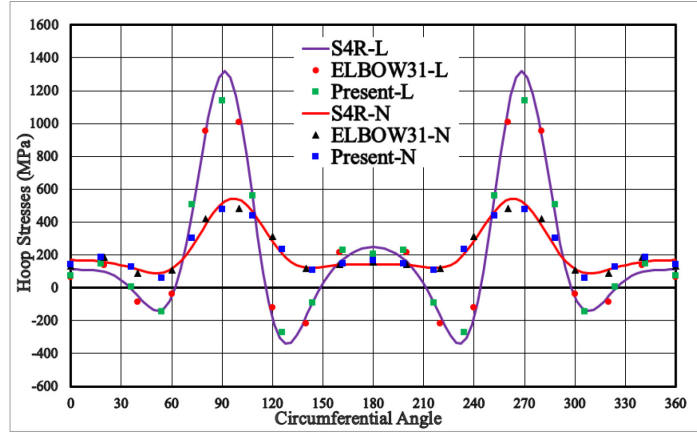
Fig. 4. 3 Pipe bend under internal pressure



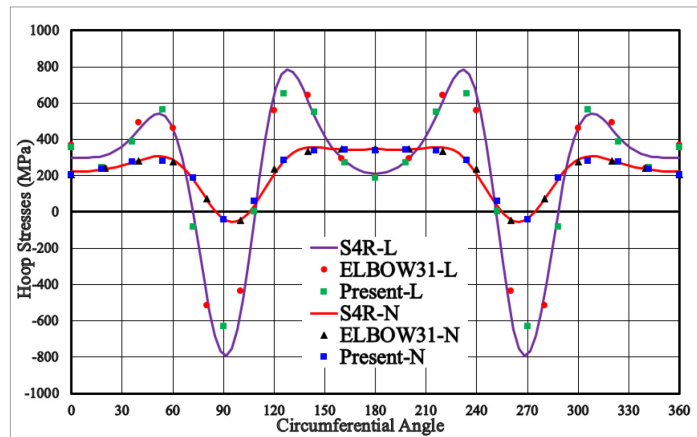
a



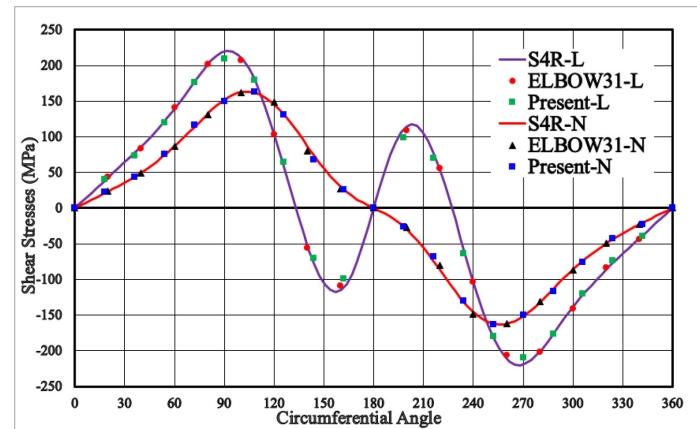
b



c



d



e

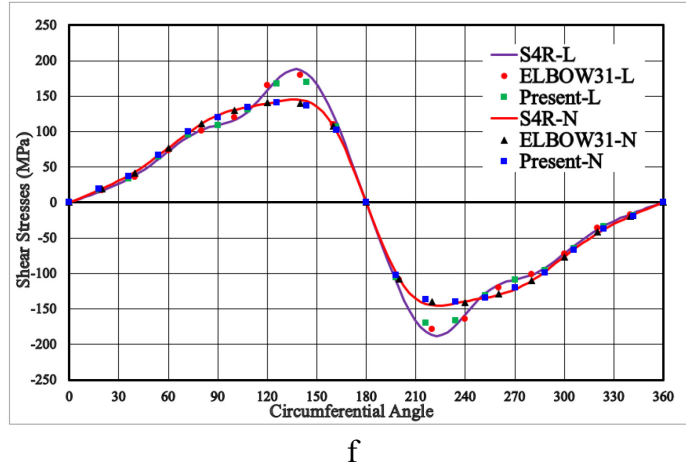


Fig. 4. 4 Stress fields versus circumferential angle at section A-A (a) Longitudinal-Inner Surface, (b) Longitudinal-Outer Surface, (c) Circumferential-Inner Surface, (d) Circumferential-Outer Surface, (e) Shear-Inner Surface, and (f) Shear-Outer Surface

4.9.2 Example 2

The pipe bend in Fig. 4. 2 has $R / D_o = 5$ and is subjected to a horizontal traction of $H = 4MPa$ and a vertical traction of $V = 4MPa$, both acting at the top section (Fig. 4. 5¹⁸). A nonlinear analysis is performed based on 10 M elements. The number of Fourier modes is varied and the displacements and stresses predicted are compared to those of the shell solution (S4R). Table 4. 5 provides the radial and longitudinal displacements at the extrados and intrados of the top section ($\theta = 90^\circ$) and the corresponding percentage differences¹⁹ between both types of solutions. As the number of Fourier modes is increased, the percentage difference between the Abaqus SR shell model and the predictions of M element model is observed to decrease. The percentage difference is 10 % when taking six Fourier modes, and tends to stabilize at nine Fourier modes, at which the percentage difference is nearly 7 %.

¹⁸ In the S4R shell model, a set of equivalent nodal forces is applied at the top section to simulate the applied tractions.

¹⁹ Percentage difference = (shell output – present formulation output) \times 100 / shell output

Table 4. 6 shows the von-Mises stresses at $\theta = 45^\circ$, at the extrados, the crown, and the intrados of the inner and outer surfaces. The highest von-Mises stresses are observed to take place at the crown. By increasing the number of Fourier modes, the predictions of these stresses are found to improve significantly at the inner and outer surfaces when compared to the S4R shell model predictions. The percentage difference between both models at the inner and outer surfaces are 12.5 % and 20.7 % respectively when using six Fourier modes whilst they reduce to 2.9 % and 5.7 % when using ten Fourier modes, in a monotonical convergence pattern. Conversely, lower values of von-Mises stresses are obtained at the extrados and intrados. At these locations, convergence exhibits an oscillatory pattern as the number of Fourier modes is increased.

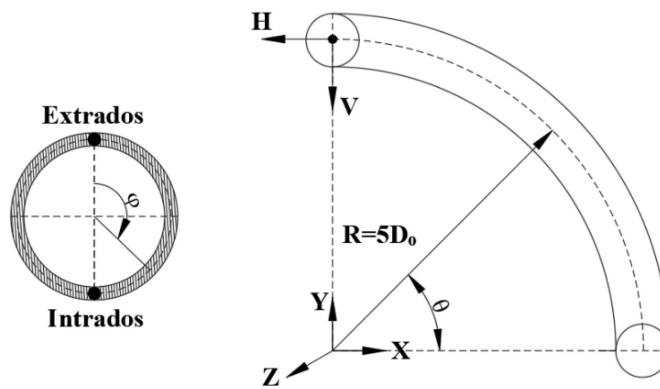


Fig. 4. 5 Pipe bend under in-plane loading

Table 4. 5 Radial and longitudinal displacements at the top section

Position	Displacement ^a		S4R	Present formulation – Number of Fourier modes				
				6	7	8	9	10
Extrados	Radial	DOFs	184152	858	990	1122	1254	1386
		mm	-142.0	-127.7	-131.9	-132.4	-132.8	-132.8
	% ^b	-	10.1	7.1	6.7	6.5	6.5	
	Longitudinal	mm	94.5	85.0	87.4	87.8	88.0	88.0
% ^b		-	10.1	7.5	7.1	6.9	6.9	
Intrados	Radial	mm	141.4	127.5	131.6	132.2	132.5	132.5
		% ^b	-	9.8	6.9	6.5	6.3	6.3
	Longitudinal	mm	57.3	51.2	52.5	52.7	52.8	52.8
		% ^b	-	10.7	8.3	8.0	7.8	7.8

^a Definitions and directions of displacement fields are presented in Section 4.5.1 (See Fig. 4. 1)

^b % = (shell output – present formulation output) × 100 / shell output

Table 4. 6 von-Mises stresses (MPa) at the inner and outer surfaces ($\theta = 45^\circ$)

Position	Surface	S4R	Present formulation – Number of Fourier modes				
			6	7	8	9	10
Extrados	Inner	60	30	58	68	50	53
	Outer	47	50	39	41	43	42
Crown	Inner	447	391	418	421	434	434
	Outer	386	306	343	354	367	364
Intrados	Inner	188	231	156	171	195	200
	Outer	193	191	187	193	189	180

4.9.3 Example 3

An out-of-plane traction $T = 50MPa$ is applied to the top section of the pipe bend with $R / D_o = 1.5$ (Fig. 4. 2) as depicted in Fig. 4. 6²⁰. A mesh study is conducted by varying the number of elements while adopting six Fourier modes under the present formulation to obtain the nonlinear response. Comparisons are provided against the S4R shell model predictions. Table 4. 7 shows the circumferential displacements at the extrados and intrados of the top section ($\theta = 90^\circ$) for various meshes along with the percentage differences from the Abaqus S4R shell model predictions. The percentage difference highly decreases when increasing the number of the elements. While the percentage differences are above 50 % when using a single element, they drop below 3.5 % when using fifteen elements.

Table 4. 8 presents von-Mises stresses at $\theta = 45^\circ$ for the inner and outer surfaces. The largest von-Mises stresses are shown to take place at the intrados. The predictions of the present formulation using three elements are in a close agreement with the predictions of the S4R model and the percentage difference is less than 3 %. Increasing the number of the elements enhances the agreement between both solutions and the percentage difference is lower than 0.9 % when fifteen

²⁰ In the S4R shell model, a set of equivalent nodal forces is applied at the top section to simulate the applied traction.

elements are used. Stresses at the extrados and crown require more elements to achieve a comparable agreement.

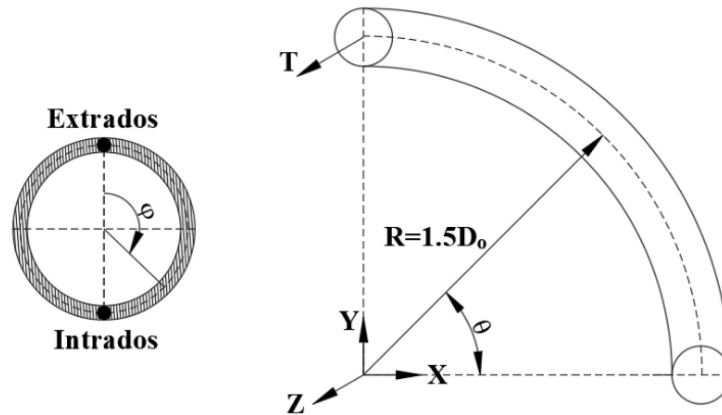


Fig. 4. 6 Pipe bend under out-of-plane loading

Table 4. 7 Circumferential displacement ^a at the top section

Position		S4R	Present formulation – Number of the elements							
			1	2	3	5	7	10	12	15
Extrados	DOFs	56100	156	234	312	468	624	858	1014	1248
	mm	24.9	8.4	17.5	20.1	22.1	23.0	23.6	23.9	24.1
	% ^b	-	66.4	29.6	19.2	11.2	7.8	5.2	4.2	3.2
Intrados	mm	15.6	6.5	11.4	12.9	14.0	14.5	14.8	15.0	15.1
	% ^b	-	58.4	26.5	17.3	10.1	7.0	4.7	3.8	2.9

^a Definitions and directions of displacement fields are presented in Section 4.5.1 (See Fig. 4. 1)

^b % = (shell output – present formulation output) × 100 / shell output

Table 4. 8 von Mises stresses (MPa) at $\theta = 45^\circ$ for the inner and outer surfaces

Position	Surface	S4R	Present formulation – Number of the elements							
			1	2	3	5	7	10	12	15
Extrados	Inner	34	37	38	41	39	38	34	35	37
	Outer	35	33	43	38	37	36	35	35	35
Crown	Inner	238	247	258	212	224	230	233	234	234
	Outer	302	251	314	248	277	287	291	292	294
Intrados	Inner	379	362	333	368	372	374	377	377	377
	Outer	359	364	320	359	355	355	355	356	356

4.9.4 Example 4

The pipe bend shown in Fig. 4. 2 is subjected at the top section to a circumferential traction T_φ which is equivalent to twisting moment $M_T = (2\pi/3)T_\varphi(r_o^3 - r_i^3)$ where r_o is the outer radius and r_i is the inner radius of the cross section (Fig. 4. 7²¹). Two pipe bend radii are examined ($R/D_o = 1.5$ and $R/D_o = 5$). The circumferential traction T_φ is taken as $150MPa$ for $R/D_o = 1.5$ and $60MPa$ for $R/D_o = 5$. Fig. 4. 8 and Fig. 4. 9 show the corresponding shear stress distributions along the circumferential direction at $\theta = 45^\circ$. Both cases exhibit an oscillatory shear stress distribution with the circumferential angle. For the case $R/D_o = 1.5$, the inner surface has a maximum shear stress of $150MPa$ at $\varphi = 104^\circ$ while the outer surface experiences a maximum shear stress of $130MPa$ at $\varphi = 90^\circ$. For $R/D_o = 5$, the maximum shear stress for the inner and outer surfaces are $62MPa$ at $\varphi = 88^\circ$ and $54MPa$ at $\varphi = 167^\circ$ respectively. The present formulation predicts shear stress distributions in close agreement to those predicted by the S4R shell and the ELBOW31 models at the shell mid-surface as well as the through-thickness variations.

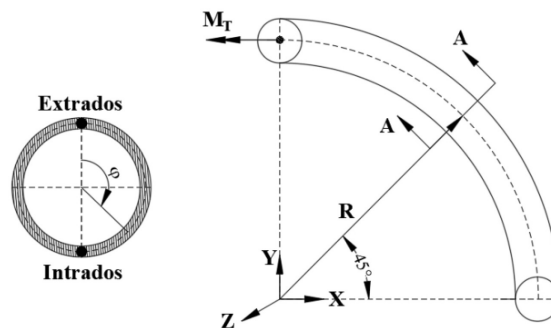


Fig. 4. 7 Pipe bend under torsional moment

²¹ The solution based on the present formulation is obtained by using ten elements and six Fourier modes while the element size of the ABAQUS models is 30 mm.

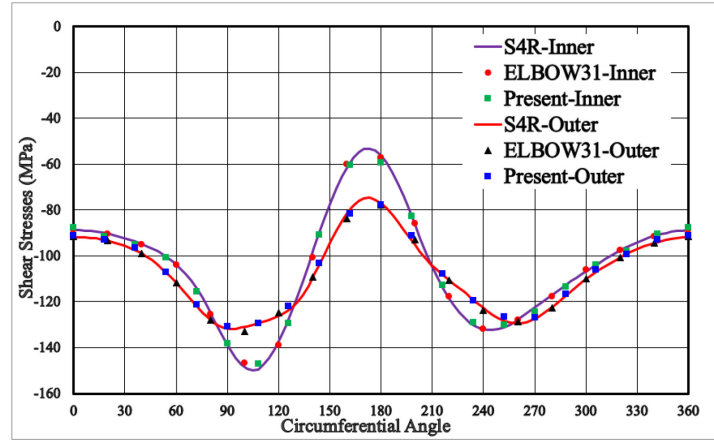


Fig. 4. 8 Shear stress distribution versus the circumferential angle for $R / D_o = 1.5$

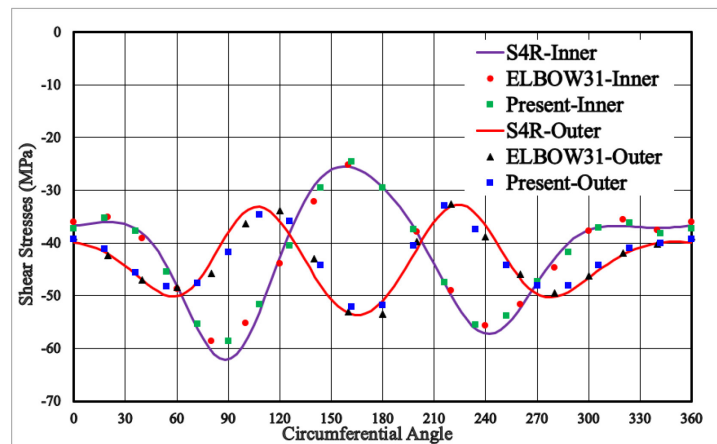


Fig. 4. 9 Shear stress distribution versus the circumferential angle for $R / D_o = 5$

4.10 Summary and Conclusions

The present study formulated and implemented a family of displacement-based geometrically nonlinear FE formulations to predict the elastic structural response of pipe bends. The formulation employs the Green-Lagrange strain tensor to characterize finite deformation-small strain effects and is based on the normality assumption of the Love-Kirchhoff thin shell theory and the Saint-Venant-Kirchhoff constitutive model. The formulation adopts the first Piola-Kirchhoff stress tensor with the conjugate gradient of the virtual displacement fields within the framework of the principle of virtual work with a total Lagrangian approach. Three C^1 continuous interpolation

schemes were examined to interpolate the displacement fields along the longitudinal direction. Circumferentially, the displacement field distributions were characterized by a number of user-specified Fourier modes. The ability of elements to capture RBM within the context of small deformation analysis has been examined through a series of eigenvalue analyses. Comparisons against models using existing shell S4R and ELBOW31 elements in ABAQUS have shown the ability of the formulation to predict the elastic structural response of pipe bends under internal pressure, in-plane loading, out-of-plane loading, and torsion.

The main findings of the work are summarized in the following:

- A systematic set of linear eigenvalue analyses have shown that, in the context of small deformation analysis, the mixed interpolation scheme (Element M) provides a better RBM representation than conventional Hermitian polynomials (H) and trigonometric interpolation (T). Also, better RBM representation is obtained when using smaller element angles and large R/D_0 values.
- The present formulation is able to accurately predict the geometrically linear and nonlinear response of pipe bends under internal pressure, as well as the nonlinear response of pipe bends under in-plane loading, out-of-plane loading, and torsion.
- The formulation accurately captures the effect of the follower loads (e.g., hydrostatic pressure)
- The nonlinear solution of the present formulation is improved with increasing the number of Fourier modes for the in-plane loading (Example 2).
- Three elements are sufficient to predict the highest von-Mises stresses at the intrados for the inner and outer surfaces with percentage difference less than 3 % against the S4R shell model for out-of-plane loading (Example 3)

- The formulation developed was shown to yield reliable results for a bend radius to outer diameter ratios ranging from 1.5 to 5.0.

4.11 Appendix 4.A: Derivatives of displacement fields with respect to coordinates

The derivatives with respect to the coordinates θ , φ , and ζ of the components of the displacement field vector $(u_\theta, u_\varphi, u_r)$ for a generic material point are given in this appendix. By differentiation of Eq.(4.12) with respect to θ , φ , and ζ , one obtains

$$u_{\theta,\theta} = u_{o\theta,\theta} + \zeta \widehat{n}_{1,\theta} \quad (4.A.1)$$

$$u_{\varphi,\theta} = u_{o\varphi,\theta} + \zeta \widehat{n}_{2,\theta} \quad (4.A.2)$$

$$u_{r,\theta} = u_{or,\theta} + \zeta \widehat{n}_{3,\theta} \quad (4.A.3)$$

$$u_{\theta,\varphi} = u_{o\theta,\varphi} + \zeta \widehat{n}_{1,\varphi} \quad (4.A.4)$$

$$u_{\varphi,\varphi} = u_{o\varphi,\varphi} + \zeta \widehat{n}_{2,\varphi} \quad (4.A.5)$$

$$u_{r,\varphi} = u_{or,\varphi} + \zeta \widehat{n}_{3,\varphi} \quad (4.A.6)$$

$$u_{\theta,\zeta} = \widehat{n}_1 = n_1 / \sqrt{n_1^2 + n_2^2 + n_3^2} \quad (4.A.7)$$

$$u_{\varphi,\zeta} = \widehat{n}_2 = n_2 / \sqrt{n_1^2 + n_2^2 + n_3^2} \quad (4.A.8)$$

$$u_{r,\zeta} = \widehat{n}_3 - 1 = n_3 / \sqrt{n_1^2 + n_2^2 + n_3^2} - 1 \quad (4.A.9)$$

Eqs.(4.A.1) to (4.A.6) require the derivatives of the components \widehat{n}_i (Eq.(4.10)) of the normal unit vector $\widehat{\mathbf{n}}$ to the deformed mid-surface with respect to the coordinates θ and φ which are given as

$$\hat{n}_{i,\alpha} = \frac{n_{i,\alpha}}{\sqrt{n_1^2 + n_2^2 + n_3^2}} - n_i \frac{n_1 n_{1,\alpha} + n_2 n_{2,\alpha} + n_3 n_{3,\alpha}}{(n_1^2 + n_2^2 + n_3^2)^{1.5}} \quad \text{where } i=1,2,3 \quad \text{and } \alpha = \theta, \varphi \quad (4.A.10)$$

Eq.(4.A.10) involves the derivatives of the components (n_1, n_2, n_3) of the normal vector \mathbf{n} to the deformed mid-surface with respect to the coordinates θ and φ which are expressed as

$$n_{1,\theta} = \left[u_{o\varphi,\theta\theta} + u_{o\theta,\theta} \sin \varphi \right] \left[u_{or,\varphi} - u_{o\varphi} \right] + \left[u_{o\varphi,\theta} + u_{o\theta} \sin \varphi \right] \left[u_{or,\varphi\theta} - u_{o\varphi,\theta} \right] \\ - \left[u_{or,\theta\theta} - u_{o\theta,\theta} \cos \varphi \right] \left[r_m + u_{o\varphi,\varphi} + u_{or} \right] - \left[u_{or,\theta} - u_{o\theta} \cos \varphi \right] \left[u_{o\varphi,\varphi\theta} + u_{or,\theta} \right] \quad (4.A.11)$$

$$n_{1,\varphi} = \left[u_{o\varphi,\theta\varphi} + u_{o\theta,\varphi} \sin \varphi + u_{o\theta} \cos \varphi \right] \left[u_{or,\varphi} - u_{o\varphi} \right] + \left[u_{o\varphi,\theta} + u_{o\theta} \sin \varphi \right] \left[u_{or,\varphi\varphi} - u_{o\varphi,\varphi} \right] \\ - \left[u_{or,\theta\varphi} - u_{o\theta,\varphi} \cos \varphi + u_{o\theta} \sin \varphi \right] \left[r_m + u_{o\varphi,\varphi} + u_{or} \right] - \left[u_{or,\theta} - u_{o\theta} \cos \varphi \right] \left[u_{o\varphi,\varphi\varphi} + u_{or,\varphi} \right] \quad (4.A.12)$$

$$n_{2,\theta} = \left[u_{or,\theta\theta} - u_{o\theta,\theta} \cos \varphi \right] u_{o\theta,\varphi} + \left[u_{or,\theta} - u_{o\theta} \cos \varphi \right] u_{o\theta,\varphi\theta} \\ - \left[u_{o\theta,\theta\theta} - u_{o\varphi,\theta} \sin \varphi + u_{or,\theta} \cos \varphi \right] \left[u_{or,\varphi} - u_{o\varphi} \right] \\ - \left[R + r_m \cos \varphi + u_{o\theta,\theta} - u_{o\varphi} \sin \varphi + u_{or} \cos \varphi \right] \left[u_{or,\varphi\theta} - u_{o\varphi,\theta} \right] \quad (4.A.13)$$

$$n_{2,\varphi} = \left[u_{or,\theta\varphi} - u_{o\theta,\varphi} \cos \varphi + u_{o\theta} \sin \varphi \right] u_{o\theta,\varphi} + \left[u_{or,\theta} - u_{o\theta} \cos \varphi \right] u_{o\theta,\varphi\varphi} \\ - \left[-r_m \sin \varphi + u_{o\theta,\theta\varphi} - u_{o\varphi,\varphi} \sin \varphi - u_{o\varphi} \cos \varphi + u_{or,\varphi} \cos \varphi - u_{or} \sin \varphi \right] \left[u_{or,\varphi} - u_{o\varphi} \right] \\ - \left[R + r_m \cos \varphi + u_{o\theta,\theta} - u_{o\varphi} \sin \varphi + u_{or} \cos \varphi \right] \left[u_{or,\varphi\varphi} - u_{o\varphi,\varphi} \right] \quad (4.A.14)$$

$$n_{3,\theta} = \left[u_{o\theta,\theta\theta} - u_{o\varphi,\theta} \sin \varphi + u_{or,\theta} \cos \varphi \right] \left[r_m + u_{o\varphi,\varphi} + u_{or} \right] - \left[u_{o\varphi,\theta\theta} + u_{o\theta,\theta} \sin \varphi \right] u_{o\theta,\varphi} \\ + \left[R + r_m \cos \varphi + u_{o\theta,\theta} - u_{o\varphi} \sin \varphi + u_{or} \cos \varphi \right] \left[u_{o\varphi,\varphi\theta} + u_{or,\theta} \right] - \left[u_{o\varphi,\theta} + u_{o\theta} \sin \varphi \right] u_{o\theta,\varphi\theta} \quad (4.A.15)$$

$$n_{3,\varphi} = \left[-r_m \sin \varphi + u_{o\theta,\theta\varphi} - u_{o\varphi,\varphi} \sin \varphi - u_{o\varphi} \cos \varphi + u_{or,\varphi} \cos \varphi - u_{or} \sin \varphi \right] \left[r_m + u_{o\varphi,\varphi} + u_{or} \right] \\ + \left[R + r_m \cos \varphi + u_{o\theta,\theta} - u_{o\varphi} \sin \varphi + u_{or} \cos \varphi \right] \left[u_{o\varphi,\varphi\varphi} + u_{or,\varphi} \right] \\ - \left[u_{o\varphi,\theta\varphi} + u_{o\theta,\varphi} \sin \varphi + u_{o\theta} \cos \varphi \right] u_{o\theta,\varphi} - \left[u_{o\varphi,\theta} + u_{o\theta} \sin \varphi \right] u_{o\theta,\varphi\varphi} \quad (4.A.16)$$

The gradient of the displacement field vector $\mathbf{u} \otimes \nabla^T$ (Eq.(4.13)) can be obtained using Eqs.(4.9), (4.12), and Eqs. (4.A.1) to (4.A.16) in terms of the components $(u_{o\theta}, u_{o\varphi}, u_{or})$ of the displacement

field vector of a point on the mid-surface and their derivatives with respect to the coordinates θ and φ .

4.12 Appendix 4.B: Derivatives of displacement fields with respect to nodal degrees of freedom

The derivatives with respect to the nodal degrees of freedom vector d_j of the components $(u_\theta, u_\varphi, u_r)$ of the displacement field vector \mathbf{u} are provided in this appendix. By differentiation on Eq.(4.12) with respect to d_j , one obtains

$$\begin{aligned} u_{\theta,d_j} &= u_{o\theta,d_j} + \zeta \widehat{n}_{1,d_j} \\ u_{\varphi,d_j} &= u_{o\varphi,d_j} + \zeta \widehat{n}_{2,d_j} \\ u_{r,d_j} &= u_{or,d_j} + \zeta \widehat{n}_{3,d_j} \end{aligned} \quad (4.B.1)$$

Eq.(4.B.1) involves the derivatives of the components \widehat{n}_i (Eq.(4.10)) of the normal unit vector $\widehat{\mathbf{n}}$ to the deformed mid-surface with respect to d_j which are expressed as

$$\widehat{n}_{i,d_j} = \frac{n_{i,d_j}}{\sqrt{n_1^2 + n_2^2 + n_3^2}} - n_i \frac{n_1 n_{1,d_j} + n_2 n_{2,d_j} + n_3 n_{3,d_j}}{(n_1^2 + n_2^2 + n_3^2)^{1.5}} \quad \text{where } i = 1, 2, 3 \quad (4.B.2)$$

Eq.(4.B.2) requires the derivatives of the components (n_1, n_2, n_3) of the normal vector \mathbf{n} to the deformed mid-surface with respect to d_j which are given as

$$\begin{aligned} n_{1,d_j} &= \left[(u_{o\varphi,\theta})_{,d_j} + u_{o\theta,d_j} \sin \varphi \right] \left[u_{or,\varphi} - u_{o\varphi} \right] + \left[u_{o\varphi,\theta} + u_{o\theta} \sin \varphi \right] \left[(u_{or,\varphi})_{,d_j} - u_{o\varphi,d_j} \right] \\ &\quad - \left[(u_{or,\theta})_{,d_j} - u_{o\theta,d_j} \cos \varphi \right] \left[r_m + u_{o\varphi,\varphi} + u_{or} \right] - \left[u_{or,\theta} - u_{o\theta} \cos \varphi \right] \left[(u_{o\varphi,\varphi})_{,d_j} + u_{or,d_j} \right] \end{aligned} \quad (4.B.3)$$

$$\begin{aligned}
n_{2,d_j} = & \left[(u_{or,\theta})_{,d_j} - u_{o\theta,d_j} \cos \varphi \right] u_{o\theta,\varphi} + \left[u_{or,\theta} - u_{o\theta} \cos \varphi \right] (u_{o\theta,\varphi})_{,d_j} \\
& - \left[(u_{o\theta,\theta})_{,d_j} - u_{o\varphi,d_j} \sin \varphi + u_{or,d_j} \cos \varphi \right] \left[u_{or,\varphi} - u_{o\varphi} \right] \\
& - \left[R + r_m \cos \varphi + u_{o\theta,\theta} - u_{o\varphi} \sin \varphi + u_{or} \cos \varphi \right] \left[(u_{or,\varphi})_{,d_j} - u_{o\varphi,d_j} \right]
\end{aligned} \tag{4.B.4}$$

$$\begin{aligned}
n_{3,d_j} = & \left[(u_{o\theta,\theta})_{,d_j} - u_{o\varphi,d_j} \sin \varphi + u_{or,d_j} \cos \varphi \right] \left[r_m + u_{o\varphi,\varphi} + u_{or} \right] \\
& + \left[R + r_m \cos \varphi + u_{o\theta,\theta} - u_{o\varphi} \sin \varphi + u_{or} \cos \varphi \right] \left[(u_{o\varphi,\varphi})_{,d_j} + u_{or,d_j} \right] \\
& - \left[(u_{o\varphi,\theta})_{,d_j} + u_{o\theta,d_j} \sin \varphi \right] u_{o\theta,\varphi} - \left[u_{o\varphi,\theta} + u_{o\theta} \sin \varphi \right] (u_{o\theta,\varphi})_{,d_j}
\end{aligned} \tag{4.B.5}$$

From Eqs.(4.9) and (4.B.2) to (4.B.5), the derivatives of the components $(u_\theta, u_\varphi, u_r)$ of the displacement field vector with respect to d_j appearing in Eq.(4.B.1) can be obtained in terms of the components $(u_{o\theta}, u_{o\varphi}, u_{or})$ of the displacement field vector of a point on the mid-surface and their derivatives with respect to θ , φ , and d_j . By differentiation of Eqs.(4.A.1) to (4.A.9) with respect to d_j , one obtains

$$(u_{\theta,\theta})_{,d_j} = (u_{o\theta,\theta})_{,d_j} + \zeta(\hat{n}_{1,\theta})_{,d_j} \tag{4.B.6}$$

$$(u_{\varphi,\theta})_{,d_j} = (u_{o\varphi,\theta})_{,d_j} + \zeta(\hat{n}_{2,\theta})_{,d_j} \tag{4.B.7}$$

$$(u_{r,\theta})_{,d_j} = (u_{or,\theta})_{,d_j} + \zeta(\hat{n}_{3,\theta})_{,d_j} \tag{4.B.8}$$

$$(u_{\theta,\varphi})_{,d_j} = (u_{o\theta,\varphi})_{,d_j} + \zeta(\hat{n}_{1,\varphi})_{,d_j} \tag{4.B.9}$$

$$(u_{\varphi,\varphi})_{,d_j} = (u_{o\varphi,\varphi})_{,d_j} + \zeta(\hat{n}_{2,\varphi})_{,d_j} \tag{4.B.10}$$

$$(u_{r,\varphi})_{,d_j} = (u_{or,\varphi})_{,d_j} + \zeta(\hat{n}_{3,\varphi})_{,d_j} \tag{4.B.11}$$

$$\left(u_{\theta,\zeta}\right)_{,dj} = \widehat{n}_{1,dj} \quad (4.B.12)$$

$$\left(u_{\varphi,\zeta}\right)_{,dj} = \widehat{n}_{2,dj} \quad (4.B.13)$$

$$\left(u_{r,\zeta}\right)_{,dj} = \widehat{n}_{3,dj} \quad (4.B.14)$$

in which (See Eq.(4.A.10))

$$\left(\widehat{n}_{i,\alpha}\right)_{,dj} = \frac{n_{i,\alpha}}{\sqrt{n_1^2 + n_2^2 + n_3^2}} \Big|_{,dj} - n_i \frac{n_1 n_{1,\alpha} + n_2 n_{2,\alpha} + n_3 n_{3,\alpha}}{\left(n_1^2 + n_2^2 + n_3^2\right)^{1.5}} \Big|_{,dj} \quad \text{where } i = 1, 2, 3 \text{ and } \alpha = \theta, \varphi \quad (4.B.15)$$

where

$$\frac{n_{i,\alpha}}{\sqrt{n_1^2 + n_2^2 + n_3^2}} \Big|_{,dj} = \frac{\left(n_{i,\alpha}\right)_{,dj}}{\sqrt{n_1^2 + n_2^2 + n_3^2}} - n_{i,\alpha} \frac{n_1 n_{1,dj} + n_2 n_{2,dj} + n_3 n_{3,dj}}{\left(n_1^2 + n_2^2 + n_3^2\right)^{1.5}} \quad (4.B.16)$$

$$n_i \frac{n_1 n_{1,\alpha} + n_2 n_{2,\alpha} + n_3 n_{3,\alpha}}{\left(n_1^2 + n_2^2 + n_3^2\right)^{1.5}} \Big|_{,dj} = n_{i,dj} \frac{n_1 n_{1,\alpha} + n_2 n_{2,\alpha} + n_3 n_{3,\alpha}}{\left(n_1^2 + n_2^2 + n_3^2\right)^{1.5}} + n_i T \quad (4.B.17)$$

in which

$$T = \frac{n_{1,dj} n_{1,\alpha} + n_1 \left(n_{1,\alpha}\right)_{,dj} + n_{2,dj} n_{2,\alpha} + n_2 \left(n_{2,\alpha}\right)_{,dj} + n_{3,dj} n_{3,\alpha} + n_3 \left(n_{3,\alpha}\right)_{,dj}}{\left(n_1^2 + n_2^2 + n_3^2\right)^{1.5}} \quad (4.B.18)$$

$$- \frac{3\left(n_1 n_{1,\alpha} + n_2 n_{2,\alpha} + n_3 n_{3,\alpha}\right)\left(n_1 n_{1,dj} + n_2 n_{2,dj} + n_3 n_{3,dj}\right)}{\left(n_1^2 + n_2^2 + n_3^2\right)^{2.5}}$$

While the mathematical terms $\widehat{n}_{i,dj}$ and $n_{i,dj}$ can be obtained from Eqs.(4.B.2) to (4.B.5), the term

$\left(n_{i,\alpha}\right)_{,dj}$ is obtained by differentiation of Eqs.(4.A.11) to (4.A.16) with respect to d_j , yielding

$$\begin{aligned}
(n_{1,\theta})_{,d_j} = & \left[(u_{o\varphi,\theta\theta})_{,d_j} + (u_{o\theta,\theta})_{,d_j} \sin \varphi \right] [u_{or,\varphi} - u_{o\varphi}] + [u_{o\varphi,\theta\theta} + u_{o\theta,\theta} \sin \varphi] \left[(u_{or,\varphi})_{,d_j} - u_{o\varphi,d_j} \right] \\
& + \left[(u_{o\varphi,\theta})_{,d_j} + u_{o\theta,d_j} \sin \varphi \right] [u_{or,\varphi\theta} - u_{o\varphi,\theta}] + [u_{o\varphi,\theta} + u_{o\theta} \sin \varphi] \left[(u_{or,\varphi\theta})_{,d_j} - (u_{o\varphi,\theta})_{,d_j} \right] \\
& - \left[(u_{or,\theta\theta})_{,d_j} - (u_{o\theta,\theta})_{,d_j} \cos \varphi \right] [r_m + u_{o\varphi,\varphi} + u_{or}] - [u_{or,\theta\theta} - u_{o\theta,\theta} \cos \varphi] \left[(u_{o\varphi,\varphi})_{,d_j} + u_{or,d_j} \right] \\
& - \left[(u_{or,\theta})_{,d_j} - u_{o\theta,d_j} \cos \varphi \right] [u_{o\varphi,\varphi\theta} + u_{or,\theta}] - [u_{or,\theta} - u_{o\theta} \cos \varphi] \left[(u_{o\varphi,\varphi\theta})_{,d_j} + (u_{or,\theta})_{,d_j} \right]
\end{aligned} \tag{4.B.19}$$

$$\begin{aligned}
(n_{1,\varphi})_{,d_j} = & \left[(u_{o\varphi,\theta\varphi})_{,d_j} + (u_{o\theta,\varphi})_{,d_j} \sin \varphi + u_{o\theta,d_j} \cos \varphi \right] [u_{or,\varphi} - u_{o\varphi}] \\
& + [u_{o\varphi,\theta\varphi} + u_{o\theta,\varphi} \sin \varphi + u_{o\theta} \cos \varphi] \left[(u_{or,\varphi})_{,d_j} - u_{o\varphi,d_j} \right] \\
& + \left[(u_{o\varphi,\theta})_{,d_j} + u_{o\theta,d_j} \sin \varphi \right] [u_{or,\varphi\varphi} - u_{o\varphi,\varphi}] + [u_{o\varphi,\theta} + u_{o\theta} \sin \varphi] \left[(u_{or,\varphi\varphi})_{,d_j} - (u_{o\varphi,\varphi})_{,d_j} \right] \\
& - \left[(u_{or,\theta\varphi})_{,d_j} - (u_{o\theta,\varphi})_{,d_j} \cos \varphi + u_{o\theta,d_j} \sin \varphi \right] [r_m + u_{o\varphi,\varphi} + u_{or}] \\
& - [u_{or,\theta\varphi} - u_{o\theta,\varphi} \cos \varphi + u_{o\theta} \sin \varphi] \left[(u_{o\varphi,\varphi})_{,d_j} + u_{or,d_j} \right] \\
& - \left[(u_{or,\theta})_{,d_j} - u_{o\theta,d_j} \cos \varphi \right] [u_{o\varphi,\varphi\varphi} + u_{or,\varphi}] - [u_{or,\theta} - u_{o\theta} \cos \varphi] \left[(u_{o\varphi,\varphi\varphi})_{,d_j} + (u_{or,\varphi})_{,d_j} \right]
\end{aligned} \tag{4.B.20}$$

$$\begin{aligned}
(n_{2,\theta})_{,d_j} = & \left[(u_{or,\theta\theta})_{,d_j} - (u_{o\theta,\theta})_{,d_j} \cos \varphi \right] u_{o\theta,\varphi} + [u_{or,\theta\theta} - u_{o\theta,\theta} \cos \varphi] (u_{o\theta,\varphi})_{,d_j} \\
& + \left[(u_{or,\theta})_{,d_j} - u_{o\theta,d_j} \cos \varphi \right] u_{o\theta,\varphi\theta} + [u_{or,\theta} - u_{o\theta} \cos \varphi] (u_{o\theta,\varphi\theta})_{,d_j} \\
& - \left[(u_{o\theta,\theta\theta})_{,d_j} - (u_{o\varphi,\theta})_{,d_j} \sin \varphi + (u_{or,\theta})_{,d_j} \cos \varphi \right] [u_{or,\varphi} - u_{o\varphi}] \\
& - [u_{o\theta,\theta\theta} - u_{o\varphi,\theta} \sin \varphi + u_{or,\theta} \cos \varphi] \left[(u_{or,\varphi})_{,d_j} - u_{o\varphi,d_j} \right] \\
& - \left[(u_{o\theta,\theta})_{,d_j} - u_{o\varphi,d_j} \sin \varphi + u_{or,d_j} \cos \varphi \right] [u_{or,\varphi\theta} - u_{o\varphi,\theta}] \\
& - [R + r_m \cos \varphi + u_{o\theta,\theta} - u_{o\varphi} \sin \varphi + u_{or} \cos \varphi] \left[(u_{or,\varphi\theta})_{,d_j} - (u_{o\varphi,\theta})_{,d_j} \right]
\end{aligned} \tag{4.B.21}$$

$$\begin{aligned}
(n_{2,\varphi})_{,dj} &= \left[(u_{or,\theta\varphi})_{,dj} - (u_{o\theta,\varphi})_{,dj} \cos \varphi + u_{o\theta,dj} \sin \varphi \right] u_{o\theta,\varphi} + \left[u_{or,\theta\varphi} - u_{o\theta,\varphi} \cos \varphi + u_{o\theta} \sin \varphi \right] (u_{o\theta,\varphi})_{,dj} \\
&+ \left[(u_{or,\theta})_{,dj} - u_{o\theta,dj} \cos \varphi \right] u_{o\theta,\varphi\varphi} + \left[u_{or,\theta} - u_{o\theta} \cos \varphi \right] (u_{o\theta,\varphi\varphi})_{,dj} \\
&- \left[(u_{o\theta,\theta\varphi})_{,dj} - (u_{o\varphi,\varphi})_{,dj} \sin \varphi - u_{o\varphi,dj} \cos \varphi + (u_{or,\varphi})_{,dj} \cos \varphi - u_{or,dj} \sin \varphi \right] \left[u_{or,\varphi} - u_{o\varphi} \right] \\
&- \left[-r_m \sin \varphi + u_{o\theta,\theta\varphi} - u_{o\varphi,\varphi} \sin \varphi - u_{o\varphi} \cos \varphi + u_{or,\varphi} \cos \varphi - u_{or} \sin \varphi \right] \left[(u_{or,\varphi})_{,dj} - u_{o\varphi,dj} \right] \\
&- \left[(u_{o\theta,\theta})_{,dj} - u_{o\varphi,dj} \sin \varphi + u_{or,dj} \cos \varphi \right] \left[u_{or,\varphi\varphi} - u_{o\varphi,\varphi} \right] \\
&- \left[R + r_m \cos \varphi + u_{o\theta,\theta} - u_{o\varphi} \sin \varphi + u_{or} \cos \varphi \right] \left[(u_{or,\varphi\varphi})_{,dj} - (u_{o\varphi,\varphi})_{,dj} \right]
\end{aligned}$$

(4.B.22)

$$\begin{aligned}
(n_{3,\theta})_{,d_j} = & \left[(u_{o\theta,\theta\theta})_{,d_j} - (u_{o\varphi,\theta})_{,d_j} \sin \varphi + (u_{or,\theta})_{,d_j} \cos \varphi \right] \left[r_m + u_{o\varphi,\varphi} + u_{or} \right] \\
& + \left[u_{o\theta,\theta\theta} - u_{o\varphi,\theta} \sin \varphi + u_{or,\theta} \cos \varphi \right] \left[(u_{o\varphi,\varphi})_{,d_j} + u_{or,d_j} \right] \\
& - \left[(u_{o\varphi,\theta\theta})_{,d_j} + (u_{o\theta,\theta})_{,d_j} \sin \varphi \right] u_{o\theta,\varphi} - \left[u_{o\varphi,\theta\theta} + u_{o\theta,\theta} \sin \varphi \right] (u_{o\theta,\varphi})_{,d_j} \\
& + \left[(u_{o\theta,\theta})_{,d_j} - u_{o\varphi,d_j} \sin \varphi + u_{or,d_j} \cos \varphi \right] \left[u_{o\varphi,\varphi\theta} + u_{or,\theta} \right] \\
& + \left[R + r_m \cos \varphi + u_{o\theta,\theta} - u_{o\varphi} \sin \varphi + u_{or} \cos \varphi \right] \left[(u_{o\varphi,\varphi\theta})_{,d_j} + (u_{or,\theta})_{,d_j} \right] \\
& - \left[(u_{o\varphi,\theta})_{,d_j} + u_{o\theta,d_j} \sin \varphi \right] u_{o\theta,\varphi\theta} - \left[u_{o\varphi,\theta} + u_{o\theta} \sin \varphi \right] (u_{o\theta,\varphi\theta})_{,d_j}
\end{aligned} \tag{4.B.23}$$

$$\begin{aligned}
(n_{3,\varphi})_{,d_j} = & \left[(u_{o\theta,\theta\varphi})_{,d_j} - (u_{o\varphi,\varphi})_{,d_j} \sin \varphi - u_{o\varphi,d_j} \cos \varphi + (u_{or,\varphi})_{,d_j} \cos \varphi - u_{or,d_j} \sin \varphi \right] \left[r_m + u_{o\varphi,\varphi} + u_{or} \right] \\
& + \left[-r_m \sin \varphi + u_{o\theta,\theta\varphi} - u_{o\varphi,\varphi} \sin \varphi - u_{o\varphi} \cos \varphi + u_{or,\varphi} \cos \varphi - u_{or} \sin \varphi \right] \left[(u_{o\varphi,\varphi})_{,d_j} + u_{or,d_j} \right] \\
& + \left[(u_{o\theta,\theta})_{,d_j} - u_{o\varphi,d_j} \sin \varphi + u_{or,d_j} \cos \varphi \right] \left[u_{o\varphi,\varphi\varphi} + u_{or,\varphi} \right] \\
& + \left[R + r_m \cos \varphi + u_{o\theta,\theta} - u_{o\varphi} \sin \varphi + u_{or} \cos \varphi \right] \left[(u_{o\varphi,\varphi\varphi})_{,d_j} + (u_{or,\varphi})_{,d_j} \right] \\
& - \left[(u_{o\varphi,\theta\varphi})_{,d_j} + (u_{o\theta,\varphi})_{,d_j} \sin \varphi + u_{o\theta,d_j} \cos \varphi \right] u_{o\theta,\varphi} - \left[u_{o\varphi,\theta\varphi} + u_{o\theta,\varphi} \sin \varphi + u_{o\theta} \cos \varphi \right] (u_{o\theta,\varphi})_{,d_j} \\
& - \left[(u_{o\varphi,\theta})_{,d_j} + u_{o\theta,d_j} \sin \varphi \right] u_{o\theta,\varphi\varphi} - \left[u_{o\varphi,\theta} + u_{o\theta} \sin \varphi \right] (u_{o\theta,\varphi\varphi})_{,d_j}
\end{aligned} \tag{4.B.24}$$

The mathematical expressions of the external force vector \mathbf{F}^E and its contribution to the stiffness matrix \mathbf{K}_Λ^F involve the derivatives of the displacement field vector \mathbf{u} with respect to d_j which can be fully obtained using Eqs.(4.B.1) to (4.B.5). While Eqs. (4.B.6) to (4.B.14) are required to obtain the derivatives of the gradient of the displacement field vector $\mathbf{u} \otimes \nabla^T$ with respect to d_j appearing in Eq. (4.14) in terms of the components $(u_{o\theta}, u_{o\varphi}, u_{or})$ of the displacement field vector

of a point on the mid-surface and their derivatives with respect to θ , φ , and d_j . Knowing Eq.(4.14) , the internal force vector \mathbf{F}^I and the tangent stiffness matrix \mathbf{K}_A^T can be obtained as well.

4.13 Appendix 4.C: Zero Energy Modes

This appendix presents a brief overview on zero energy modes, provides graphical representations of eigenvectors associated with the lowest eight eigenvalues of Finite Element M reported in Table 4. 1, and shows the strain field distributions induced by these eigenvectors.

Spurious zero energy modes

When a displacement mode corresponds to a zero eigenvalue and is associated with rigid body motion, it will have zero strains/strain energy. Conversely, spurious zero eigenvalues are associated with displacement modes which represent non-zero states of deformation and zero strains at all the integration points. These spurious modes often result from a low order of the numerical integration (e.g., reduced integration). Thus, increasing the order of the numerical integration (e.g., adopting full integration) can eliminate these spurious zero energy modes.

While rigid body motion modes uniformly generate zero strains over the element, spurious energy modes induce zero strains only at all the integration points but lead to non-zero strains elsewhere within the element. Therefore, rigid body modes can be distinguished from spurious energy modes by a graphical representation of eigenvectors associated with zero eigenvalues and examining the magnitudes of strain fields over the element domain. For more details, the reader is referred to Ref [31].

Illustrative example

In the following, the writer of the present dissertation provides a simple and well-known eigenvalue analysis for a truss element to give an insight on the rigid body displacements, rotations, and combined modes in order to facilitate the understanding of subsequent sections.

Fig. 4. C. 1a shows a 1D plane truss element with four degrees of freedom and its stiffness matrix is 4x4. Under the small deformation hypothesis, the linear eigenvalue analysis of the unconstrained (i.e., prior to enforcing restraining boundary conditions) stiffness matrix of the truss element possesses three zero eigenvalues which corresponds to two rigid body displacement modes and a single rigid body rotation mode as shown in Figures 4. C. 1 b-d, respectively. The normalized eigenvectors associated with these zero eigenvalues are $V_1 = \{0, 1/\sqrt{2}, 0, 1/\sqrt{2}\}$, $V_2 = \{1/\sqrt{2}, 0, 1/\sqrt{2}, 0\}$, and $V_3 = \{1/\sqrt{2}, 0, -1/\sqrt{2}, 0\}$. It can also be verified that any linear combination of these three eigenvectors will also be an eigenvector with a zero mode as shown in Fig. 4. C. 1e. The graphical representations of the magnified rigid body displacement modes (e.g., $5V_1$ in Fig. 4. C. 1b and $5V_2$ in Fig. 4. C. 1c) do not stretch while the graphical representations of the magnified rigid body rotation mode ($5V_3$ in Fig. 4. C. 1d) and the combined rigid body mode ($5V_1 + 5V_3$ in Fig. 4. C. 1e) seem to be stretched. Therefore, the graphical representations of the magnified rigid body rotation and combined modes may not provide an appropriate representation to distinguish between rigid body eigenvectors (corresponding to zero strain) and spurious zero energy modes under the small deformation hypothesis. Consequently, examining strain fields distributions over the element provides a better tool to distinguish between rigid body and spurious energy modes.

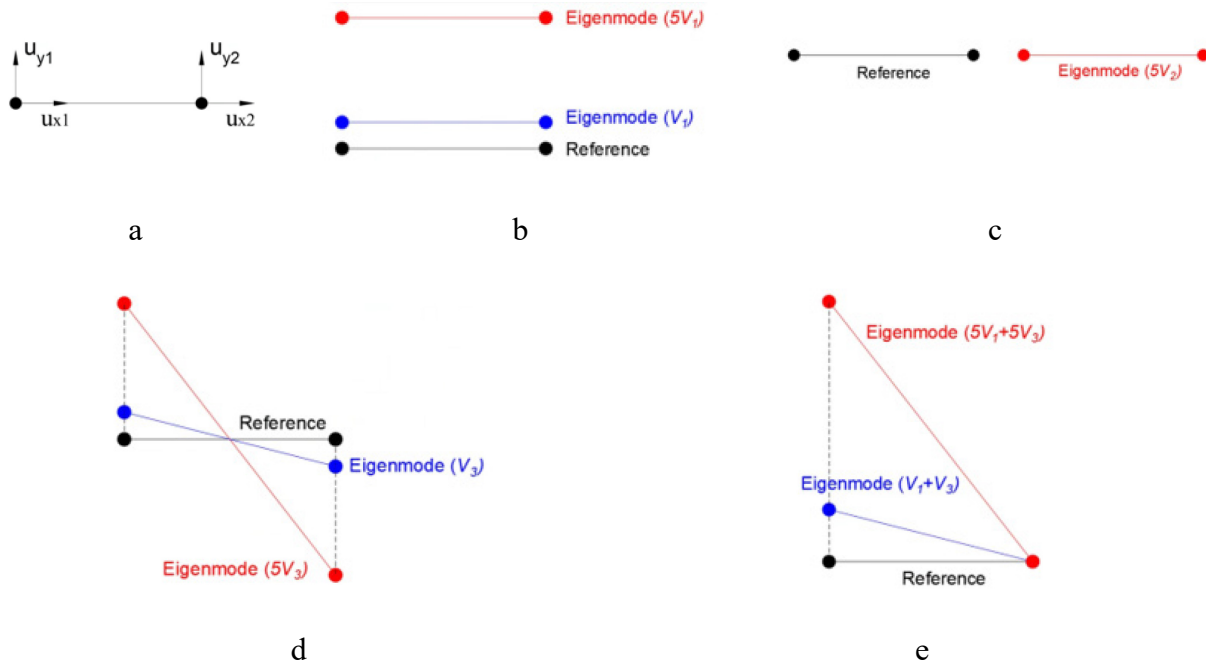


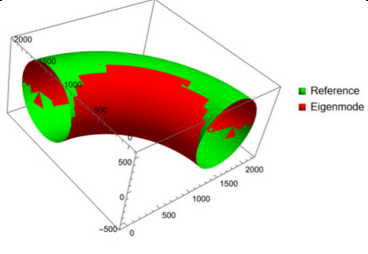
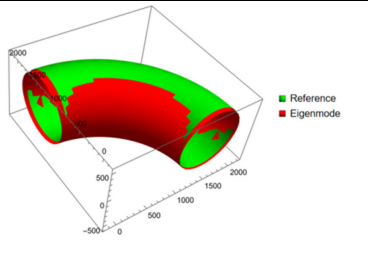
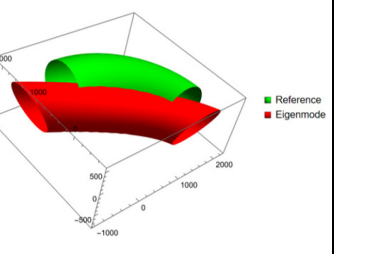
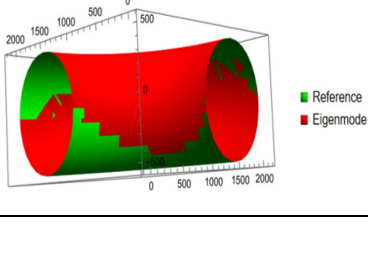
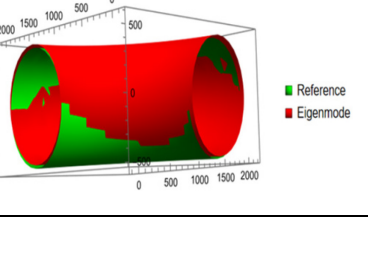
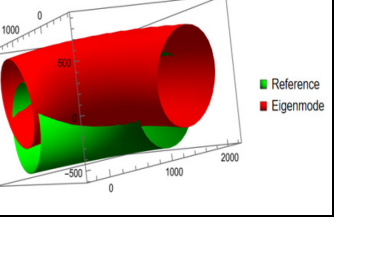
Fig. 4. C. 1 1D truss element and corresponding rigid body modes (i.e., eigenmodes) (a) Degrees of freedom of the truss element, (b) Vertical rigid body displacement mode, (c) Horizontal rigid body displacement mode, (d) Rigid body rotation mode, and (e) Combined rigid body mode.

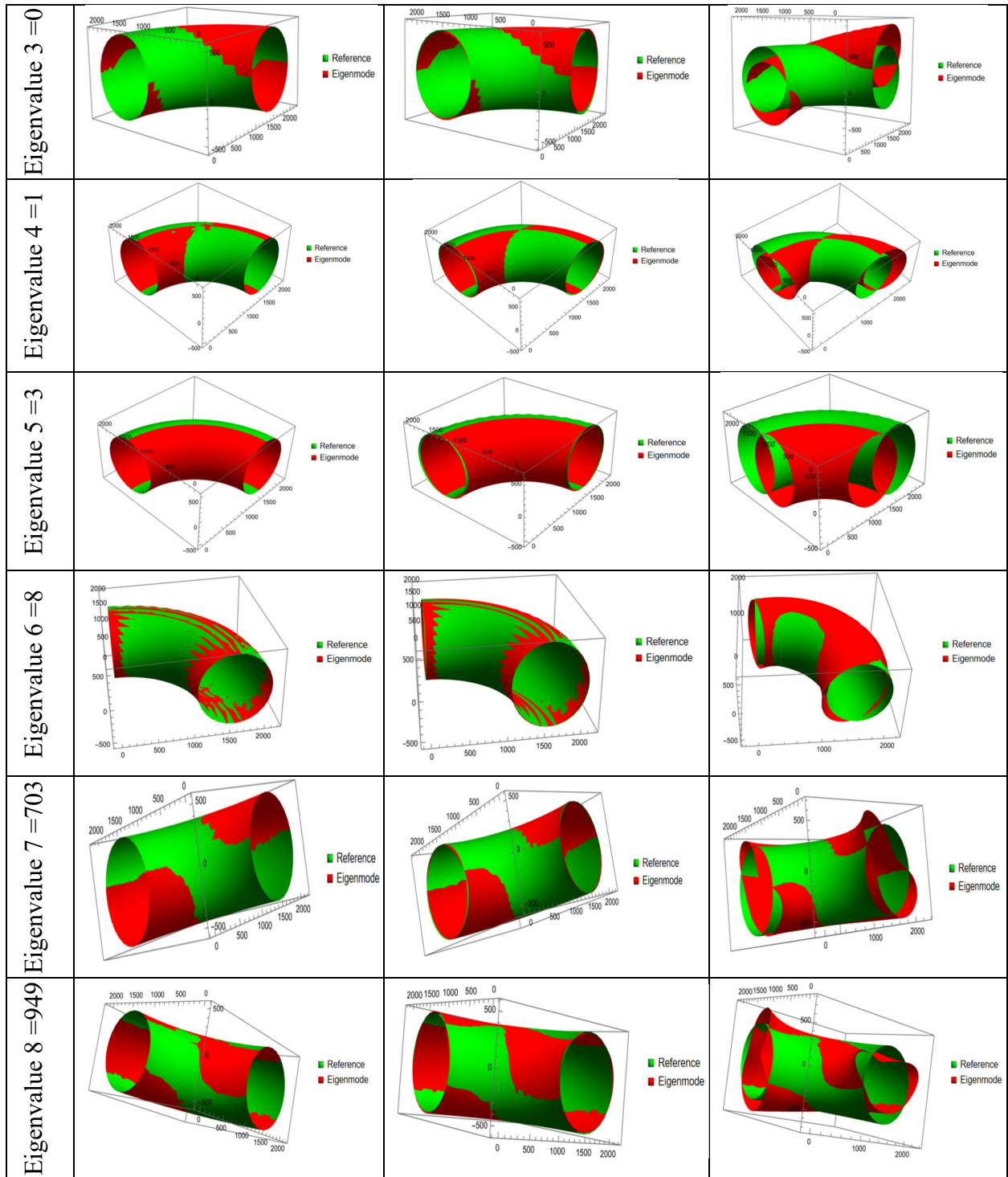
Graphical representation of eigenvectors and strain fields

The lowest eight eigenvalues (e.g., 0, 0, 0, 1, 3, 8, 703, and 949) reported in Table 4. 1 based on Element M are associated with the normalized eigenvectors V_i where $i = 1, 2, \dots, 8$. The graphical representation of these normalized eigenvectors and their magnified versions ($100V_i$ and $1000V_i$) are provided in Table 4. C. 1 (e.g., the second, third, and fourth columns, respectively) in an attempt to assess the physical nature of these eigenvectors; whether they represent rigid body modes or spurious energy modes. One can differentiate between the reference configuration and eigenmode of the pipe bend under consideration in the case of magnified eigenvector $1000V_i$ while such a differentiation cannot be easily noticed by comparing the graphics for cases (V_i and $100V_i$). Nevertheless, one cannot identify the physical nature of the eigenvectors from the graphical

representations provided in the fourth column since these representations seem to be stretched due to the magnification and/or the combination of eigenvectors associated with rigid body rotation as highlighted in the previous Illustrative example. Therefore, all strain field distributions (e.g., longitudinal, circumferential, and shear) corresponding to zero eigenvalues (i.e., Eigenvalues 1-3) are provided at the inner, middle, and outer pipe bend surfaces to identify the physical nature of the eigenvectors. Figures 4. C. 2-4 provide 2D contour plots for strain field distributions induced due to the magnified eigenvector $1000V_i$ and any point on the pipe bend surface is defined by the tangential angle θ on the vertical axis and the circumferential angle φ on the horizontal axis. Since the magnitudes of all strain field distributions corresponding to zero eigenvalues are almost zero at the three different surfaces, the associated eigenvectors are rigid body modes. Also, strain field distributions corresponding to Eigenvalues 4-6 (e.g., non-zero eigenvalues) are found to be very small. Therefore, the above analysis suggests that Element M is able to exactly represent three rigid body motion modes and to accommodate the remaining rigid body modes in an approximate sense.

Table 4. C. 1 Graphical representation of eigenmodes corresponds to the lowest eight eigenvalues obtained in Table 4. 1 using Element M

	V_i	$100V_i$	$1000V_i$
Eigenvalue 1 = 0			
Eigenvalue 2 = 0			



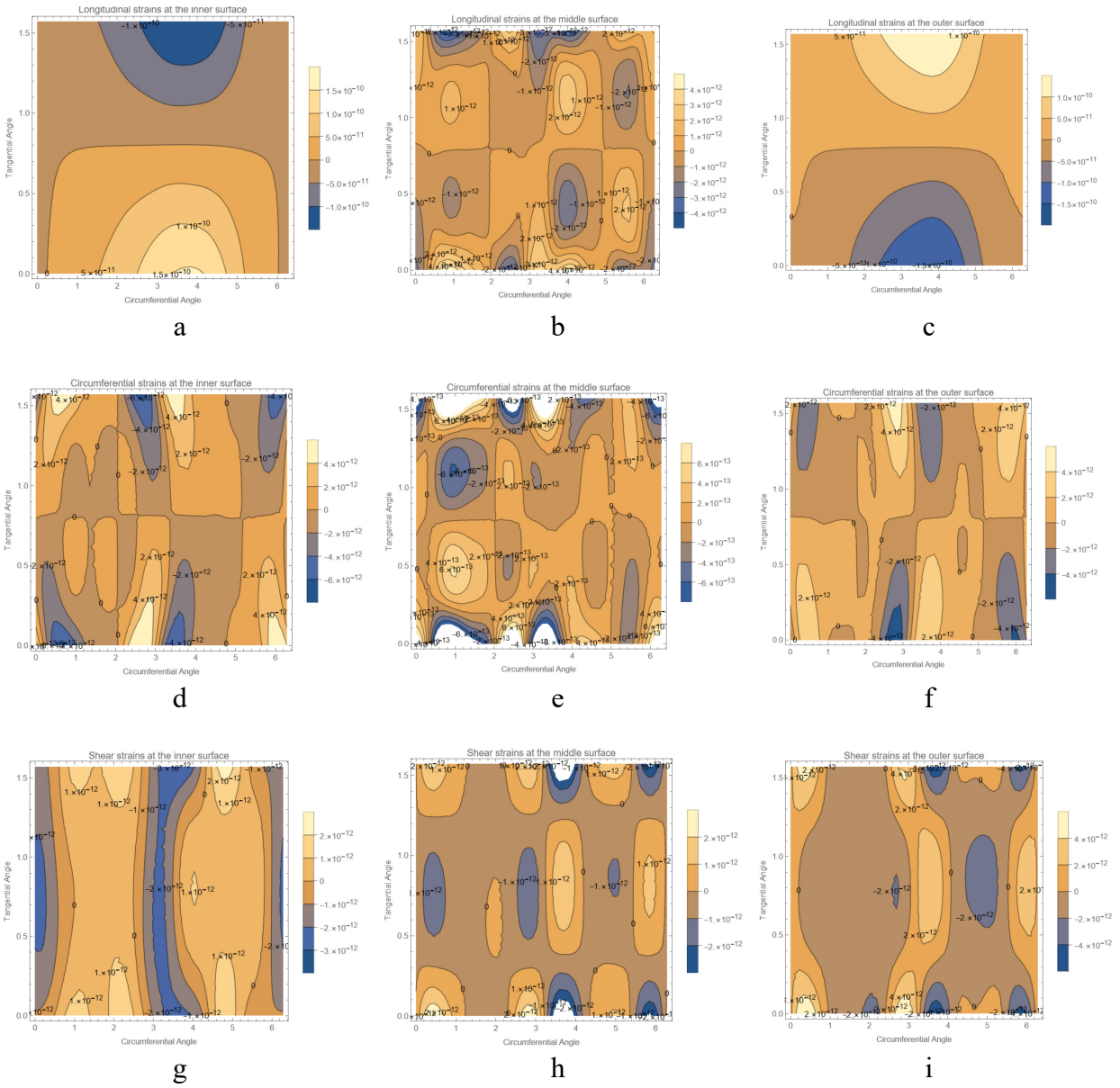


Fig. 4. C. 2 Strain field distributions over the element corresponding to the first zero eigenvalue induced by magnified eigenvector $1000V_i$ (a) Longitudinal - Inner Surface, (b) Longitudinal - Middle Surface, (c) Longitudinal -Outer Surface, (d) Circumferential - Inner Surface, (e) Circumferential -Middle Surface, (f) Circumferential -Outer Surface, (g) Shear - Inner Surface, (h) Shear -Middle Surface, and (i) Shear -Outer Surface

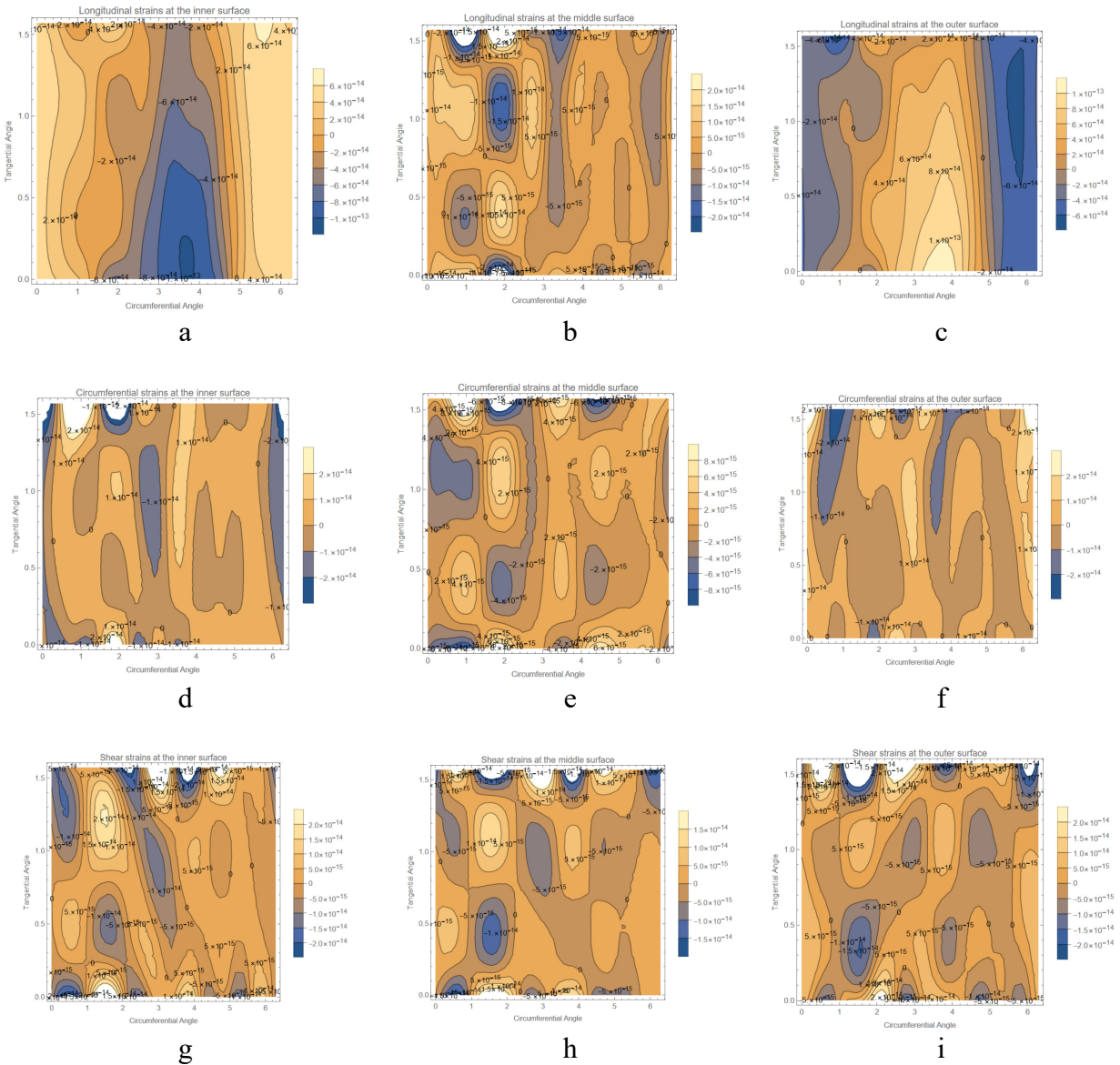


Fig. 4. C. 3 Strain field distributions over the element corresponding to the second zero eigenvalue induced by magnified eigenvector $1000V_i$ (a) Longitudinal - Inner Surface, (b) Longitudinal -Middle Surface, (c) Longitudinal -Outer Surface, (d) Circumferential - Inner Surface, (e) Circumferential -Middle Surface, (f) Circumferential -Outer Surface, (g) Shear - Inner Surface, (h) Shear -Middle Surface, and (i) Shear -Outer Surface

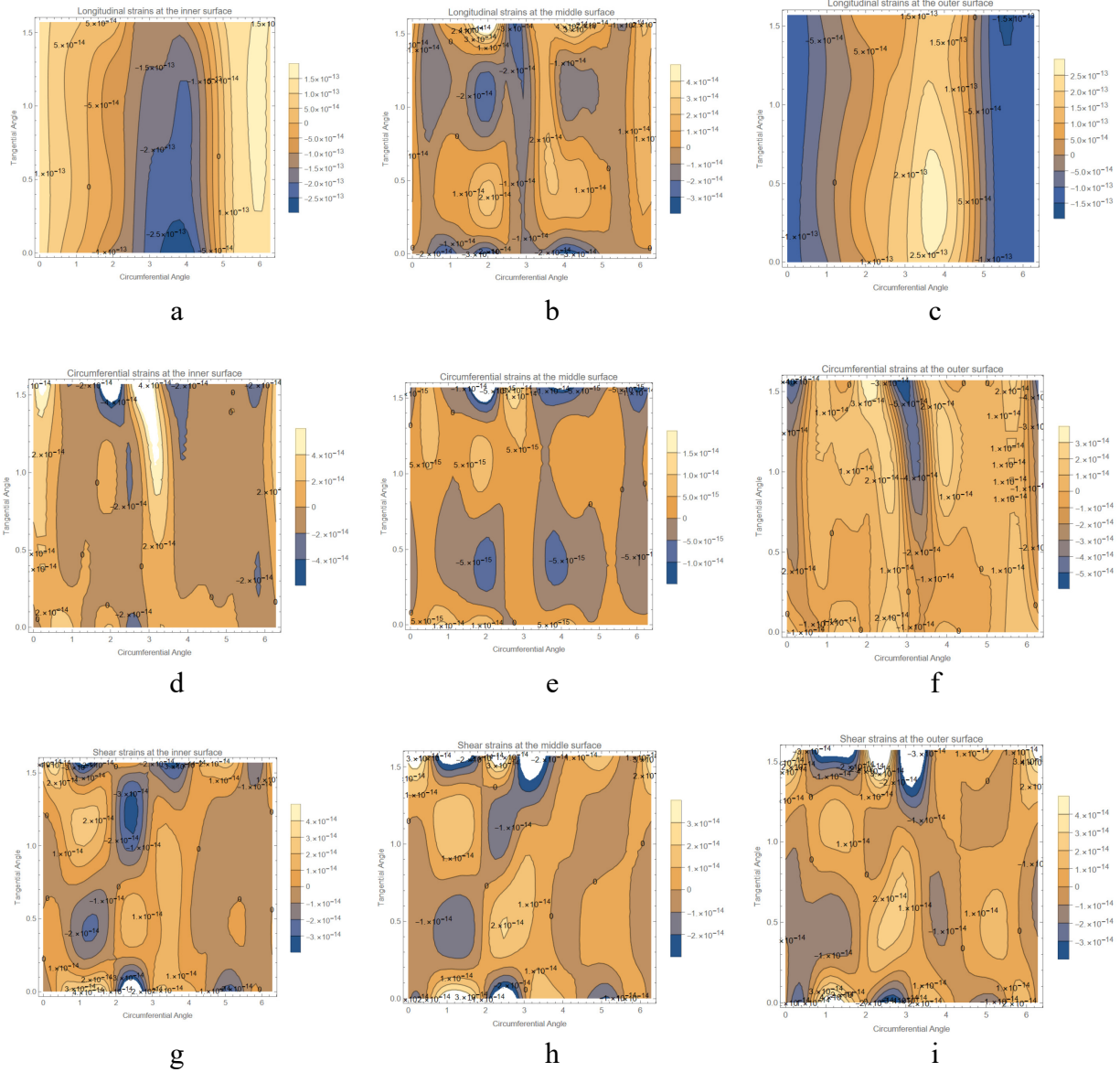


Fig. 4. C. 4 Strain field distributions over the element corresponding to the third zero eigenvalue induced by magnified eigenvector $1000V_i$ (a) Longitudinal - Inner Surface, (b) Longitudinal - Middle Surface, (c) Longitudinal -Outer Surface, (d) Circumferential - Inner Surface, (e) Circumferential -Middle Surface, (f) Circumferential -Outer Surface, (g) Shear - Inner Surface, (h) Shear -Middle Surface, and (i) Shear -Outer Surface

4.14 Nomenclature

$\tilde{\mathbf{B}}$	Body force vector per unit reference volume
\mathbf{d}	Vector of degrees of freedom
d_i, d_j	Components of degrees of freedom vector
$\bar{\mathbf{d}}$	Vector of virtual degrees of freedom
E	Young's Modulus
\mathbf{e}_r	Unit vector in the radial direction
\mathbf{e}_θ	Unit vector in the tangential direction
\mathbf{e}_φ	Unit vector in the circumferential direction
$\mathbf{F}^{(I)}$	Internal force vector
$\mathbf{F}^{(E)}$	External force vector
$\mathbf{H}(\theta)$	Interpolation functions in the tangential direction
h	Pipe wall thickness
\mathbf{K}	Stiffness matrix
\mathbf{K}^F	Exact contribution of the external force vector in the stiffness matrix
\mathbf{K}^T	Exact tangent stiffness matrix
\mathbf{K}_A^F	Approximated contribution of the external force vector in the stiffness matrix
\mathbf{K}_A^T	Approximated tangent stiffness matrix
\mathbf{L}	Vector of shape functions for Fourier series interpolation
L	Length of the element
m	Total Fourier terms /modes
\mathbf{N}	Vector normal to the mid-surface in the un-deformed configuration
$\hat{\mathbf{N}}$	Unit vector normal to the mid-surface in the un-deformed configuration
\mathbf{n}	Vector normal to the mid-surface in the deformed configuration
$\hat{\mathbf{n}}$	Unit vector normal to the mid-surface in the deformed configuration
n	Total number of the nodal degrees of freedom
n_1, n_2, n_3	Components of the normal vector \mathbf{n}

$\hat{n}_1, \hat{n}_2, \hat{n}_3$	Components of the normal unit vector $\hat{\mathbf{n}}$
\mathbf{P}	The first Piola-Kirchhoff stress tensor
\mathbf{R}	Residual force vector
\mathbf{R}_0	The position vector of a point on the mid-surface in the un-deformed configuration
\mathbf{r}_0	The position vector of a point on the mid-surface in the deformed configuration
r	Radial coordinate as measured from the origin point
r_m	Mid-surface radius
S_o	The original surface that encloses volume V_o
$\tilde{\mathbf{T}}_N$	Applied traction vector per unit reference surface dS_0 normal to the unit vector $\hat{\mathbf{N}}$
\mathbf{u}	Displacement vector for a generic point
$\bar{\mathbf{u}}$	Virtual displacement vector for a generic point
\mathbf{u}_0	Displacement vector for a point on the mid-surface
u_{or}	Radial displacement of a point on the mid-surface
$u_{o\theta}$	Tangential displacement of a point on the mid-surface
$u_{o\varphi}$	Circumferential displacement of a point on the mid-surface
u_r	Radial displacement
u_θ	Tangential displacement
u_φ	Circumferential displacement
V_o	The original volume
∇	The gradient operator with respect to the un-deformed configuration
ζ	Radial coordinate as measured from the mid-surface
ν	Poisson's ratio
θ	Tangential coordinate
φ	Circumferential coordinate

4.15 Acknowledgments

The authors express their gratitude to TC Energy, and Enbridge Pipelines Inc. for their technical assistance and discussions.

4.16 Funding

This research was partially funded by: NSERC, MITACS, Enbridge Pipelines Inc., and TC Energy.

4.17 References

- [1] Von Karman, T., 1911, "Ueber Die Formänderung Dünnwandiger Rohre, Insbesondere Federnder Ausgleichrohre," *Z. Ver. Deut. Ing.*, 55(Part2), pp.1889–1895.
- [2] Vigness, I., 1943, "Elastic Properties of Curved Tubes," *J. Appl. Mech.*, 55, pp.102–120.
- [3] Kafka, P. G., and Dunn, M. B., 1953, "Stiffness of Curved Circular Tubes with Internal Pressure," Boeing Airplane, Chicago, IL.
- [4] Wood, J. D., 1958, "The flexure of a uniformly pressurized circular, cylindrical shell" *J. Appl. Mech.*, 25, pp. 453-458.
- [5] Dodge, W. G., and Moore, S. E., 1972, "Stress Indices and Flexibility Factors for Moment Loadings on Elbows and Curved Pipes," *Welding Research Council Bulletin* 179.
- [6] Hong, S.-P., An, J.-H., Kim, Y.-J., Nikbin, K., and Budden, P. J., 2011, "Approximate Elastic Stress Estimates for Elbow Under Internal Pressure," *Int. J. Mech. Sci.*, 53(7), pp. 526–535.
- [7] WeiB, E., Lietzmann, A., and Rudolph, J., 1996 "Linear and Nonlinear Finite-Element Analysis of Pipe Bends," *Int. J. Pres. Ves. & Piping.*, 67, pp. 211-217.
- [8] Abdulhamed, D., Adeeb, S., Cheng, R., and Martens, M., 2016, "The Influence of the Bourdon Effect on Pipe Elbow," *ASME Paper No. IPC2016-64659*.
- [9] Abdulhamed, D., 2017 "The Behavior of Pipe Bends under Internal Pressure and In-Plane Bending Loading," *Doctoral dissertation, University of Alberta, Edmonton, Canada*.
- [10] Ohtsubo, H., and Watanabe, O., 1978, "Stress Analysis of Pipe Bends by Ring Elements," *ASME J. Pressure Vessel Technol.*, 100(1), pp. 112–122.
- [11] Bathe, K. J., and Almeida, C. A., 1980, "A Simple and Effective Pipe Elbow Element, Linear Analysis," *J. Appl. Mech.*, 47(1), pp. 100–193.
- [12] Bathe, K. J., and Almeida, C. A., 1982, "A Simple and Effective Pipe Elbow Element, Pressure Stiffening Effects," *J. Appl. Mech.*, 49(4), pp. 914–915.
- [13] Bathe, K. J., and Almeida, C. A., 1982, "A Simple and Effective Pipe Elbow Element, Interaction Effects," *J. Appl. Mech.*, 49, pp. 165–171.
- [14] Militello, C., and Huespe, A. E., 1988, "A Displacement- Based Pipe Elbow Element," *Comput. Struct.*, 29(2), pp. 339–343.

- [15] Fonseca, E. M. M., de Melo, F. J. M. Q., Oliveira, C. A. M., 2006, "Numerical analysis of piping elbow for in-plane bending and internal pressure," *Thin-Walled Struct.*, 44, pp.393-398.
- [16] Basaran, S., 2008, "Lagrangian and Eulerian Descriptions in Solid Mechanics and Their Numerical Solutions in hpk Framework," Doctoral dissertation, The University of Kansas, Kansas, United states.
- [17] Holzapfel, G. A., 2000, "Nonlinear Solid Mechanics: A Continuum Approach for Engineering," Chichester: Wiley.
- [18] Bonet, J., and Wood, R., 2008, "Nonlinear Continuum Mechanics for Finite Element Analysis," Cambridge: Cambridge University Press. doi:10.1017/CBO9780511755446
- [19] Bathe, K. J., 1996, "Finite Element Procedures in Engineering analysis," Prentice Hall, New Jersey.
- [20] Simulia ABAQUS. 2017. User's Manual version 6.6 documentation
- [21] ADINA R& D, Inc. 2012. Theory and Modeling Guide Volume I
- [22] ANSYS, Inc. ELBOW290, Retrieved from https://www.mm.bme.hu/~gyebro/files/ans_help_v182/ans_elem/Hlp_E_ELBOW290.htm
- [23] Li, T., 2016, "On the formulation of a pipe element for a pipe structure with variable wall thickness," *Ocean Eng.* 117, 398–410.
- [24] Li, T., 2017, "On the formulation of a pipe element II: An orthogonal polynomial pipe element," *Ocean Eng.* 129, 279–290.
- [25] Li, T., 2017, "On the formulation of a 3D smooth curved pipe finite element with arbitrary variable cross-section," *Thin-Walled Structures.* 117, 314–331.
- [26] Duan, L., Zhao, J., 2019, "A geometrically exact cross-section deformable thin-walled beam finite element based on generalized beam theory," *Comput. Struct.*, 218, pp.32-59.
- [27] Meroueh, K. A., 1986, "On a Formulation of a Nonlinear Theory of Plates and Shells with Applications," *Comput. Struct.*, 24(5), pp. 691-705.
- [28] Campello, E. M. B., Pimenta, P. M., Wriggers, P., 2003, "A triangular finite shell element based on a fully nonlinear shell formulation," *Computational Mechanics*, 31, pp. 505-518.
- [29] Ivannikov, V., Tiago, C., Pimenta, P. M., 2014, "On the boundary conditions of the geometrically nonlinear Kirchhoff-Love shell theory," *Int. J. Solids Struct.*, 51, pp. 3101-3112.
- [30] Dawe, D. J., 1972, "Rigid-body motions and strain-displacement equations of curved shell finite elements," *Int. J. Mech. Sci.*, 14, pp 569-578
- [31] Retrieved from http://www.visualfea.com/manual-cbt/chapter/05_02chap.htm

Chapter 5

Shell Finite Element Formulation of Ovalized Thin-Walled Pipes

5.1 Abstract

Non-traditional shell finite element formulations are developed to accurately predict the geometrically nonlinear structural response of ovalized straight and curved pipes. To consider initial geometric imperfections of an imperfect pipe, three configurations are considered within the proposed formulations. Kinematic assumptions of the Love-Kirchhoff thin shell theory are adopted and elastic material characterization follows the Saint-Venant-Kirchhoff constitutive model. To account for geometric nonlinearity, total Lagrangian approach is employed within the framework of the virtual work principle expressed in terms of the first Piola-Kirchhoff stress tensor. Several examples demonstrate the accuracy and superiority of the present formulations by comparisons against the general shell models under various loading conditions.

Keywords

Ovalized pipes, Geometrically nonlinear finite element, First Piola-Kirchhoff stress tensor, Virtual work principle, Initial ovality, Geometric imperfections.

5.2 Introduction

Several engineering fields (oil and gas, Petro-chemicals, water supply, bio-mechanical application, etc.) depend on pipeline transmission systems for conveying fluids to their required destinations.

The design of these systems essentially requires efficient structural analyses to achieve an optimal level of integrity and performance. Although beam theories with rigid cross sections are intensively used to analyze 1D structures, the complex deformation patterns of piping systems cannot be accurately captured by these theories due to ovalization and warping effects associated with the flexibility of hollow cross-sections. The review of the literature focuses on three relevant aspects in the following subsections: (1) pipe finite element solutions, (2) principle of virtual work for nonlinear solutions, and (3) influence of initial ovality on pipe response.

5.2.1 Pipe finite element solutions

Analytical studies [1-5] were developed to predict the structural response of piping systems. However, such methods are not amenable to modelling complex geometries in piping systems and considering nonlinear effects. Therefore, numerical solutions (e.g., Finite Element Analysis) have become imperative in such applications. Solid [6-7] and conventional shell [8-9] finite element (FE) formulations can accurately predict the linear and nonlinear structural response of piping systems under general loading/boundary conditions. However, the rather high computational cost and significant effort in building and post-processing the pipeline models make their usage limited in practical design environments, particularly when modelling long lines of pipes. An efficient and computationally effective FE formulation is hence required to achieve a balance between the accuracy of the solution and the associated computational cost and modelling effort [10-17].

Over the last few decades, FE formulations especially tailored for pipes were developed for the structural analysis of piping systems in the linearly elastic regime. This includes the work of Weicker et al [10-11] who developed a FE formulation for straight pipes based on the thin shell

theory and shape functions were obtained by solving the equilibrium equations. Ohtsubo and Watanabe [12] developed a toroidal shell FE formulation for curved pipes (e.g., pipe bends) based on the thin shell theory assumptions by characterizing the displacement fields using Fourier series along the circumferential direction and cubic Hermitian function along the longitudinal direction. The approximate representation of rigid body motion was reported as drawback in [13]. Bathe and Almeida [13] proposed a simple FE formulation, which combined traditional beam deformation modes described by cubic polynomial functions with cross-sectional deformation modes characterized by Fourier series expansions in the circumferential coordinate. Pressure stiffening [14] and interaction effects [15] were captured enhancing the element's capabilities while the warping displacements were ignored. Militello and Huespe [16] characterized the longitudinal displacement fields by using Fourier series to capture warping displacements omitted in [13]. Fonseca et al [17] utilized higher polynomial or trigonometric functions to characterize the distribution of displacement fields along the longitudinal direction and Fourier series to characterize the distribution of displacement fields in the circumferential direction. This formulation was limited to the in-plane loading and internal pressure.

5.2.2 Principle of virtual work for nonlinear solutions

The principle of virtual work within the Lagrangian description is intensively adopted in solid mechanics to construct nonlinear FE formulations [18]. The internal virtual work can be formulated in terms of various energetic conjugate pairs [19-20]. The most common energetic conjugate pair used in the Lagrangian description is the second Piola-Kirchhoff stress tensor and the Green-Lagrange strain tensor. Based on this energetic conjugate pair, Ref [21] introduced an incremental approach to develop nonlinear FE formulations. In addition, fully geometric nonlinear

FE formulations were developed for beams (e.g., [22]) and shells (e.g., [23]) within the framework of the Carrera Unified Formulation (CUF). However, the treatment of follower effect of pressure was not captured in [22-23]. Most commercial FE software packages (e.g., ANSYS [24], ABAQUS [25], ADINA [26]) adopt the same energetic conjugate pair to construct nonlinear FE formulations (e.g., ELBOW elements) for the analysis of straight and curved pipes. On other hand, the first Piola-Kirchhoff stress tensor and the gradient of virtual displacement fields can be used as alternative energetic conjugate pair of the internal virtual work. Attia et al. [27-28] adopted this energetic conjugate pair and proposed a family of geometrically nonlinear FE formulations for the structural analysis of circular straight and curved pipes. The developed elements for modelling pipes assume the cross section to be initially circular, which implies that no initial geometric imperfections produced due to the manufacturing process can be modelled. This limitation will be further addressed in this paper.

5.2.3 Influence of initial ovality on the pipe response

Many FE solutions, based either on conventional shell or solid elements, studied the effect of initial geometric imperfections on the response of straight and curved pipes under various loading conditions. Initial ovality, as one type of initial geometric imperfections, is known to have a significant influence on the collapse pressure of straight pipelines laid in ultra-deep water and subjected to high external pressure [29-30]. A dramatic reduction in the collapse pressure was reported when increasing the initial ovality and outer diameter-thickness ratio (D/t). For example, the collapse pressure decreased by more than 50% for a pipe with $D/t=30$ and a 5% initial ovality subjected only to external pressure [29]. However, the effect of initial ovality on the collapse pressure is negligible in cases involving a combination of bending and external pressure since the

ovality induced by bending action (Brazier effect) is typically higher than the initial ovality [30]. Research on the effect of initial geometric imperfections on pipe bends subjected to in-plane bending, pressure (internal or external), and temperature [31-37] showed that initial ovality is the most significant type of geometric imperfections in the analysis of pipe bends. Under external pressure [37], small ovality percentages (e.g., 1% and 2 %) were reported to tangibly decrease the collapse pressure while collapse loads for the other loading cases [31-36] were notably affected by higher levels of initial ovality.

Li [38-40] recently adopted the incremental approach in [21] to develop three-dimensional FE formulations for the analysis of straight and curved pipes with generic cross section. The current study proposes novel and simple shell FE formulations for the geometrically nonlinear analysis of straight and curved pipes with cross sections involving initial cross-sectional imperfection patterns. Treatment of nonlinear equilibrium equations follows the approach introduced in [27-28]. Four different aspects can be noticed between the current formulations and those developed in [38-40]:

- 1- Energetic conjugate pair of the internal virtual work and the linearization technique of the nonlinear equations;
- 2- Type of formulations (e.g., shell vs three dimensional);
- 3- The approach adopted to model the general geometry of the cross-section; and
- 4- Mathematical treatment of follower pressure loads.

Although a general cross section is assumed in the present study, Section 5.8 Numerical Examples are focused on the analysis of initially ovalized straight and curved pipes since the literature review demonstrates that initial ovality is the most significant geometric imperfection.

5.3 Assumptions

The following assumptions are made within the present FE formulation:

1. Pipe material is characterized by the Saint-Venant-Kirchhoff constitutive model;
2. The pipe cross section is assumed to be generic;
3. The thin shell theory kinematic assumptions are employed, i.e.,
 - I. Straight lines normal to the un-deformed mid-surface of the shell remain straight and normal to the mid-surface of the deformed configuration.
 - II. The thickness of the shell remains constant throughout deformation.
4. In the radial direction, the normal stress component is assumed to be zero;
5. The formulation captures the follower effects of the pressure; and
6. The initial configuration is assumed to be stress-free configuration (i.e., no residual stresses are considered ²²)

5.4 Preliminaries

5.4.1 Geometry

Fig. 5. 1 depicts the cross section of a pipe (either straight or curved) in three configurations: an initial (un-deformed) Ω^i , and deformed Ω^d . Since the initial configuration Ω^i of the cross section is considered to have a general geometry that accounts for initial geometric imperfections, a third configuration (reference) Ω^r is introduced that has perfectly circular cross-section with uniform

²² The influence of residual stresses can be included by deriving constitutive equations which characterize the mechanical behavior of elastic residually stressed pipes. A virtual stress-free configuration needs to be assumed to derive these constitutive equations given the residual stresses and material properties of the assumed stress-free configuration. For more details, the reader is referred to Ref [41].

wall thickness. A point P (Fig. 5. 1) can be described by position vectors \mathbf{X}^r , \mathbf{X}^i , and \mathbf{X}^d in the reference, initial, and deformed configurations, respectively.

5.4.2 Notation

The following notation will be used:

- 1) Symbols of the form $\mathbf{A}_{(a,b)}$ denote two-point second order tensors (e.g., deformation gradient tensor) that transforms a quantity (e.g., tangential vector or area vector) from configuration a to configuration b .
- 2) Symbols of the form $\mathbf{B}_{(a)}$ denote second order tensors (e.g., Green-Lagrange strain tensor) defined in the configuration a .
- 3) Symbols of the form $\mathbf{u}_{(a,b)}$ denote the displacement vector describing the motion of a point from configuration a to configuration b .

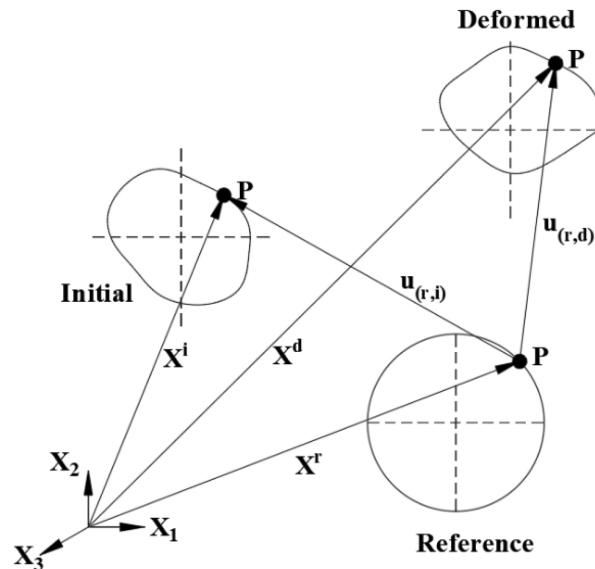


Fig. 5. 1 Cross section of a pipe in three configurations

5.5 Formulation

5.5.1 Deformation gradient tensors

The deformation gradient tensor $\mathbf{F}_{(r,d)}$ relates a tangential vector $d\mathbf{X}^r$ in the reference configuration to the vector $d\mathbf{X}^d$ in the deformed configuration, i.e.,

$$d\mathbf{X}^d = \mathbf{F}_{(r,d)} d\mathbf{X}^r \quad (5.1)$$

Similarly, one obtains

$$d\mathbf{X}^i = \mathbf{F}_{(r,i)} d\mathbf{X}^r \quad (5.2)$$

$$d\mathbf{X}^d = \mathbf{F}_{(i,d)} d\mathbf{X}^i \quad (5.3)$$

From Eqs.(5.1) and (5.2), by substituting into Eq.(5.3), one obtains the relationship between the deformation gradient tensors

$$\mathbf{F}_{(i,d)} = \mathbf{F}_{(r,d)} \mathbf{F}_{(r,i)}^{-1} \quad (5.4)$$

The determinants of the above tensors satisfy the equality

$$\det \mathbf{F}_{(i,d)} = \det \mathbf{F}_{(r,d)} \det \mathbf{F}_{(r,i)}^{-1} = \det \mathbf{F}_{(r,d)} / \det \mathbf{F}_{(r,i)} \quad (5.5)$$

5.5.2 Strain and stress tensors expressed in the initial configuration

In the present formulation, the “geometrically imperfect” pipe under consideration is assumed to occupy the initial (un-deformed) configuration. The deformed configuration, on the other hand, represents the “geometrically imperfect” pipe under external loading. The Green-Lagrange strain tensor $\mathbf{E}_{(i)}$ induced by loading referenced to the initial configuration is

$$\mathbf{E}_{(i)} = 0.5 \left[\mathbf{F}_{(i,d)}^T \mathbf{F}_{(i,d)} - \mathbf{I} \right] \quad (5.6)$$

where $\mathbf{F}_{(i,d)}^T$ denotes the transpose of the deformation gradient tensor $\mathbf{F}_{(i,d)}$, and \mathbf{I} is the identity tensor. The present formulation adopts the Saint-Venant-Kirchhoff constitutive tensor \mathbf{C} (Assumption 1, see Section 5.3) to relate the second Piola-Kirchhoff stress tensor $\mathbf{S}_{(i)}$ to the Green-Lagrange strain tensor given in Eq.(5.6), i.e.,

$$\mathbf{S}_{(i)} = \mathbf{C} : \mathbf{E}_{(i)} = 0.5 \left[\mathbf{C} : \left(\mathbf{F}_{(i,d)}^T \mathbf{F}_{(i,d)} - \mathbf{I} \right) \right] \quad (5.7)$$

The corresponding first Piola-Kirchhoff stress tensor $\mathbf{P}_{(i,d)}$ can be obtained from

$$\mathbf{P}_{(i,d)} = \mathbf{F}_{(i,d)} \mathbf{S}_{(i)} = 0.5 \mathbf{F}_{(i,d)} \left[\mathbf{C} : \left(\mathbf{F}_{(i,d)}^T \mathbf{F}_{(i,d)} - \mathbf{I} \right) \right] \quad (5.8)$$

From Eq.(5.4), by substituting into Eq.(5.8), one obtains

$$\mathbf{P}_{(i,d)} = 0.5 \mathbf{F}_{(r,d)} \mathbf{F}_{(r,i)}^{-1} \left[\mathbf{C} : \left(\mathbf{F}_{(r,i)}^{-T} \mathbf{F}_{(r,d)}^T \mathbf{F}_{(r,d)} \mathbf{F}_{(r,i)}^{-1} - \mathbf{I} \right) \right] \quad (5.9)$$

5.5.3 First Piola-Kirchhoff stress tensor in terms of deformation gradient tensors

The first Piola-Kirchhoff stress tensors $\mathbf{P}_{(r,d)}$ and $\mathbf{P}_{(i,d)}$ can be expressed in terms of the Cauchy stress tensor $\boldsymbol{\sigma}$ by

$$\mathbf{P}_{(r,d)} = \det \mathbf{F}_{(r,d)} \boldsymbol{\sigma}^T \mathbf{F}_{(r,d)}^{-T} \quad (5.10)$$

$$\mathbf{P}_{(i,d)} = \det \mathbf{F}_{(i,d)} \boldsymbol{\sigma}^T \mathbf{F}_{(i,d)}^{-T} \quad (5.11)$$

From Eqs. (5.10) and (5.11), one obtains

$$\mathbf{P}_{(r,d)} = \left[\frac{\det \mathbf{F}_{(r,d)}}{\det \mathbf{F}_{(i,d)}} \right] \mathbf{P}_{(i,d)} \mathbf{F}_{(i,d)}^T \mathbf{F}_{(r,d)}^{-T} \quad (5.12)$$

From Eqs.(5.4), (5.5), and (5.9), by substituting into Eq.(5.12), one obtains the first Piola-Kirchhoff stress tensor $\mathbf{P}_{(r,d)}$ in terms of the deformation gradient tensors $\mathbf{F}_{(r,d)}$ and $\mathbf{F}_{(r,i)}$ as

$$\mathbf{P}_{(r,d)} = 0.5 \det \mathbf{F}_{(r,i)} \mathbf{F}_{(r,d)} \mathbf{F}_{(r,i)}^{-1} \left[\mathbf{C} : \left(\mathbf{F}_{(r,i)}^{-T} \mathbf{F}_{(r,d)}^T \mathbf{F}_{(r,d)} \mathbf{F}_{(r,i)}^{-1} - \mathbf{I} \right) \right] \mathbf{F}_{(r,i)}^{-T} \quad (5.13)$$

5.5.4 Principle of virtual work

Owing to the simplicity of the chosen reference configuration, it is expedient to express the principle of virtual work in the reference configuration as opposed to the more complex initial configuration, i.e.,

$$\int_{V^r} \mathbf{P}_{(r,d)} : \mathbf{G}_{(r,d)}^* dV^r = \int_{S^r} \left[\tilde{\mathbf{T}}_{\mathbf{N}} \cdot \mathbf{u}_{(r,d)}^* \right] dS^r + \int_{V^r} \left[\tilde{\mathbf{B}} \cdot \mathbf{u}_{(r,d)}^* \right] dV^r \quad (5.14)$$

in which S^r is the reference surface area that encloses the reference volume V^r and the left-hand side of Eq.(5.14) represents the internal virtual work obtained by the inner product of the first Piola-Kirchhoff stress tensor $\mathbf{P}_{(r,d)}$ provided in Eq.(5.13) and the gradient of the virtual displacement vector $\mathbf{G}_{(r,d)}^*$. The right-hand side of Eq.(5.14) represents the external virtual work due to the applied traction vector $\tilde{\mathbf{T}}_{\mathbf{N}}$ and the body force vector $\tilde{\mathbf{B}}$, both defined in the reference configuration. The virtual displacement vector $\mathbf{u}_{(r,d)}^*$ is taken as a linear function of the virtual nodal degrees of freedom \mathbf{d}^* , i.e., $\mathbf{u}_{(r,d)}^* = \left[\partial \mathbf{u}_{(r,d)} / \partial \mathbf{d} \right] \mathbf{d}^*$, and one recalls that $\mathbf{u}_{(r,d)}$ is the displacement vector between reference and deformed configurations, and \mathbf{d} is the nodal degrees of freedom vector.

5.6 Force vectors and stiffness matrix

This section briefly discusses the force vectors and the stiffness matrix obtained from the principle of virtual work. More details can be found under Sections 3.4 and 3.5 in Chapter 3. By differentiating Eq.(5.14) with respect to the virtual nodal degrees of freedom vector \mathbf{d}^* , one recovers the equilibrium equations

$$\begin{aligned} \mathbf{F}^{(I)}(\mathbf{d}) - \mathbf{F}^{(E)}(\mathbf{d}) &= \mathbf{0} \\ \mathbf{F}^{(I)}(\mathbf{d}) &= \int_{V^r} \mathbf{P}_{(r,d)} : \left[\partial \mathbf{G}_{(r,d)}^* / \partial \mathbf{d}^* \right] dV^r = \int_{V^r} \mathbf{P}_{(r,d)} : \left[\partial \mathbf{G}_{(r,d)} / \partial \mathbf{d} \right] dV^r \\ \mathbf{F}^{(E)}(\mathbf{d}) &= \int_{S^r} \left[\left(\partial \mathbf{u}_{(r,d)} / \partial \mathbf{d} \right)^T \tilde{\mathbf{T}}_N \right] dS^r + \int_{V^r} \left[\left(\partial \mathbf{u}_{(r,d)} / \partial \mathbf{d} \right)^T \tilde{\mathbf{B}} \right] dV^r \end{aligned} \quad (5.15)\text{a-c}$$

in which $\mathbf{F}^{(I)}(\mathbf{d})$ is the internal force vector and $\mathbf{F}^{(E)}(\mathbf{d})$ is the external force vector. The equilibrium equations (Eq.(5.15)) are linearized through a Taylor series expansion and solved iteratively for the nodal displacement vector \mathbf{d} yielding

$$\left[\mathbf{F}^{(I)} - \mathbf{F}^{(E)} \right]_{\mathbf{d}=\mathbf{d}_g} + \left[\mathbf{K}^T - \mathbf{K}^F \right]_{\mathbf{d}=\mathbf{d}_g} (\mathbf{d} - \mathbf{d}_g) = \mathbf{0} \quad (5.16)$$

in which \mathbf{K}^T is the tangent stiffness matrix and \mathbf{K}^F represents the contribution of the external force vector to the stiffness matrix at a given nodal degrees of freedom vector \mathbf{d}_g and are respectively obtained by differentiating the internal and external force vectors with respect to \mathbf{d} . The formulation adopts the following approximations for the stiffness matrix, i.e.,

$$\begin{aligned} \mathbf{K}^T &\approx \mathbf{K}_A^T = \int_{V^r} \left[\partial \mathbf{P}_{(r,d)} / \partial \mathbf{d} \right] : \left[\partial \mathbf{G}_{(r,d)} / \partial \mathbf{d} \right] dV^r \\ \mathbf{K}^F &\approx \mathbf{K}_A^F = \int_{S^r} \left(\partial \mathbf{u}_{(r,d)} / \partial \mathbf{d} \right)^T \left[\partial \tilde{\mathbf{T}}_N / \partial \mathbf{d} \right] dS^r + \int_{V^r} \left(\partial \mathbf{u}_{(r,d)} / \partial \mathbf{d} \right)^T \left[\partial \tilde{\mathbf{B}} / \partial \mathbf{d} \right] dV^r \end{aligned} \quad (5.17)\text{a-b}$$

The derivative of the first Piola-Kirchhoff stress tensor $\mathbf{P}_{(r,d)}$ with respect to \mathbf{d} appearing in Eq.(5.17) is obtained by taking the derivative of Eq.(5.13) yielding

$$\begin{aligned}
& \partial \mathbf{P}_{(r,d)} / \partial d_j = \\
& 0.5 \det \mathbf{F}_{(r,i)} \left(\partial \mathbf{F}_{(r,d)} / \partial d_j \right) \mathbf{F}_{(r,i)}^{-1} \left[\mathbf{C} : \left(\mathbf{F}_{(r,i)}^{-T} \mathbf{F}_{(r,d)}^T \mathbf{F}_{(r,d)} \mathbf{F}_{(r,i)}^{-1} - \mathbf{I} \right) \right] \mathbf{F}_{(r,i)}^{-T} \\
& + 0.5 \det \mathbf{F}_{(r,i)} \mathbf{F}_{(r,d)} \mathbf{F}_{(r,i)}^{-1} \left\{ \mathbf{C} : \left[\mathbf{F}_{(r,i)}^{-T} \left(\partial \mathbf{F}_{(r,d)}^T / \partial d_j \right) \mathbf{F}_{(r,d)} \mathbf{F}_{(r,i)}^{-1} + \mathbf{F}_{(r,i)}^{-T} \mathbf{F}_{(r,d)}^T \left(\partial \mathbf{F}_{(r,d)} / \partial d_j \right) \mathbf{F}_{(r,i)}^{-1} \right] \right\} \mathbf{F}_{(r,i)}^{-T}
\end{aligned} \tag{5.18}$$

where d_j ($j=1,2,\dots,n$) is the j^{th} component of the nodal degrees of freedom vector. The deformation gradient tensors $\mathbf{F}_{(\dots)}$ are related to the corresponding gradients of the displacement vectors $\mathbf{G}_{(\dots)}$ through

$$\begin{aligned}
\mathbf{F}_{(r,d)} &= \mathbf{G}_{(r,d)} + \mathbf{I} & , & \quad \partial \mathbf{F}_{(r,d)} / \partial d_j = \partial \mathbf{G}_{(r,d)} / \partial d_j \\
\mathbf{F}_{(r,i)} &= \mathbf{G}_{(r,i)} + \mathbf{I} & , & \quad \partial \mathbf{F}_{(r,i)} / \partial d_j = \partial \mathbf{G}_{(r,i)} / \partial d_j
\end{aligned} \tag{5.19a-b}$$

From Eqs.(5.15), (5.17), (5.18), and (5.19), the internal force vector (Eq.(5.15)) and the approximated tangent stiffness matrix (Eq.(5.17)) are obtained in terms of the gradients of the displacement vectors ($\mathbf{G}_{(r,d)}$ and $\mathbf{G}_{(r,i)}$) and their derivatives with respect to d_j . The external force vector (Eq.(5.15)) and its contribution in the stiffness matrix (Eq.(5.17)) involve the displacement vector $\mathbf{u}_{(r,d)}$ and its derivative with respect to d_j .

5.7 Displacement fields

5.7.1 Straight Pipes

5.7.1.1 Reference configuration r / Configuration b (e.g., deformed or initial configuration)

The position vector of a point on the pipe (Fig. 5. 2) in the reference configuration is characterized by three coordinate lines z , φ , and r along the longitudinal, circumferential, and radial directions $\{\mathbf{e}_z, \mathbf{e}_\varphi, \mathbf{e}_r\}$. The pipe has a mid-surface radius r_m with $r(\zeta) = r_m + \zeta$ where ζ is a radial

coordinate defined from the mid-surface pointing outward and bounded by $\zeta \in [-h/2, h/2]$ in which h is the wall thickness in the reference configuration . The displacement vector $\mathbf{u}_{(r,b)}$ that relates a point in the reference configuration to a point in Configuration b is obtained by adopting the kinematic constraint of Love-Kirchhoff thin shell theory (Assumption 3, see Section 5.3) as

$$\mathbf{u}_{(r,b)} = \mathbf{u}_{\mathbf{o}(r,b)} + \zeta (\hat{\mathbf{n}} - \hat{\mathbf{N}}) \quad (5.20)$$

where $\mathbf{u}_{\mathbf{o}(r,b)}$ is the mid-surface displacement vector and $\hat{\mathbf{N}}$ and $\hat{\mathbf{n}}$ are unit vectors normal to the mid-surface in the reference configuration and in Configuration b , respectively. While $\hat{\mathbf{N}}$ is the

unit vector in the radial direction \mathbf{e}_r , the direction of $\hat{\mathbf{n}}$ is obtained by dividing the vector

$$\mathbf{n} = \left(\frac{\partial \mathbf{X}_0^b}{\partial z} \right) \times \left(\frac{\partial \mathbf{X}_0^b}{\partial \varphi} \right)$$

by its norm, where \mathbf{X}_0^b is the position vector of a point on the mid-surface of the pipe in Configuration b . The gradient of the displacement vector $\mathbf{u}_{(r,b)}$ is defined

as $\mathbf{G}_{(r,b)} = \mathbf{u}_{(r,b)} \otimes \nabla^T$ where \otimes represents the dyadic product and ∇ is the gradient operator with

respect to the reference configuration given in cylindrical coordinates as

$$\nabla = \left\langle \frac{\partial}{\partial z} \mid \left(\frac{1}{r} \right) \frac{\partial}{\partial \varphi} \mid \frac{\partial}{\partial r} \right\rangle^T \quad (5.21)$$

Given the mid-surface displacement vector $\mathbf{u}_{\mathbf{o}(r,b)}$, one can obtain the displacement vector $\mathbf{u}_{(r,b)}$

using Eq.(5.20) and its gradient $\mathbf{G}_{(r,b)}$ using Eq.(5.21).

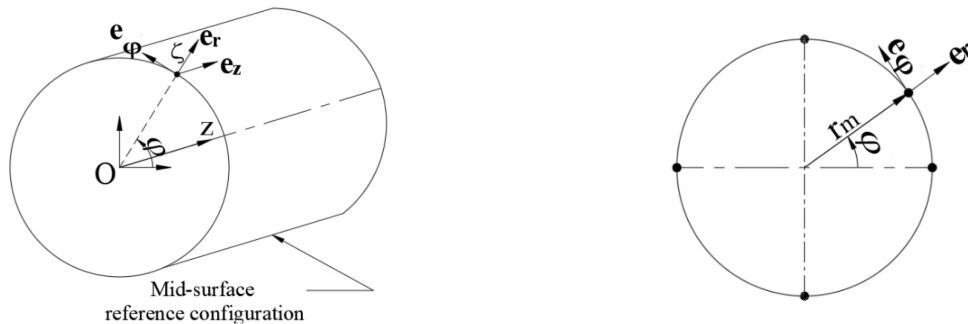


Fig. 5. 2 Pipe coordinate and vector bases in the reference configuration of a straight pipe

5.7.1.2 Characterizing the initial configuration relative to the reference configuration

The cross section of the “imperfect” pipe, which occupies the initial configuration, has a general geometry that represents the initial geometric imperfections. This cross section is characterized by a mid-surface displacement vector $\mathbf{u}_{\mathbf{o}(r,i)}$ relative to the reference configuration. For example, the initial ovality can be characterized by the displacement vector

$$\mathbf{u}_{\mathbf{o}(r,i)} = [f(z) \cos 2\varphi] \mathbf{e}_r \quad (5.22)$$

where $f(z)$ represents the variation of the initial ovality along the longitudinal direction. This variation can be characterized, for instance, by two initial ovality parameters O_1 and O_2 , i.e.,

$f(z) = [H_1(z)O_1 + H_2(z)O_2]$ such that the displacement vector $\mathbf{u}_{\mathbf{o}(r,i)}$ is

$$\mathbf{u}_{\mathbf{o}(r,i)} = [H_1(z)O_1 + H_2(z)O_2] \cos 2\varphi \mathbf{e}_r \quad (5.23)$$

where $H_1(z)$ and $H_2(z)$ are functions that characterize the distribution of initial ovality along coordinate z and O_1 and O_2 characterize the initial ovality values at the ends of the element.

Functions $H_1(z)$ and $H_2(z)$ can be considered to have a Linear distribution (i.e., the initial ovality is assumed to be C^0 continuous) or to follow a Hermitian distribution (C^1 continuous ovality) i.e.,

$$H_1 = (1 - z/L) \quad , \quad H_2 = z/L \quad (5.24)$$

$$H_1 = 2(z/L)^3 - 3(z/L)^2 + 1 \quad , \quad H_2 = -2(z/L)^3 + 3(z/L)^2 \quad (5.25)$$

where L is the length of the element. Uniform initial ovality can be characterized by equating the values of O_1 and O_2 . By following the procedure described in Section 5.7.1.1 (Eqs.(5.20) and (5.21)), one can obtain the displacement vector $\mathbf{u}_{(r,i)}$ and its gradient $\mathbf{G}_{(r,i)}$.

5.7.1.3 Characterizing the deformed configuration relative to the reference configuration

The mid-surface displacement vector $\mathbf{u}_{o(r,d)}$ is assumed to take the form $\mathbf{u}_{o(r,d)} = u_{ok} \mathbf{e}_k$, i.e.,

$$u_{ok} = \left\langle \mathbf{L}(z, \varphi) \right\rangle_{1 \times 4(2m+1)}^T \left\{ \mathbf{d} \right\}_{k \ 4(2m+1) \times 1} \quad k = z, \varphi, r \quad (5.26)$$

in which $\left\{ \mathbf{d} \right\}_{k \ 4(2m+1) \times 1}$ is degrees of freedom vector, $\left\langle \mathbf{L}(z, \varphi) \right\rangle_{1 \times 4(2m+1)}^T$ is the vector of interpolation functions.

$$\left\langle \mathbf{L}(z, \varphi) \right\rangle^T = \left\langle \mathbf{H}(z)^T \mid \cos \varphi \mathbf{H}(z)^T \mid \sin \varphi \mathbf{H}(z)^T \mid \cos 2\varphi \mathbf{H}(z)^T \mid \sin 2\varphi \mathbf{H}(z)^T \mid \dots \mid \cos m\varphi \mathbf{H}(z)^T \mid \sin m\varphi \mathbf{H}(z)^T \right\rangle \quad (5.27)$$

where m is the number of Fourier modes taken, and $\mathbf{H}(z)$ is shape functions vector along the longitudinal direction taken as

$$\mathbf{H}(z) = \left\langle 2(z/L)^3 - 3(z/L)^2 + 1 \quad z[(z/L) - 1]^2 \quad -2(z/L)^3 + 3(z/L)^2 \quad (z^2/L)[(z/L) - 1] \right\rangle^T \quad (5.28)$$

By following the procedure described in Section 5.7.1.1 (Eqs.(5.20) and (5.21)), one can obtain the displacement vector $\mathbf{u}_{(r,d)}$ and its gradient $\mathbf{G}_{(r,d)}$. For the explicit mathematical expressions of $\mathbf{G}_{(r,d)}$ and its derivative with respect to the nodal degrees of freedom vector \mathbf{d} , the reader is referred to Chapter 3 or Ref [27].

5.7.2 Treatment of pipe bends

The reference geometry of a curved pipe (Fig. 5. 3) can be characterized by replacing the rectilinear longitudinal coordinate z introduced in Section 5.7.1.1 with the curvilinear longitudinal coordinate θ . The procedure discussed in Section 5.7.1 for obtaining the displacement vector $\mathbf{u}_{(r,b)}$ and its gradient $\mathbf{G}_{(r,b)}$ for a straight pipe remains valid for a curved pipe with two exceptions

: (1) Vector \mathbf{n} must be determined by $\mathbf{n} = \left(\partial \mathbf{X}_0^b / \partial \theta \right) \times \left(\partial \mathbf{X}_0^b / \partial \varphi \right)$, and (2) Gradient operator ∇ with respect to the reference configuration must be expressed in toroidal coordinates, i.e.,

$$\nabla = \left\langle (1/s) \partial / \partial \theta \mid (1/r) \partial / \partial \varphi \mid \partial / \partial r \right\rangle^T \quad (5.29)$$

in which $s = R + (r_m + \zeta) \cos \varphi$ and R is the elbow radius of the curved pipe (Fig. 5. 3).

Additionally, characterizing the initial and deformed configurations relative to the reference configuration introduced in Sections 5.7.1.2 and 5.7.1.3 of a straight pipe remains valid for a curved pipe with two adjustments:

- 1- Linear and Hermitian interpolation functions of the initial ovality (See Eq.(5.24) and (5.25) for straight pipes) become dependent on the longitudinal curvilinear coordinate θ instead of z as given in Eqs.(5.30) and (5.31)

$$H_1 = \left(1 - \theta / \theta_f \right) \quad , \quad H_2 = \theta / \theta_f \quad (5.30)$$

$$H_1 = 2 \left(\theta / \theta_f \right)^3 - 3 \left(\theta / \theta_f \right)^2 + 1 \quad , \quad H_2 = -2 \left(\theta / \theta_f \right)^3 + 3 \left(\theta / \theta_f \right)^2 \quad (5.31)$$

where θ_f is the angle of the element bend (Fig. 5. 3).

- 2- The interpolation function vector $\mathbf{L}(\theta, \varphi)$ (Eq.(5.27) for straight pipes) also becomes dependent on the longitudinal curvilinear coordinate θ instead of z , i.e.,

$$\langle \mathbf{L}(\theta, \varphi) \rangle^T = \left\langle \mathbf{H}(\theta)^T \mid \cos \varphi \mathbf{H}(\theta)^T \mid \sin \varphi \mathbf{H}(\theta)^T \mid \cos 2\varphi \mathbf{H}(\theta)^T \mid \sin 2\varphi \mathbf{H}(\theta)^T \mid \dots \mid \cos m\varphi \mathbf{H}(\theta)^T \mid \sin m\varphi \mathbf{H}(\theta)^T \right\rangle \quad (5.32)$$

where $\mathbf{H}(\theta)$ is the shape functions vector along the longitudinal direction, i.e.,

$$\mathbf{H}(\theta) = \left\{ \begin{array}{l} \frac{(-\theta + \theta_f) \cos(0.5\theta_f) + \sin(\theta - 0.5\theta_f) - \sin(0.5\theta_f)}{\theta_f \cos(0.5\theta_f) - 2 \sin(0.5\theta_f)} \\ \frac{\csc^2(0.5\theta_f) [-\theta + \theta_f \cos(\theta - \theta_f) + (\theta - \theta_f) \cos \theta_f - \sin \theta + \sin(\theta - \theta_f) + \sin \theta_f]}{-4 + 2\theta_f \cot(0.5\theta_f)} \\ -\frac{-\theta \cos(0.5\theta_f) + \sin(\theta - 0.5\theta_f) + \sin(0.5\theta_f)}{\theta_f \cos(0.5\theta_f) - 2 \sin(0.5\theta_f)} \\ \frac{\csc^2(0.5\theta_f) (\theta - \theta_f + \theta_f \cos \theta - \theta \cos \theta_f - \sin \theta + \sin(\theta - \theta_f) + \sin \theta_f)}{4 - 2\theta_f \cot(0.5\theta_f)} \end{array} \right\} \quad (5.33)$$

Hence, displacement vectors ($\mathbf{u}_{(r,i)}$ and $\mathbf{u}_{(r,d)}$) and their gradient ($\mathbf{G}_{(r,i)}$ and $\mathbf{G}_{(r,d)}$) for a curved pipe can be obtained. Again, the explicit mathematical expressions of $\mathbf{G}_{(r,d)}$ and its derivative with respect to the nodal degrees of freedom vector \mathbf{d} are provided in Chapter 4 or Ref [28].

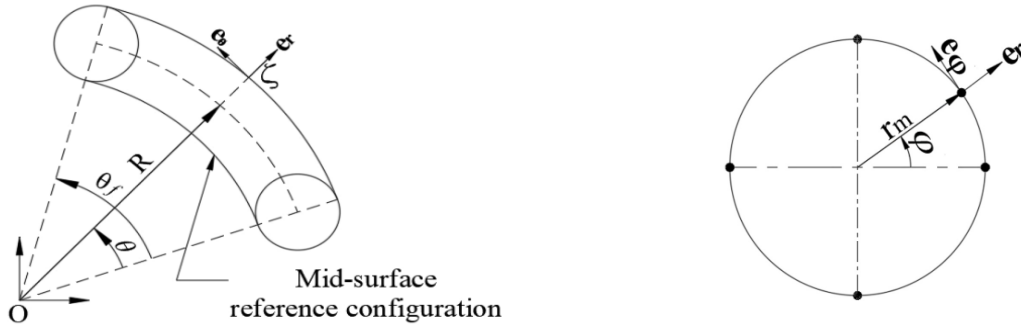


Fig. 5. 3 Pipe coordinate and vector bases in the reference configuration of a curved pipe

5.8 Numerical Examples

5.8.1 Straight Pipes

The straight pipe in Fig. 5. 4 has a mid-surface radius $r_m = 500mm$ and a uniform wall thickness $h = 20mm$. Pipe material is steel with a Young's modulus $E = 210GPa$ and a Poisson's ratio $\nu = 0.3$. Both ends are assumed to be completely fixed. Two initial imperfection scenarios are

modeled (Example 1 and Example 2) using the present formulation and the S4R shell element within the ABAQUS library²³ for comparisons. Table 5. 1 provides details of initial imperfection scenarios, initial ovality characterizations, and loading conditions.



Fig. 5. 4 Geometry of straight pipe

Table 5. 1 Inputs of Example 1 and Example 2

	Example 1 (Section 5.8.1.1)	Example 2 (Section 5.8.1.2)
$L(m)$	6	10
Imperfection Scenario	Non-uniform initial ovality ²⁴ along the entire length (Fig. 5. 5)	a) Uniform initial ovality b) Non-uniform initial ovality c) zero initial ovality (Fig. 5. 6)
Initial ovality characterization	a) Linear distributed (Eq.(5.24)) b) Hermitian distributed (Eq.(5.25))	Hermitian interpolation (Eq.(5.25))
Loading case	a) Internal Pressure (Section 5.8.1.1.1) b) External Pressure (Section 5.8.1.1.2)	Internal Pressure

²³ The S4R model of the imperfect pipe is obtained by assuming initially circular cross-section. Then, initial imperfections are simulated by editing the coordinates of nodes in the input file.

²⁴ Initial ovality value = Initial ovality percentage \times mid-surface radius/100

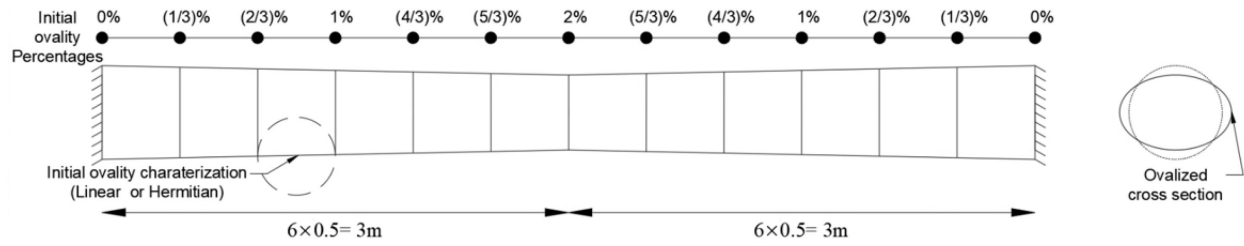


Fig. 5. 5 Geometry of the imperfect pipe in Example 1

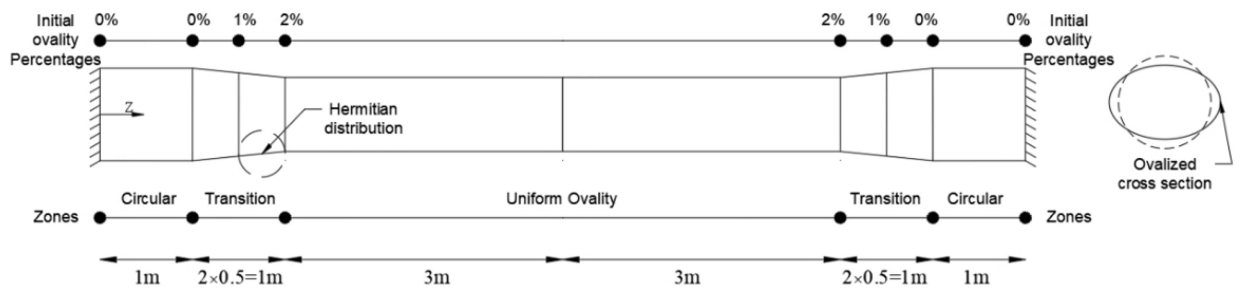


Fig. 5. 6 Geometry of the imperfect pipe in Example 2

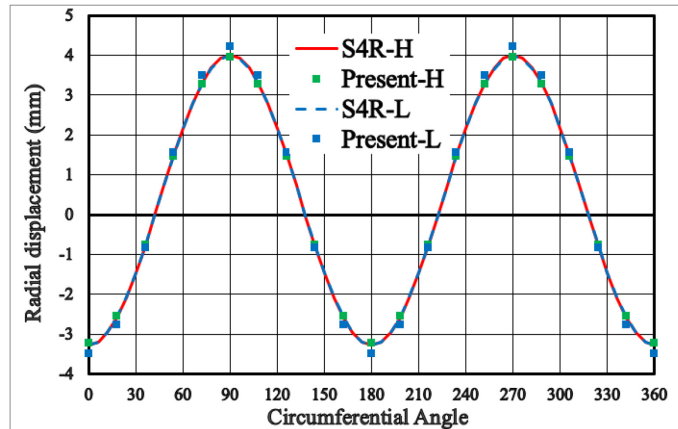
5.8.1.1 Example 1

5.8.1.1.1 Internal Pressure Loading

An imperfect pipe (Fig. 5. 5) is subjected to internal pressure of 5MPa at the inner surface. The present formulation adopts six Fourier modes and twelve elements along the length (i.e., the length of a single element is 500 mm). The mesh size of the S4R model is 50mm ²⁵. Two distributions of the initial ovality along the elements are investigated: Linear (L) and Hermitian (H) distributions. Both models predict an oscillatory distribution of the displacements along the circumferential direction at mid-span (Fig. 5. 7). In a similar manner, Fig. 5. 8 depicts an oscillatory distribution for the hoop stresses at the same cross-section. The modelling of initial ovality in the S4R model using the linear imperfection scheme (Eq.(5.24)) generates displacements and stresses that are

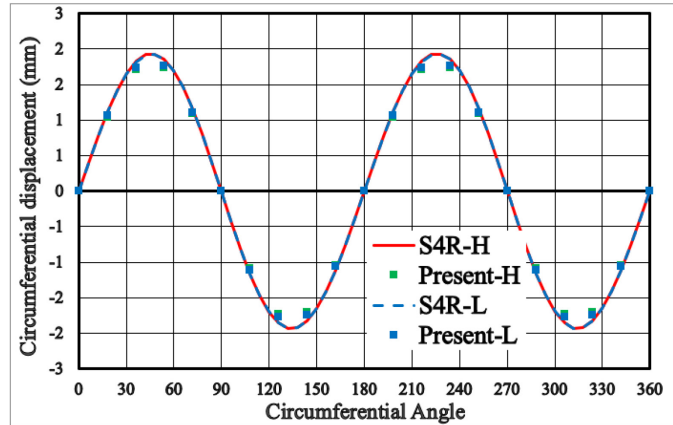
²⁵ The number of degrees of freedom is 1,014 and 43,560 for the present formulation and the S4R model, respectively.

nearly identical to those obtained using the Hermitian imperfection scheme (Eq.(5.25)) (Fig. 5. 7 and Fig. 5. 8) since the S4R model is based on numerous facet elements with small kinks in between them. In contrast, stress predictions of the present formulation are highly affected by the type of the initial ovality (Fig. 5. 8) where the linear characterization of the initial ovality induces a kink at mid-span while the Hermitian characterization provides a smooth transition of pipe ovality at mid-span. Hoop stress predictions induced by the Hermitian ovalization characterization are thus in excellent agreement with those of the S4R model whereas the linear ovalization characterization induces inaccurate hoop stress predictions. However, displacement predictions in both ovalization patterns are very close and in a close agreement with S4R predictions. If the pipe is assumed to be perfectly circular, the hoop stress distribution would be constant and equal to 121.8 MPa ²⁶ which is about half of the maximum hoop stress in this example. Therefore, the proper modelling of initial ovality is essential to accurately predict the structural response and the concomitant stress distribution.



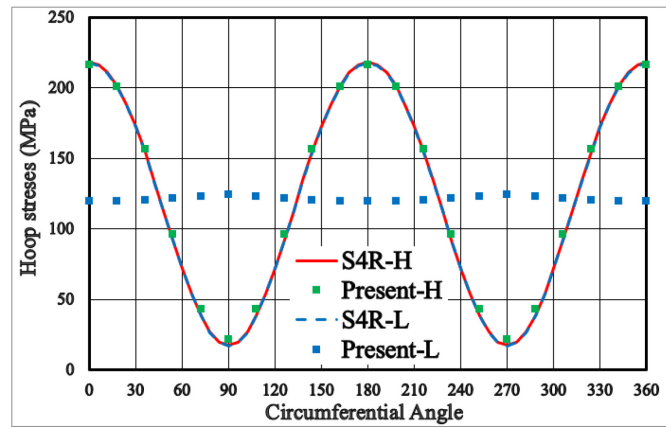
a

²⁶ This value is obtained from a S4R model adopting initially circular cross section.

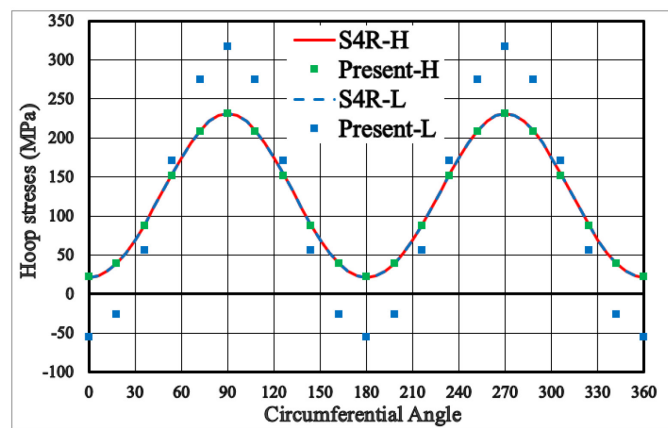


b

Fig. 5. 7 Displacement field distributions along the circumferential direction at $z = 3m$.
 (a) Radial and (b) Circumferential



a



b

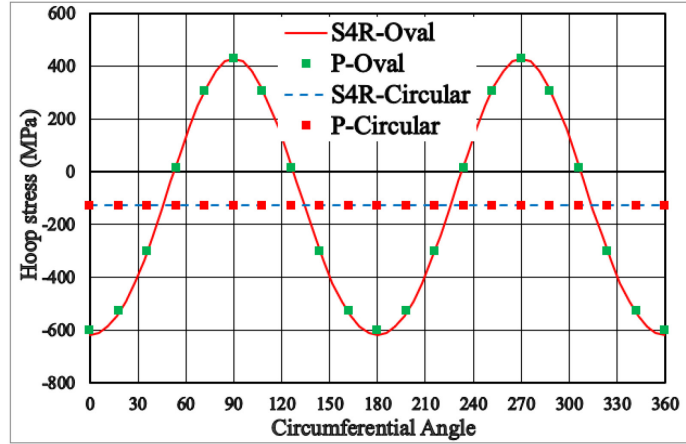
Fig. 5. 8 Hoop stress distributions under internal pressure at $z = 3m$ for the
 (a) Inner Surface and (b) Outer Surface

5.8.1.1.2 External Pressure Loading

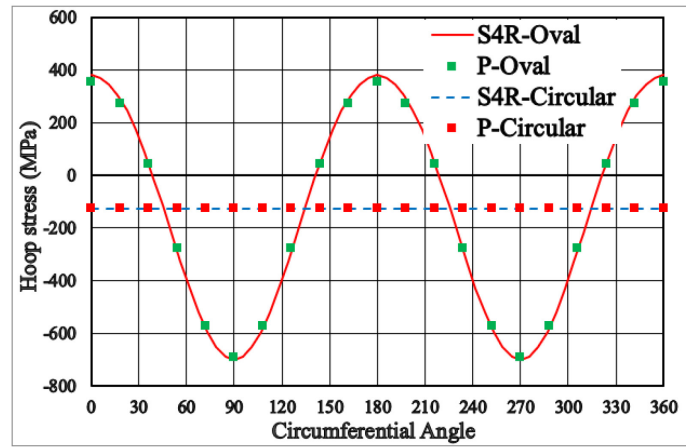
A uniform external pressure of 5MPa is applied to the outer surface of the imperfect pipe (Fig. 5. 5). A Hermitian distribution of the initial ovality is taken along the elements. Three runs are conducted under the present formulation based on (M) Fourier modes and (E) elements (M=6, E=12), (M=8, E=12), and (M=6, E=20). The mesh size of the S4R shell model was kept constant at 50 mm. Hoop stress distributions along the circumferential direction at the mid-span of the pipe are presented in Fig. 5. 9 for the inner and outer surfaces. The predictions of the oval cross section exhibit an oscillatory response with a maximum tensile hoop stress of 428 MPa (Fig. 5. 9a) and a maximum compressive hoop stress of 700 MPa (Fig. 5. 9b). This compares to a compressive hoop stress of 127 MPa for perfectly circular cross section with no ovality. An excellent agreement is obtained between the predictions generated by the present formulation and those based on the S4R model²⁷. The comparison shows that the formulation is able to accurately capture the response of the pipe under external pressure with and without an ovality.

Table 5. 2 presents the hoop stress values at $\varphi = 0$ and $\varphi = 90^\circ$ at the inner and outer surface using three sets of Fourier modes and elements. Hoop stress predictions do not change when the number of Fourier modes is increased from six to eight while increasing the number of the elements from 12 to 20 tangibly decreases the percentage differences. Under the same value of pressure (e.g., 5MPa), the external pressure loading on the ovalized pipe generates much higher hoop stresses than the internal pressure loading (as evidenced by comparing Fig. 5. 8 and Fig. 5. 9). It is also observed that the present formulation requires more elements under external pressure than under internal pressure to accurately predict the structural response.

²⁷ Predictions of the present formulation shown in Fig.9 are based on six Fourier modes and twenty elements.



a



b

Fig. 5. 9 Hoop stress distributions under external pressure at $z = 3m$ for the (a) Inner Surface and (b) Outer Surface

Table 5. 2 Hoop stress values (MPa) at the inner and outer surfaces

Surface	Circumferential angle		S4R	Present (P)		
				(M=6, E=12)	(M=8, E=12)	(M=6, E=20)
Inner	0°	Value	-621	-585	-585	-602
		% ^a	-	5.8	5.8	3.1
	90°	Value	428	402	402	427
		% ^a	-	6.1	6.1	0.2
Outer	0°	Value	380	334	334	352
		% ^a	-	12.1	12.1	7.4
	90°	Value	-701	-667	-667	-689
		% ^a	-	4.9	4.9	1.7

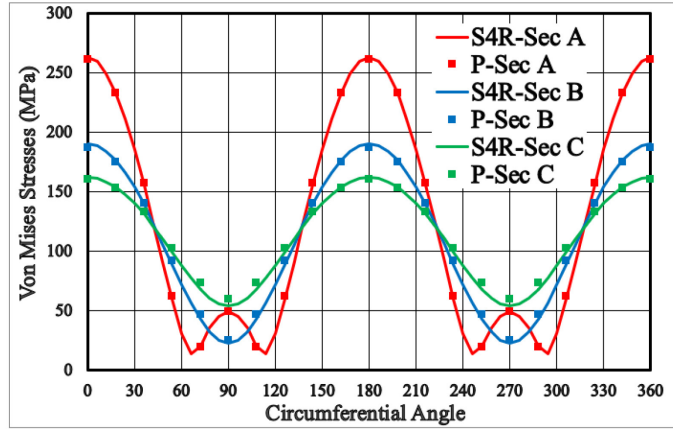
^a % = (shell output – present formulation output) × 100 / shell output

5.8.1.2 Example 2

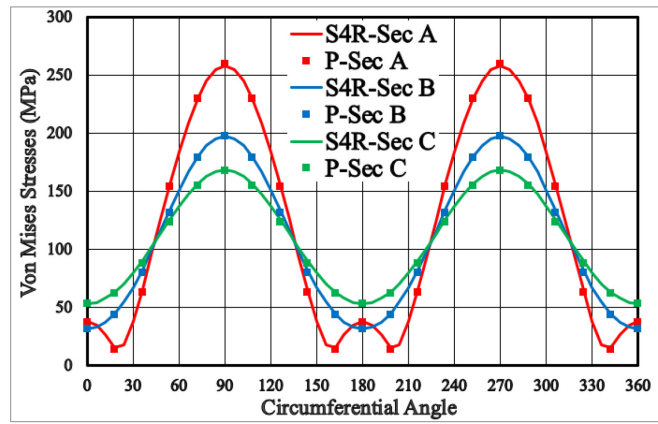
The present example examines the response of a pipe with the initial imperfection scenario illustrated in Fig. 5. 6 where the pipe is divided into three zones: (a) a zone of circular cross-section with no ovality, (b) a zone of varying ovality ranging from circular cross-section at one end to a fully ovalized section at the other end following a Hermitian characterization between ends, and (c) a zone of uniform ovality. The imperfect pipe is subjected to internal pressure of 5MPa applied to the inner surface of the pipe. The present formulation employs six Fourier modes and twenty elements while mesh size of the S4R model is 50 mm^{28} . Stress distributions at three cross sections are examined at (a) Section A at mid-span $z = 5\text{ m}$, (b) Section B at the end of the transition zone $z = 2\text{ m}$, and (c) Section C at the middle of the transition zone $z = 1.5\text{ m}$. Fig. 5. 10 depicts the von Mises stress distributions along the circumferential direction at Sections A, B, and C for the inner and outer surfaces. The von Mises stresses exhibit an oscillatory response at all three cross-sections. However, the maximum von Mises stress at Section A is 261 MPa (Fig. 5. 10a), that at Sections B is 198 MPa and that at Section C is 167 MPa (Fig. 5. 10b). The proximity of the predictions of the present model to those of the shell S4R model at the three cross-sections considered is indicative of the ability of the present formulation to accurately predict the stress distributions including the through-wall thickness variations.

Table 5. 3 provides the maximum hoop stress values at the different cross-sections. The constant hoop stress value in a circular cross-section is provided for comparison. At Section A, it is of interest to note that the ovalized cross-section has a maximum hoop stress value that exceeds twice that of a circular cross section.

²⁸ The number of degrees of freedom for the present formulation is 1,638 and 72,372 for the S4R model.



a



b

Fig. 5. 10 Von Mises stress distribution along the circumferential direction at the (a) Inner Surface and (b) Outer Surface

Table 5. 3 Maximum hoop stress values (MPa)

	Circular	Sec A	Sec B	Sec C
Max. Hoop Stress	122	291	225	186
Ratio ^a	-	2.4	1.8	1.5

^a Ratio = oval hoop stress / circular hoop stress

5.8.2 Curved Pipes

The outer diameter D_o of the perfect 90° pipe bend shown in Fig. 5. 11 is 1066.8mm and its wall thickness h is 9.525mm . Young's modulus for the pipe steel is $E = 210\text{GPa}$ and the Poisson's ratio $\nu = 0.3$. A Hermitian characterization of the ovalization along the elements is considered

(Table 5. 4) with maximum ovality percentage of 4 % at mid-section ($\theta = 45^\circ$) and zero ovality at both ends ($\theta = 0^\circ, 90^\circ$). The bottom end is assumed to be completely fixed while the top end's boundary conditions depend on the loading condition as shown in Table 5. 5. Three loading conditions are examined (Table 5. 5): (1) Internal pressure (Example 3), (2) In-plane loading (Example 4), and (3) Out-of-plane loading (Example 5). The present formulation adopts eight Fourier modes and ten elements. The mesh size is 30 mm in the Abaqus shell S4R model²⁹.

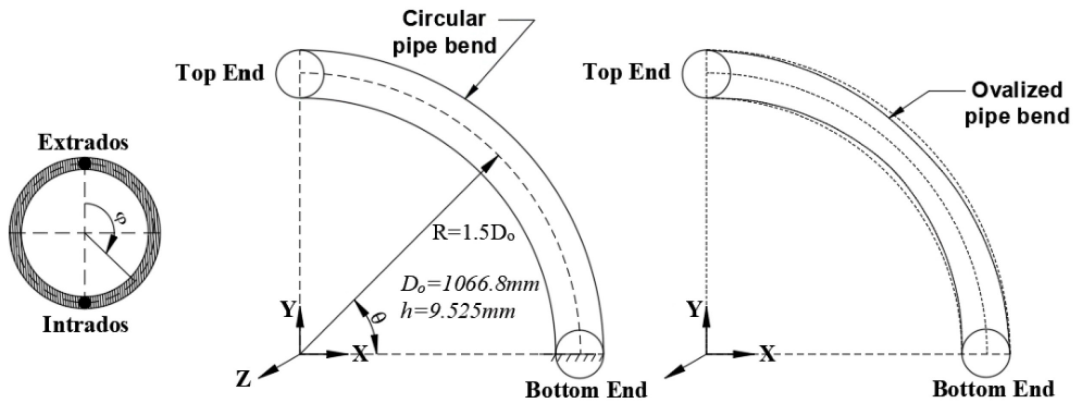


Fig. 5. 11 Geometry of the pipe bend

Table 5. 4 Initial ovality profile of the pipe bend (symmetric at $\theta = 45^\circ$)

Longitudinal coordinate θ (deg)	0	9	18	27	36	45
Initial Ovality percentage %	0	0.8	1.6	2.4	3.2	4
Initial Ovality value (mm) ^a	0	4.23	8.46	12.69	16.92	21.15

^a Initial ovality value = Initial ovality percentage \times mid-surface radius/100

²⁹ The number of degrees of freedom in the present formulation is 1,122 that in the S4R shell model is 56,100.

Table 5. 5 Loading cases of the curved pipe

	Example 3 (Sec 5.8.2.1)	Example 4 (Sec 5.8.2.2)	Example 5 (Sec 5.8.2.3)
Traction	P=3.5MPa	H=V=40MPa	T=50MPa
Top End	Free	Rigid ³⁰	Rigid
Cross section			

5.8.2.1 Example 3

The inner surface of the imperfect pipe bend shown in Fig. 5. 11 is subjected to an internal pressure of 3.5MPa. Fig. 5. 12 depicts an oscillatory response for the displacement fields along the circumferential direction at mid-section ($\theta = 45^\circ$). Table 5. 6 provides the maximum values of the longitudinal and radial displacements obtained from the present formulation and the S4R shell model assuming oval and circular cross sections. The predictions of the present model for the ovalized bend are in close agreement with those based on the S4R shell model and the percentage

³⁰ Rigid means that the cross section deforms as a single node. No ovality or warping is allowed.

difference are below 5%. The close proximity of the displacement predictions of the present formulation to those based on the S4R shell model showcases the ability of the present model to capture the response of the ovalized bend. The bend with the perfectly circular cross-section is associated with a stiffer radial and longitudinal responses than that with an ovalized cross-section.

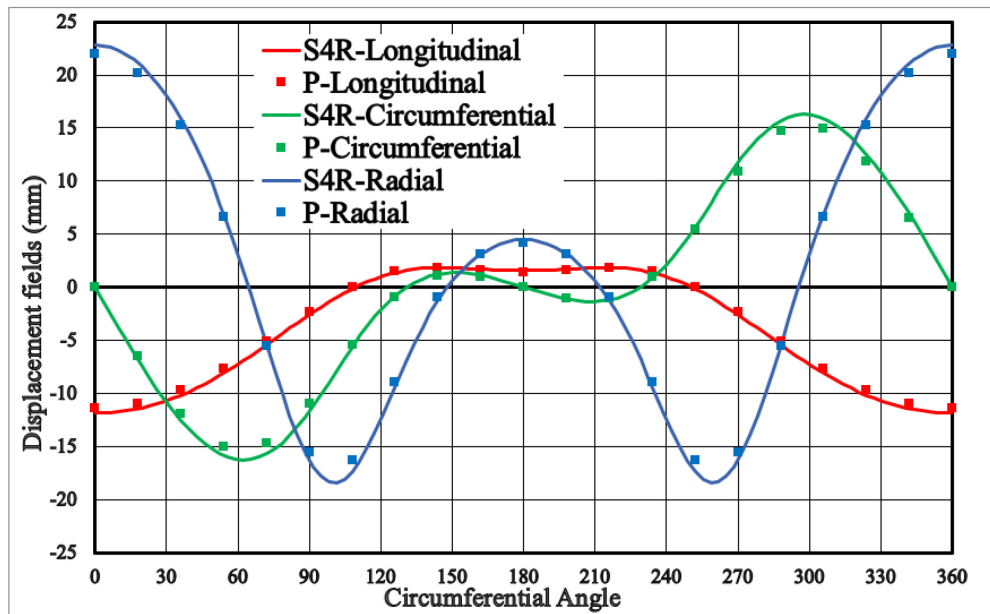


Fig. 5. 12 Displacement field distributions along the circumferential angle at $\theta = 45^\circ$.

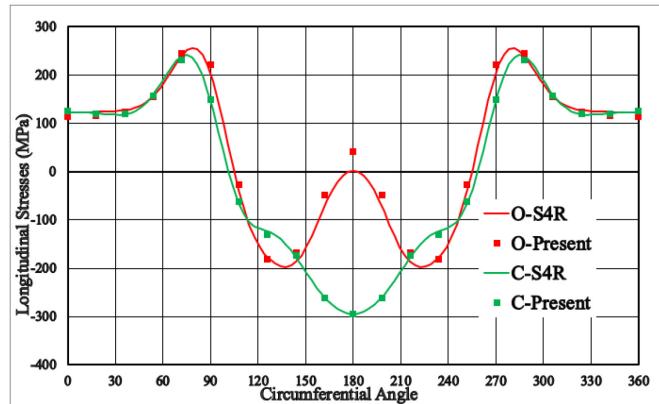
Table 5. 6 Values of maximum longitudinal and radial displacements (mm)

	S4R shell model		Present formulation	
	Oval	Circular	Oval	Circular
Max. Longitudinal displacement	-11.86	-10.19	-11.35	-9.72
% ^a	-	14.1	4.3	18
Max. Radial displacement	22.77	17.62	21.94	16.87
% ^a	-	22.6	3.6	25.9

^a % = (shell oval displacement – other displacement) × 100 / shell oval displacement

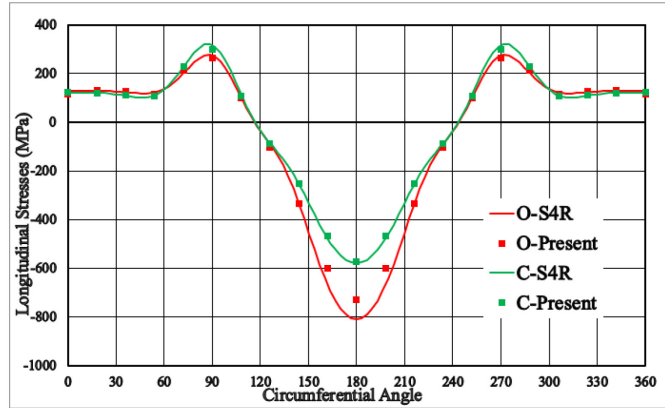
5.8.2.2 Example 4

Horizontal $H = 40\text{MPa}$ and vertical $V = 40\text{MPa}$ tractions are applied at the top end of the pipe bend as illustrated in Table 5. 5³¹. Oval (O) and circular (C) cross-sections are assumed to verify the effect of the initial ovality under in-plane loading. The oscillatory responses of the longitudinal and hoop stress distributions at mid-section ($\theta = 45^\circ$) are shown in Fig. 5. 13 for the inner and outer surfaces. The difference between the solutions of oval and circular cross-sections assumptions is highly pronounced around $\varphi = 180^\circ$. The circular bend experiences maximum compressive longitudinal (Fig. 5. 13a) and hoop (Fig. 5. 13c) stresses higher than the ovalized pipe at the inner surface. In contrast, these maximum stresses at the outer surface are higher in case of the ovalized pipe (Fig. 5. 13b and Fig. 5. 13d). The predictions of the present model with and without ovality are in close agreement with those based on the S4R shell model and the percentage differences at the outer surface are below 10 % for maximum compressive longitudinal stress and 5 % for maximum compressive hoop stress. The close proximity of the stress predictions of the present formulation to those based on the S4R shell model demonstrates the ability of the present formulation to capture the response of the ovalized pipe under in-plane loading.

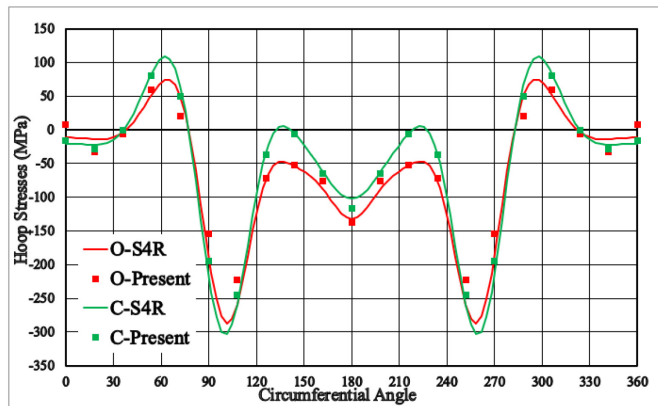


a

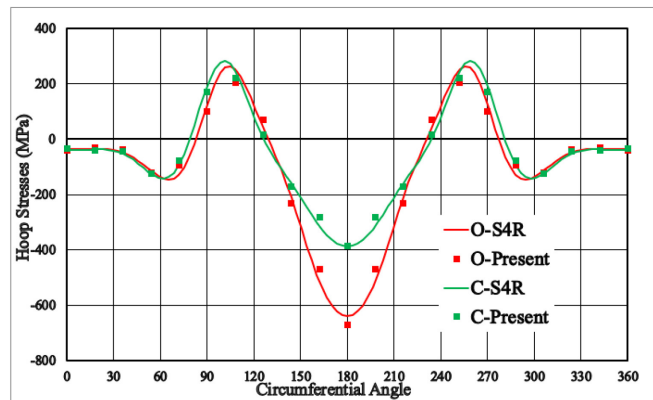
³¹ A set of equivalent nodal forces are applied in the S4R shell model to simulate the applied tractions.



b



c

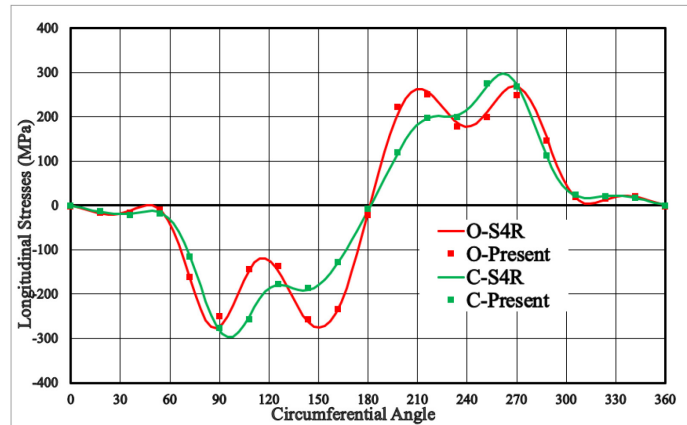


d

Fig. 5. 13 Stress fields along the circumferential angle at $\theta = 45^\circ$ for the (a) Longitudinal - Inner Surface, (b) Longitudinal -Outer Surface, (c) Hoop - Inner Surface, and (d) Hoop -Outer Surface

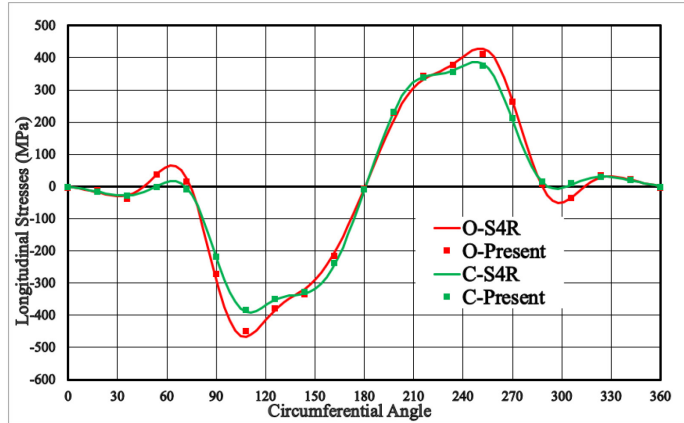
5.8.2.3 Example 5

The bend pipe shown in Fig. 5. 11 is subjected to a traction³² $T = 50MPa$ at the top end of the pipe bend in the positive Z-direction as demonstrated in Table 5. 5. Fig. 5. 14 depicts the longitudinal and hoop stress distributions along the circumferential direction at the mid-section ($\theta = 45^\circ$) for the inner and outer surfaces. The solution based on oval cross-section assumption is associated with higher longitudinal stresses at the outer surface (Fig. 5. 14b) and larger hoop stresses at both surfaces (Fig. 5. 14c and Fig. 5. 14.d) when compared to those of a pipe bend with a perfectly circular cross section. The predictions of the present formulations are in excellent agreement with those generated by the S4R shell model. The proximity of the stress predictions of the present formulation to those based on the S4R shell model shows the high accuracy of the present formulation to properly capture the structural response of a pipe bend under out-of-plane loading with and without ovality.

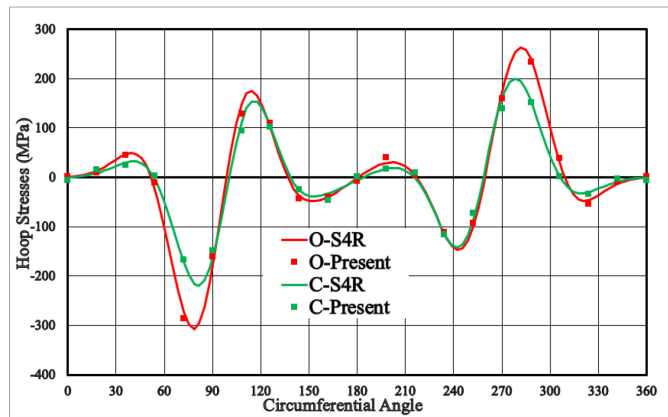


a

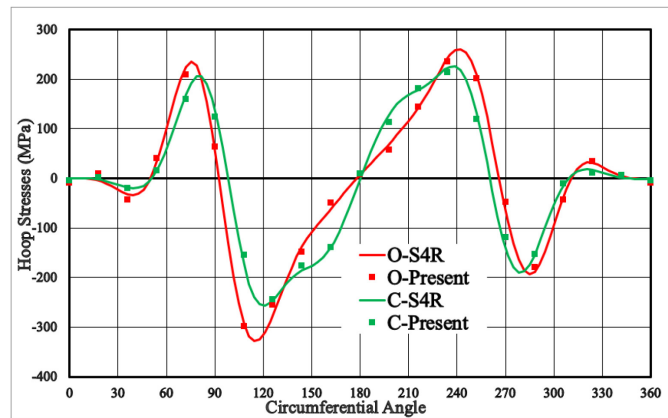
³² A set of equivalent nodal forces are applied in the S4R shell model to simulate the applied tractions.



b



c



d

Fig. 5. 14 Stress fields along the circumferential angle at $\theta = 45^\circ$ for the (a) Longitudinal - Inner Surface, (b) Longitudinal -Outer Surface, (c) Hoop - Inner Surface, and (d) Hoop -Outer Surface

5.9 Summary

A simple and novel FE formulation is developed for simulating the geometrically nonlinear structural response in the elastic regime for initially ovalized straight and curved pipes. An initially circular cross-sectional pipe configuration is utilized as a mediator configuration between the initial (e.g., ovalized pipes) and deformed configurations. The framework of the principle of virtual work is adopted in conjunction with the total Lagrangian approach. The Saint Venant Kirchhoff constitutive model is adopted to relate the second Piola-Kirchhoff stress tensor to the Green-Lagrange strain tensor. The kinematic constraints of Love-Kirchhoff thin shell theory are enforced within the assumed displacement fields. Several numerical examples are provided to assess the displacement and stress predictions of the present formulation against those generated by the S4R shell model within the ABAQUS library. The present formulation is able to accurately predict the structural response of initially ovalized straight and curved pipes under various loading conditions. The main findings of the present study can be summarized as follow:

1. While the type of initial ovality distribution along the length of the element has no effect on the S4R shell model, it is highly influential in the present formulation.
2. The type of pressure applied (i.e., internal versus external) has a significant influence on the response of initially ovalized straight pipes.
3. The number of elements needed of the ovalized straight pipes under external pressure is higher than that needed under internal pressure to accurately capture the structural response.
4. For a pipe having a uniform initial ovality zone under internal pressure, the section located at mid-zone experiences higher von Mises stresses than that located at the beginning of the ovality zone.

5. An initially ovalized pipe bend under internal pressure exhibits a more flexible radial and longitudinal responses than that of a similar pipe bend with a perfectly circular cross-section.
6. Eight Fourier modes are required to accurately predict the structural response of initially ovalized pipe bends under in-plane and out-of-plane loading.
7. In general, the modelling of initial ovality provides a significantly different response from similar pipes with no ovality. Thus, the modelling of initial ovality is imperative for the accurate prediction of the pipe structural response.

5.10 Nomenclature

$\tilde{\mathbf{B}}$	Body force vector per unit reference volume
\mathbf{C}	The Saint-Venant-Kirchhoff constitutive tensor
d_j	The j^{th} component of the nodal degrees of freedom vector
\mathbf{d}	Nodal degrees of freedom vector
\mathbf{d}^*	Virtual nodal degrees of freedom vector
$d\mathbf{X}^d$	A tangential vector in the deformed configuration
$d\mathbf{X}^i$	A tangential vector in the initial configuration
$d\mathbf{X}^r$	A tangential vector in the reference configuration
E	Young's Modulus
$\mathbf{E}_{(i)}$	The Green-Lagrange strain tensor defined in the initial configuration
\mathbf{e}_r	Unit vector in the radial direction
\mathbf{e}_z	Unit vector in the longitudinal direction of a straight pipe
\mathbf{e}_θ	Unit vector in the longitudinal direction of a curved pipe
\mathbf{e}_ϕ	Unit vector in the circumferential direction
\mathbf{I}	Identity tensor
$\mathbf{F}^{(I)}$	Internal force vector
$\mathbf{F}^{(E)}$	External force vector
$\mathbf{F}_{(i,d)}$	The deformation gradient tensor that transform a tangential vector from the initial configuration to the deformed configuration
$\mathbf{F}_{(r,d)}$	The deformation gradient tensor that transform a tangential vector from the reference configuration to the deformed configuration
$\mathbf{F}_{(r,i)}$	The deformation gradient tensor that transform a tangential vector from the reference configuration to the initial configuration

$\mathbf{G}_{(r,d)}$	The gradient of the displacement field vector between the reference and deformed configurations
$\mathbf{G}_{(r,i)}$	The gradient of the virtual displacement field vector between the reference and initial configurations
$\mathbf{G}^*_{(r,d)}$	The gradient of the virtual displacement field vector between the reference and deformed configurations
h	Pipe wall thickness in the reference configuration
$\mathbf{H}(z)$	Shape functions in the longitudinal direction of a straight pipe
$\mathbf{H}(\theta)$	Shape functions in the longitudinal direction of a curved pipe
\mathbf{K}	Stiffness matrix
\mathbf{K}^F	Exact contribution of the external force vector to the stiffness matrix
\mathbf{K}^T	Exact tangent stiffness matrix
\mathbf{K}_A^F	Approximated contribution of the external force vector to the stiffness matrix
\mathbf{K}_A^T	Approximated tangent stiffness matrix
L	Length of the element
\mathbf{L}	Interpolation functions vector
m	Total Fourier terms /modes
\mathbf{N}	Vector normal to the mid-surface in the reference configuration
$\hat{\mathbf{N}}$	Unit vector normal to the mid-surface in the reference configuration
\mathbf{n}	Vector normal to the mid-surface in the deformed configuration
$\hat{\mathbf{n}}$	Unit vector normal to the mid-surface in the deformed configuration
O_1, O_2	Values of the initial ovality at the ends of the element
$\mathbf{P}_{(i,d)}$	The first Piola-Kirchhoff stress tensor that transform an area vector from the initial configuration to the deformed configuration
$\mathbf{P}_{(r,d)}$	The first Piola-Kirchhoff stress tensor that transform an area vector from the reference configuration to the deformed configuration
R	Elbow radius of a curved pipe
r	Radial coordinate as measured from the origin point
r_m	Mid-surface radius
S^r	The reference surface that encloses volume V^r
$\mathbf{S}_{(i)}$	The second Piola-Kirchhoff stress tensor defined in the initial configuration
$\tilde{\mathbf{T}}_{\mathbf{N}}$	Applied traction vector per unit reference surface dS^r normal to the unit vector $\hat{\mathbf{N}}$
$\mathbf{u}_{(r,d)}$	Displacement vector for a generic point between the reference and deformed configurations
$\mathbf{u}_{(r,i)}$	Displacement vector for a generic point between the reference and initial configurations
$\mathbf{u}^*_{(r,d)}$	Virtual displacement vector for a generic point between the reference and deformed configurations
$\mathbf{u}^*_{(r,i)}$	Virtual displacement vector for a generic point between the reference and initial configurations

$\mathbf{u}_{o(r,d)}$	Displacement vector for a point on the mid-surface between the reference and deformed configurations
$\mathbf{u}_{o(r,i)}$	Displacement vector for a point on the mid-surface between the reference and initial configurations
u_{or}	Radial displacement of a point on the mid-surface
u_{oz}	Longitudinal displacement of a point on the mid-surface of a straight pipe
$u_{o\theta}$	Longitudinal displacement of a point on the mid-surface of a curved pipe
$u_{o\varphi}$	Circumferential displacement of a point on the mid-surface
V^r	The reference volume
\mathbf{X}^d	Position vector of a point in the deformed configuration
\mathbf{X}^i	Position vector of a point in the initial configuration
\mathbf{X}^r	Position vector of a point in the reference configuration
\mathbf{X}_o^b	Position vector of a point on the mid-surface of the pipe in Configuration b
z	Longitudinal coordinate of a straight pipe
∇	The gradient operator with respect to the reference configuration
ζ	Radial coordinate as measured from the mid-surface
θ	Longitudinal coordinate of a curved pipe
θ_f	Angle of the curved pipe
ν	Poisson's ratio
$\boldsymbol{\sigma}$	The Cauchy stress tensor
φ	Circumferential coordinate
Ω^d	Deformed configuration
Ω^i	Initial configuration
Ω^r	Reference configuration

5.11 Acknowledgments

The authors express their gratitude to TC Energy, and Enbridge Pipelines Inc. for their technical assistance and discussions.

5.12 Funding

This research was partially funded by: NSERC, MITACS, Enbridge Pipelines Inc., and TC Energy.

5.13 References

- [1] Von Karman, T., 1911, "Ueber Die Formänderung Dünnwandiger Rohre, Insbesondere Federnder Ausgleichrohre," *Z. Ver. Deut. Ing.*, 55(Part2), pp.1889–1895.
- [2] Vigness, I., 1943, "Elastic Properties of Curved Tubes," *J. Appl. Mech.*, 55, pp.102–120.
- [3] Kafka, P. G., and Dunn, M. B., 1953, "Stiffness of Curved Circular Tubes with Internal Pressure," Boeing Airplane, Chicago, IL.
- [4] Wood, J. D., 1958, "The flexure of a uniformly pressurized circular, cylindrical shell" *J. Appl. Mech.*, 25, pp. 453-458.
- [5] Dodge, W. G., and Moore, S. E., 1972, "Stress Indices and Flexibility Factors for Moment Loadings on Elbows and Curved Pipes," *Welding Research Council Bulletin* 179.
- [6] Hong, S.-P., An, J.-H., Kim, Y.-J., Nikbin, K., and Budden, P. J., 2011, "Approximate Elastic Stress Estimates for Elbow Under Internal Pressure," *Int. J. Mech. Sci.*, 53(7), pp. 526–535.
- [7] WeiB, E., Lietzmann, A., and Rudolph, J., 1996 "Linear and Nonlinear Finite-Element Analysis of Pipe Bends," *Int. J. Pres. Ves. & Piping.*, 67, pp. 211-217.
- [8] Abdulhamed, D., Adeeb, S., Cheng, R., and Martens, M., 2016, "The Influence of the Bourdon Effect on Pipe Elbow," ASME Paper No. IPC2016-64659.
- [9] Abdulhamed, D., 2017 "The Behavior of Pipe Bends under Internal Pressure and In-Plane Bending Loading," Doctoral dissertation, University of Alberta, Edmonton, Canada.
- [10] Weicker, K., Salahifar, R., and Mohareb., M., 2010, "Shell Analysis of Thin-Walled Pipes. Part I-Field equations and solution," *Int. J. Pres. Ves. & Piping.*, 87, pp.402-413.
- [11] Weicker, K., Salahifar, R., and Mohareb., M., 2010, "Shell Analysis of Thin-Walled Pipes. Part II-Finite Element Formulation," *Int. J. Pres. Ves. & Piping.*, 87, pp.414-423.
- [12] Ohtsubo, H., and Watanabe, O., 1978, "Stress Analysis of Pipe Bends by Ring Elements," *ASME J. Pressure Vessel Technol.*, 100(1), pp. 112–122.
- [13] Bathe, K. J., and Almeida, C. A., 1980, "A Simple and Effective Pipe Elbow Element, Linear Analysis," *J. Appl. Mech.*, 47(1), pp. 100–193.
- [14] Bathe, K. J., and Almeida, C. A., 1982, "A Simple and Effective Pipe Elbow Element, Pressure Stiffening Effects," *J. Appl. Mech.*, 49(4), pp. 914–915.
- [15] Bathe, K. J., and Almeida, C. A., 1982, "A Simple and Effective Pipe Elbow Element, Interaction Effects," *J. Appl. Mech.*, 49, pp. 165–171.
- [16] Militello, C., and Huespe, A. E., 1988, "A Displacement- Based Pipe Elbow Element," *Comput. Struct.*, 29(2), pp. 339–343.
- [17] Fonseca, E. M. M., de Melo, F. J. M. Q., and Oliveira, C. A. M., 2006, "Numerical Analysis of Piping Elbows for In-Plane Bending and Internal Pressure," *Thin-Walled Struct.*, 44, pp.393-398.
- [18] Basaran, S., 2008, "Lagrangian and Eulerian Descriptions in Solid Mechanics and Their Numerical Solutions in hpk Framework," Doctoral dissertation, The University of Kansas, Kansas, United states.
- [19] Holzapfel, G. A., 2000, "Nonlinear Solid Mechanics: A Continuum Approach for Engineering," Chichester: Wiley.
- [20] Bonet, J., and Wood, R., 2008, "Nonlinear Continuum Mechanics for Finite Element Analysis," Cambridge: Cambridge University Press. doi:10.1017/CBO9780511755446
- [21] Bathe, K. J., 1996, "Finite Element Procedures in Engineering analysis," Prentice Hall, New Jersey.

- [22] Pagani, A., and Carrera, E., 2018, "Unified formulation of geometrically nonlinear refined beam theories," *Mech. Adv. Mater. Struc.*, 25(1), pp. 15-31
- [23] Wu, B., Pagani, A., Chen, W. Q., and Carrera, E., 2019, "Geometrically nonlinear refined shell theories by Carrera Unified Formulation," *Mech. Adv. Mater. Struc.*, DOI: 10.1080/15376494.2019.1702237
- [24] ANSYS, Inc. ELBOW290, Retrieved from https://www.mm.bme.hu/~gyebro/files/ans_help_v182/ans_elem/Hlp_E_ELBOW290.htm
- [25] Simulia ABAQUS. 2017. User's Manual version 6.6 documentation
- [26] ADINA R& D, Inc. 2012. Theory and Modeling Guide Volume I
- [27] Attia, S., Mohareb, M., Martens, M., Ghodsi, N., Li, Y. and Adeeb, S., 2021 "Shell Finite Element Formulation for Geometrically Nonlinear Analysis of Straight Thin-Walled Pipes". "under Review"
- [28] Attia, S., Mohareb, M., Martens, M., Ghodsi, N., Li, Y. and Adeeb, S., 2021 "Shell Finite Element Formulation for Geometrically Nonlinear Analysis of Curved Thin-Walled Pipes". "under Review"
- [29] Fallqvist, B., "Collapse of thick deepwater pipelines due to hydrostatic pressure," Master dissertation, Royal Institute of Technology, Stockholm, Sweden.
- [30] Toscano, R. G., 2009, "Collapse and post-collapse behavior of steel pipes under external pressure and bending. Application to deep-water pipelines," Doctoral dissertation, Universidad de Buenos Aires, Argentina.
- [31] Veerappan, A. R., and Shanmugam, S., 2006, "Stress analysis of pipe bends subjected to internal pressure fluid pressure using the finite element technique," *J. Strain Analysis*, 41(8), pp. 561-573.
- [32] Veerappan, A. R., and Shanmugam, S., 2008, "Analysis for Flexibility in the Ovality and Thinning Limits of Pipe Bends," *ARNP JEAS*, 3(1), pp. 31-41
- [33] Christo Michael, T., Veerappan, A. R., and Shanmugam, S., 2012, "Effect of ovality and variable wall thickness on collapse loads in pipe bends subjected to in-plane bending closing moment," *Eng. Fract. Mech.*, 79, pp.138-148.
- [34] Christo Michael, T., Veerappan, A. R., and Shanmugam, S., 2012, "Comparison of plastic limit and collapse loads in pipe bends with shape imperfections under in-plane bending and an internal pressure," *Int. J. Pres. Ves. & Piping.*, 99-100, pp.23-33
- [35] Buckshumiyar, A., Veerappan, A. R., and Shanmugam, S., 2014, "Determination of collapse loads in pipe bends with ovality and variable wall thickness under internal pressure and in-plane opening moment," *Int. J. Pres. Ves. & Piping.*, 123-124, pp.1-9.
- [36] Chen, Y., and Parker, J., 2012, "The Effect of Ovality and Thickness variations on Stress Analysis of Tube Bends Under Internal Pressure," ASME Paper No. PVP2012-78113
- [37] El-Gebaly, S. H., 2016, "Ultra Deepwater Pipe Bend Design Guidelines," Doctoral dissertation, University of Surrey, England.
- [38] Li, T., 2016, "On the formulation of a pipe element for a pipe structure with variable wall thickness," *Ocean Eng.* 117, 398–410.
- [39] Li, T., 2017, "On the formulation of a pipe element II: An orthogonal polynomial pipe element," *Ocean Eng.* 129, 279–290.
- [40] Li, T., 2017, "On the formulation of a 3D smooth curved pipe finite element with arbitrary variable cross-section," *Thin-Walled Structures.* 117, 314–331.

[41] Johnson, B., E., and Hoger, A., 1995, "The Use of a Virtual Configuration in Formulating Constitutive Equations for Residually Stressed Elastic Materials," *Journal of Elasticity*. 41: 177-215

Chapter 6 Summary & Conclusion

6.1 Summary and conclusion

The present dissertation, in Chapter 2, investigates the structural response of ELBOW elements implemented in ABAQUS under internal pressure. A standalone 90° pipe bend is studied to demonstrate the effect of pipe bend radius, boundary conditions, and material characterization on the different stress fields. Although ELBOW elements are able to accurately capture the sophisticated response of a pipe bend under internal pressure, the modelling techniques for boundary conditions have a tangible effect on the stress results. Moreover, the present study recommends using ELBOW elements in the modelling of the straight portions adjacent to pipe bends, while PIPE elements can be utilized for the remaining straight segments in long pipeline transmission systems. In addition, ASME B16.49-2017 equation for the pipe bend thickness and previously published stress estimate equations are assessed in comparison to elbow and shell model predictions in ABAQUS.

Starting with the principle of virtual work for static equilibrium expressed in the reference configuration and formulated in terms of the first Piola-Kirchhoff stress tensor, generalized expressions of force vectors and stiffness matrix are derived in terms of generic displacement fields. These expressions are thus applicable for various applications (e.g., beams, shells). Additionally, contribution of follower pressure load into the external force vector and the stiffness matrix is recovered in the developed formulations.

For initially circular thin-walled straight pipes, the kinematic assumptions of the Love-Kirchhoff thin shell theory are adopted to characterize displacement fields in a cylindrical coordinate system. The unit vector normal to the deformed configuration is obtained while avoiding introducing any approximations. Mid-surface displacement fields are interpolated using cubic Hermitian polynomials along the longitudinal direction while the variation of the displacement fields along the circumferential direction is described using: (1) Fourier series expansion, (2) Spline interpolation, and (3) Mixed Fourier-Spline interpolation. The performance and predicting accuracy of the elements are assessed through comparisons with finite element models based on shell and elbow elements in ABAQUS under various loading conditions. The results demonstrate the ability of the elements to predict the displacement and stress fields. In particular, the element based on Fourier series interpolation is shown to provide accurate predictions.

For initially circular thin-walled curved pipes, the displacement fields are described in a toroidal coordinate system based on the kinematic constraints of the thin shell theory. Fourier series are adopted to characterize the displacement fields along the circumferential direction while three C^1 continuous schemes (e.g., Hermitian, Trigonometric, and Mixed) are used to interpolate the displacement fields along the longitudinal direction. Eigenvalue analyses are performed to assess the ability of the elements to represent rigid body motion. The element based on mixed interpolation scheme demonstrates its efficiency to capture rigid body motion modes. Comparisons with other shell and elbow models highlight the accuracy and versatility of the proposed formulation.

In Chapters 3 and 4, the reference configuration is assumed to coincide with the un-deformed configuration. In contrast, Chapter 5 introduces three configurations for the pipe under consideration to consider initial geometric imperfections. These configurations are: (1) un-deformed configuration that represents the imperfect pipe, (2) deformed configuration, and (3) reference configuration which is assumed to have a perfectly circular cross-section with uniform wall thickness. The first Piola-Kirchhoff stress tensor expressed in the reference configuration is formulated in terms of the strains induced by the deformation of the pipe from the un-deformed to the deformed configurations. This idea allowed the writer to re-use computer codes developed in Chapters 3 and 4 to add the contribution of initial geometric imperfections with relatively simple modification to these codes. Several examples are solved on ovalized straight and curved pipes to assess the accuracy of the present formulations by comparisons against the general shell models under various loading conditions. In general, the predictions (e.g., displacements and stresses) of the proposed formulations are very close to those obtained from general shell models.

6.2 Limitations of the developed formulations

FE formulations proposed in the present dissertation are developed to predict the geometrically nonlinear structural response of linearly elastic isotropic thin-walled straight and curved pipes subjected to general static loading. Although these FE formulations are able to capture finite deformations (e.g., finite rotations), they are formulated based on small strain theory. Currently, these formulations are implemented under the Wolfram Mathematica platform.

6.3 Proposed future work

Since the generalized force vectors and stiffness matrix in the present study are expressed in terms of generic displacement fields, the present formulation can be seamlessly applied to other shell geometries (e.g., spherical and parabolic domes). The formulation can be modified for thick shells capturing the through thickness shear strains by adopting appropriate kinematic constraints. In addition, the formulation can be extended to account for material constitutive models (e.g., hyperelastic, hypo-elastic, elasto-plastic), to capture finite strains, and for dynamic analysis. Also, the current formulations can be incorporated within a general-purpose FE software (e.g., ABAQUS) for practicality purposes.

References

- Von Karman, T., 1911, "Ueber Die Formänderung Dünnwandiger Rohre, Insbesondere Federnder Ausgleichrohre," *Z. Ver. Deut. Ing.*, 55(Part2), pp.1889–1895.
- Vigness, I., 1943, "Elastic Properties of Curved Tubes," *J. Appl. Mech.*, 55, pp.102–120.
- Kafka, P. G., and Dunn, M. B., 1953, "Stiffness of Curved Circular Tubes with Internal Pressure," Boeing Airplane, Chicago, IL.
- Turner, C. E., and Ford, H., 1957, "Examination of the Theories for Calculating the Stresses in Pipe Bends Subjected to In-Plane Bending," *Proc. Inst. Mech. Engrs.*, 171: 513-515.
- Smith, R. T., 1967, "Theoretical Analysis of the Stresses in Pipe Bends Subjected to Out-of-Plane Bending," *J. Mech. Eng. Sci.*, 9(2).
- Clark, R.A., and Reissner, E., 1951, "Bending of Curved Tubes," *Advances in Applied Mechanics*, Academic Press, New York, Vol. 2, pp.93-122.
- Cheng, D. H., and Thailer, H. J., 1968, "In-Plane Bending of Curved Circular Tubes," *J. Eng. Ind. Trans.*, ASME Paper No. 68-PVP-12.
- Hong, S.-P., An, J.-H., Kim, Y.-J., Nikbin, K., and Budden, P. J., 2011, "Approximate Elastic Stress Estimates for Elbow Under Internal Pressure," *Int. J. Mech. Sci.*, 53(7), pp. 526–535.
- WeiB, E., Lietzmann, A., and Rudolph, J., 1996 "Linear and Nonlinear Finite-Element Analysis of Pipe Bends," *Int. J. Pres. Ves. & Piping.*, 67, pp. 211-217.
- Abdulhamed, D., 2017 "The Behavior of Pipe Bends under Internal Pressure and In-Plane Bending Loading," Doctoral dissertation, University of Alberta, Edmonton, Canada.
- Ohtsubo, H., and Watanabe, O., 1978, "Stress Analysis of Pipe Bends by Ring Elements," *ASME J. Pressure Vessel Technol.*, 100(1), pp. 112–122.
- Bathe, K. J., and Almeida, C. A., 1980, "A Simple and Effective Pipe Elbow Element, Linear Analysis," *J. Appl. Mech.*, 47(1), pp. 100–193.
- Bathe, K. J., and Almeida, C. A., 1982, "A Simple and Effective Pipe Elbow Element, Pressure Stiffening Effects," *J. Appl. Mech.*, 49(4), pp. 914–915.
- Bathe, K. J., and Almeida, C. A., 1982, "A Simple and Effective Pipe Elbow Element, Interaction Effects," *J. Appl. Mech.*, 49, pp. 165–171.
- Militello, C., and Huespe, A. E., 1988, "A Displacement- Based Pipe Elbow Element," *Comput. Struct.*, 29(2), pp. 339–343.
- Abo-Elkhier, M., 1990, "Analysis of Pipe Bends Using Pipe Elbow Element," *Comput. Struct.*, 37(1), pp. 9–15.
- Yan, A. M., Jospin, R. J., and Nguyen, D. H., 1999, "An Enhanced Pipe Elbow Element-Application in Plastic Limit Analysis of Pipe Structures," *Int. J. Numer. Methods. Eng.*, 46(3), pp.409-431.
- Fonseca, E. M. M., de Melo, F. J. M. Q., and Oliveira, C. A. M., 2006, "Numerical Analysis of Piping Elbows for In-Plane Bending and Internal Pressure," *Thin-Walled Struct.*, 44, pp.393-398.
- Weicker, K., Salahifar, R., and Mohareb., M., 2010, "Shell Analysis of Thin-Walled Pipes. Part I-Field equations and solution," *Int. J. Pres. Ves. & Piping.*, 87, pp.402-413.
- Weicker, K., Salahifar, R., and Mohareb., M., 2010, "Shell Analysis of Thin-Walled Pipes. Part II-Finite Element Formulation," *Int. J. Pres. Ves. & Piping.*, 87, pp.414-423.

- Basaran, S., 2008, “Lagrangian and Eulerian Descriptions in Solid Mechanics and Their Numerical Solutions in hpk Framework,” Doctoral dissertation, The University of Kansas, Kansas, United states.
- Holzapfel, G. A., 2000, “Nonlinear Solid Mechanics: A Continuum Approach for Engineering,” Chichester: Wiley.
- Bonet, J., and Wood, R., 2008, “Nonlinear Continuum Mechanics for Finite Element Analysis,” Cambridge: Cambridge University Press. doi:10.1017/CBO9780511755446
- Bathe, K. J., 1996, “Finite Element Procedures in Engineering analysis,” Prentice Hall, New Jersey.
- Bathe, K. J., and Almeida, C. A., 1982, “A Simple and Effective Pipe Elbow Element, Some Nonlinear Capabilities,” *J. Appl. Mech.*, 49(1), pp.165–173.
- ADINA R& D, Inc.2012. Theory and Modeling Guide Volume I
- ANSYS, Inc. ELBOW290, Retrieved from https://www.mm.bme.hu/~gyebro/files/ans_help_v182/ans_elem/Hlp_E_ELBOW290.html
- Simulia ABAQUS. 2017.User’s Manual version 6.6 documentation
- Zeng, L., Jansson, L. G., and Venev, Y., 2014, “On Pipe Elbow Elements in ABAQUS and Benchmark Test,” ASME Paper No. PVP2014-28920.
- Bryan, B. J., 1994, *Static Analysis of a Piping System with Elbows (WSRCMS-94-075)*, Minneapolis, MN.
- Pagani, A., and Carrera, E., 2018, “Unified formulation of geometrically nonlinear refined beam theories,” *Mech. Adv. Mater. Struc.*, 25(1), pp. 15-31
- Wu, B., Pagani, A., Chen, W. Q., and Carrera, E., 2019, “Geometrically nonlinear refined shell theories by Carrera Unified Formulation,” *Mech. Adv. Mater. Struc.*, DOI: 10.1080/15376494.2019.1702237
- Duan, L., Zhao, J., 2019, “A geometrically exact cross-section deformable thin-walled beam finite element based on generalized beam theory,” *Comput. Struct.*, 218, pp.32-59.
- Meroueh, K. A., 1986, “On a Formulation of a Nonlinear Theory of Plates and Shells with Applications,” *Comput. Struct.*, 24(5), pp. 691-705.
- Campello, E. M. B., Pimenta, P. M., Wriggers, P., 2003, “A triangular finite shell element based on a fully nonlinear shell formulation,” *Computational Mechanics*, 31, pp. 505-518.
- Ivannikov, V., Tiago, C., Pimenta, P. M., 2014, “On the boundary conditions of the geometrically nonlinear Kirchhoff-Love shell theory,” *Int. J. Solids Struct*, 51, pp. 3101-3112.
- Fallqvist, B., “Collapse of thick deepwater pipelines due to hydrostatic pressure,” Master dissertation, Royal Institute of Technology, Stockholm, Sweden.
- Toscano, R. G., 2009, “Collapse and post-collapse behavior of steel pipes under external pressure and bending. Application to deep-water pipelines,” Doctoral dissertation, Universidad de Buenos Aires, Argentina.
- Veerappan, A. R., Shanmugam, S., 2006, “Stress analysis of pipe bends subjected to internal pressure fluid pressure using the finite element technique,” *J. Strain Analysis*, 41(8), pp. 561-573.
- Christo Michael, T., Veerappan, A. R., Shanmugam, S., 2012, “Effect of ovality and variable wall thickness on collapse loads in pipe bends subjected to in-plane bending closing moment,” *Eng. Fract. Mech.*, 79, pp.138-148.

- Christo Michael, T., Veerappan, A. R., Shanmugam, S., 2012, “Comparison of plastic limit and collapse loads in pipe bends with shape imperfections under in-plane bending and an internal pressure,” *Int. J. Pres. Ves. & Piping.*, 99-100, pp.23-33
- Buckshumiyan, A., Veerappan, A. R., Shanmugam, S., 2014, “Determination of collapse loads in pipe bends with ovality and variable wall thickness under internal pressure and in-plane opening moment,” *Int. J. Pres. Ves. & Piping.*, 123-124, pp.1-9.
- Love, A.E.H., 1892, “A treatise on the Mathematical Theory of Elasticity,” 1st Edition, Cambridge University Press.
- Sanders, J.L., 1959, “An Improved First Approximation Theory for Thin Shells,” NASA TR-R24
- Lur’ye, A.I., 1940, “General theory of elastic shells,” *Prikl Mat Mekh*, vol.4, No.4, pp. 7-34
- Novozhilov, V.V., 1964, “Theory of Thin Elastic Shells,” 2nd Edition, P. Noordhoff, Groningen
- Flugge, W., 1973. “Stresses in Shells,” Springer-Verlag, New York Heidelberg Berlin
- Salahifar, R., 2011 “Analysis of Pipelines Systems under Harmonic Forces,” Doctoral dissertation, University of Ottawa, Ontario, Canada.
- Attia, S., Mohareb, M., Martens, M., Yoosef-Ghodsi, N., Li, Y., and Adeeb, S., 2021, “Numerical Assessment of Elbow Element Response Under Internal Pressure,” *ASME. J. Pressure Vessel Technol.*, 143(5): 051302. <https://doi.org/10.1115/1.4050091>
- Johnson, B., E., and Hoger, A., 1995, “The Use of a Virtual Configuration in Formulating Constitutive Equations for Residually Stressed Elastic Materials,” *Journal of Elasticity*. 41: 177-215
- El-Gebaly, S. H., 2016, “Ultra Deepwater Pipe Bend Design Guidelines,” Doctoral dissertation, University of Surrey, England.
- Li, T., 2016, “On the formulation of a pipe element for a pipe structure with variable wall thickness,” *Ocean Eng.* 117, 398–410.
- Li, T., 2017, “On the formulation of a pipe element II: An orthogonal polynomial pipe element,” *Ocean Eng.* 129, 279–290.
- Li, T., 2017, “On the formulation of a 3D smooth curved pipe finite element with arbitrary variable cross-section,” *Thin-Walled Structures*. 117, 314–331.
- Dawe, D. J., 1972, “Rigid-body motions and strain-displacement equations of curved shell finite elements,” *Int. J. Mech. Sci.*, 14, pp 569-578
- Adeeb, S. First and Second Piola Kirchhoff Stress Tensors. Retrieved from <https://sameradeeb-new.srv.ualberta.ca/stress/first-and-second-piola-kirchhoff-stress-tensors/>
- Petersen, K., Pedetsen, M. The Matrix Cookbook. Retrieved from <https://www.ics.uci.edu/~welling/teaching/KernelsICS273B/MatrixCookBook.pdf>